Stable polymer glasses

by

Junjie Yin

A thesis
presented to the University of Waterloo
in fulfillment of the
thesis requirement for the degree of
Doctor of Philosophy
in
Physics (Nanotechnology)

Waterloo, Ontario, Canada, 2023

Examining Committee Membership

The following served on the Examining Committee for this thesis. The decision of the Examining Committee is by majority vote.

External Examiner:	Mark D. Ediger Professor, Dept. of Chemistry, University of Wisconsin–Madison
Supervisor(s):	James A. Forrest Professor, Dept. of Physics and Astronomy, University of Waterloo
Internal Member:	Jeff Z. Y. Chen Professor, Dept. of Physics and Astronomy, University of Waterloo
Internal-External Member:	Jean Duhamel Professor, Dept. of Chemistry, University of Waterloo
Other Member(s):	David Hawthorn Professor, Dept. of Physics and Astronomy, University of Waterloo

Author's Declaration

This thesis consists of material all of which I authored or co-authored: see Statement of Contributions included in the thesis. This is a true copy of the thesis, including any required final revisions, as accepted by my examiners.

I understand that my thesis may be made electronically available to the public.

Statement of Contributions

This thesis contains four main content chapters: Chapters. 3, 4, 5, and 6. Three of these chapters are written based on four co-authored papers.

Chapter 3 is based on the following paper of which I am the second author: A. N. Raegen, **J. Yin**, Q. Zhou, & J. A. Forrest. Ultrastable monodisperse polymer glass formed by physical vapour deposition. *Nature Materials*, 19(10), 1110-1113 (2020). DOI: 10.1038/s41563-020-0723-7 [1]. I contributed to helping develop the sample preparation and characterization techniques, producing part of the experimental data, data analysis, writing and editing the paper and supplementary material as well as answering reviewer comments.

Section 5.2 in Chapter 5 is based on the following paper of which I am the first author: **J. Yin**, C. Pedersen, M. F. Thees, A. Carlson, T. Salez, & J. A. Forrest. Surface and bulk relaxation of vapor-deposited polystyrene glasses. *The Journal of Chemical Physics*, 158(9), 094901 (2023). DOI: 10.1063/5.0133668 [2]. I contributed to all of the experimental part including sample preparation and characterizations, data analysis, generating all figures with the experimental data I collected and data from the numerical solutions obtained by my co-author Pedersen, writing and editing the main paper and the supplementary material, as well as answering reviewer comments.

Section 6.1 in Chapter 6 is based on the following paper of which I am the first author: **J. Yin** & J. A. Forrest. Film thickness dependent stability and glass transition temperature of polymer films produced by physical vapor deposition. *Physical Review Letters*, 130(16), 168101 (2023). DOI: 10.1103/PhysRevLett.130.168101 [3]. I contributed to all of the experimental part including sample preparation and characterizations, data analysis, generating all figures, writing and editing the main paper as well as answering reviewer comments.

Section 6.2 in Chapter 6 is based on an ongoing work: **J. Yin**, S. Karimi & J. A. Forrest. Rejuvenation in thin films of ultrastable PS prepared by physical vapor deposition. *In preparation* (2023) [4]. I have contributed to the experiments including sample preparation and characterizations, producing all the preliminary data and performing preliminary data analysis.

Abstract

This thesis presents investigations on stable polymer glasses prepared through physical vapour deposition from different perspectives. This is the first time that polymers have been used in simple vapour deposition and made into stable glass.

The ability of our lab to create stable polymer glasses with exceptional stability and extremely long lifetimes is demonstrated through the preparation and characterization of ultrastable PS as well as PMMA glasses. Compared to liquid cooled regular glasses, these materials exhibit enhanced kinetic stability, low fictive temperatures and high density characteristic of stable glasses. With a molecular weight distribution that can be controlled with vapour deposition, stable polymer glasses have high tunabilities on properties such as the glass transition temperature, which is one of the most important factors that differentiate them from stable molecular glasses. By controlling the substrate temperature and deposition rate, a variety of stable polymer glasses are prepared and characterized.

Attempts at preparing stable polymer glass with higher molecular weight are reported, including two different methods–using higher molecular weight sources and crosslinking as-deposited glasses with ultraviolet radiation. Although the molecular weight is still limited in our studies, valuable lessons are learned about vapour deposited stable glasses. The highest molecular weight to be achieved from simple vapour deposition is limited by the competition between the deposition rate and the rate of chain scission. The mass distributions in vapour deposited glass films are characterized after UV treatment, and interesting measurements from ellipsometry are linked to possible processes that could occur in vapour deposited polymer glasses during UV treatment.

The enhanced surface dynamics is considered to be critical in the process of making stable glasses. Thus the surface properties of stable polymer glasses including their surface morphology and surface relaxation are studied. Observations of unique morphology features on the surface of some glasses are reported and the reasons behind them are explored. With the aid of gold nanoparticles, quantitative characterizations of the surface and bulk dynamics under external perturbations are performed. The build-up of polymer material around the nanoparticle provides a quantitative measure of the surface mobility, and the final bulk embedding of the nanoparticle describes the bulk dynamics of stable polymer glasses. With a slower bulk dynamics in stable glasses as expected, the surface evolution of the as-deposited films and the rejuvenated films are both enhanced compared to the bulk and are not easily distinguishable from each other.

Investigations on stable polymer glasses confined to thin films are reported. The influence of film thickness on properties of glassy thin films including their glass transition temperature has been extensively studied for many years. Similarly, film thickness dependence in stable glasses for thin films down to 11 nm is observed. Particularly, the thickness dependence of the glass transition temperature, thermodynamic and kinetic stability including the onset temperature, fictive temperature and the increased density are studied. The results support the existence of a surface mobile layer, and it is found that glass stability decreases with decreasing film thickness, as determined by different measures of stability. The rejuvenation process from a stable glass to a supercooled liquid is also investigated and the results show that rejuvenation appears to happen below the traditionally defined onset temperature, suggesting that a fraction of the film is not stable in the as-deposited glasses. The fraction of stable glasses is quantitatively analyzed in thin films, and the rejuvenation rate is also found to be dependent on film thickness.

The glass transition in polymer thin films has been a vibrant research area for three decades and the new type of material–stable glass–has also attracted great research interest since it was first discovered. At the intersection of these two research fields, stable polymer glasses are an excellent candidate for contributing into both fields and hopefully will open up a new area of research on its own. By studying these materials from different perspectives in this thesis, we hope to provide valuable insights into many fundamental questions about the surface dynamics in thin films, the limit of packing in amorphous materials, and the nature of the complex and fascinating phenomenon–the glass transition.

Acknowledgements

I am grateful for all the support and help I have received from my mentors, colleagues, friends and family during my PhD studies. It would have been impossible for me to navigate through the difficult times especially with impact that the COVID-19 pandemic has had on an experimental PhD student.

First of all, I would like to express my sincere gratitude to my supervisor James A. Forrest. It has been a great experience working in the Forrest lab for the past several years. Without his guidance and support this thesis wouldn't be possible. I am thankful for all the trust he has given me, as well as the opportunities he provided me with to present at international conferences since I was a first year master's student. His enthusiasm towards research and his encouragement during these years has helped me grow into a better researcher.

I would also like to thank the members of my supervisory committee: Jeff Z. Y. Chen, David Hawthorn, and Jean Duhamel. I appreciate the support and input from every one of them in our regular committee meetings, the comprehensive exam, as well as the thesis examination. In particular, I would like to thank Jean for carefully reading my thesis and pointing out many typographical errors that I have missed. I am thankful for the opportunities to participate in the events at the Institute for Polymer Research (IPR) where Jean is the director, for the IPR award, and for his suggestions when I consulted him about career options. I also thank Mark D. Ediger for being my external examiner and providing insightful comments and suggestions. I appreciate the collaboration opportunities with Stefan H. J. Idziak, Christian Pedersen, Andreas Carlson, and Thomas Salez, from whom I learned a lot.

The physics department and the Waterloo Institute of Nanotechnology (WIN) has provided me with much help in my time here. I am grateful for being awarded the WIN Nanofellowships. The use of the ellipsometer in the Quantum-Nano Fabrication and Characterization Facility (QNFCF) facility is acknowledged. I also appreciate the technical support from the Science Technical Services.

My life at Waterloo has been enjoyable thanks to my friends here, including my fellow students, previous and current members in the Forrest lab. I would like to thank Shipei Zhu, Adam. N. Raegen, Tiana Trumpour, Zhaohui Cai, Qi Zhou, Michael F. Thees, Sakiba Shahnaz, Saba Karimi, Mahnoor Mehmood, Qirui Liu, and Romey Zhang for their support and helpful discussions. I also thank every one of my friends in Waterloo for their friendship and kindness.

Finally, I would like to thank my family for their support and love. My parents Baocai Yin and Ziping Wang have always had my back throughout my life, no matter what I am pursuing and where I am studying. My siblings Yijia and Haoyang have given me the fun and happiness of being a big sister, although I have been away from them for a big part of their lives. My partner and best friend Junan Lin has shared the same PhD life as mine, and I am so glad that we went through this journey together. His love and understanding has supported me to become a better person.

Dedication

This is dedicated to my family.

Table of Contents

List of Figures

List of Tables

Chapter 1

Introduction

Glasses are disordered solids that play an important role in our daily life. From window glass and optical fibers made of amorphous silica to many industrial polymeric glasses, their wide range of applications have shaped our lives in every possible way. Despite their abundant presence, the nature of glasses is still mysterious to us and the research on glasses has been an ongoing marathon. Nobel Laureate Philip Anderson commented in 1995 [29], "The deepest and most interesting unsolved problem in solid state theory is probably the nature of glass and the glass transition."

Recently, new insights have been provided by the exciting discovery of ultrastable glasses near the limits of the densest amorphous packing in the form of an "ideal glass" which may be the ground state that ordinary glasses are trying to reach. In this thesis, we explore these newly discovered materials and hope to gain a better understanding of glasses. Not only on the fundamental level, the study of stable glasses is also important on the applied level. Studies of stable glasses have also suggested that they are attractive candidates for better organic light-emitting diodes (OLEDs) [30], higher quality mirrors for the Laser Interferometer Gravitational-Wave Observatory (LIGO) [31], more robust packaging, etc.

1.1 Structure of this thesis

This thesis covers most of the work I conducted during my Ph.D. studies on stable polymer glasses. This is the first time stable polymer glasses have been prepared through simple physical vapour deposition and I am the first Ph.D. student during our lab's exploration and development in this research area. This means that we have developed every aspect of the process along the way. To date, we are the only group with this demonstrated capacity. Among all of the exploratory studies included in this thesis, some of them turned out to contribute to this area of research with significant impact. Although some of the projects were not as successful in making scientific progress, they still provide meaningful insights into these novel materials and could help guide future research. In this thesis we include both the studies that are published or going to be published [1, 2, 3, 4], as well as those that did not end up in publications. Another paper [32] that was published during my Ph.D. of which I am the first author is not covered in this thesis.

The structure of the thesis is as follows.

In Chapter 1 basic concepts about polymers, glasses, and the glass transition are presented. Studies on glassy thin films and their interfacial dynamics are reviewed, and stable glasses by physical vapour deposition are introduced. In Chapter 2 the experimental techniques used to prepare and characterize these materials are described. Chapter 3 is based on a paper of which I am the second author [1], where we report the preparation and characterization of ultrastable PS as well as PMMA glasses, which demonstrates the ability to apply physical vapour deposition to polymers and create stable glasses for the first time. In chapter 4, two projects are reviewed where we push our limits and pursue stable polymer glass with the highest molecular weight. In this attempt, we use two different methods–using higher molecular weight sources and crosslinking as-deposited glasses with ultraviolet radiation. Chapter 5 also contains two parts. In Section 5.1 I report observations of their special morphology features and explore the reasons behind them. Section 5.2 is based on a paper of which I am the first author [2], where we quantitatively characterize the surface mobility of vapour deposited stable polymer glass utilizing external perturbations. In Chapter 6 I investigate stable polymer glasses confined to thin films in two aspects. Section 6.1 is based on a paper of which I am the first author [3], where we find that similar to regular confined films, the film thickness also influences the properties of stable glasses including their stability and glass transition temperature. Section 6.2 is an ongoing, unpublished work [4] where we study the thickness dependence of the transformation process from a stable glass to a supercooled liquid. Chapter 7 summarizes this thesis and suggests some future work.

1.2 Polymers

Polymers are large molecules that consist of many repeating units–monomers–connected by covalent bonds. From synthetic polymers such as polystyrene and polyethylene to natural polymers such as DNA, proteins and natural rubber, polymers play an important part in the daily life and the human history with their broad range of properties and applications.

The number of monomers that a polymer contains is defined as its degree of polymerization or polymerization index, N. Thus the molecular weight of a polymer is $M = NM_{\mathrm{mon}}$, where M_{mon} is the molecular weight of a monomer. Polymers with large N values are also called macromolecules. With smaller N values (typically lower than 20), the properties of the material change significantly upon the addition or removal of one monomer, and such polymers are also called oligomers.

Polymers that contain only one type of monomers are called homopolymers, while those containing two or more types of monomers are called heteropolymers [33]. For example, polystyrene is a homopolymer while DNA is a heteropolymer consisting of 4 types of monomers (nucleotides).

Polymer samples normally contain a distribution of components with different lengths. In order to describe the average size of the entire sample, there are two common ways to calculate the average molecular weight–the number average molecular weight, M_{n}, and the weight average molecular weight, M_{w}:

$$M_{\mathrm{n}} = \frac{\sum N_i M_i}{\sum N_i} = \sum n_i M_i \tag{1.1}$$

$$M_{\mathrm{w}} = \frac{\sum N_i M_i^2}{\sum N_i M_i} = \sum w_i M_i \tag{1.2}$$

where M_i is the molecular weight of a polymer chain, and N_i is the number of polymer chains with molecular weight M_i. n_i and w_i represent the number fraction and weight fraction of a particular component, respectively. In either way of calculation, the fractions of all components always add up to 1, expressed as $\sum n_i = 1$ and $\sum w_i = 1$. On both sides of M_n, there are equal numbers of polymers, while on both sides of M_w, there are equal weights of polymers.

Polydispersity index (PDI) is defined by the ratio of the weight average molecular weight to the number average molecular weight

$$\mathrm{PDI} = \frac{M_{\mathrm{w}}}{M_{\mathrm{n}}} \tag{1.3}$$

and it describes how broad the molecular weight distribution is. If all the polymers in a sample have the same degree of polymerization, PDI is equal to 1, and the sample is called monodisperse. The larger PDI is, the broader the molecular weight distribution is. When the properties under study are sensitive to the value of N, a small PDI is normally preferred because it is easier to look at individual N's. For an intuitive understanding of PDI a simple example is given below. A sample contains half, by number, of polymers with molecular weight 1000 g/mol, and the other half with molecular weight 2000 g/mol. M_{n} of this sample is calculated to be 1500 g/mol, and M_{w} is 1667 g/mol. Thus PDI of this sample is 1.11. Although 1.11 seems relatively small, the corresponding sample is far from monodisperse. In real cases the polymers are more likely to have a smoother distribution of different molecular weights rather than shown in this particular example, but this calculation demonstrates that in some cases M_{w}, M_{n} and PDI may not fully describe the distribution of a polymer sample.

Even the most monodisperse synthetic polymers have a polydispersity index (PDI) of about 1.01 [34], which still contain many different N values. This fact is closely related to the process of producing synthetic polymers, polymerization, which is the process of connecting monomers together into one polymer chain. Common types of polymerization include step-growth polymerization, chain-growth polymerization, and living anionic polymerization, which is a special case of chain-growth.

Step-growth polymerization refers to the process in which stepwise reactions among functional groups of monomers form polymers. Typical polymers produced by step-growth include polyamide (nylon), polyester, and polyether [35]. Chain-growth polymerization refers to the process in which monomers are added onto the active sites of a growing polymer successively. Typical polymers produced by chain-growth include polyethylene, polypropylene, and polyvinyl chloride [36]. Being a special case of chain-growth, living polymerization is a process in which the termination step of the polymer growth is eliminated, and the rate of chain initiation is much larger than chain propagation, making the polymer growth easier to control. Different methods normally lead to different polydispersity indices. The typical PDI from step-growth is around 2, and for common chain-growth such as free radical polymerization, PDI can be from 1.5 to 2. Living anionic polymerization normally leads to a PDI less than 1.2, which can even reach a number very close to 1, provided proper conditions [37].

The degree of polymerization N is a major factor that determines many properties of polymers. For example, physical properties of alkanes change dramatically as its N value increases. For alkanes composed of 4 or fewer carbon atoms, they are present in the gas phase at room temperature. With 5 to 16 carbon atoms, they turn into the liquid phase. With 17 or more carbon atoms they become solids.

As the reader goes through this thesis, it will be noticed that most of the materials studied here are traditionally defined as oligomers as they have relatively low molecular weight. It should be noted that in the current use of the term polymer, it is not the molecular weight that distinguishes these material from other molecules with comparable molecular weights. The key differentiating factor is the high tunability that comes with polymers. In the case of small molecules, the physical and chemical properties do not vary from batch to batch. However, the ability to control N values and the distribution of molecular weight in polymer samples give them a wide range of properties even with their relatively low molecular weight.

1.3 Glass and glass transition

Glasses are disordered solids that play an important role in our world. Window glass, optical fibers made of amorphous silica, and many polymeric glasses are widely utilized in our daily life. It is found that most water in the universe may exist in the glassy state [38]. Structurally, a glass is almost indistinguishable from its forming liquid, unlike a crystal which is structurally ordered in contrast to a liquid. From this perspective, glass can be viewed as a liquid whose molecules cannot flow. This commonly-seen but mysterious fact and the existence of glass itself are still to be understood. As Anderson commented in 1995 [29], “The deepest and most interesting unsolved problem in solid state theory is probably the theory of the nature of glass and the glass transition.”

1.3.1 Phenomenology in glass-forming materials

Fig. 1.1 illustrates the enthalpy or molar volume of a liquid as temperature is lowered. If crystallization is avoided on cooling, the system enters the supercooled liquid region, where particle motions slow down increasingly with decreasing temperature. At the glass transition temperature T_{g}, molecular rearrangements become so slow that the system appears to be kinetically “frozen” on the laboratory timescale and falls out of equilibrium. Curve 1 represents the formation of such a glass. Slower cooling produces a denser and more stable glass, as curve 2 shows, since it provides more time for molecular rearrangements. With a slower cooling rate, T_{g} decreases and the system can stay on curve 3 (extrapolation from the equilibrium state) for longer before the glass transition. The density of glass can also be raised through isothermal aging below T_{g}. It can therefore be seen that the properties of a glass depend on the process of its formation and its thermal history.

Compared to the liquid-crystal transition, liquid-glass transition is evidently different from the figure. Phase transitions are classified by Ehrenfest [39] based on the behaviour of

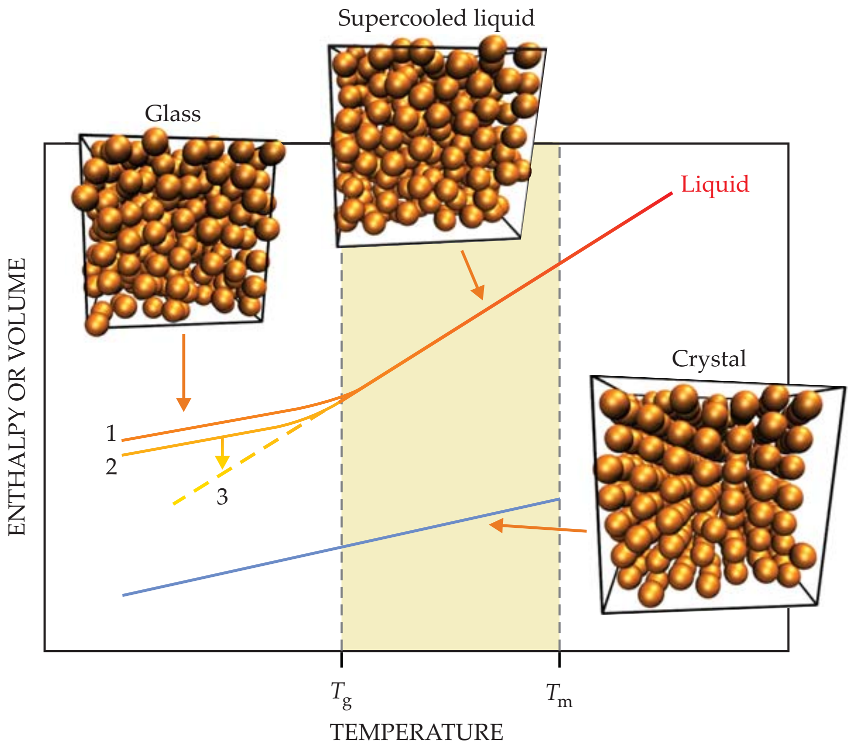

Figure 1.1: Temperature dependence of a liquid's enthalpy or molar volume. Different processes produce different glasses. Typical particle configurations are shown for a glass, a supercooled liquid, and a crystal. Figure from Ref. [5].

the thermodynamic free energy. When the first derivatives of the free energy such as volume and entropy are discontinuous, it is a first-order phase transition. The liquid-crystal transition is therefore first order. When the first derivatives are continuous but second derivatives such as thermal expansion coefficients and heat capacity are discontinuous, it is classified as a second-order phase transition. Under this definition, the glass transition resembles a second-order phase transition since the second derivatives go through a step at T_g. However, it is generally believed that the glass transition is not a thermodynamic transition but rather a kinetic one since it is not a transition between states of thermodynamic equilibrium. With the crystal being the true equilibrium state, the glass is regarded as a kinetically locked state. There is no structural difference between the liquid and the glass, and the only difference is the dynamic slow down due to the increase of density. Whether an underlying second-order phase transition exists in the limit of infinitely long relaxation times is still under debate.

Kinetics

During the glass transition upon cooling, physical properties including density, modulus, heat capacity, refractive index and viscosity of the system change significantly. The timescale of molecular motion increases dramatically as the temperature approaches T_{g}. A convenient definition of the glass transition is the temperature at which the relaxation time is 100 s or the viscosity is 10^{13} poise (10^{12} Pa $\cdot$ s) [6]. Based on the different temperature dependence of viscosity, glass-forming materials are categorized into "strong" vs "fragile" liquids, as shown in Fig. 1.2.

The dependence of viscosity on temperature of "strong" liquids such as silica is well described by the Arrhenius functionality:

$$\eta = A \exp\left(\frac{E_{\mathrm{a}}}{k_{\mathrm{B}}T}\right), \tag{1.4}$$

where A and E_{a} are temperature-independent constants and k_{B} is Boltzmann's constant. It is worth noting that strong liquids typically have network structures of covalent bonds, while molecules in fragile liquids typically interact through nondirectional, noncovalent forces [7]. For "fragile" liquids, the viscosity and relaxation time scales are quite non-Arrhenius and can be approximately described by the empirical Vogel-Fulcher-Tammann (VFT) equation [40, 41, 42]:

$$\eta = A \exp\left(\frac{B}{T - T_0}\right), \tag{1.5}$$

where A and B are temperature-independent constants and T_0 is called the VFT temperature. When $T_0 = 0$, the Arrhenius equation is recovered. When $T_0 > 0$, the behaviour is non-Arrhenius, and the viscosity (or relaxation time) is expected to diverge at T_0. The VFT equation is equivalent to another widely known equation, the Williams-Landel-Ferry (WLF) equation [43]:

$$\log(a_T) = \frac{-C_1(T - T_s)}{C_2 + (T - T_s)}, \tag{1.6}$$

where T_s is the reference temperature, C_1 and C_2 are temperature independent constants, and $a_T = \tau(T)/\tau(T_s)$ or $a_T = \eta(T)/\eta(T_s)$ is the ratio of relaxation times or viscosities at temperatures T and T_s, respectively.

Fragile liquids display non-exponential response to various perturbations [44]. This behaviour is often described by the stretched exponential function, or Kohlrausch–Williams–Watts (KWW) function [45, 46]. The response function $F(t)$ of a system (e.g. the strain resulting

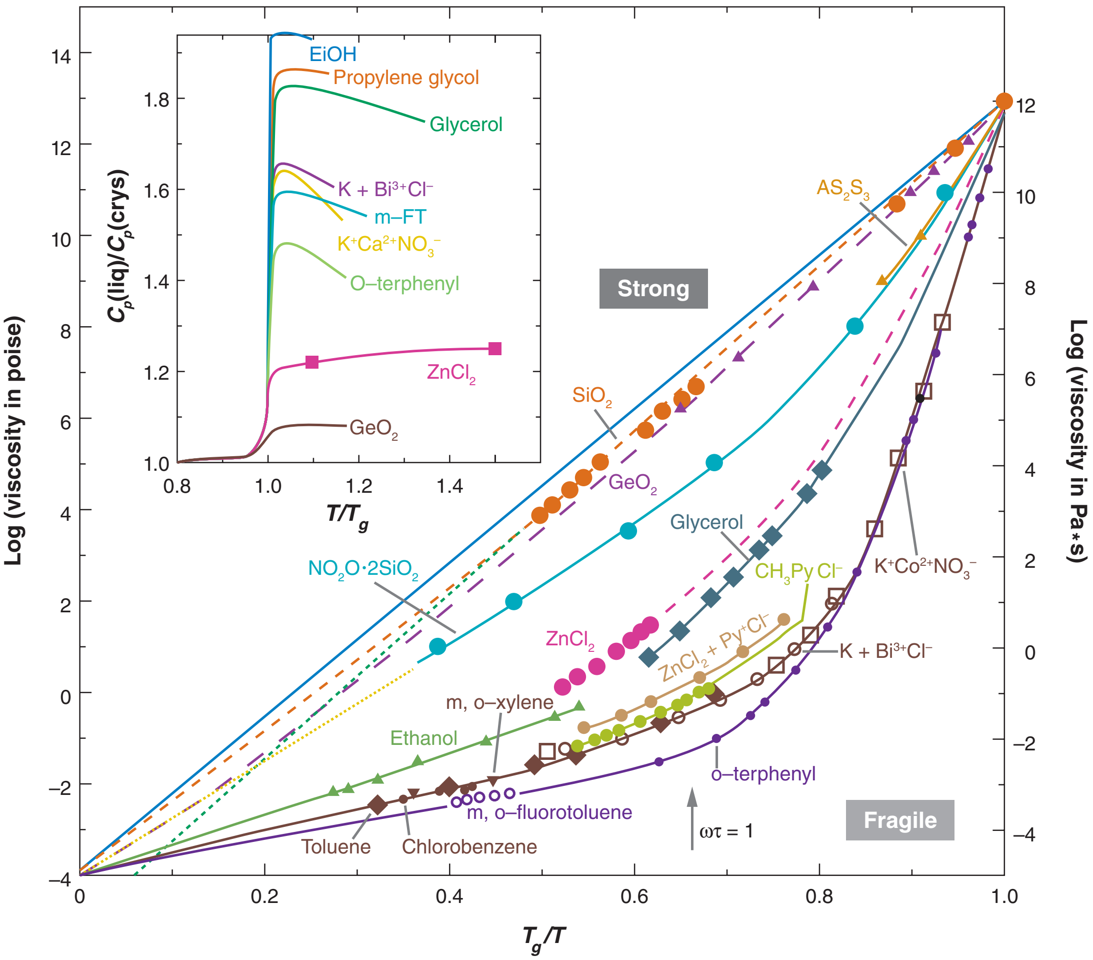

Figure 1.2: A T_g-scaled Arrhenius plot of liquid viscosities. “Strong” liquids exhibit Arrhenius behaviours, while “fragile” liquids exhibit non-Arrhenius behaviours. Figure from Ref. [6].

from an applied stress, or the stress in response to an imposed deformation) follows:

$$F(t) = \exp\left[-\left(\frac{t}{\tau}\right)^{\beta}\right], \tag{1.7}$$

where τ is a characteristic relaxation time, which often has non-Arrhenius temperature dependence. When $\beta = 1$, the exponential function is recovered. A smaller β value stretches the exponential more. This behaviour is believed to be related to the spatial heterogeneity of the system. Whether the distinct domains relax identically in a non-exponential manner or differently with various exponential behaviours remains unknown [47].

At temperatures much higher than the glass transition temperature, the dielectric relaxation time of the liquid has an Arrhenius temperature dependence and there is a single relaxation peak. This relaxation is named the α-relaxation (segmental relaxation) and it is the main structural relaxation in polymers. The single relaxation peak splits into two at lower temperatures for most materials [48]. The secondary relaxation is name the β-relaxation and has a smaller amplitude than the α-relaxation. The β-relaxation (faster) is believed to be a precursor of the structural α-relaxation, related to local vibrations. While the α-relaxation becomes non-Arrhenius at lower temperatures, the β-relaxation remains Arrhenius.

Thermodynamics

One of the most important quantities in describing the thermodynamics of glasses is the entropy, which is directly related to the nature of glassy states. Entropy is a function of the state of the system which depends on the density of states of a system. A higher density of states at a specific energy level means there are more states available for occupation, which is favoured with a higher probability. If we compare a system in its liquid state with its glassy state under a microscope, there is no obvious difference to the eye. As can be seen from the schematics in Fig. 1.1, unlike any other phase transitions [49], glass formation does not cause a sharp structural change in the system or create any order. Instead, the density of states in equilibrium reduces with decreasing temperature, causing the slowing down of molecular rearrangements, and the relaxation time of the system increases rapidly. Finally, the liquid falls out of equilibrium and forms a glass at the glass transition temperature T_{g}. During this process, conventional order parameters do not capture the change, and only observables related to the density of states are able to describe the transition. Therefore, entropy, specifically configurational entropy, has naturally become a quantity of interest and plays a central role in glass science.

From calorimetric measurements, the entropy of a system can be obtained through integrating over the measured specific heat. Upon glass formation, the specific heat drops to a lower value, causing a kink in the entropy of the system, as Fig. 1.3 shows. The slope of the entropy curve is the larger for the liquid and supercooled liquid, compared to that for the glass and crystal. This leads to the entropy crisis, or Kauzmann paradox [50]: if the system remained in the supercooled liquid state as temperature is continuously lowered, the entropy of the liquid would be equal to and even less than that of the crystal at some point. This point is known as the Kauzmann temperature T_{K}. It is counterintuitive that a glass with disordered structure could have equal entropy, or degree of randomness, as a crystal with perfectly ordered structure. Below T_{K}, the entropy can even become negative at a finite temperature, which violates the third law of thermodynamics.

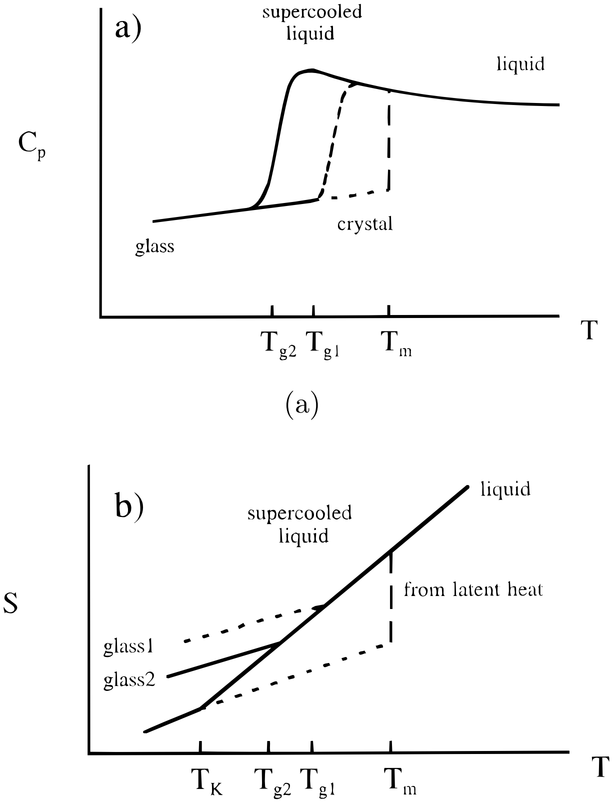

(a)

(b)

Figure 1.3: A schematic diagram of the specific heat (a) and the entropy (b) of a crystal, liquid, supercooled liquid, and glass as a function of temperature. The cooling rate in the formation of glass 1 (dashed curve) is faster than that for glass 2 (solid curve). Figure from Reference [7].

Experimentally, the crisis is always avoided with a kinetic glass transition, causing the entropy to decrease at a slower rate at $T < T_{\mathrm{g}}$. However, in theoretical considerations that is devoid of experimental ambiguities, there appears to be nothing to prevent the crisis even at very low temperatures, as shown in computer simulations [51].

1.3.2 Theories of the glass transition

Entropy theories

In his own attempt to solve the Kauzmann paradox [50], Kauzmann proposed that spontaneous crystallization or kinetic arrest eventually prevents entropy crisis in experiment. It is also in this paper that Kauzmann defined glass as "an amorphous or non-crystalline material in which certain internal degrees of freedom characteristic of the liquid state have not had time to come into thermodynamic equilibrium with their surroundings". This definition emphasizes the kinetic nature of an experimental glass transition, but is an implication for revealing a hidden thermodynamic second-order phase transition to an "ideal glass" which is free of the kinetic constraints. As a matter of fact Kauzmann never excluded the possibility of a thermodynamic glass transition.

The concept of an ideal glass has been used in other attempts in solving the Kauzmann paradox [52, 53]. If the liquid transforms to the ideal glass state with the densest possible random packing at T_{K}, the crisis is then avoided. The configurational entropy of a system can be defined based on the Boltzmann entropy [54]:

$$S_{\mathrm{conf}} = k_{\mathrm{B}} \ln \Omega, \tag{1.8}$$

where Ω is the number of configurational states available in the system. The configurational entropy is regarded as the entropy from the availability of different configurations to the structure, and therefore S_{conf} of the ideal glass is zero and equal to that of the ideal crystal. Unlike crystals, the orderliness of an ideal glass is less obvious in structure, and it is described as a "long range amorphous order". In the theoretical work on polymer chains by Gibbs and DiMarzio [52], it is shown that at the critical temperature T_{K}, a thermodynamic second-order phase transition from liquid to glassy state occurs, where the decreasing configurational entropy S_{conf} reaches zero and remains zero below T_{K}. Since S_{conf} is a logarithm of the number of configurations, the system stays in its ground state with minimum energy when S_{conf} vanishes. This work indicates that the ideal glass is a genuine phase of matter through a second-order thermodynamic phase transition.

As mentioned previously, the most significant feature of glasses compared to liquids is their slow dynamics. In 1965, the connection between the thermodynamic quantity S_{conf} and the dynamic phenomenology in glass formation was first build by Adam and Gibbs [55], using the concept of cooperatively rearranging regions. They described the relation between relaxation time τ and configurational entropy S_{conf} as

$$\tau \propto \exp\left(\frac{1}{TS_{\mathrm{conf}}}\right), \tag{1.9}$$

where the relaxation time diverges at the Kauzmann temperature. It is not hard to understand this relation since the driving force behind relaxations is the possibility to explore distinct states, quantified by S_{conf}. The Adam and Gibbs relation provides an excellent description on the relaxation behaviour of supercooled liquids. In fact, the empirical VFT equation[40, 41, 42] that has been widely used to describe dynamics of glass-forming materials is readily derived from the Adam and Gibbs relation. This relation provides a thermodynamic explanation on the kinetics, and is in support of the underlying thermodynamic transition to an ideal glass with a unique configuration. For many fragile liquids, the value T_0 in the VFT equation is very close to T_{K} obtained from calorimetric measurements [56], which provides stronger support in the connection between dynamics and thermodynamics.

S_{conf} has been experimentally measured and numerically simulated in various materials and models. Studies by Berthier et al. [57, 58] show that extrapolation of equilibrium data suggests that S_{conf} vanishes at $T_{\mathrm{K}} > 0$ in three dimensions, and at $T_{\mathrm{K}} = 0$ in two dimensions. These results support the existence of entropy crisis, although not necessarily a thermodynamic glass transition.

Mean field theory

Since the work of Gibbs and DiMarzio [52] on the configurational entropy S_{conf} using mean-field approximations, there have been a plenitude of studies on the entropy crisis based on mean-field theory (MFT), with the famous random first order transition (RFOT) theory being one of them [57]. The mean field theory associates the growing dynamic lengthscales with an ideal glass transition [59, 60], consistent with the findings of previous thermodynamics theories.

In the mean-field theory describing the phase transition between a gas and a liquid, the free energy has two minima corresponding to gas and liquid states. The order parameter, density, readily distinguishes the two states. The glass state, however, is much more difficult to be distinguished from the liquid state by its density, so another order parameter named the overlap function Q has been introduced to serve as the new order parameter. Q characterizes the degree of similarity of the density profiles of two equilibrium configurations and is inversely related to entropy. For two uncorrelated profiles such as in the liquid

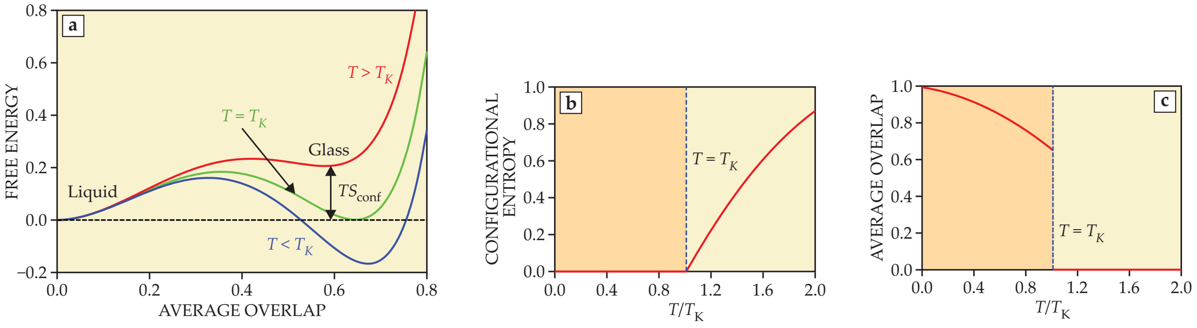

(a) (b) (c)

Figure 1.4: Mean-field theory of the equilibrium liquid–glass phase transition. (a) The free energy as a function of the average overlap. (b) Configurational entropy vanishes at T_K on cooling. (c) Below T_K, the glass state is the thermodynamically stable phase with high average overlap. Figure from Reference [5].

state, $Q \approx 0$ being the minimum, while for two similar profiles such as in the glassy state, $Q \approx 1$ being the maximum. The free energy $V(Q)$ can then be expressed as a function of an order parameter Q [61, 62], as Fig. 1.4 shows. As expected, at high temperatures the global minimum of $V(Q)$ is at $Q = 0$, and the metastable glass state has a local minimum as Q approaches 1. To occupy the glass state which is a restricted part of its potential energy landscape, the system has to pay a free energy cost of TS_{conf}. At the Kauzmann temperature T_K, the two minima have the same value of $V(Q)$ and the free energy cost becomes zero, corresponding to a zero configurational entropy. Below T_K, the glass state becomes the stable state with a higher overlap. The discontinuous change in Q is similar to the case of a first order phase transition, and the ideal glass transition is therefore named a random first order transition [5].

In the mean-field limit, the exact solution to the glass-transition problem has been obtained for infinite dimensions [57, 63, 64], where the theory explains the viscous slowdown of a glass-forming system through the rarefaction of the number of glassy metastable states upon approaching T_K. However, results for infinite dimensions in the mean-field limit may break down completely when finite dimensional fluctuations are involved according to past researches on phase transitions [5]. New computational techniques are being developed to study the validity of MFT in finite dimensions [64, 65, 66], and recent studies [57, 58] have shown that the thermodynamic transition occurs at absolute zero in two dimensions and at a finite temperature in three dimensions, suggesting that the lower critical dimension for the long-range amorphous order is $d = 2$.

Potential energy landscape

The potential energy landscape (PEL) [67, 68] provides a framework for interpreting the phenomenology involved in glass transition. For an N-body system, the potential energy is represented by $\mathbf{\Phi}(\mathbf{r}_1 \cdots \mathbf{r}_N)$, where $\mathbf{r}_i$ accounts for position, orientation, velocity and other relevant parameters of the each particle. The potential energy landscape can be illustrated in a one-dimensional representation as shown in Fig. 1.5. The points for which $d\mathbf{\Phi}/d\mathbf{r} = 0$ are the local minima on the landscape, and they represent metastable states (also named inherent structures) of the system, with the thermodynamically stable state at absolute zero being the global minimum. The local minima, or basins, are separated by barriers which represent the activation energy to transition from one state to another. The landscape picture separates molecular motion into distinct potential energy minima and vibration within a minimum. As the temperature decreases, the average potential energy lowers. "T_A" in Fig. 1.5 is where non-Arrhenius dynamics appears, and the characteristic time scale for molecular reorientation at this point is typically on the order of nanoseconds. "T_g" is normally the energy level that is reached with a cooling rate of 1 K/min. By cooling the material more slowly or aging the material, the materials is brought deeper down in the landscape.

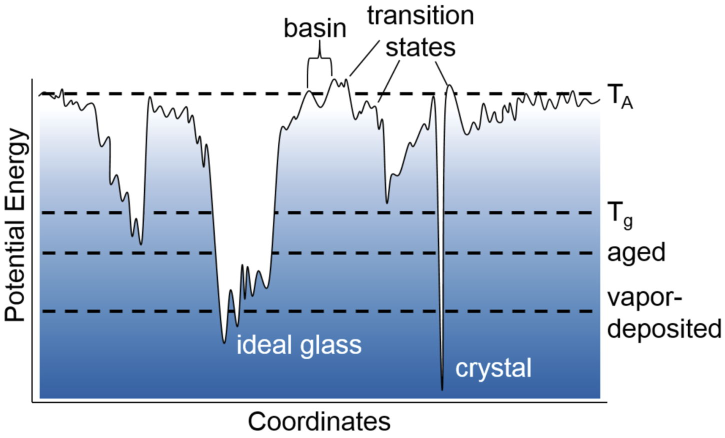

Figure 1.5: Schematic representation of the potential energy landscape of a glass-forming system. Figure from Reference [8].

The configurational entropy $S_\mathrm{conf} = k_\mathrm{B} \ln \Omega$ is related to the number of configurational states Ω in a system. In the picture of potential energy landscape, Ω is equivalent to the number of minima or inherent structures. At high temperatures the system is able to sample all possible configurations of the system. At lower temperatures available states become fewer and fewer with lower potential energy and the entropy of the system decreases. The system does not have enough energy to overcome the higher barriers and becomes trapped in local minima. With infinitely slow cooling or infinitely long aging, the configurational entropy of the system finally reaches zero, corresponding to a unique configuration. This final state is known as the ideal glass state, which presumably has the densest possible amorphous packing. The concept of ideal glass appears in the potential energy landscape as a natural consequence, although its existence remains to be proved.

One of the biggest problems with the PEL model is that it is impractical to be used in real world problems, since it is almost impossible to define the energy landscape of a system with large degrees of freedom. Since it is largely static, it is incapable of describing the exact transition from a supercooled liquid to a glass [69]. However, it satisfactorily describes the thermodynamics, dynamics, and the structure of disordered systems, and offers an attractive route to understand the microscopic basis of glass formation and the concept of an ideal glass.

Free volume theory

When temperature decreases, the density of a glass increases and becomes high enough so that particles/monomers get in the way of each other when they move. The free volume theory is one way to describe this effect [43, 70, 71, 72, 73, 74]. In contrast to the thermodynamic models introduced above, the free volume theory is based on kinetics. At higher density, the free volume decreases, so particles need to cooperate to make room for relaxation. During the development of the free volume theory, there have been different versions in the definition of free volume. In Fig. 1.6 the different regions in the entire sample volume are shown.

Of the entire volume V of a system, the temperature dependent "vibrational volume", V_{vib}, takes the largest fraction, which corresponds to the underlying solid-like contribution to the total volume. It consists of a "hard core" volume shown in black and the nearby space shown in gray. In different versions of definitions of the free volume, a key difference is the categorization of the surrounding space in gray. In many of the earlier studies including those by Fox and Flory [70, 71, 72] and Williams, Landel, and Ferry [43], the vibrational volume V_{vib} are considered as "occupied volume" and only the white space ($V_{\text{free:exs}}$ in the figure) is regarded as the free volume since it is the fraction beyond solid-like range of motion and is key for allowing the system to behave like a liquid. In some other works [73, 74, 75], a "total free volume" is defined as all the volume excluding the hard cores, which is the V_{free} shown in the figure, composed of the gray and white space together.

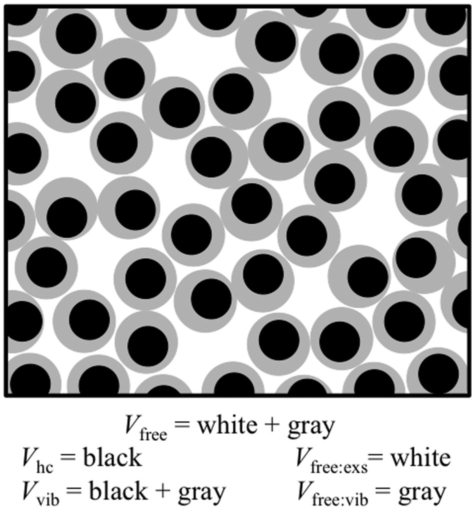

Figure 1.6: Schematic diagram showing the various contributions to the total volume. The black regions represent the hard cores of the particles/monomers. The gray regions represent the surrounding volume expected to be covered by simple solid-like vibrational motion. The white regions are the extra free space available in the system, beyond the expected solid-like range of motion. Figure from Ref. [9].

The different types of free volume can be related to different thermal expansion coefficients ($\alpha = (1/V)(\partial V/\partial T)_P$). For the "total free volume", $\alpha_{\text{L}} = (1/V)(\partial V_{\text{free}}/\partial T)_P$, or equivalently, $(\partial V_{\text{free}}/\partial T)_P = V\alpha_{\text{L}}$, where α_{L} is the liquid thermal expansion coefficient. For the "excess free volume", $(\partial V_{\text{free:exs}}/\partial T)_P = (\partial V_{\text{free}}/\partial T)_P - (\partial V_{\text{free:vib}}/\partial T)_P \approx V(\alpha_{\text{L}} - \alpha_{\text{G}})$, where α_{G} is the glass thermal expansion coefficient. The crystalline solid often has a similar value as that of the glass. Fig. 1.7 is a diagram showing the different types of volume and the overall volume change with temperature.

In Fig. 1.7 the relations of different types of volume and their temperature dependence are easily seen. Corresponding to the gray area in Fig. 1.6, $V_{\text{free:vib}} = V_{\text{vib}} - V_{\text{hc}} = V_{\text{free}} - V_{\text{free:exc}}$. The temperature dependence of V_{vib} is often considered to be that of the glass, i.e., solid-like. The excess free volume, $V_{\text{free:exs}}$, is temperature dependent in the liquid state, yet temperature independent in the glassy state. This appears in the figure as the fact that the liquid has a higher thermal expansion coefficient than the glass. When the system transforms into a glass, $V_{\text{free:exs}}$ becomes frozen and fixed due to imperfections in packing that waste space. As the temperature decreases below T_{g}, the glass only contracts through a reduction in $V_{\text{free:vib}}$.

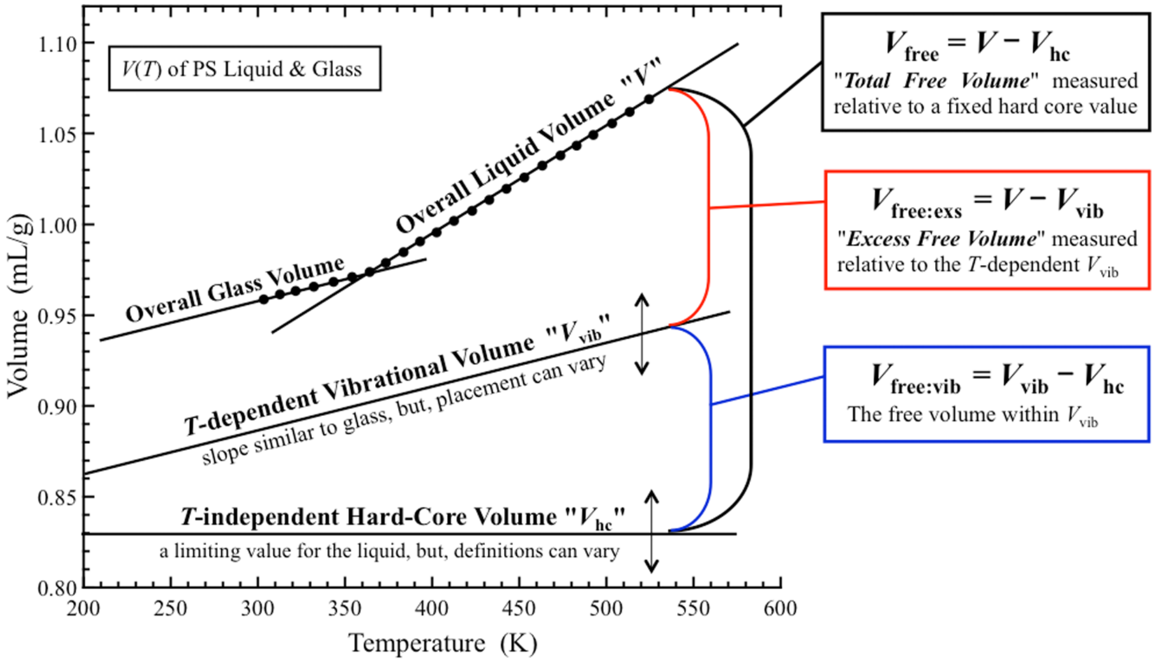

Figure 1.7: Diagram showing the overall volume as well as the different contributions as a function of temperature for PS liquid and glass. Figure from Ref. [9].

Free volume does not only depend on temperature, but also on the chain length (molecular weight) of a polymer sample. Since intermolecular distances are longer than covalent bonds, chain end units have large free volume compared to units on the backbone. Therefore a higher molecular weight polymer sample with lower fraction of chain ends will have less free volume. The glass transition temperature is thus also affected by the molecular weight. This relation is described in the Fox-Flory equation [76]:

$$T_g = T_{g,\infty} - \frac{K}{M_n} \tag{1.10}$$

where $T_{g,\infty}$ is the maximum glass transition temperature that can be achieved at a theoretical infinite molecular weight and K is an empirical parameter that is related to the free volume present in the polymer sample. With lower molecular weight, T_g of a polymer sample decreases.

Assuming the fraction of free volume is f, the Doolittle equation [33, 77] describes the viscosity based on the simple Arrhenius relation:

$$\eta \sim \exp\left(\frac{B}{f}\right), \tag{1.11}$$

where B is an empirical constant. Assuming further that the free volume has a linear temperature dependence,

$$f = \alpha_f (T - T_\infty), \tag{1.12}$$

where α_f is the thermal expansion coefficient of the free volume. Combining the above two equations one can get the WLF equation which was first applied to polymer melts by Williams, Landel, and Ferry [43]:

$$\begin{aligned}
\frac{\eta}{\eta_0} &= \exp\left(B\left[\frac{1}{f} - \frac{1}{f_0}\right]\right) && (1.13)\\
&= \exp\left(\frac{B}{\alpha_f}\left[\frac{1}{T - T_\infty} - \frac{1}{T_0 - T_\infty}\right]\right) && (1.14)\\
&= \exp\left(\frac{B}{\alpha_f}\left[\frac{T_0 - T}{(T - T_\infty)(T_0 - T_\infty)}\right]\right) && (1.15)\\
&= \exp\left(\frac{B}{f_0}\frac{(T_0 - T)}{(T - T_\infty)}\right) && (1.16)
\end{aligned}$$

Although the equation leads to the WLF equation (or equivalently, the VFT equation), the assumptions used in the derivation including Eqn. 1.11 and Eqn. 1.12 are unsubstantiated and it's thus just a phenomenological description of the temperature dependence of viscosity.

The free volume theory is successful in explaining different observations near the glass transition temperature, but it also has problems. For example, if the slow dynamics was mainly caused by the decrease in free volume, the glass transition would disappear when the temperature is decreased at a constant volume. However, there are both experimental [78] and numerical [79] evidence of the isochoric glass transition.

Mode-coupling theory

Using the kinetics of a simple hard sphere model, the mode-coupling theory (MCT) [80, 81] characterizes the dynamics of the glass transition. Starting from the density of particles in a liquid and using the autocorrelation function, MCT makes detailed predictions on behaviours of the liquid, the supercooled liquid, and the glassy state [69]. Above the melting temperature, the liquid has exponential relaxation. A supercooled liquid undergoes three regimes: 1. free and collisional events leading to the short timescale decay (α-relaxation); 2. caging of particles by their nearest neighbours resulting in a plateau and subsequent cage-breaking resulting in another decay (β-relaxation); 3. at long times, a stretched exponential form of relaxation. For a glass, there is a sharp transition from an ergodic regime to a non-ergodic regime as the temperature is decreased below the mode-coupling temperature T_{MCT}, which freezes the structure in the non-ergodic regime.

MCT successfully predicts a glass transition and the caging effect. The description of the early stages of viscous slowdown for fragile liquids and the multi-step relaxations have been verified in experiments [7]. However, T_{MCT} is typically 30–50 K higher than the experimental T_{g}, and the transition predicted is too sharp compared to experimental observations. Moreover, it does not work as satisfactorily for strong liquids [82]. Another weakness of MCT is that it does not describe the real system below T_{MCT}. The concept of an ideal glass, consequently, is not involved in MCT.

1.4 Thin film glasses and interfacial dynamics

When glass forming materials are confined in small sizes, the glass transition and other physical properties of the material may be expected to change due to the system's interaction with its boundaries. Among the earliest studies on the confinement effect, porous media was used and the glass transition temperature T_{g} of the material confined in the nano-pores was measured [83, 84, 85]. It was found that depending on the interaction between the glass forming material and the porous media, T_{g} could be either increased or decreased. Enhanced dynamics and the existence of a mobile layer was proposed in explaining the observations. However, the interaction between the glassy material and the media made it difficult to explain the exact nature of such effects.

In the mean time period, there was a growing number of studies on polymer thin films. These films can be easily prepared and are widely used in various applications including packaging, transistors [86] and batteries [87]. Over the past few decades, nano-confined glassy thin films have been studied extensively and it is abundantly observed that the confinement and the interfacial effects play an essential role in altering the interfacial dynamics and the properties of thin films. Numerous studies have shown that the physical properties of polymer thin films can strongly deviate from those of bulk materials. These properties include the glass transition temperature [10, 11, 88, 89, 90, 91, 92, 93, 94, 95, 96, 97, 98, 99], viscosity [17, 18, 100, 101], mechanical modulus [102, 103, 104], fragility[105, 106, 107, 108, 109] and physical aging rates [110, 111, 112, 113]. The techniques in include ellipsometry [10, 88, 89, 90, 93, 94, 95, 97, 109, 112], Brillouin light scattering [11, 90], X-ray and neutron reflectivity [109], differential scanning calorimetry [96, 107, 108], atomic force microscopy [17, 18, 100, 102, 103, 104], dielectric spectroscopy [91, 92, 94, 99, 114, 115], fluorescence spectroscopy [96, 98, 108, 110, 111], etc. In this section, we briefly review studies on thin film glasses and the role of interfaces.

1.4.1 T_{g} measurements

Among the many different ways of characterizing the interfacial effects on glass properties, the glass transition temperature is one of the most useful and representative quantity in describing the dynamics of a glass forming material.

The first study which revealed the effect of film thickness on T_{g} was the experiment by Keddie, Jones and Cory [10], where they measured T_{g} of PS thin films with different thicknesses and molecular weights by ellipsometry, and observed the reduction in T_{g} for films less than 100 nm thick. Fig. 1.8 shows that compared to the bulk value, T_{g} decreases monotonically with decreasing film thickness, and the reduction is independent of molecular weight within the range measured. The data can be nicely fit with an empirical equation:

$$T_{\mathrm{g}}(d) = T_{\mathrm{g}}(\infty)\left[1-\left(\frac{A}{d}\right)^{\delta}\right], \tag{1.17}$$

where d is the film thickness. The best fit is obtained with $T_{\mathrm{g}}(\infty) = 373.8$ K, the characteristic length $A = (3.2 \pm 0.6)$ nm and the exponent $\delta = 1.8 \pm 0.2$. Using a model with a mobile surface layer whose thickness $\xi(T)$ diverges at $T_{\mathrm{g}}(\infty)$:

$$\xi(T) = A\left(1-\frac{T}{T_{\mathrm{g}}(\infty)}\right)^{-1/\delta}, \tag{1.18}$$

the authors recovered an expression for the thickness dependence of T_{g} of the form of Eqn. 1.17.

With the existence of a liquid-like surface layer, the thermal expansion coefficient (expansivity) of the glass is also altered. For thinner films, the larger fraction of the surface layer is expected to lead to a larger expansivity. Assuming an average size of the mobile layer $\bar{\xi}$, the glass expansivity can be calculated by simply adding up the different

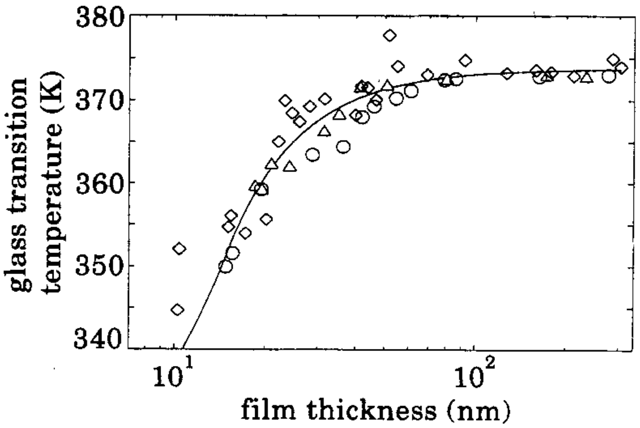

Figure 1.8: The glass transition temperature T_{g} with respect to film thickness for PS of 3 different molecular weights. Triangles represent MW = 120 kg/mol, circles represent MW = 500.8 kg/mol, and diamonds represent MW = 2900 kg/mol. The solid line is a best fit to the data (except for the two data points with the lowest thicknesses) using Eqn. 1.17, with $T_{\mathrm{g}}(\infty) = 373.8$ K, $A = 3.2$ nm and $\delta = 1.8$. Figure from Ref. [10].

contributions:

$$\alpha = \frac{\bar{\xi}}{d}(\alpha_{\mathrm{melt}} - \alpha^{\infty}_{\mathrm{glass}}) + \alpha^{\infty}_{\mathrm{glass}}, \tag{1.19}$$

where $\bar{\xi}$ is the average size of the mobile layer within the temperature range measured, α_{melt} is the expansivity in the melt, and $\alpha^{\infty}_{\mathrm{glass}}$ is the glass expansivity in bulk material.

As shown in Fig. 1.9, Eqn. 1.19 is found to describe the experimental results effectively. The solid line is a best fit which gives an average mobile layer thickness $\bar{\xi}$ of 8 (± 0.8) nm. Using Eqn. 1.18 $\bar{\xi}$ is estimated to be 13 (± 3) nm, which is in fair agreement with the former value.

For polymer thin films spincast onto silicon substrates (supported films) including the samples in Ref. [10], the polymer has two interfaces with one being with the air (called the free surface) and the other one being with the substrate. In investigating the interfacial effect, the role of the silicon substrate and its interaction with the polymer is unclear. In order to avoid the difficulties with the combined influences of the substrate and the free air, Forrest et al. [11] studied the glass transition of freely standing films, which eliminates the substrate entirely.

This study also shows a reduction in T_{g}, but the amount of reduction is much larger compared to supported PS films as shown in the inset of Fig. 1.10. With two surfaces

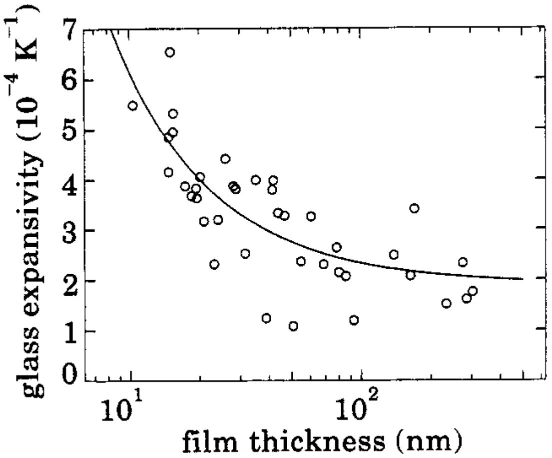

Figure 1.9: The glass expansivity with respect to film thickness for PS of all 3 different molecular weights. The solid line is a best fit to the data using Eqn. 1.19, with α_{melt} fixed at 7.2×10^{-4} K^{-1}. Best fit values of $\alpha_{\text{glass}}^{\infty}$ and $\bar{\xi}$ are 1.9×10^{-4} ($\pm\ 2 \times 10^{-5}$) K^{-1} and 8 (± 0.8) nm, respectively. Figure from Ref. [10].

present, the larger reduction in T_{g} is in support of the existence of a mobile layer.

The role of the free surface was more evidently shown in a study by Sharp et al. [12] using a novel sample geometry. By simply capping the free surface of Si supported PS films by evaporating metal layers on top, T_{g} may or may not be altered depending on the choice of evaporated metal. However, when two films each with thickness $h/2$ (one being Si supported and the other one supported by a NaCl crystal substrate and coated with a metal layer) are placed together with their free surfaces in contact and then annealed, the T_{g} reduction is shown to disappear for all film thicknesses studied, as shown in Fig. 1.11. Once the capping metal layer is removed, the T_{g} reduction is recovered just like a normal uncapped thin film supported on silicon. This study shows that covering the free surface eliminates T_{g} reductions and removing the capping layer recovers the reductions. It provides compelling evidence that the existence of free surfaces is directly responsible for T_{g} reductions in polymer thin films.

The effect of thickness on T_{g} has also been studied for poly(methyl methacrylate) (PMMA) thin films by Keddie, Jones, and Cory [88]. For PMMA films on Au substrates, a similar T_{g} reduction is observed as in PS thin films. However, for PMMA films on Si substrates the thickness dependence is reversed, with an increasing T_{g} for thinner and thinner films. This study shows that the T_{g} is influenced by both the free surface and the

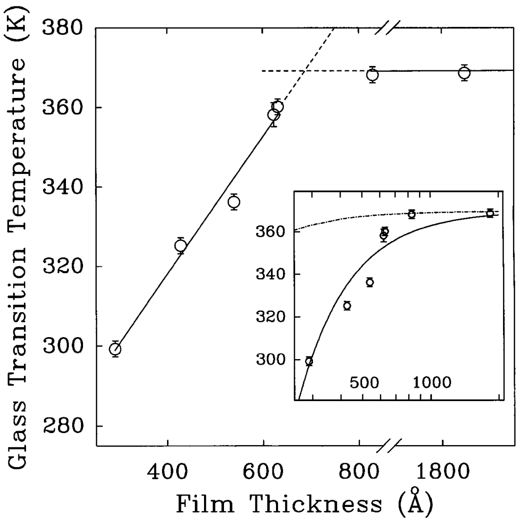

Figure 1.10: The glass transition temperature T_g with respect to film thickness for freely standing PS films. The solid (and dashed) lines are a fit of the data to a linear function of T_g proposed by the authors. In the inset the data in this study (symbols) is compared to the data of Ref. [10] (dashed line), with the solid line being a fit to Eqn. 1.17. Figure from Ref. [11].

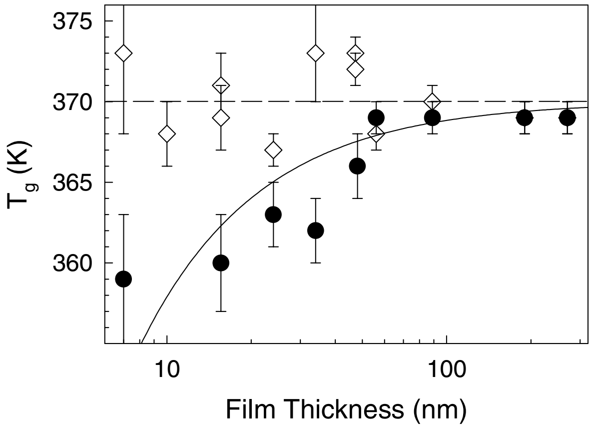

Figure 1.11: The glass transition temperature T_g with respect to film thickness for $2(h/2)$ PS films before (hollow diamonds) and after (solid circles) the removal of the metal layer. Figure from Ref. [12].

sample-substrate interactions. In fact it was found that a weakly adsorbing substrate could enhance the dynamics, leading to a decrease in T_{g}, while a strongly adsorbing substrate could slow down the dynamics, leading to an increase in T_{g} [97]. PS-Si interactions are relatively week, and thus the free surface dominates the thickness dependence. PMMA is also weakly adhesive on Au substrates, so its T_{g} reduction is similar to that of PS supported on silicon. However, there exist strong attractive interactions between PMMA and Si substrates, which lead to higher T_{g}'s in thinner films.

1.4.2 Probing the free surface

At temperatures near the bulk T_{g}, a 10 K increase in temperature roughly results in a decrease in the segmental and terminal relaxation times, which corresponds to an increase in mobility, by a factor of 1000 [116]. As the previous section shows, T_{g} is significantly reduced in thin films for as much as 70 K in freely standing PS films in Fig. 1.10. These T_{g} reductions are expected to correspond to huge changes in the mobility, particularly the surface mobility since the free surface is believed to be responsible for such effects. Therefore, there have been extensive studies to directly probe the dynamics on the surface of both polymers and small molecules, and different techniques have been developed including nanoparticle embedding [13, 117, 118, 119, 120, 121, 122], nanohole relaxation [16, 123], stepped film relaxation [18], tobacco mosaic virus perturbations [124, 125, 126], surface grating relaxation [19, 127, 128], etc.

Teichroeb et al. [13] performed the first nanoparticle embedding experiment, where 10 nm and 20 nm gold nanoparticles were introduced onto PS films. Above T_{g}, the polymer wets the gold nanoparticles and later the nanoparticles embed into the film in order to minimize the surface energy. Below T_{g}, if the entire film is truly in the glassy state including the surface, the nanoparticle should stay on the surface without any embedding. However, their experiments show that this is not the case.

Fig. 1.12 shows the evolution of the apparent height of the nanoparticles at different temperatures. For nanoparticles on bare silicon, the apparent height stays constant with time. Above T_{g}, the nanoparticle fully embeds into the film as expected. Below T_{g}, the nanoparticle does not stay on the surface, but partially embeds into the film by a few nanometers. The fact that the amount of embedding is the same for 10 nm and 20 nm nanoparticles suggests that the partial embedding is due to the existence of a mobile layer and that this value may correspond to the thickness of the mobile layer at the corresponding temperature.

In the study by Fakhraai and Forrest [16], nanohole relaxation was used to study the

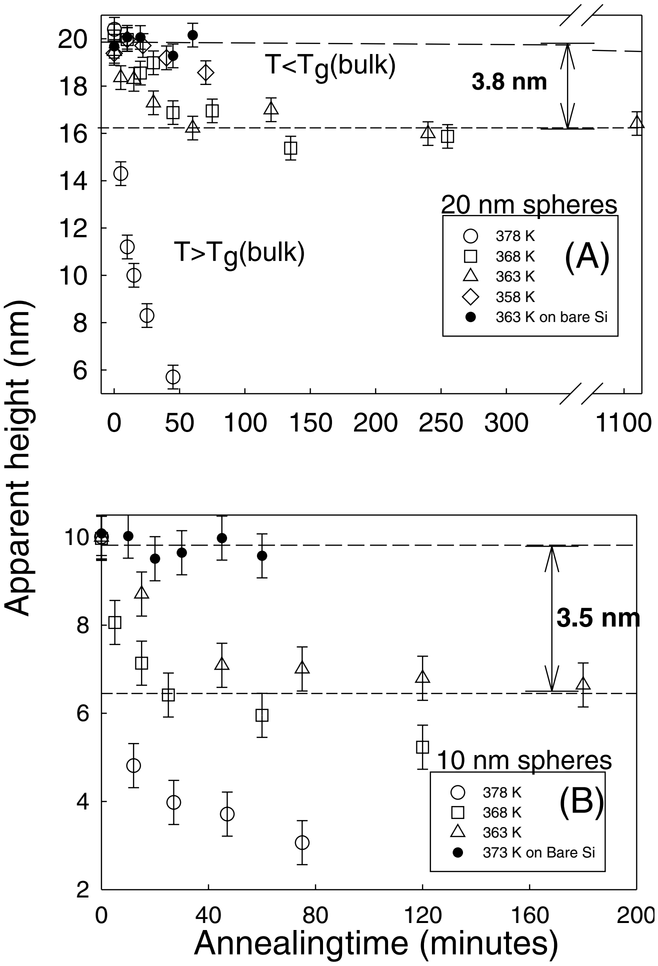

Figure 1.12: The apparent height of gold nanospheres with respect to time for temperatures from 358 to 378 K for the 20 nm spheres (a), and for 363 to 378 K for the 10 nm spheres (b). Figure from Ref. [13].

surface of PS thin films. By partially embedding gold nanoparticles and then removing them with mercury, nanoholes with a depth of a few nanometers were created on the surface. The temporal evolution of the nanoholes were monitored with atomic force microscope at different temperatures and it was found that the depths could be described by single exponential functions. Relaxation times were then extracted from the exponential functions and plotted in Fig. 1.13.

Fig. 1.13 shows that the surface relaxation occurs at all temperatures measured (down

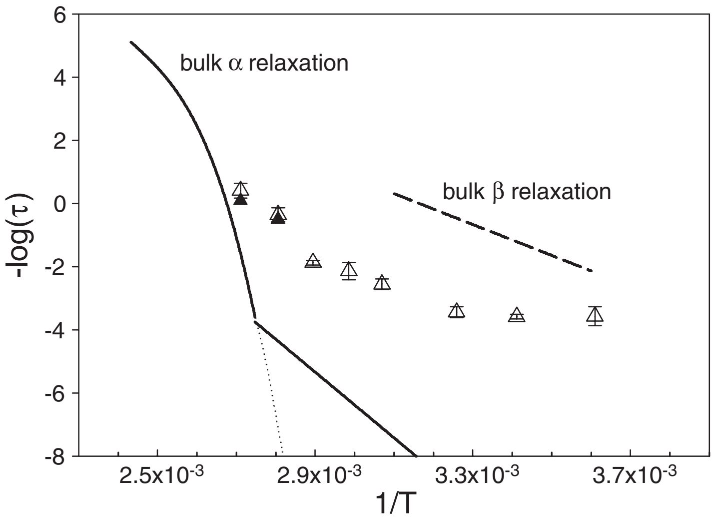

Figure 1.13: Measured surface relaxation times (symbols) compared to bulk α (solid line) [14] and β (dashed line) [15] relaxations of PS. Figure from Ref. [16].

to 277 K which is $\sim$ 100 K below bulk T_{g}). The surface relaxation deviates from the bulk VFT curve and its temperature dependence is very weak below the bulk T_{g} value, which becomes immeasurable for temperatures less than 307 K. This result is also in support of the existence of a mobile surface layer.

The surface dynamics of molecular glasses have also been studied using perturbation of nanoparticles. In the study by Daley et al. [121], the evolution of the surface of 1,3-bis-(1-naphthyl)-5-(2-naphthyl)benzene (TNB) glass was monitored in response to gold nanoparticles on the surface. Before bulk embedding occurred, an initial buildup stage was observed where material accumulated towards the vicinity of the nanoparticle at temperatures below the bulk T_{g}, which was believed to be a result of the surface flow. The temperature dependencies of surface and bulk relaxation processes were thus directly compared and it was found that surface flow (characterized through initial buildup) exhibited a weaker temperature dependence compared to bulk flow (characterized through embedding).

To study the viscosity and surface mobility of low molecular weight PS, Yang et al. [17, 129] developed a method to monitor thermally induced surface morphology with AFM. Fig. 1.14 shows a collection of data for PS films with various thicknesses. The dashed line in Fig. 1.14(b) is the viscosity data for bulk material and it can be seen that only the films with the largest thicknesses follow the bulk curve, whereas thinner films have smaller values and show an Arrhenius temperature dependence. The data deviating from the bulk curve in Fig. 1.14(b) is found to collapse onto the solid line in Fig. 1.14(a) with Arrhenius temperature dependence. This way the data is divided into two regions, with the thinner films collapsing on the Arrhenius line and the thicker films following the bulk curve. By modeling the film as a bilayer system with a bulk-like layer and a mobile surface layer, the authors found that the surface layer with a thickness of less than 2.3 nm is responsible for the reduction in the viscosity and thereby T_g.

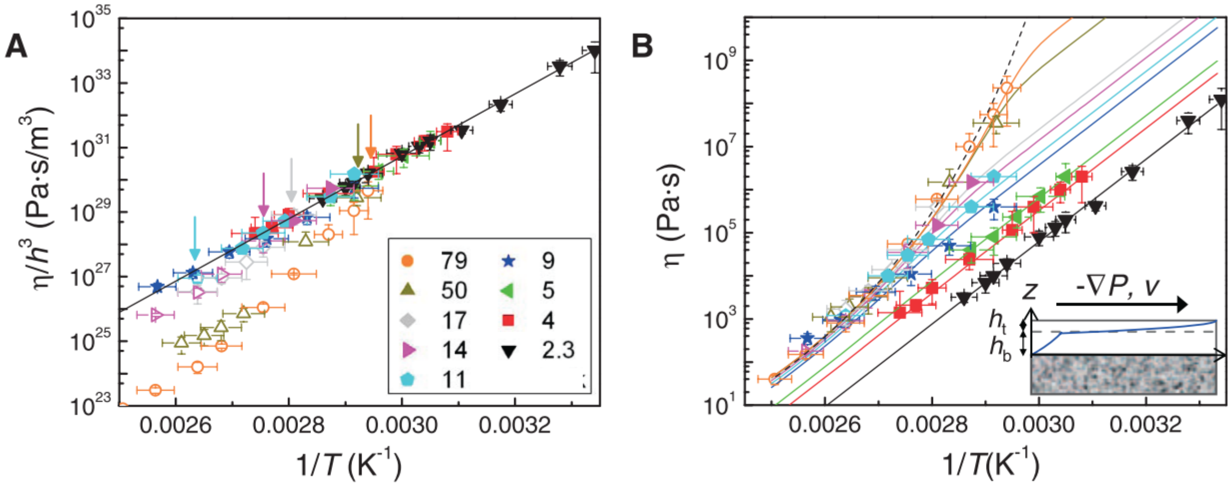

Figure 1.14: (a) η/h^3 as a function of temperature for PS films with different thicknesses from 2.3 nm to 79 nm, where η is the viscosity and h is the film thickness. Solid symbols represent data that collapse into the solid straight line which has Arrhenius temperature dependence. The rest of the data are represented by open symbols. The arrows indicate where the data of each thicknesses start to depart from the solid line. (b) Viscosity η as a function of temperature. Figure from Ref. [17].

Chai et al. probed the surface of low molecular weight PS films with a simple geometry of a stepped film [18]. By creating a step with two films and monitoring the flattening of the step, they provided quantitative evidence for the existence of a mobile surface layer. From above T_g to below T_g, a sharp transition from bulk flow to localized flow on the near surface layer was observed. The mobility (defined in terms of thickness and viscosity) of the bulk and the surface at different temperatures were obtained by fitting the height profile to either the capillary-driven thin-film equation or the glassy thin-film equation. As shown in Fig. 1.15, the bulk mobility of the stepped films follows the VFT law above the bulk T_g. Below T_g, the mobility is limited to the surface and it deviates from the bulk VFT and shows an Arrhenius temperature dependence.

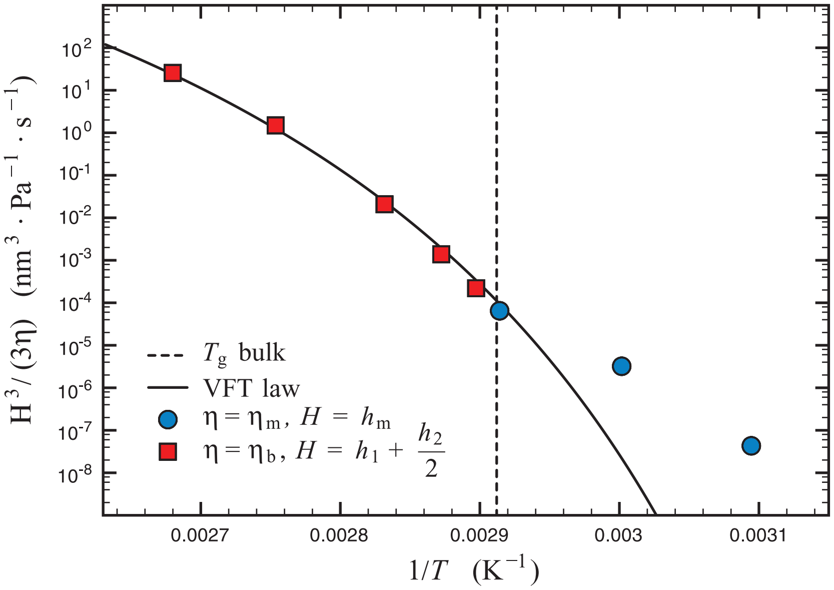

Figure 1.15: Mobility with respect to temperature. Red squares represent bulk mobility above the bulk T_g and are determined by fitting the height profile to the capillary-driven thin-film equation. Blue circles represent surface mobility below the bulk T_g and are determined by fitting the height profile to the glassy thin-film equation. Figure from Ref. [18].

Surface gratings are another type of geometry used to probe the surface dynamics of polymer. In the study by Zhang and Yu [19], periodic gratings were patterned on the surface of low molecular weight PS and the flattening of the surface was monitored at various temperatures above and below T_g.

As shown in Fig. 1.16, compared to the bulk diffusion coefficients D_v above T_g which follow the bulk VFT law, the surface diffusion coefficients D_s measured below T_g deviate from the bulk behaviours with weaker temperature dependence, and the values are orders of magnitude larger than the bulk diffusion. This study also suggests the existence of a surface layer with enhanced dynamics. The similar behaviours are found in PS as well as several small molecules [19, 127, 128, 130, 131, 132], which indicates that the enhanced surface dynamics is a general phenomenon across different systems. Depending on the specific materials, there are still variations in the diffusion coefficients depending on their molecular size and intermolecular interactions [19, 131].

In summary, there have been extensive efforts in studying the surface dynamics of glassy

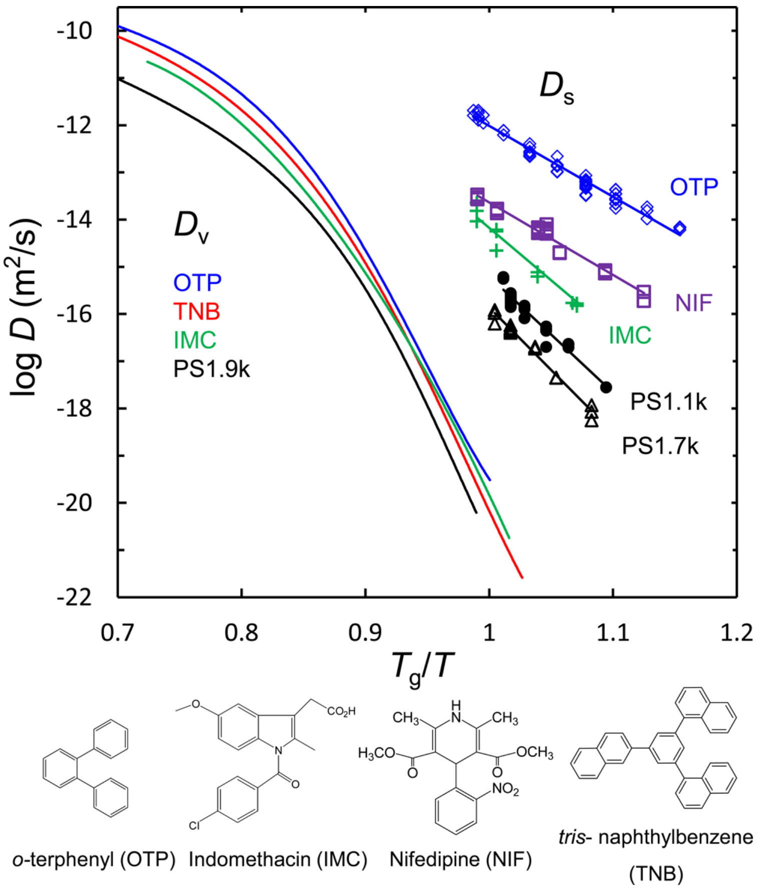

Figure 1.16: Surface and bulk diffusion coefficients (D_s and D_v) with respect to temperature normalized by T_g of each material. Figure from Ref. [19].

films using different kinds of probes [133]. These studies vary in experimental designs, techniques, materials, but they collectively suggest that the dynamics near the free surface are significantly enhanced compared to the bulk. The temperature dependence of surface dynamics are also found to be weaker than in the bulk. With the bulk being immobile, the mobile surface allows for surface relaxation under external perturbations. Despite of the many experimental and theoretical achievements in understanding the thin film glasses and their surface dynamics, there are still many open questions including the thickness of the mobile surface layer. Based on the recent discoveries, how we should tackle the glass transition problem and understand the formation of glasses does not have a clear answer yet and requires further investigations.

1.5 Stable glass by physical vapour deposition

1.5.1 Discovery of stable glass

In addition to its importance in thin film glasses and the glass transition problem, the surface dynamics of glasses also plays a key role in the ability to form a new type of glasses which have been called stable glasses [134, 135]. The chase after the conceptual ideal glass has been on for many decades, and the recent discovery of vapour deposited stable glasses made a big step forward [136].

Made in the laboratory within a short period of time, such stable glasses are close to the ideal glass and can have exceptionally high kinetic stability. Their relaxation timescales are so long that the only comparable glasses in nature are ambers that have been aged for millions of years. Instead of using the conventional method of cooling a liquid, glasses are made by placing molecules one by one onto a substrate through physical vapour deposition. In addition to its high kinetic stability, the density and modulus of vapour deposited glasses can also be greatly enhanced compared to traditional glasses [136, 137, 138, 139, 140, 141].

1.5.2 Properties of stable glass compared to regular glass

An example is shown in Fig. 1.17, where the film thickness of a vapour deposited indomethacin glass is measured during heating and cooling scans. During the first heating, the as-deposited glass stays in the glassy state and does not transform into a liquid until at a much higher temperature than the glass transition temperature. During the second heating scan after liquid-cooling, the glass exhibits an onset temperature equal to T_{g}, which shows that it has been rejuvenated to an ordinary glass. The high onset temperature (T_{onset}) on the first heating scan indicates that the as-deposited glass has enhanced kinetic stability than the liquid-cooled glass. The extrapolated liquid line and the line of the as-deposited glass intersect at the temperature called fictive temperature, T_{f}, which is a common measure of stability in stable glasses. T_{f} can be understood as the temperature the glass fell out of equilibrium as if the glass was prepared by liquid cooling. A bigger difference between T_{f} and T_{g} thus means a greater stability. Another feature in the figure that measures the stability if the density increase Δ_{ρ}, which is obtained from the gap between the as-deposited glass line and the liquid-cooled glass line. The as-deposited glass has a lower thickness corresponding to a higher density than the ordinary glass.

It is believed that the efficient packing and exceptional properties of stable glasses are mostly due to the highly mobile surfaces of glasses [134, 135]. The dynamics on the surface

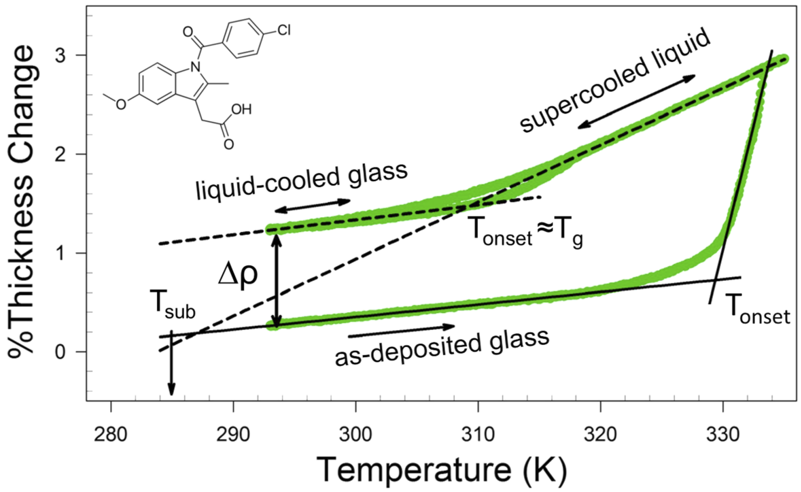

Figure 1.17: Ellipsometrically measured film thickness of a vapour deposited indomethacin glass. Figure from Ref. [8].

are fast enough to provide sufficient configurational sampling to approach equilibrium before the next layer is deposited on top.

The relaxation times of vapour deposited glass can be extremely long [142], which indicates their extremely low configurational entropy according to the Adam and Gibbs relation in Eqn. 1.9. Fig. 1.18 is a collection of S_{conf} data on molecular glasses as a function of temperature. Consistent with the prediction by Gibbs and DiMarzio, the S_{conf} of all glasses are on a trend whose extrapolation leads to an entropy crisis at a finite temperature. Compared to liquid cooled glasses, vapour deposited glasses are further down the decreasing curve and very close to the critical point.

In a study of computer simulations on vapour-deposited glasses [143], the optimal temperature for preparing ultrastable glasses is found to coincide with the Kauzmann temperature T_{K}, where the configurational entropy approaches zero. This observation indicates that there might be an underlying thermodynamic connection between optimal vapour deposited glasses and ideal glasses. This study also shows that there are significant structural distinctions between optimal glasses and ordinary glasses prepared by cooling, with the former being truly amorphous and uniformly packed, while the latter exhibiting a larger fraction of locally ordered clusters.

The effect of substrate temperature on glass stability has also been studied experimentally [140, 141, 144, 145]. It has been found that substrate temperatures near 0.85 T_{g}

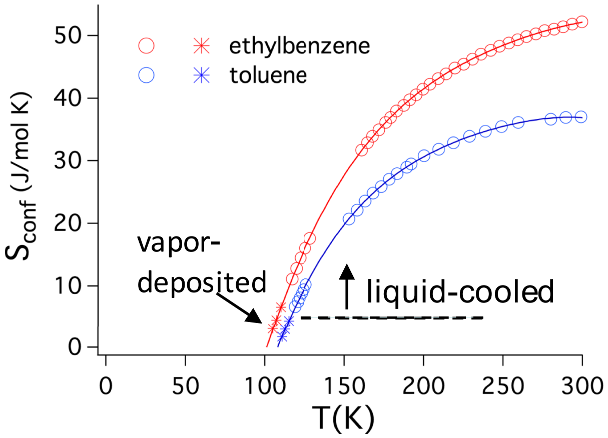

Figure 1.18: Configurational entropy of toluene and ethylbenzene with respect to temperature. Figure from Ref. [8].

result in the greatest stability both thermodynamically and kinetically for many molecular glasses. With higher or lower temperatures, glasses deposited are less stable. This temperature has been explained in terms of three different regimes [140]. At high temperatures near T_g, an equilibrium supercooled liquid is formed on the substrate during deposition. Once they are cooled below T_g, they become liquid cooled glasses just like regular glasses. Therefore they exhibit little stability compared to regular glasses. At optimal or intermediate substrate temperatures, significant stability is observed because surface mobility is high enough to take advantage of the substantial thermodynamic driving force for moving lower in the energy landscape. At even lower temperatures, mobility at the surface is so low that the system has little opportunity to utilize the large thermodynamic driving force for equilibration and thus little stability is expected.

The deposition rate also affects the glass stability and it has been studied for several molecular glass formers [134, 141, 146, 147, 148]. It is shown to only influence the stability at lower temperatures, where lower deposition rates lead to glasses with higher stability in general.

1.5.3 Importance of stable glass

The fundamental question of whether the ideal glass exists has been puzzling glass scientists for decades, and the nature of the glass state still lacks a definitive explanation even though people have been handling glasses for thousands of years. Given that the densest packing of crystal, a much simpler state than glass, was only mathematically proved recently [149] (more than 400 years after the Kepler conjecture was first proposed [150]), it is not surprising that disordered systems are still under research.

The ability to produce ultrastable glasses has enabled us to explore further into the nature of all glasses and the glass transition problem. These materials will not only benefit the development of condensed matter physics, but also contribute to many other fields from astronomy [31] to computer science [151]. As commented by Ediger [8], such glasses are "near the limits of what is possible for amorphous packing arrangements". With near equilibrium configurations, these materials are excellent candidates for studying the glass transition problem and pursuing the ideal glass.

Since the seminal paper by Swallen et al. [136], there have been extensive studies on stable glasses, trying to reveal the extreme properties of amorphous solids. Most of the materials used in vapour deposition were small molecules, with few examples of metallic glasses [152, 153]. Polymers, in principle, are an attractive candidate for ideal glasses and stable glasses, since many atactic polymers are poor crystal formers. In the past few decades, the surface of polymer thin films has been extensively studied, and it is commonly believed that surface mobility in polymer films are enhanced compared to the bulk. With the key role of surface mobility in forming stable glasses, they should be very suitable for making stable glasses through physical vapour deposition.

However, due to the low vapour pressure and high sensitivity to thermal degradation of polymer sample, vapour deposition is problematic for polymers. To vaporize them, the evaporation temperature has to be high enough to achieve meaningful deposition rate, but the temperature has to be below a threshold to prevent chain scissions or oxidation. Despite the difficulties, there are several studies that use PS in physical vapour deposition [154, 155, 156] although no stability was reported. Besides physical vapour deposition, Guo et al. reported the first possible stable PMMA glasses using the matrix assisted pulsed laser deposition (MAPLE) technique [157]. Contrary to stable molecular glasses with increased density and lower enthalpy, the stable PMMA glasses were actually 40% less dense and had a higher enthalpy than regular glasses. Yoon et al. reported stable polymer glasses of Teflon AF 1600 through vacuum pyrolysis deposition which exhibited lower fictive temperatures [158]. However, during the deposition the polymer chains are broken and then reformed, and the molecular weight decreases after the deposition, which makes it questionable to compare the deposited glass with the original material.

In this thesis we demonstrate the possibility of applying simple physical vapour deposition to low molecular weight polymers. Preparation techniques for creating stable polymer glasses are introduced. Using different characterization techniques, we investigate the their properties including stability, surface dynamics, film thickness dependence, etc. By studying these materials from different perspectives, we hope to gain insights into questions about the complex and fascinating phenomenon–the glass transition.

Chapter 2

Experimental Techniques

2.1 Materials

The main material used in this thesis is polystyrene (PS) with $M_\mathrm{w} = 1200$ g/mol catalogue no. 1024 from Scientific Polymer Products. From mass spectrometry measurements, it has a distribution of N values from 3 to 22, with PDI = 1.19. In Chapter 4, higher molecular weight PS is also used, including sample no. P9720-S with $M_\mathrm{n} = 1300$ g/mol, $M_\mathrm{w} = 1400$ g/mol, PDI = 1.08, and sample no. P8921-S with $M_\mathrm{n} = 2800$ g/mol, $M_\mathrm{w} = 3000$ g/mol, PDI = 1.09 from Polymer Source Inc.

In Chapter 3, poly(methyl methacrylate) (PMMA) has also been used, with $M_\mathrm{n} = 1000$ g/mol and PDI = 1.15, sample no. P11179D-MMA from Polymer Source Inc.

2.2 Distillation of polymers

In this thesis, physical vapour deposition is used to prepare stable glass. Since the as-purchased PS material ($M_\mathrm{w} = 1200$ g/mol) has a broad distribution in N values, if it is used directly as the deposition source, the components with the lowest molecular weight will be deposited first, resulting in a glass transition temperature that is too low for glass formation or further characterizations. In Chapter 5.1, it is shown that the low molecular weight components are also believed to be the cause of undesired surface morphology and affect stable glass formation.

To separate PS samples into more monodisperse fractions, vacuum distillation has been used in a previous study in our group [159]. It is known that the vapour pressure of polymers are much smaller compared to volatile materials. During the evaporation, there is a trade-off between the vapour pressure and the thermal stability of the material. As the N value increases, the vapour pressure of the polymer decreases, and the temperature needed to effectively evaporate the material increases significantly. However, as temperature increases the polymer may also start to thermally degrade. Therefore there is a limited temperature window for the evaporation. For PS, thermal degradation is found to occur at near 570 K [160]. Therefore all the distillations and vapour depositions for PS have to remain below this temperature.

In this thesis, distillation is performed as a pre-processing step before using the material as the deposition source. The distillation is carried out in a separate vacuum chamber, where the as-purchased material is used as the source on the bottom and a collector plate is attached to the lid of the chamber. Each time the source is heated to an elevated temperature for a few hours and the material deposited on the top plate is collected after each run. The same temperature is used for the following run if the distillation rate is still high, or a higher temperature is used in the next run to collect materials with higher molecular weight. This process is repeated until the low molecular weight portions have all been evaporated, or the temperature can not be raised higher due to thermal degradation concerns.

The product to be used later in the physical vapour deposition process is either the components that are distilled into highly monodisperse fractions, or the material left in the source plate with a truncated distribution where the low molecular weight components are evaporated off. Thereby the lowest remaining components will be deposited first in the deposition chamber.

2.3 Physical vapour deposition

Physical vapour deposition has been found to be a convenient way of making stable glass, compared to the natural cooling and aging process that are on geological timescales to achieve similar stability of the glass. As shown in Fig. 2.1, during the physical vapour deposition, the source material is heated in a vacuum and evaporates into the chamber. The vapour particles travel in the vacuum and condense on the substrate where they form a film. Depending on the substrate temperature, deposition rate and other factors, the resulting film can have different properties.

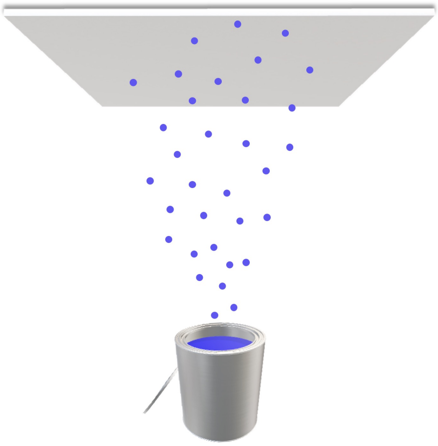

Figure 2.1: Schematic illustration of physical vapour deposition.

Vapour deposition in our lab is carried out using an ORCA temperature controlled organic materials evaporation source installed in a Korvus Technology HEX deposition unit. Before being brought into the deposition chamber, the source material is pre-distilled either into monodisperse portions or with truncated distribution in molecular weight where the lowest N values are removed. The typical deposition rate in most of our experiments is 0.05 nm/s, as measured by a quartz crystal microbalance (QCM). The chamber has a base pressure of 10^{-5} mbar during depositions.

The substrate stage can be cooled or heated by Peltier elements on both ends. There are two types of stages built for our deposition chamber. One is a stainless steel sheet that bridges the two ends, and most depositions with a uniform substrate temperatures were done with this stage. The other stage is a temperature-gradient stage, where the substrate silicon wafer bridges the stainless steel units on both ends. A detailed introduction on the temperature-gradient bridge is included in Chapter 5.1.6, where this bridge is mostly used. By individually controlling the temperature on each end, different positions on the substrate can have different temperatures.

In our deposition chamber, the source and the QCM are installed on separate wall panels, and the substrate is attached to the ceiling. With this geometry, the actual deposition rate for the substrate is different from the nominal rate from the QCM. Across the length of the substrate (∼7.5 cm), there is also a gradient and the film thickness can vary by a factor of up to 4, depending on which wall the source crucible is installed on.

2.4 Ellipsometry

Ellipsometry is an optical technique for obtaining properties of surfaces and thin films by measuring the change of light polarization upon reflection or transmission. For example, in our lab it is typically used to determine film thickness and refractive index of thin films. One of the advantages of ellipsometry is its contact-free and non-destructive measurements. It is a very versatile technique which can measure film thicknesses for single layers or multiple layers, ranging from a few angstroms to micrometers with high accuracy and precision. Depending on the type of light source, ellipsometers can be categorized into single-wavelength ones and spectroscopic ones. In this thesis, both types have been used in data collection.

For a typical ellipsometer, there are four core components in the light path: polarizer (P), compensator (C), sample (S), and analyzer(A). Throughout these components, the polarization of the light changes and properties about an unknown sample can be extracted when the other components are known. For example, Fig. 2.2 is an example configuration of an ellipsometer. The order of the main components in the light path is the polarizer (P), the following quarter-wave plate which is also called the compensator (C), the sample (S), and the analyzer(A), and thus it is known as a “PCSA” configuration. In Section 2.4.2 another ellipsometer with a “PSCA” configuration is also introduced.

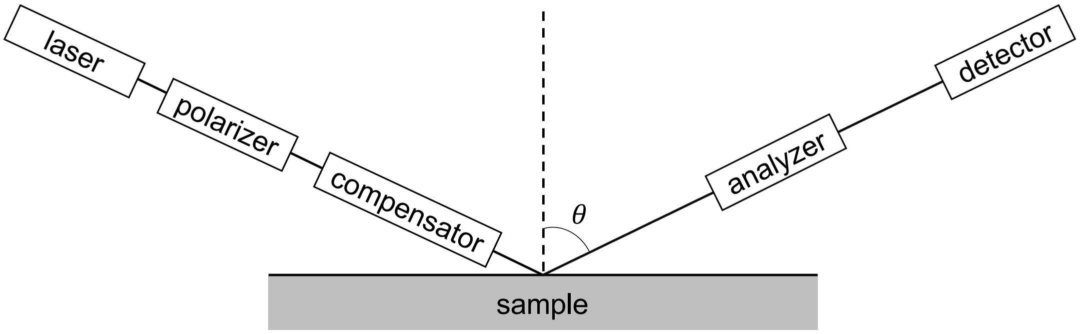

Figure 2.2: Schematic diagram of the nulling ellipsometer.

Since the ellipsometry does not directly measure physical quantities of the sample, but rather the polarization change upon light interaction, a model has to be constructed to describe the relationship between sample-related properties and the polarization change they cause. The procedure of extracting sample properties can be summarized as follows:

1. Perform measurement of the sample and obtain the light polarization change.

2. Based on estimates of properties including thickness and optical constants, construct a model to calculate the predicted response of the incident light.
3. Compare the predicted values to experimental data. By varying the initial estimates of sample properties, improve the agreement between model and data.
4. Through regression, the best match can be found which corresponds to the deduced properties of the sample.

In order to predict the change in light polarization based on the model, a mathematical method is needed to describe the polarization state of light as it interacts with different components of the ellipsometer as well as the sample. One of the common approach is using Jones calculus [161]. In Section 2.4.1, we demonstrate this approach with a nulling ellipsometer which has a "PCSA" configuration.

2.4.1 Single-wavelength nulling ellipsometry

The single-wavelength ellipsometer (EXACTA 2000, Waterloo Digital Electronics) in our lab uses a laser wavelength of 632.8 nm and an incident angle of 60°. The schematic diagram of its configurations is shown in Fig. 2.2.

First, the laser generates linearly polarized light, which is converted to circularly polarized after passing through the quarter-wave plate. The light then enters the polarizer (P) and the polarization becomes linear again. After another quarter-wave plate, the light becomes elliptically polarized before hitting the sample. Upon reflection from the sample, it travels through the analyzer (A) and finally reaches the detector. The nulling ellipsometer works by automatically tuning the polarizer and analyzer angles until the light reflected from the sample is linearly polarized so that the light intensity can be zero after passing through the analyzer. The angle accuracy of this nulling ellipsometer is 6×10^{-4} degrees [162].

Once the null condition is found, the P and A values can be used in determining the sample properties. Given only two data points (P and A), at most two unknown quantities can be obtained. Typically film thickness and refractive index are the two quantities of most interest in our studies, given that the optical properties of the substrate are known.

Below we go through the Jones calculus [161] for the configuration as shown in Fig. 2.2.

As light travels in the $+z$ direction in an isotropic material, its electric field lies in the $x - y$ plane. The Jones vector representing this light is

$$\begin{pmatrix} E_{0,x} \\ E_{0,y} \end{pmatrix} \exp(i\omega t) \tag{2.1}$$

The time component $\exp(i\omega t)$ can be omitted for simplicity, as long as it is brought back in real calculations when necessary. For a linearly polarized light at an angle θ to the x axis, the x and y components are in phase and the Jones vector is given by

$$\begin{pmatrix} E_0 \cos\theta \\ E_0 \sin\theta \end{pmatrix} \tag{2.2}$$

where E_0 is the amplitude of the electric field. For circularly polarized light, there is a phase difference of 1/4 cycle between the x and y components, and its Jones vector is

$$\begin{pmatrix} E_0 \\ \pm i E_0 \end{pmatrix} \tag{2.3}$$

Remember that for nulling ellipsometry measurements, we are only interested in the polarization state of light. Thus only the relative amplitudes and the relative phase difference are of interest.

When light interacts with an optical element or a sample surface, the polarization state will change. Therefore, a 2×2 matrix called a Jones matrix can be used to represent such a transformation. Trivially, a medium which does not change the polarization state can be represented by a 2×2 identity matrix. A non-absorbing linear polarizer with its transmission axis coincident with the x axis is given by

$$\begin{pmatrix} 1 & 0 \\ 0 & 0 \end{pmatrix} \tag{2.4}$$

The Jones matrix of a linear polarizer at an angle P to the x axis can be found by first rotating the coordinate system by an angle P, applying the above matrix, and then rotating the coordinate system back. The result is given by

$$\begin{pmatrix} \cos^2 P & \sin P \cos P \\ \sin P \cos P & \sin^2 P \end{pmatrix} \tag{2.5}$$

Similarly, a quarter-wave plate with its fast axis coincident with the x axis is

$$\begin{pmatrix} 1 & 0 \\ 0 & -i \end{pmatrix} \tag{2.6}$$

since it retards the component along the slow axis by 1/4 cycle relative to the component along the fast axis. A quarter-wave plate with its fast axis at an angle Q to the x axis can be found to be

$$\begin{pmatrix} \cos^2 Q - i \sin^2 Q & (1+i)\sin Q \cos Q \\ (1+i)\sin Q \cos Q & \sin^2 Q - i \cos^2 Q \end{pmatrix} \tag{2.7}$$

When $Q = 45°$ and only relative quantities are considered, the matrix can be simplified as

$$\begin{pmatrix} 1 & i \\ i & 1 \end{pmatrix} \tag{2.8}$$

Finally, the reflection from an isotropic sample surface can be given by

$$\begin{pmatrix} R_p & 0 \\ 0 & R_s \end{pmatrix} \tag{2.9}$$

where R_p is the reflection coefficient for light with its electric field in the plane of incidence, and R_s is the reflection coefficient for light with its electric field perpendicular to the plane of incidence.

Now we have all the important components to model the light through the ellipsometer. After the linearly polarized light from the laser source passes through the first quarter-wave plate, it becomes circularly polarized. It is worth mentioning the purpose of having a circularly polarized light before it passes through the polarizer. From matrix 2.5, the incident light with components E_x and E_y passes through the polarizer at an angle P and becomes

$$(E_x \cos P + E_y \sin P) \begin{pmatrix} \cos P \\ \sin P \end{pmatrix} \tag{2.10}$$

If the incident light is circularly polarized, E_x and E_y are equal in size and 90° out of phase (i.e., $E_x = \pm i E_y$). Then the intensity of the transmitted light will not depend on P.

After the polarizer, the light can be represented by $\begin{pmatrix} \cos P \\ \sin P \end{pmatrix}$. Applying matrix 2.7

which represents the quarter-wave plate right before the sample, the light becomes

$$\begin{pmatrix} E_{p,i} \\ E_{s,i} \end{pmatrix} = \begin{pmatrix} \cos\, Q\, \cos\, (P - Q) + i\, \sin\, Q\, \cos\, Q \\ \sin\, Q\, \cos\, (P - Q) + i\, \cos\, Q\, \cos\, Q \end{pmatrix} \tag{2.11}$$

which represents elliptically polarized light. Upon reflection from the sample, the polarization state is given by

$$\begin{pmatrix} E_{p,r} \\ E_{s,r} \end{pmatrix} = \begin{pmatrix} R_p & 0 \\ 0 & R_s \end{pmatrix} \begin{pmatrix} E_{p,i} \\ E_{s,i} \end{pmatrix} \tag{2.12}$$

If the reflected light can be completely extinguished by the analyzer, which is the principle of a nulling ellipsometer, it must be linearly polarized. $E_{p,r}$ and $E_{s,r}$ must be in phase, which means their ratio must be a real number. This gives

$$\Im(\frac{R_p}{R_s} E_{p,i} E^*_{s,i}) = 0 \tag{2.13}$$

where $\Im$ represents the imaginary part and the * represents the complex conjugate. The ratio of R_p and R_s can be written as

$$\frac{R_p}{R_s} = \tan\psi \exp(i\Delta) = \tan\psi\cos\Delta + i\tan\psi\sin\Delta \tag{2.14}$$

where $\tan\psi$ is the ratio of the amplitudes and $\Delta = \Delta_p - \Delta_s$ is the relative phase change of p polarized light compared to s polarized light. Based on Eqn. 2.13, plugging in Eqn. 2.11 and Eqn. 2.14 gives the condition that a null must satisfy:

$$\tan(2P - 2Q) = -\sin 2Q \tan\Delta \tag{2.15}$$

The A value can be found by solving

$$\begin{pmatrix} \cos^2 A & \sin A\cos A \\ \sin A\cos A & \sin^2 A \end{pmatrix} \begin{pmatrix} E_{p,r} \\ E_{s,r} \end{pmatrix} = \begin{pmatrix} 0 \\ 0 \end{pmatrix} \tag{2.16}$$

which leads to

$$\tan A = \tan\psi \frac{\cos(2P - 2Q)\cos\Delta\sin 2Q - \sin(2P - 2Q)\sin\Delta}{\cos(2P - 2Q)\cos 2Q - 1} \tag{2.17}$$

In conventional nulling ellipsometers, $Q = \pm 45^\circ$. In the case of $Q = +45^\circ$, there are two P and A pairs that satisfy the null setting:

$$P_2 = -\Delta/2 - \pi/4, A_2 = \psi \tag{2.18}$$

and

$$P_4 = -\Delta/2 + \pi/4, A_4 = -\psi \tag{2.19}$$

In the case of $Q = -45°$, there are also two P and A pairs that satisfy the null setting:

$$P_1 = \Delta/2 - \pi/4, A_1 = \psi \tag{2.20}$$

and

$$P_3 = \Delta/2 + \pi/4, A_3 = -\psi \tag{2.21}$$

The subscripts from 1 to 4 correspond to the 4 different zones by convention.

Now we have the P and A solutions if reflection coefficients R_p and R_s of the sample are known. In order to derive the physical properties of the sample from measured P and A values, the Fresnel coefficients need to be introduced. For a bare semi-infinite isotropic medium, the Fresnel reflection and transmission coefficients are

$$r_p = \frac{n_2 \cos\theta_1 - n_1 \cos\theta_2}{n_2 \cos\theta_1 + n_1 \cos\theta_2} \tag{2.22}$$

$$t_p = \frac{2n_1 \cos\theta_1}{n_2 \cos\theta_1 + n_1 \cos\theta_2} \tag{2.23}$$

$$r_s = \frac{n_1 \cos\theta_1 - n_2 \cos\theta_2}{n_1 \cos\theta_1 + n_2 \cos\theta_2} \tag{2.24}$$

$$t_p = \frac{2n_1 \cos\theta_1}{n_1 \cos\theta_1 + n_2 \cos\theta_2} \tag{2.25}$$

where n_1 and n_2 are the refractive index of the medium for the incident and transmitted light, respectively, and θ_1 and θ_2 are the angle of incidence and refraction respectively.

Now consider a thin film sample on a known substrate, which is the most common case in our studies. With the one layer on top of the substrate, the situation is much more complex with multiple reflections as shown in Fig. 2.3. In order to treat the film as one interface and find the total reflection and transmission coefficient, all the reflections and transmissions can be added.

If the electric field of the incident light is assumed to have amplitude A, the light interacts with the first interface, the amplitude of the reflected part is $r_{12}A$, and the

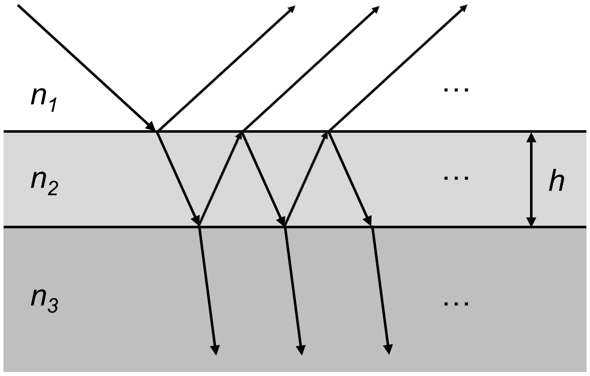

Figure 2.3: Light reflections in a thin film.

amplitude of the transmitted part is $t_{12}A$. The transmitted light travels in the film of thickness h until it interacts with the 2,3 interface. During the path in the film, the phase of the electric field shifts by $\exp(i\delta) = \exp(ik_z h) = \exp(ik\cos\theta_2 h) = \exp(i2\pi n_2 \cos\theta_2 h/\lambda)$, where λ is the vacuum wavelength of the light. Then the electric field incident at the 2,3 interface is given by $t_{12}A\exp(i\delta)$. Similarly, part of the electric field is reflected back into the film and obtains another phase shift when it gets to the 1,2 interface again. Further, part of it is reflected again and this process is repeated. By adding all the components, the total reflection coefficient is given by

$$R_{\text{total}} = r_{12} + t_{12}t_{21}r_{23}e^{-2i\delta}[1 + r_{21}r_{23}e^{-2i\delta} + (r_{21}r_{23}e^{-2i\delta})^2 + \cdots] \tag{2.26}$$

From the Fresnel coefficients it is easy to prove the relations $r_{12} = -r_{21}$ and $t_{12}t_{21} = 1 - r_{12}^2$. Using these relations together with the fact that $\frac{1}{1-x} = 1 + x + x^2 + x^3 + \cdots$, R_{total} can be simplified to

$$R_{\text{total}} = \frac{r_{12} + r_{23}\exp(-2i\delta)}{1 + r_{12} + r_{23}\exp(-2i\delta)} \tag{2.27}$$

The total transmission coefficient can be obtained using the same method. It is

$$T_{\text{total}} = \frac{t_{12} + t_{23}\exp(-2i\delta)}{1 + r_{12} + r_{23}\exp(-2i\delta)} \tag{2.28}$$

It is important to note that when calculating R_{total} and T_{total} for the p polarization, the p Fresnel coefficients r_p and t_p should be used. When calculating R_{total} and T_{total} for the s polarization, the s Fresnel coefficients r_s and t_s should be used.

Therefore, with a thin film sample on top of a known substrate, the P and A (ψ and

Δ) values can be used to solve for the refractive index n and the thickness h of the film by applying Eqn. 2.27 for the p and s polarization, where r's are directly related to n's and h is incorporated in the phase change δ. In practice, when extracting h and n from P and A measurements, one first uses estimated h and n values to calculate the predicted P and A, and compares with the measured values. By minimizing the error between calculation and measurement through varying the estimated h and n, the best match can be found, which corresponds to the real h and n values.

In reality, the typical model used in our studies is slightly more complicated. Based on the simple 3-slab model–air+polymer+silicon, there is one more layer of native silicon oxide between the polymer film and the silicon substrate. The thickness and refractive index of the silicon oxide layer also have to be known in order to limit the number of unknown quantities to a maximum of two. In using such a model, one can use the same Eqn. 2.27 to calculate the total reflection coefficient of the first layer, except that the r_{23} coefficient needs to be replaced by the total reflection coefficient R_{23} of the layer underneath it. R_{23} can be obtained using the same equation, with r_{12} and r_{23} replaced by r_{23} and r_{34}, and using the correct phase shift through the respective layer. Since the properties of the silicon oxide layer are known, R_{23} is known and the problem is solved in the same way as a 3-slab model.

In our studies, we are often interested in the change of thickness and refractive index during heating and cooling, from which we can determine quantities such as the glass transition temperature and the thermal expansion coefficients. To do this, a series of P and A pairs are measured by the ellipsometer during a set temperature run, and the data is later converted to corresponding h and n pairs.

Fig. 2.4 is an example of the P and A data as a function of temperature, together with the fitted h and n values for the thin film sample.

2.4.2 Spectroscopic ellipsometry

Another type of ellipsometer that has been used in our studies is a spectroscopic ellipsometer (J. A. Woollam M-2000DI). It has a rotating compensator, variable incident angles from 45° to 90°, and a wavelength range of 193-1690 nm. The configuration is shown in Fig. 2.5 which is known as a "PSCA" configuration. Instead of P and A data from a nulling ellipsometer, the spectroscopic ellipsometer generates $\psi(\lambda)$ and $\Delta(\lambda)$ data, which are the amplitude and phase of the ratio of R_p and R_s. Since the data is measured as a function of wavelength, a Cauchy model can be used in describing the refractive index of non-absorbing

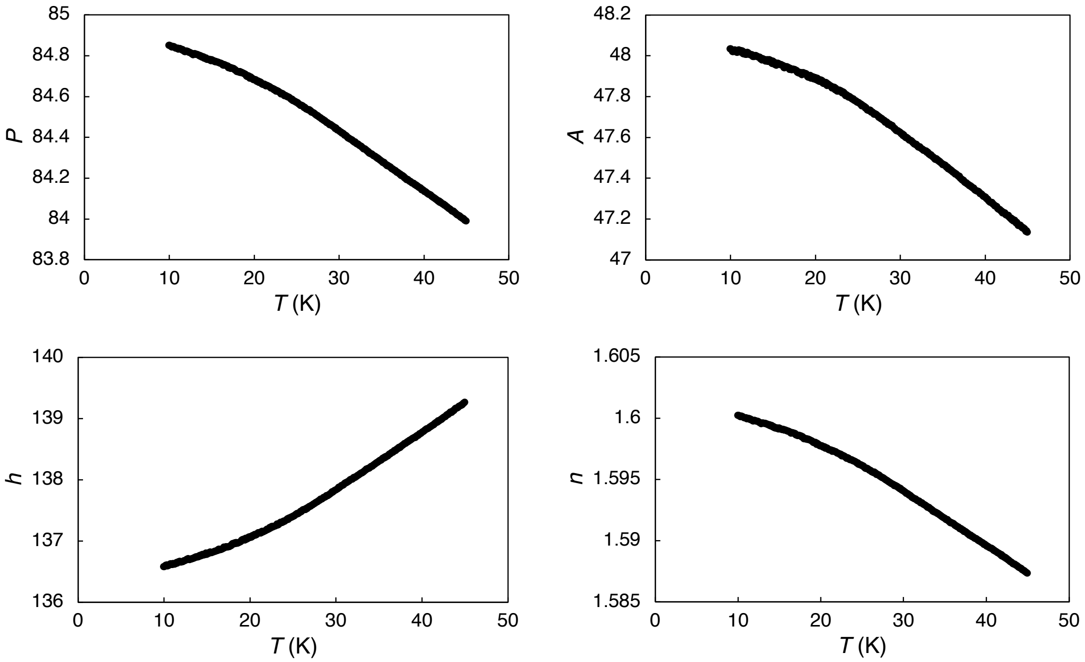

Figure 2.4: P and A data measured by the nulling ellipsometer during the cooling of a PS film, as well as the fitted thickness h and refractive index n.

thin film samples:

$$n(\lambda) = A + \frac{B}{\lambda^2} \tag{2.29}$$

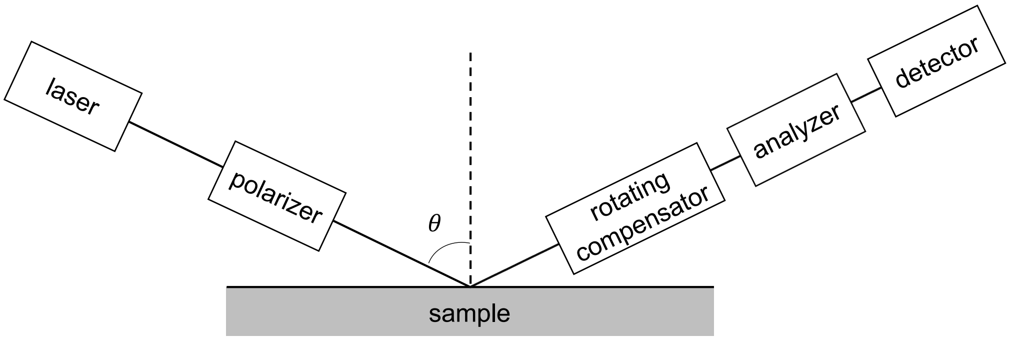

Figure 2.5: Schematic diagram of the spectroscopic ellipsometer.

Similar to the procedure in nulling ellipsometry, a model is built based on estimates of sample thickness and refractive index (in this case, A and B parameters). The fitting is performed using the CompleteEase software. In varying the estimates, a best match between the calculation and data can be found by minimizing the mean squared error (MSE).

The typical model used is the same as the one used for nulling ellipsometry, with air, polymer film, silicon oxide, and silicon substrate from top to bottom. Since polystyrene used in our studies absorbs light in the UV spectrum, the wavelength range used in fitting is set to > 400 nm.

An advantage of using the Woollam ellipsometer is that real-time fitting can be done during the measurements. This is especially helpful when measuring stable glass samples, since it is easier to make sure the rejuvenation is completed at a high enough temperature while preventing the film from dewetting at too high temperatures.

Fig. 2.6 is an example of the ψ and Δ data as a function of wavelength for a PS thin film sample at 288 K. The film thickness h and refractive index n are fitted to be 172 nm and 1.608 using a Cauchy model.

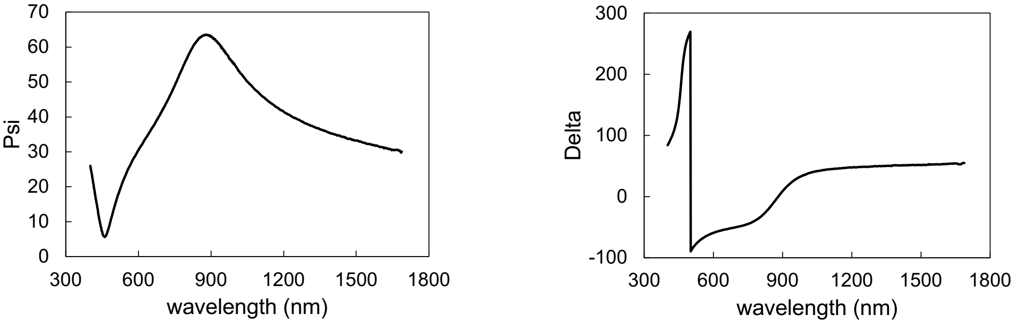

Figure 2.6: ψ and Δ data measured by the spectroscopic ellipsometer of a PS film at 288 K.

2.5 Atomic force microscopy

When working with materials on small scales, different types of microscopy are needed to go beyond the limit of the human eye. Optical microscopy reaches to approximately one micrometer due to the limitations set by the wavelength of visible light. Scanning probe microscopy is capable of a resolution in the atomic range, by using a sharp tip to scan and detect the surface properties. Atomic force microscopy is one type of scanning probe microscopy, which uses a non-conducting tip and construct an image of the surface based on the interaction force between the tip and the surface while the surface is scanned.

Fig. 2.7 is a schematic illustration of the configuration of an AFM. On the end of a long flexible cantilever, there is a sharp tip that "feels" the surface through its interaction with the surface. Depending on the distance between the tip and the sample, as well as the properties of the two, the interaction force varies and the cantilever is bent to a various degree. As shown in Fig. 2.8, there are three different regimes of the interaction force between the tip and the sample, approximately described by the Lennard-Jones potential. When they are very close, which means the tip is in contact with the surface, the Pauli repulsion dominates and there is a strong repulsive force. For slightly longer distances there is a larger van der Waals attraction and the force becomes attractive. If the tip is very far away from the surface, the force becomes negligible. It is worth mentioning that in the attractive regime, the force is not a monotonic function of the distance. Point 1 and 2 in the figure can have the same force with different distances. In real practice, the AFM has to be set to work only on the left or the right of the minimum to ensure a monotonic relationship between the force and the distance.

To detect the interaction, a laser light is shined on the back of the cantilever, and reflected onto a photodiode that detects its deflection. As the tip is scanned across the surface, or equivalently, the surface is scanned across the x-y plane (the case shown in the figure), the direction and the degree of the laser deflection changes according to the tip-sample distance and thus the force. The laser signal is sent into the feedback loop, and depending on the mode that the AFM is operating in, the feedback system can adjust the height of the cantilever by a piezoelectric element so that some measurable quantity remains constant, such as the interaction force, the oscillation frequency shift, or the oscillation amplitude, etc. In this way, the z-direction data is recorded at every point in the x-y plane and an image of the surface can be constructed.

The AFM can operate in contact mode, non-contact mode, or intermittent contact mode/tapping mode, depending on the requirements of the experiment. In the contact mode, the cantilever is not oscillated, and either a constant force or a constant height is maintained during the scan. In the constant force mode, a certain setpoint value of the force is selected via a certain deflection of the cantilever, and the feedback system adjusts the height of the cantilever to keep a constant distance between the tip and the sample. In the constant height mode, no feedback is involved and the change in deflection is recorded.

In both the non-contact mode and the tapping mode, the cantilever is oscillated at or near the resonance frequency by the piezoelectric element. In the non-contact mode the tip

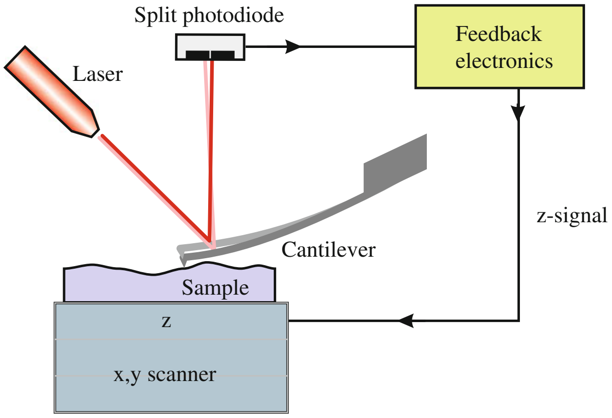

Figure 2.7: Schematic illustration of a typical AFM. Figure from Ref. [20].

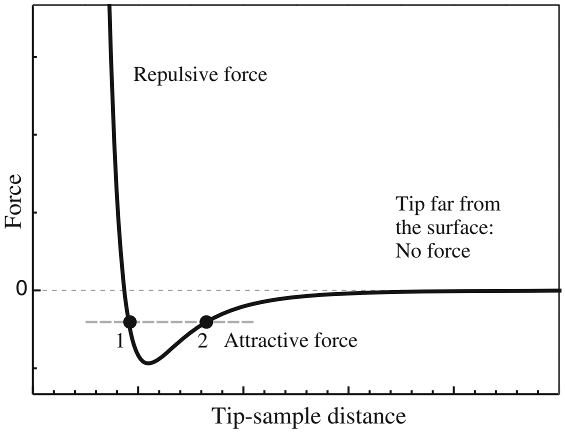

Figure 2.8: Force between the tip and the sample. Figure from Ref. [20].

does not contact the surface at all, and in the tapping mode the tip is in contact with the surface part of the time. During the scan, the van der Waals attraction decreases the resonance frequency of the cantilever. The feedback system adjusts the average tip-to-sample distance to maintain a constant oscillation amplitude or frequency. The measurement of the tip-to-sample distance at each location on the surface is used to create a topographic image of the sample surface. In addition to the topographic image, the phase image can be obtained in the tapping mode as well. The phase shift of the oscillation due to the tip-sample interaction contains information about the energy dissipation during the oscillation, which is related to sample properties.

In this thesis, a JPK Nanowizard 3 atomic force microscope is used for the study of the surface of stable glass. The tapping mode is used to protect both the sample and the tip, since the hard contact involved in the contact mode may easily damage the soft surface and also decrease the sharpness of the tip very quickly. Tips are type PPP-NCSTR from Nanosensors, with a tip radius of curvature < 10 nm and tip height 10–15 µm. The resolution of all measurements are 512×512. Gwyddion (version 2.58) is used for image analysis. In experiments where the sample is brought to an elevated temperature, a JPK High Temperature Heating Stage is used instead of a regular stage.

2.6 Matrix assisted laser desorption/ionization-time of flight mass spectrometry

To determine the molecular weight and the distribution of N's in our vapour-deposited glasses, matrix assisted laser desorption/ionization – time of flight (MALDI-TOF) mass spectrometry was applied. It is a technique to ionize samples into charged molecules, and then measure their mass-to-charge (m/z) ratio.

The ionization part is MALDI. The analyte is first mixed with an excess amount of a matrix compound. The mixture is deposited on a target plate having multiple spots for several different samples to be applied. A laser pulse irradiates one of the spot, and rapidly heats it. The laser energy is absorbed by the matrix which gets desorbed and ionized, and carries the analyte molecules into the gas phase. During the flight of the mixture, collisions among particles usually result in the ionization of the analyte, either through protonation or deprotonation with the matrix molecules. Most commonly, the analyte molecules carry a single positive charge during this process.

The TOF part is the mass analyzer, where an electric field is applied to accelerate the ions, and then they enter a field free region to drift before hitting the detector. After the acceleration, the ions have a potential energy

$$E = zeV \tag{2.30}$$

where e is the electron charge, and V is the voltage applied in the electric field. At the end of the acceleration, the potential energy is converted into kinetic energy at the start of the drifting

$$zeV = \frac{1}{2}mv^2 \tag{2.31}$$

where m is the ion mass, and v is the velocity of the drifting ion. Ions with different m/z values therefore have different velocities

$$v = \sqrt{\frac{2zeV}{m}} \tag{2.32}$$

and the detector is able to differentiate them based on the time they spend during the same path

$$t = d\sqrt{\frac{m}{2zeV}} \tag{2.33}$$

where d is the length of the known path. Further, the mass-to-charge ratio is simply

$$m/z = \frac{2eVt^2}{d^2} \tag{2.34}$$

Many MALDI-TOF instruments are equipped with a reflectron that reflects ions using another electric field. This increases the ion flight path and the difference in the time of flight, thus increasing resolution.

In this thesis, a Bruker Autoflex Speed MALDI-TOF mass spectrometer is used in the reflectron mode. It is equipped with a 2kHz Nd:YAG UV laser (355 nm). It is highly sensitive and is able to measure samples with extremely small amounts. Most samples in this thesis are thin films of $\sim$ 100 nm on a silicon wafer of $\sim$ 1 cm × 1 cm, and dissolving only a fraction of the film is sufficient for its mass analysis. The matrix used in our measurements is dithranol (226.23 g/mol) mixed with silver trifluoroacetate.

2.7 Preparation of gold nanoparticles

Gold nanoparticles are used in the study of the surface of stable glass in this thesis. The following recipe of synthesizing gold nanoparticles is borrowed from Ref. [163] and Ref. [26]:

1. All glasswares are carefully cleaned using lab detergent and rinsed thoroughly using deionized water.

2. Make a gold salt solution (1 mM) of 0.017 g $HAuCl_4 \cdot xH_2O$ (5×10^{-5} mol) in 50 mL deionized water. Make sure to use glass pipettes to handle gold salts when making solution as $HAuCl_4 \cdot xH_2O$ can erode metal utensils.

3. Make a citric acid solution of 0.0385 g $C_6H_5O_7Na_3 \cdot 2H_2O$ in 3.846 g of deionized water.
4. Heat the gold salt solution in a flask for about 30 minutes until boiling while it is being stirred.
5. When the gold salt solution boils, rapidly add the citric acid solution and speed up stirring for about 15 minutes until the color of the mixture is stable (wine red).
6. Continue heating for another 5 minutes to make sure that the suspension is stabilized.
7. Divide the gold colloidal into small glass bottles and cool to room temperature before sealing.

The above recipe creates gold nanoparticles with size around 20 nm. Decreasing the citrate solution volume or concentration results in larger nanoparticles.

Chapter 3

Preparation and characterization of stable polymer glasses

This chapter is reproduced from the following paper with the permission of Springer Nature:

A. N. Raegen, **J. Yin**, Q. Zhou, & J. A. Forrest. Ultrastable monodisperse polymer glass formed by physical vapour deposition. *Nature Materials*, 19(10), 1110-1113 (2020). DOI: 10.1038/s41563-020-0723-7 [1].

This paper describes our lab's development of a process to make ultrastable polymer glass samples as well as characterization of the samples. A. N. Raegen performed experiments including physical vapour deposition, ellipsometry and mass spectrometry, data analysis, produced most of the data on PS samples and contributed to the writing and editing of the manuscript. I performed experiments including physical vapour deposition, ellipsometry and mass spectrometry, data analysis, produced the data on PMMA samples and contributed to the discussion leading to the first draft and editing of the manuscript. Q. Zhou performed experiments including physical vapour deposition and ellipsometry, data analysis, produced the data on the anisotropy of PS samples and contributed to the editing of the manuscript. J. A. Forrest conceived the experiments, contributed to data analysis, wrote the draft manuscript and contributed to the editing of the manuscript.

3.1 Abstract

Stable glasses prepared by vapour deposition are an analogue of glassy materials aged for geological time scales. The ability to prepare such materials allows the study of near ideal glassy systems. We report the preparation and characterization of stable glasses of polymers prepared by physical vapour deposition. By controlling substrate temperature, deposition rate, and polydispersity, we prepare and characterize a variety of stable polymer glasses. These materials display the kinetic stability, low fictive temperatures and high density characteristic of stable glasses. Extrapolation of measured transformation times between the stable and normal glass provides estimates of the relaxation times of the equilibrium supercooled liquid at temperatures as much as 30 K below the glass transition temperature. These results demonstrate that polymer stable glasses are an exciting and powerful tool in the study of ultrastable glass and disordered materials in general.

3.2 Introduction

The observation of ultrastable glasses [8, 136] is one of the most exciting recent developments in the ongoing quest to understand the dynamics of glass forming materials, and the formation of glassy solids. The ability to make these materials through vapour deposition [136], circumvents the alternative approach of aging for thousands or even millions of years, and has allowed the creation of glasses tantalizingly similar to so called "ideal glass" prepared in the limit of infinitely slow cooling to the Kauzmann temperature T_{K}. These glasses also exhibit exceptional kinetic stability due to their high density, and for thin films, appear only to form the normal supercooled liquid upon heating well beyond the glass transition temperature, T_{g}, of the ordinary glass by nucleation at one or both surfaces [164].

In order to fully exploit measurements of vapour deposited glasses to learn about ideal glass, the stable glasses formed and measured should be the same as those that would be obtained if the corresponding glass forming liquid were cooled at an arbitrarily slow rate, or the glass was aged for sufficiently large times. Unfortunately this correspondence is not completely realized in small molecule stable glasses as they are almost exclusively birefringent [165]. This anisotropy has been studied extensively and an understanding has arisen based on comparisons with molecular dynamics simulations [166, 167]. Interestingly, it was noted in simulations of evaporated polymers [168] that stable glasses composed of small flexible polymers do not exhibit this anisotropy. These simulations made the important suggestion that glasses made of small polymer molecules may be maximally dense disordered materials without the detraction of anisotropy. Polymers are also an attractive candidate for ideal glasses as many atactic polymers are poor crystal formers, and the liquid can be the actual equilibrium state. Polymers also have an extraordinary degree of tunability in terms of the T_{g} value as well as the physical and chemical properties.

Vapour deposition is an uncommon technique for preparing polymer samples, as the polymers themselves have very low vapour pressures and are sensitive to thermal degradation. This thermal sensitivity places strict limitations on the temperature ranges that can be employed during their processing. Despite this, there have been several reports of depositing polystyrene (PS) films [154, 155, 156] using physical vapour deposition (PVD). The thermal sensitivity of polymers has impacted attempts to make polymer stable glasses, though a number of "interesting polymer glasses" have been produced [8]. The first reports of possible stable polymer glass used a matrix assisted technique to deposit the polymers [157]. The samples exhibited kinetic stability characteristic of stable glass, but were actually less dense than the rejuvenated polymer due to the formation of nanostructured films upon deposition. A more recent investigation by Yoon et al. [158] used vacuum pyrolysis to produce films of amorphous fluoropolymer. In this process, molecular bonds are broken and new ones formed during the deposition. The deposited glassy films exhibited low fictive temperatures, but were certainly affected by their deposition process. The study suggested the molecular weight of the deposited molecules was lower than the original material, an indication of bond cleavage during deposition. This (as well the lack of definitive evidence for kinetic stability, or increases in density) places significant limitations on the correspondence between the deposited polymer samples and those that could have been prepared by sufficient aging. The technique is also restricted to polymers that will reform the same chemical material after pyrolysis.

Perhaps the simplest approach to obtain a polymer stable glass with the same properties as a material that had been cooled from the equilibrium liquid is to follow the PVD process used for small molecule ultrastable glasses. In order to obtain appreciable deposition rates at temperatures below those where thermal degradation occurs requires the use of higher vapour pressure, near-oligomeric materials. The ability to produce a stable glass depends strongly on the relation between the substrate temperature and the normally measured T_g of the material. The T_g value of near oligomeric materials is a very strong function of the polymerization index N, and most commercially available polymers, even those considered to be very monodisperse, have many different N components. This can lead to unexpected results when trying to thermally deposit films from even moderately polydisperse materials [156]. From these considerations it would seem that direct thermal evaporation of highly monodisperse oligomers is a promising route to produce ultrastable polymer glass films. For the case of atactic PS, there is the added advantage that except for an extremely small concentration of stereoregular molecules [169], there is no crystal ground state.

In this paper and accompanying supplementary information, we describe the application of physical vapour deposition of ultra-monodisperse samples to produce polymer stable glass. While we present mostly data for poly (oligomeric) styrene, we also demonstrate the generality of the technique by producing and measuring stable glasses of poly(methyl methacrylate) (PMMA). The techniques are general and should be applicable to a wide range of polymer systems. The deposited films are physically characterized by ellipsometry [140], and chemically characterized by mass spectroscopy. The actual deposited films typically exhibit 2–4 neighbouring N components.

3.3 Demonstration of kinetic stability

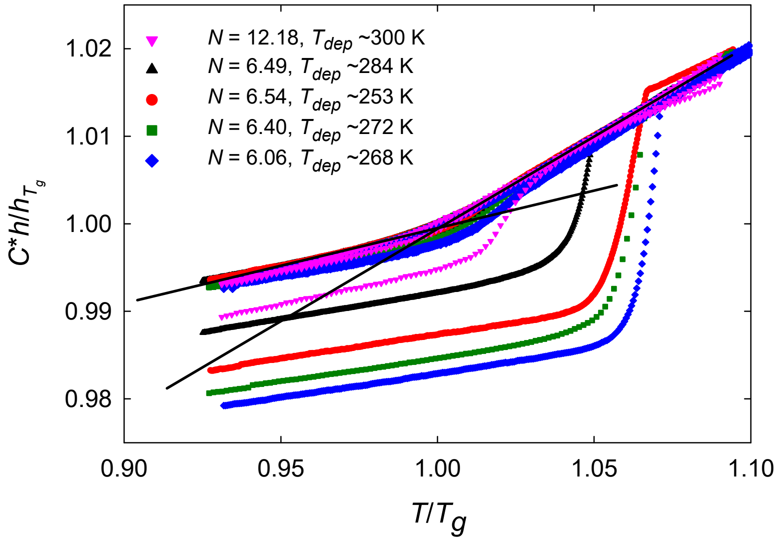

Figure 3.1: Thickness change versus temperature for initial and subsequent heating and cooling cycles of various kinetically stable glasses. Substrate temperatures are listed in the legend. Films had thickness $\gtrsim$ 100 nm. From top to bottom: $N = 12.18$, $T_\mathrm{g} = 314.6$ K, $T_\mathrm{f} = 303$ K; $N = 6.49$, $T_\mathrm{g} = 300.7$ K, $T_\mathrm{f} = 286.5$ K; $N = 6.54$, $T_\mathrm{g} = 299.9$ K, $T_\mathrm{f} = 275.5$ K; $N = 6.40$, $T_\mathrm{g} = 300.1$ K, $T_\mathrm{f} = 274.2$ K; $N = 6.06$, $T_\mathrm{g} = 298.6$ K, $T_\mathrm{f} = 272.7$ K. Deposition rates are 0.05 nm/s or less for all samples. Both axes are normalized to their values at the glass transition temperature of the sample. The black lines represent the $h(T)$ data in glassy and melt region used to determine T_g and T_f.

Fig. 3.1 demonstrates our ability to prepare kinetically stable polymer glass for polystyrene (PS) of N values in the range 6–12. Similar data for PMMA with $N \sim 10$ is provided in

Fig. 3.11 (supplementary discussion). Fig. 3.1 shows the thickness (as determined by ellipsometry) of a first heating (lower curve) as well as subsequent cooling and second heating (upper curves) of a PS glass deposited onto a substrate at temperatures below T_{g}. Thicknesses have been scaled (by a factor $\simeq 1$) to have the same liquid slope. This scaling was found to be necessary to collapse the curves, and thought to be a consequence of small differences in the manual alignment of samples. This figure shows that the as-deposited films have lower thickness (higher density) than the same films after heating. The transformation from high density deposited film to normal liquid occurs at temperatures significantly above the measured T_{g} value. This is the same kinetic stability observed in other stable glass materials. After the kinetic transformation to the ordinary liquid, the heating curve is quantitatively the same as all subsequent heating curves. Upon cooling we can measure the T_{g}, the difference in density between the stable glass and ordinary glass $\Delta\rho$ and the fictive temperature T_{f}. All cooling curves are essentially identical. The T_{g} is measured as the intersection between the linear regions of the glassy and liquid states upon cooling, and the T_{f} as the intersection between the extrapolated liquid line and the as-deposited glass. The T_{f} value can be thought of as a T_{g} for the vapour deposited material if it were prepared by cooling an equilibrium liquid. The T_{g} values from smallest N to largest N differ by 15 K, and so are scaled to T_{g}. As expected, the T_{f} of the ordinary glass is very similar to the measured T_{g} value. In this example the T_{f} values measured for PS range from about 10K below the measured T_{g} value to 33 K below the measured T_{g} value. Samples that have relatively low T_{g} values are kept chilled after preparation to prevent rejuvenation at ambient temperatures.

Fig. 3.1 and Figs. 3.5 and 3.6 in supplementary methods demonstrate the ability to make stable polymer glass over a wide range of experimental parameters. However, there are notable qualifications that result directly from the polymeric nature of the material. For the case of molecular glass, regardless of the M_{w} of the molecule, each deposition is always the same material. The deposited films may have the different stability, density etc, but they are the same material with the same T_{g} value. This important consistency is removed for polymeric materials- even those that could reasonably be considered as oligomeric. The exact material that is being deposited during any one deposition depends on the detailed distribution of N-mers. This, in turn, depends on the temperature of the evaporation source, and the amount of time the source has been heated (as smaller N are evaporated first due to their higher vapour pressure). Thus, it is almost impossible to make precisely the same sample twice, and we continuously characterize the actual deposited samples by mass spectroscopy. Although (as shown in Fig. 3.1) we can often scale by the measured T_{g} of normal glass in order to remove the N dependence, there are other ways in which N dependence is more critically important, and why we have focused on the region $N \sim 6-7$

in much of our paper. For example for larger N (≥ 10) we are able to use vapour deposition to make stable glass, but for the most stable glasses, we are not able to characterize the stability in terms of T_f and $\Delta\rho$ for the full range of substrate temperatures. The reason for this is that these materials are so stable that when heated, they sublime before they can rejuvenate to a normal supercooled liquid. This results in an inability to actually measure T_f and $\Delta\rho$ over a large parameter range. For N values much smaller than ~ 6, the T_g is low enough that the materials partially rejuvenate under ambient conditions. We have elected to show data in Fig. 3.1 for $N \sim 6 - 7$ as these materials are the ones we can fully characterize over the widest range of other parameters. To demonstrate our ability to prepare and characterize stable glasses (although not over full range of stability) with larger N, Fig. 3.1 also includes data for a stable glass with $N = 12.2$. Notice that the slight curvature in heating the $N = 12.2$ sample above T_g is due to sublimation mentioned above. We have investigated the distribution of N as a function of the source temperature (Fig. 3.7 in supplementary methods) and find that we can reliably produce monodisperse films with $N \sim 13$ with this particular source before chain scission results in the occurrence of small N components and resultant loss of monodispersity.

3.4 Chemical and physical characterization of deposited films

Fig. 3.2 shows the distributions of N obtained from Matrix assisted Laser Desorption and Ionization- Time of Flight (MALDI-TOF) data for different materials. The as-purchased PS material is shown in Fig. 3.2(a). The polydispersity index (PDI) of the as-purchased material is calculated on the basis of the data to be 1.19. Fig. 3.2(b) shows a fractionally distilled component prepared from the same as-purchased material. This fraction has $\bar{N} = 6.04$ and a PDI of 1.005. The extraordinary sensitivity of the MALDI-TOF technique allows us to measure the deposited film, and Fig. 3.2(c) shows material that has been removed from two (~ 100 nm thick) deposited films after ellipsometric investigation. The histogram at smaller N has $\bar{N} = 6.20$ and PDI of 1.005. The histogram at larger N ($\bar{N} = 12.18$, PDI = 1.005) is for a sample that was pretreated to remove small N components rather than being previously fully distilled. This difference in $\bar{N}$ between distilled and deposited materials is because once evaporation has started we do not immediately collect the material, but wait until we achieve the desired deposition rate (as monitored by quartz microbalance). Since the smaller N oligomer has a higher vapour pressure than that of larger N, the evaporated material evolves from having more of the smaller N to more of the larger N as evaporation proceeds. We note that this will result in multiple evaporations

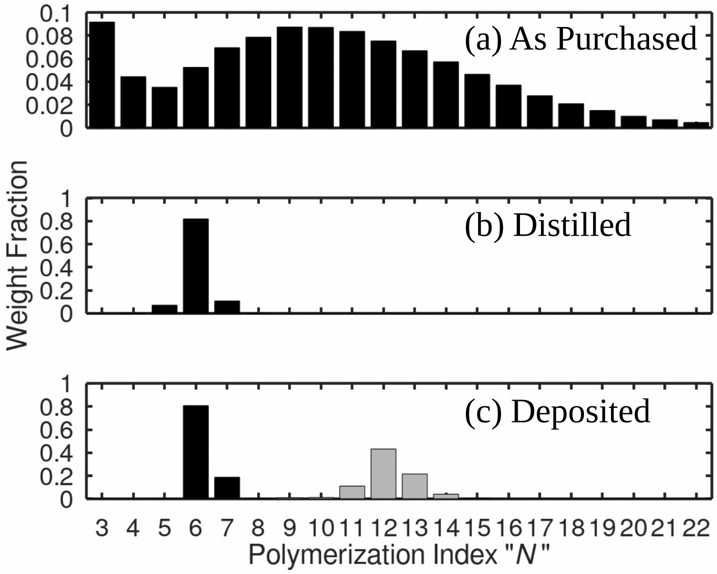

Figure 3.2: MALDI-TOF data for polymers in different phases of stable glass production. (a) as-purchased (b) after distillation (c) after deposition. The bottom plot (c) also shows the distribution of N for the $N = 12.2$ material shown in Fig. 3.1.

from the same source to produce samples that have slightly different N and hence slightly different T_g. For this reason, it is not possible to always prepare samples with the same N distribution, and thus not possible to prepare samples with exactly the same value of T_g. In order to make comparisons between samples with slightly different T_g, we usually consider the reduced temperature T/T_g.

Fig. 3.3 shows the difference in density (at T_g and as measured through the film thickness) of a collection of PS stable glasses as a function of the measured T_f (prepared by varying the substrate temperature as shown in Fig. 3.5). Each value of $\Delta\rho$ is derived from a thickness versus temperature plot like Fig. 3.1. The density changes vary from a fraction of a percent for samples with T_f fairly close to T_g to values as large as 1.6% for a sample with T_f being ~ 25 K below the T_g value. The largest density increases are very comparable to the largest measured in ultrastable organic glasses. The same ellipsometric technique is used to measure density in the molecular glasses. This increase in density is one of the underlying factors giving rise to kinetic stability. Measurement of birefringence provides information about the anisotropy due to molecular ordering. Birefringence measurements (detailed in supplementary discussions and Figs. 3.9 and 3.10) show we can place a bound

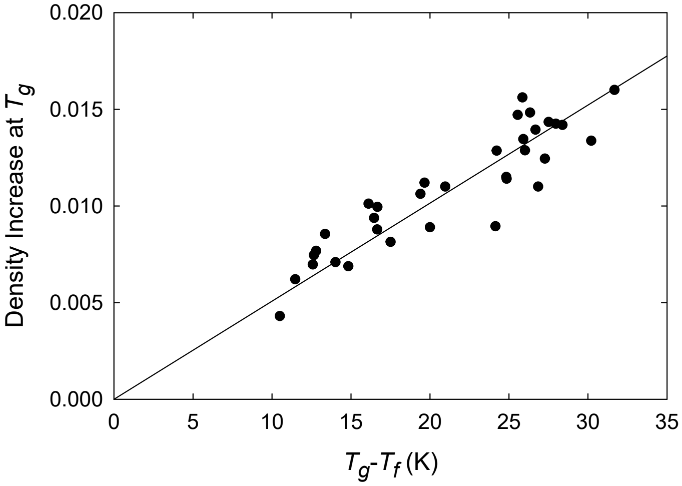

Figure 3.3: The density increase in stable glass films compared to normal films as measured at T_{g}.

on birefringence for all of the PS samples of ($|n_{xy} - n_z| < 0.01$).

3.5 Probing kinetics through rejuvenation of stable glass

One of the most fascinating aspects of stable glass materials is that they have properties of glasses aged for extremely large times and, as such, have the potential to provide insight into the dynamics of the densest possible ("ideal") disordered materials. Of particular interest in any glass forming material is measurements of the relaxation times for temperatures below T_{g} and approaching T_{K}. Of course, such measurements necessarily require one of two options. Either the experiments require an amount of time as large as the relaxation time (perhaps millions of years or more) or an extrapolation of data from more accessible times must be used. Recently, Ediger [8] has suggested the use of transformation kinetics (from stable glass to ordinary liquid) to estimate the relaxation times of the vapour deposited samples.

We performed isothermal transformation kinetics studies for a number of PS stable glasses with N ranging from 6 to 10, and substrate temperatures, T_{dep}, in the plateau region (of Fig. 3.5) $T_{\mathrm{dep}} < 268$ K. These transformation times data are shown in Fig. 3.4

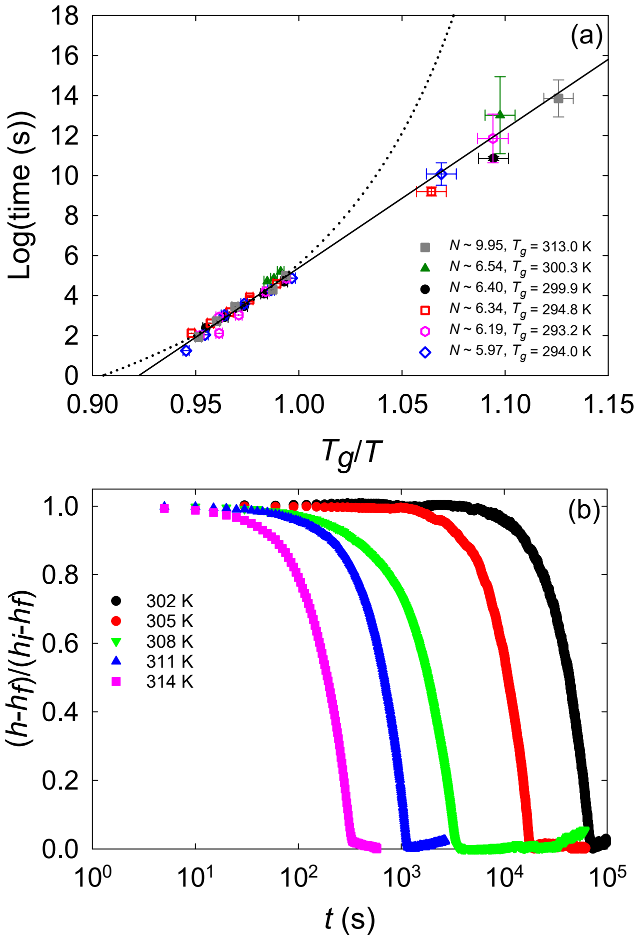

Figure 3.4: Estimating relaxation times for stable glass films of PS. Fig. 3.4(b) shows rejuvenation data used to obtain transformation times. Fig. 3.4(a) shows transformation times (from stable to ordinary glass) at various temperatures for six different depositions (having T_g and N described in the legend). This is shown as data points with $T_\mathrm{g}/T < 1$. Vertical axis error bars on the extrapolated values reflect the error in the best fit slope. The solid line is a best linear fit to the collective relaxation time data as a function of $\frac{T_\mathrm{g}}{T}$. A VFT fit to the measured rejuvenation times is shown as the long dashed curve.

and Fig. 3.8 in the supplementary discussion. Fig. 3.4(b) shows typical transformation kinetic data (in this case for $N = 6.4$). These data can be used to obtain rejuvenation times. Fig. 3.8 shows rejuvenation times for a number of stable glasses versus inverse temperature. The actual measured data points are those with times less than about 10^6 s. The measured data for a particular sample (at different rejuvenation temperatures) are fit to Arrhenius temperature dependence. This best fit is then extrapolated to the measured T_f to obtain the estimated relaxation time of the as-prepared stable glass. It is evident from Fig. 3.8 that the rejuvenation times show significant dependence on the particular N and T_g. We normalize the data by scaling all temperatures with the natural temperature scale of T_g. Fig. 3.4 shows that this simple T_g/T scaling allows all of the data to collapse onto a single curve. The solid line and dashed lines in Fig. 3.4 are fits to all of the scaled data (all values for $T_\mathrm{g}/T < 1$). The symbols for $T_\mathrm{g}/T > 1$ are the Arrhenius extrapolations (to $T_\mathrm{g}/T_\mathrm{f}$) from Fig. 3.8. The solid line is an Arrhenius fit to all of the collective scaled data and suggests that the relaxation (aging) times of the prepared stable glasses range from 10 years for the least stable glass to 3 million years for the most stable. Since the transformation data occurs over a relatively small range compared to the required extent of extrapolation, it is not possible to distinguish Arrhenius temperature dependence from Vogel-Fulcher-Tamman (VFT) on the basis of our data. For the case of VFT fits to the data, the extrapolated aging times range from 3 million years to 10^{43} years. The best VFT fit value of $T_\mathrm{g}/T_\mathrm{V}$ to all measured times is 1.169. This is in quantitative agreement with the value of 1.170 obtained in Yang et al. [17] for viscosity measurements of PS with a M_w of 2400 g/mol. We have also performed a much more limited set of transformation measurements on the PMMA and in that case (shown in Fig. 3.11 in the supplementary discussion) the sample with $T_\mathrm{g} - T_\mathrm{f}$ =21 K ($T_\mathrm{g}/T_\mathrm{f} = 1.07$), the extrapolated lifetime was $10^{13.6}$ s. This lifetime is significantly greater than the value for PS with similar $T_\mathrm{g}/T_\mathrm{f}$ and indicates that PMMA exhibits greater kinetic stability than PS.

3.6 Outlook

We have demonstrated a technique that can be used to make stable glass films of any polymer material that exhibits a range of polymerization index with sufficient vapour pressure. The technique allows for near continuous tunability of the T_g value for low N polymers that is not found in any other stable glass material. This is combined with the large range of chemical properties provided by polymers. These two aspects make this approach ideal for production of designer stable glass materials that can cover many application areas. Following the assertions from simulations [168], the low anisotropy of these materials makes them an ideal analogue of well-aged materials and a promising direction for future work aimed at probing near ideal glasses.

3.7 Method

The starting polymers in this case are for the PS M_w = 1200 g/mol Catalog #1024 from Scientific Polymer Products, and for the PMMA M_n = 1000 g/mol, $M_\mathrm{w}/M_\mathrm{n}$ = 1.15 catalog P11179D-MMA from Polymer Source Inc. Processing of the as-purchased samples is a two step process. In the first step, the material is either thermally distilled into highly monodisperse fractions in a separate vacuum chamber [159], or the low M_w components are evaporated off in the separate chamber so that the lowest remaining components will be deposited [159]. MALDI-TOF mass spectroscopy measurement of the as-purchased PS material indicate $N-$mer's from $N = 3$ to $N = 22$. In the second step, deposition of the material (either pre-distilled fractions or truncated M_w distributions) is carried out using an ORCA temperature controlled organic materials evaporation source installed in a Korvus technologies HEX deposition unit with a base pressure of 1×10^{-5} mbar. The sample stage is cooled by a Peltier cooler to a minimum value of $\sim$ 250 K. The commonly used deposition rate, as measured by Quartz microbalance is 0.05 nm/s. Ellipsometric measurements for density, kinetic stability and rejuvenation studies are made with an EXACTA 2000 Faraday-modulated self-nulling ellipsometer with Linkam temperature controlled stage. Ellipsometric studies of birefringence are made with a J.A. Woollam M-2000 spectroscopic ellipsometer. Typical heating and cooling rates for ellipsometric studies are 1 K/min. Mass spectroscopy measurements are made using a Bruker Autoflex Speed MALDI system.

3.8 Supplementary methods

Sample preparation is invariably a two step process. The first step is either distillation of the polymer into a specific narrow range of N, or evaporation of low N components so that upon heating the smallest remaining N will deposit first. MALDI spectra show that in addition to expected isotopic peaks, we see an extra peak for each N-mer which contains an extra oxygen atom. This extra oxygen atom is very likely a due to some fraction of the polymers as prepared have an $-OH$ end group (the other molecules have simple $-H$ termination). This different end group has the effect that N-styrene oligomers prepared from this original material have slightly higher T_g values than N-styrene oligomers with sec-butyl termination that we have discussed previously [159].

Fig. 3.5 demonstrates the effect of the temperature of the substrate during deposition on the stability of the formed glass. This graph shows data for both $N = 6.5 - 7$ (circles) and $N = 12.2$ (square). The solid line is given by $T_\mathrm{dep} = T_\mathrm{f}$. For this data, the deposition rate is kept constant at 0.05 nm/s. It can be seen that for deposition temperatures near

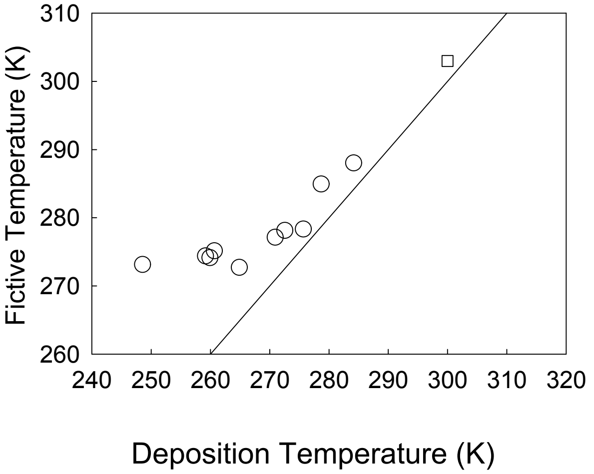

Figure 3.5: Measured fictive temperature T_{f} as a function of the deposition temperature of the substrate T_{dep}. This graph shows data for both $N = 6.5 - 7$ (circles) and $N = 12.2$ (square). The deposition rate is kept constant at 0.05 nm/s.

but below the T_{g} of the material, the T_{f} value is very close to the deposition (substrate) temperature. This linear relationship does not persist, and T_{f} becomes more weakly dependent on temperature as T_{dep} decreases beyond $\sim T_{\mathrm{g}} - 20$ K. This behaviour, quantified in Fig. 3.5, is the same behaviour measured in Ref. [145] for 1,3,5–triarylbenzene (small molecule glass former).

While the deposition rate as measured by the QCM is fixed at ~ 0.05 nm/s, the actual deposition rate for a particular (~ 0.8 cm sample) depends on its position on the entire silicon substrate (7.5 cm), and the actual value can vary by a factor of ~ 4. The deposition rate in vapour deposited glasses has been shown to be an important factor in their stability [136]. Fig. 3.6 shows the dependence of T_{f} for PS stable glass on deposition rate for a substrate held at ~ 40 K below the T_{g} value. Our goal in producing the data for Fig. 3.6 was to ensure that we knew the parameters that would allow us to reproduce films of a particular stability. All of the data in Fig. 3.6 come from only four separate depositions and the different rates are determined by geometric considerations because of the angle between the centre of the source and the substrate. In this case we have also used MALDI to measure the distribution of N-mers and find that $\bar{N}$ for these samples are between 6.5 and 7.0. Fig. 3.6 shows that $T_{\mathrm{f}}/T_{\mathrm{g}}$ roughly increases linearly with deposition rate, and seems to level off at deposition rates $\lesssim 0.5$ nm/s. Increased deposition rate can have a

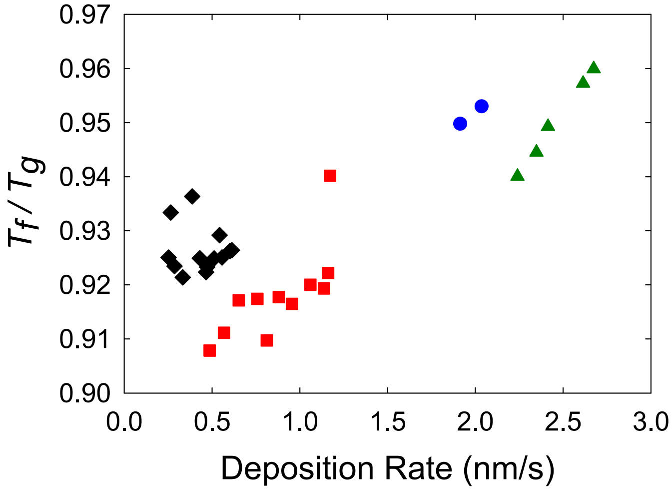

Figure 3.6: $T_{\mathrm{f}}/T_{\mathrm{g}}$ as a function of deposition rate. The data is obtained from three different depositions with nominal (QCM) rates of 0.16 nm/s, 0.31 nm/s, 0.51 nm/s, 0.75 nm/s. The different rates for each symbol are obtained from taking samples at different positions within the wafer. The substrate temperature is 260 K.

dual effect on the stability of the resulting film. If the deposition rate is too high then the surface mobility may not be sufficient to allow the sample to find the lower energy/entropy states. In addition to this direct effect, vapour deposition can lead to heating of the sample. We have noticed increases/decreases in measured temperature of the substrate upon starting/stopping deposition as large as 1–3 K for the highest deposition rates. It is not clear how large the actual temperature change is in the deposited material. As seen in Fig. 3.5, increasing temperature can also lower the stability of the final sample. Except for the data shown in Fig. 3.6, we have chosen to use a deposition rate of 0.05 nm/s or lower in all samples.

Thermal deposition techniques can only be applied to produce materials of up to some finite N value as thermal degradation will eventually be a limiting factor. This limiting N is likely material dependent. At temperatures larger than some critical value, we would expect to see evidence of this thermal degradation such as chain scission leading to deposition of otherwise unexpected smaller N components. Fig. 3.7 shows an example of this for PS. In this case, the MALDI data for deposited films shows that deposition leads to very monodisperse samples with an $\bar{N}$ which increases with increasing temperature. This behaviour persists up to a source temperature of $\sim$ 557 K. At this T we have mainly

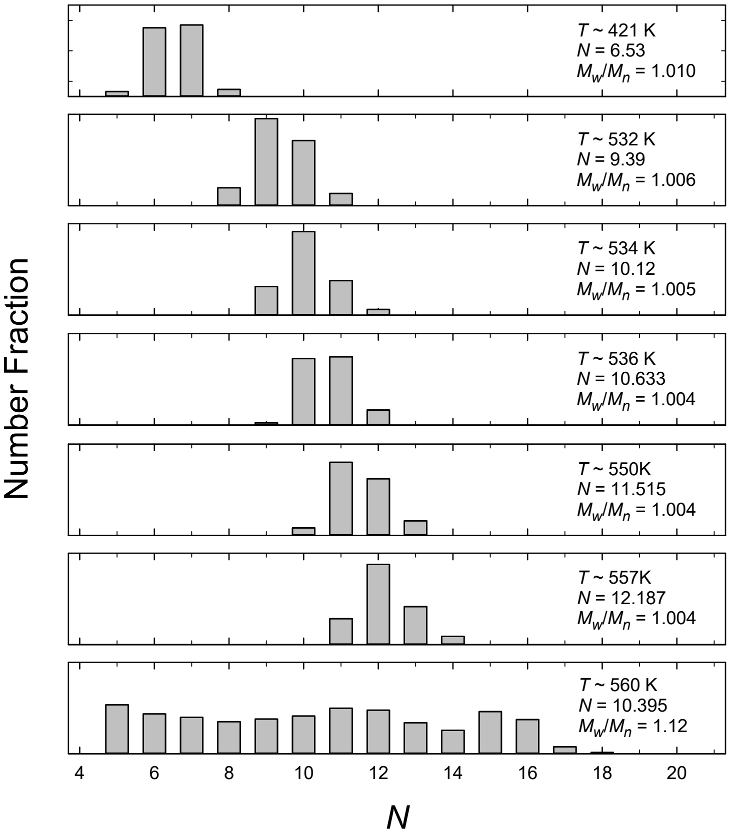

Figure 3.7: MALDI results showing distribution of N with different source temperatures, and the onset of thermally induced chain scission.

$N = 12$, but with noticeable 11, 13, 14 components. Increasing the source temperature only slightly beyond this critical value to 560 K leads to small increases in yield of these larger N, but more notable is the occurrence of many small N components. This leads to significant increases in the polydispersity index. From this we would suggest that $T = 557$ K is a reasonable upper limit for deposition of PS films, and leads to a practical limit of $N = 12 - 13$ with reasonable deposition rates. The fact that Fig. 3.7 does show the ability to deposit N values as large as 17–18 suggests that highly monodisperse sources may be able to be used to deposit films with N as large as 17–18 but under much reduced deposition rate.

3.9 Supplementary discussion

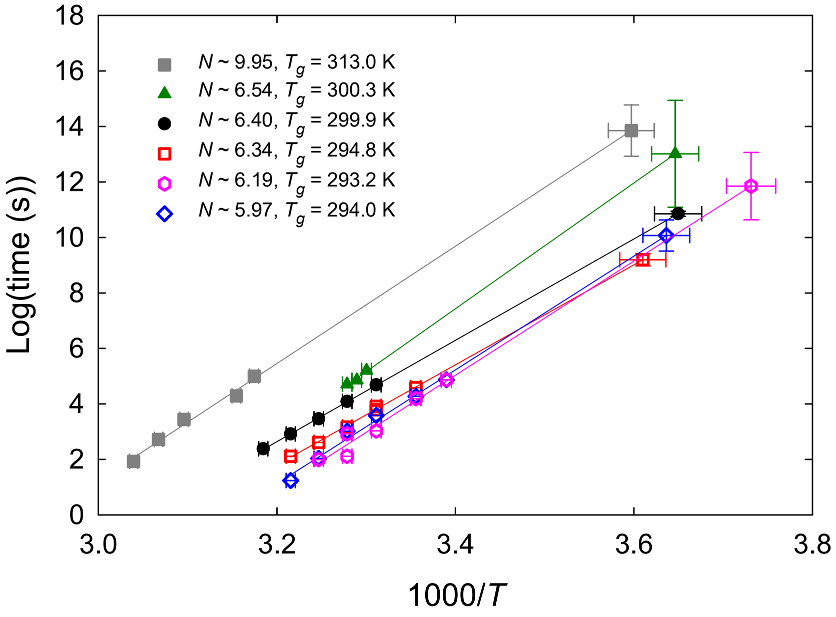

Figure 3.8: Transformation data for PS stable glass films with $6 < N < 10$ before scaling to measured T_{g}.

Fig. 3.8 shows the rejuvenation time data (used in the manuscript's Fig. 3.4) before it is scaled to T_{g}. This shows the real spread in the data, and the critical importance of being able to scale to the T_{g} (as each sample is a slightly different polymer). In Fig. 3.8 the symbols at smaller times (less than about 10^6 seconds) are the measured rejuvenation times. For each independent set the values of $\log \tau$ versus $1/T$ are fit to a line and the resulting best fit line is extrapolated to the measured T_{f} of the stable glass to get the estimated lifetime of the as-prepared stable glass. The error bars for the extrapolated times are determined by the uncertainty in the fit value of each linear slope. Thus the data in Fig. 3.8 shows the results of 6 different linear fits, and all of the points at larger times are not measured times but obtained from the extrapolated lines. We note that the N values range from 5.97 to 9.95 in this graph.

Ellipsometry has shown vapour deposited stable glasses to be almost exclusively birefringent with $n_{xy} \neq n_z$ [165]. Because of the relative placement of the organic source and

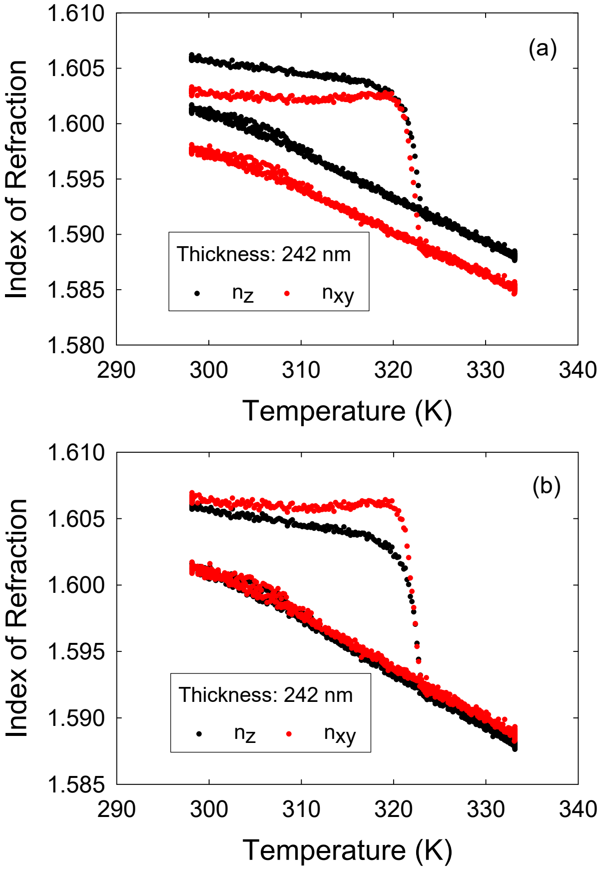

Figure 3.9: Refractive index from modelling of ellipsometric data during first heating, first cooling and second heating on a film with $N = 6.5$.

the cold substrate in our deposition chamber, the samples end up being wedge shaped, with an approximate thickness gradient of 2.6%/mm. Over the ellipsometry spot size of 2–5 mm, this leads to a thickness difference of $\sim 5 - 13\%$. The fact that the substrate and free surface are not parallel is known to have an effect on quantitative ellipsometry modelling [170]. Despite these experimental limitations that have prevented a full study of anisotropy, we have performed measurements on a series of $N = 6.5 - 7$ stable glasses as well as assorted other material with N up to 12.7. Fig. 3.9 shows the modelled refractive indices in the plane of the sample n_{xy} and out of the plane of incidence n_z for a full heat-cool-heat cycle for one of the samples used to generate Fig. 3.6. The upper figure shows the indices directly obtained from the model fit. The fact that there is residual anisotropy

($n_{xy} \neq n_z$) after the samples has been heated beyond T_g suggests that level of anisotropy is an artefact of modelling our samples in a slab model. The lower plot shows the same data, but with n_{xy} shifted so that the sample is forced to be isotropic after heating (as is seen in the molecular glasses). We note that even if the sample is anisotropic, this degree of anisotropy is quite small (much smaller than in most molecular glass reports).

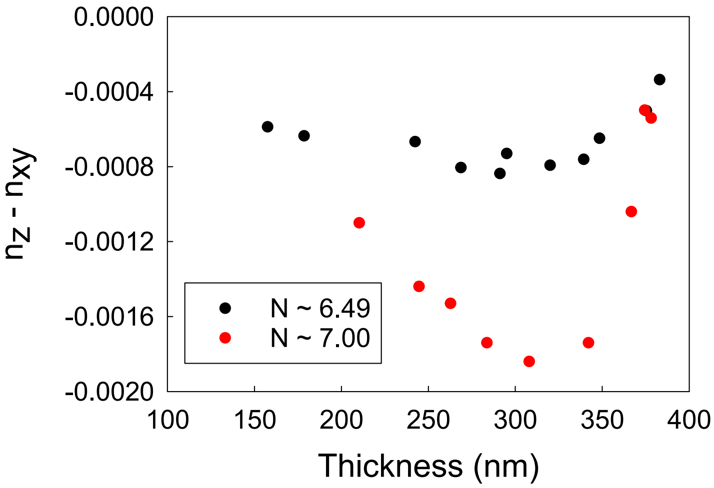

Figure 3.10: Anisotropy difference upon rejuvenating a stable glass on a series of films with $N = 6.5, 7$.

By employing the assumption typically used in molecular glass systems (that heating above T_g removes any anisotropy), we can calibrate the measurements. This process (assumes that heating above T_g will always remove anisotropy, and that the equilibrium state is isotropic) leads to the symbols shown in Fig. 3.10. These symbols are the change in anisotropy induced by heating above T_g. Together with Fig. 3.9, this data shows that both the stable glass, and the rejuvenated glass show no anisotropy within 0.005, and no change in anisotropy upon rejuvenation to within 0.002. It is also important to note that the change in anisotropy upon rejuvenation exhibits a film thickness dependence. This is unexpected, and we believe it is also an artefact of fitting our wedge shaped films to a slab model. We have also made measurements on other samples with N as high as 12.7 (which has a T_g of 320 K), and none have shown an anisotropy ($|n_{xy} - n_z| > 0.01$). While this does not yet allow us to make strongly definitive statements about anisotropy, we are confident to say that compared with small molecule glasses [140] where $|n_{xy} - n_z|$ can be as large as 0.08, these polymers are very isotropic in the range $6 < N < 13$.

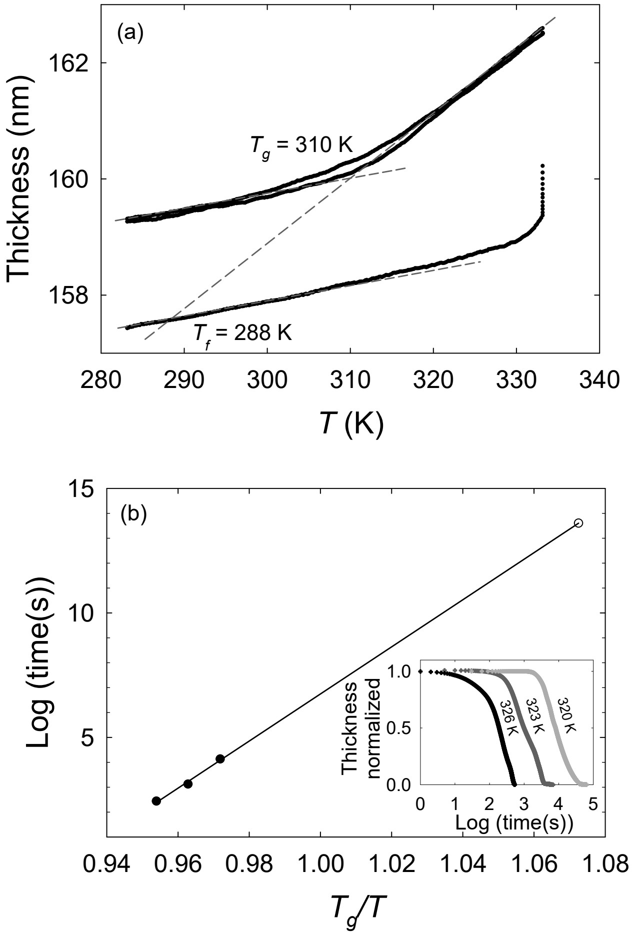

Figure 3.11: (a) A PMMA thin film stable glass with T_{g} = 310 K and T_{f} = 288 K. (b) Kinetic transformation data for a PMMA sample made with deposition rate of 0.03 nm/s, T_{dep} = 250 K. The dashed lines are linear fits to the $h(T)$ in the glassy and melt states used to determine T_{g} and T_{f}.

As discussed in the manuscript, we also made stable glass of PMMA. The amount of data we collected for PMMA was not nearly as extensive as for PS, and was designed to show that applicability of the technique to another common polymer. The T_{f} values measured for PMMA range from about 10 K below the measured T_{g} value to 20 K below the measured T_{g} value. The heating run also shows that unaged samples after the first heating have $T_{\mathrm{f}} \sim T_{\mathrm{g}}$ as expected. We also performed an abbreviated series of transformation experiments on PMMA. Fig. 3.11(a) shows an example of a kinetic scan on a PMMA stable glass film. Fig. 3.11(b) shows the transformation data and resultant extrapolation to T_{f}. The results are discussed in the main manuscript.

Chapter 4

Pursuing high molecular weight stable polymer glass

As introduced in the previous chapter, the highest N we have been able to obtain from vapour deposition of PS is ~ 18. Such degree of polymerization is in fact commonly categorized as "oligomers" instead of the "polymers". Although they have the unique properties of polymers including tunability with N as opposed to molecular glasses, we ask ourselves the question: Is it possible to go beyond this limit and create stable polymer glass with higher molecular weight?

4.1 Using high N polymer as deposition source

The most straight-forward way to explore this possibility is to simply replace the source material with higher molecular weight polymers. If we are able to evaporate the high N components and deposit them on the substrate, we may be able to exceed the limit and make stable "polymer" glass.

4.1.1 $M_{\mathrm{w}} = 3000$ g/mol as deposition source

As with most part of this thesis, PS was chosen to be the representative polymer in this exploration. The original source material used in the last chapter is PS1200. Since it has a broad distribution of N from 3 to 22 with PDI = 1.19 and has to be pre-distilled before vapour deposition, in this chapter we use a higher molecular weight PS with a narrow distribution so that it can be directly used as the source. The first replacement used in this chapter is PS3000, with $M_\mathrm{n} = 2800$ g/mol, $M_\mathrm{w} = 3000$ g/mol, PDI = 1.09 purchased from Polymer Source Inc.

In starting the deposition, the source temperature was raised slowly until the deposition happens at a noticeable rate as observed from the QCM. The temperature increase was performed in 50 K steps. In each step the pressure in the chamber increased first due to evaporation of polymers, and then reduced with continuous pumping. The pressure was allowed to reduce and equilibrate before each next step. Due to the resolution of the deposition rate shown in the software, a constant zero within uncertainty was shown throughout the deposition. The fact that the material was being deposited was confirmed by the gradual increase in the value of film thickness deposited on the QCM. The source temperature was held at 553 K after opening the shutter, with a substrate temperature of 293 K and a base pressure of 3.6×10^{-5} mbar. The deposition was carried out during a period of three days, and stopped when the QCM thickness reached 78 nm.

The film was characterized by ellipsometry and mass spectrometry. Ellipsometry shows no glass transition during heating and cooling scans from 298 K to 328 K, and the films shows a liquid expansivity throughout this temperature region. Mass spectrometry result is shown in Fig. 4.1, where only $N = 4$ and $N = 5$ are present in the film without any higher N components. This indicates chain scission happening during the deposition, since similar N components should all have a much higher deposition rate at the same source temperature, according to depositions performed with the previous source material. The fact that only 78 nm was deposited during three days suggests that no observable deposition of the original components was achieved, and the existence of $N = 4$ and $N = 5$ are likely due to chain scission of higher N components under the high temperature.

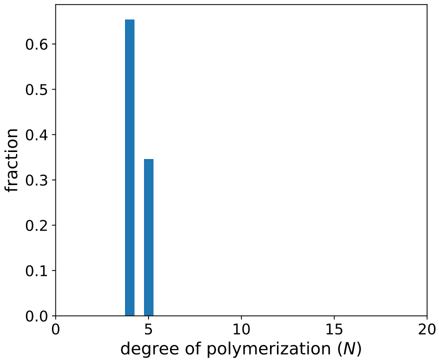

Figure 4.1: N distribution of the film deposited from PS3000.

4.1.2 $M_{\mathrm{w}} = 1400$ g/mol as deposition source

It seems the N components in PS3000 are too high for vapour deposition, even under the extremely slow rate. The next source material we tried was PS1400, with $M_{\mathrm{n}} = 1300$ g/mol, $M_{\mathrm{w}} = 1400$ g/mol, PDI = 1.08 purchased from Polymer Source Inc. The source crucible was thoroughly washed and rinsed with toluene before being introduced in the chamber. After the chamber was brought to vacuum, the crucible was baked at 673 K for two hours in order to drive off any potential impurities. Then it was left at 573 K for overnight, with a base pressure of 1.7×10^{-5} mbar. The source material PS1400 was added in the crucible after the cleaning procedure. Mass spectrometry result from the source material PS1400 is shown in Fig. 4.2. It has a distribution of N from 4 to 17, with $N = 13$ being the highest fraction. The average polymerization index $\bar{N}$ is 11.8.

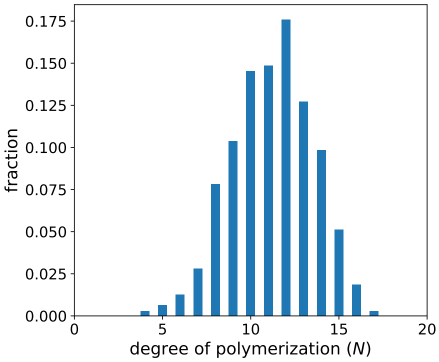

Figure 4.2: N distribution of PS1400.

Three depositions were carried out using this polymer. Films from each deposition were examined using mass spectrometry to observe the change in N distribution.

Same with the deposition with PS3000, the source temperature was first raised slowly in 50 K steps. Since PS1400 has a lower average molecular weight, the temperature it needs to evaporate the relatively small N's is significantly lower. After reaching 473 K, there was already a noticeable deposition rate of 0.005 nm/s according to the QCM. Thereby the shutter of the substrate was opened and the first deposition started at 473 K with a substrate temperature of 293 K and a base pressure of 2×10^{-5} mbar. During a period of two days, the source temperature was increased in 10 K steps every time the film thickness stopped increasing, until it reached 543 K. The deposition was stopped when the QCM thickness reached 61.3 nm. Mass spectrometry result from the first deposition is shown in Fig. 4.3. The average polymerization index $\bar{N}$ is 10.0, and its PDI is 1.035. Compared to the source material, it has a slightly narrower distribution, and is shifted to lower N's. The plot indicates that most of the lower N's are collected with a similar fraction compared to the source, while there are still some higher N that was not deposited.

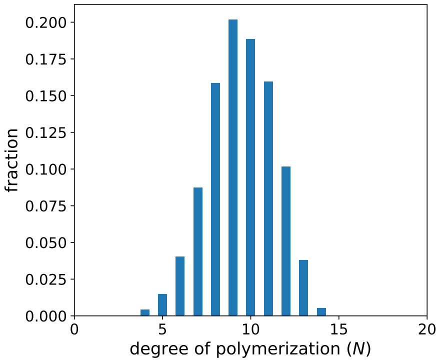

Figure 4.3: N distribution of the film obtained from the first deposition from PS1400.

It is also worth mentioning that from the ellipsometry measurement performed on the deposited film, no glass transition is observed during heating and cooling scans from 298 K to 348 K, and the films shows a liquid expansivity throughout this temperature region. The fact that this source material has lower T_{g} compared to the regular source material PS1200 used throughout this thesis has been explained in previous studies [1, 159]. The current material PS1400 has sec-butyl end groups, and in the regular material PS1200 some fraction of the polymers have an $-OH$ end group (the other molecules have simple $-H$ termination) which has been found to result in higher T_{g} values in the N-styrene oligomers prepared from it, possibly due to hydrogen bonding.

The second deposition was performed with the material left in the source from the previous deposition. The source temperature was maintained at 543 K, and the substrate temperature was 293 K as the previous deposition. After two days, 80 nm was deposited according to the QCM. Mass spectrometry result from this deposition is shown in Fig. 4.4. The average polymerization index $\bar{N}$ is 9.3, which is lower than the first deposition, and its PDI is 1.112, which is higher. The higher peak at $N = 5$ as well as the higher fraction in lower N's in general suggests that there could be chain scission happening already in this deposition. However, it can be noticed that $N = 15$ which is absent from the first deposition is collected in this deposition, although $N = 16$ which is present in the source material is still missing. Thereby a third deposition is conducted in attempt to collect even higher N's.

The film from the second deposition was also characterized with ellipsometry under

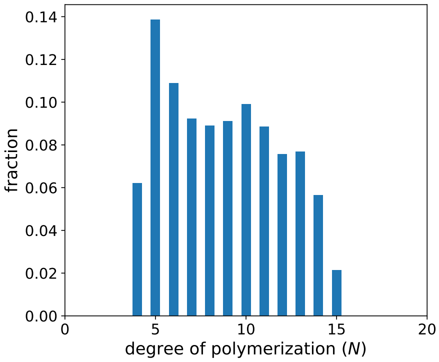

Figure 4.4: N distribution of the film obtained from the second deposition from PS1400.

heating and cooling scans. Fig. 4.5 demonstrates that it is a stable glass, with increased kinetic stability (higher T_{onset} than T_{g}), low T_{f}, and increased density.

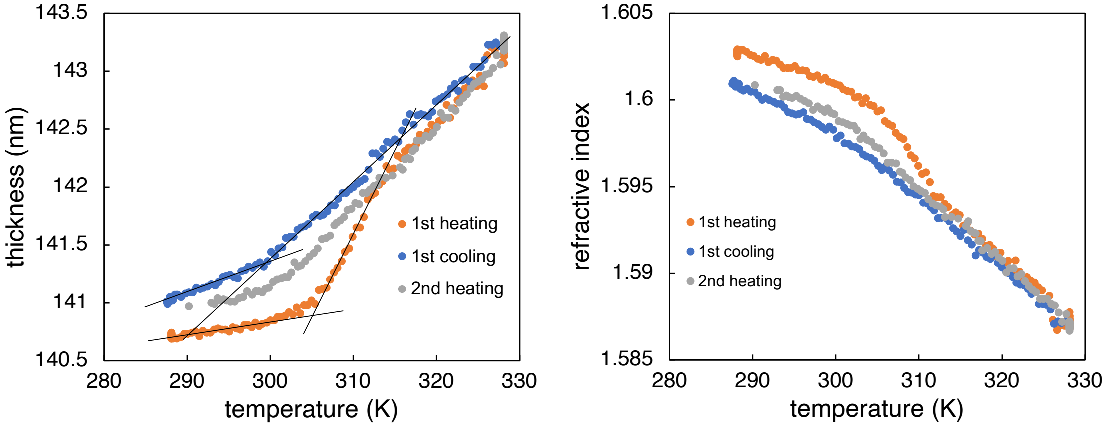

Figure 4.5: Thickness and refractive index change with respect to temperature of the film obtained from the second deposition from PS1400.

The third deposition was performed with the source temperature maintained at 543 K, and the substrate temperature at 268 K. After four days, 60 nm was deposited according to the QCM. Mass spectrometry result from this deposition is shown in Fig. 4.6. The average polymerization index $\bar{N}$ is 6.3 and its PDI is 1.097. It is evident that higher N components could not be collected and most of the film deposited is likely to be the product of chain scission.

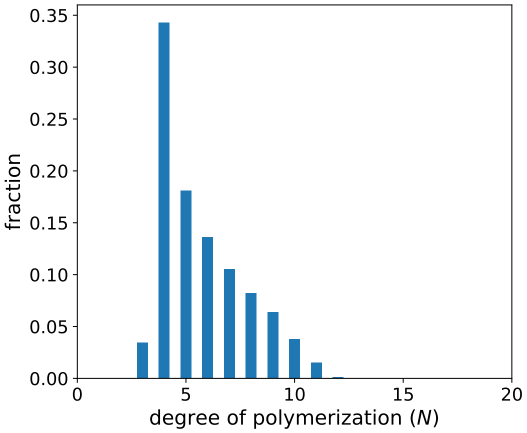

Figure 4.6: N distribution of the film obtained from the third deposition from PS1400.

4.1.3 Conclusion

All of the depositions in attempt to achieve higher molecular weights, together with experiments introduced in Chap. 3 indicate one conclusion: it is very difficult to obtain PS with $N > 20$ through vapour deposition. As N increases, the rate of deposition decreases, and thus higher temperatures are needed to reach a reasonable deposition rate. Even with extremely slow deposition as demonstrated in this section, it appears that the rate of deposition finally becomes comparable to the rate of chain scission due to the high temperature, and N could not be further increased by simple deposition. This is not only a practical limit for experiments, but a real limit for vapour deposition of PS.

4.2 UV crosslinking of vapour-deposited polymer

Since simple direct deposition has a practical limit of less than 20 in the highest N obtained in vapour-deposited glass, the only possible way to pursue higher N's seem to be increasing the molecular weight after the film is deposited. For PS under current study, it is known that ultraviolet (UV) radiation can induce crosslinking in the system [21, 171, 172]. In this project we propose the question: Can UV treatment increase the molecular weight of vapour-deposited PS and help us obtain high molecular weight stable glass?

4.2.1 Photochemical reactions in polystyrene

Exposure to UV radiation is known to induce different reactions in polymers [173]. In the presence of air, photooxidative degradation causes breaking of chains, produces free radical and reduces the molecular weight. Mechanical properties of polymers can thus be deteriorated. On the other hand, crosslinking reaction can also happen which increases the molecular weight. Therefore, by keeping the system in an inert atmosphere, an increase in molecular weight may be achieved through UV radiation.

PS is one of the most commonly used commercial polymers nowadays and its reactions under UV treatment has been extensively explored [21, 171, 172, 174, 175, 176, 177, 178]. Fig. 4.7 and Fig. 4.8 include some of the most commonly acknowledged reactions in PS under UV radiation. When exposed to UV, PS could form free radicals through dehydrogenation on the phenyl-bearing carbon atom or its neighbouring carbon atom. The radicals can then follow two different reaction paths depending on the presence or absence of oxygen. When oxygen is absent or low in amount, crosslinking reaction can happen between different chains, and a network can thereby be formed. Crosslinking can also happen indirectly through unsaturation first and then reactions between radical species with double bonds. The chain could also break between the carbon atoms after absorbing the photon energy. When oxygen is presence in the environment, oxidative degradation occurs leading to either chain scission or modification of the chain. It is therefore clear that in order to achieve an increase in the molecular weight, oxygen needs to be prevented in the UV treatment.

Since PS is non-transparent in the UV regime, the UV radiation will be partly absorbed as it transmits through the film. It is thus important to make sure that the film thickness is appropriate and the UV light is able to transmit through the film to crosslink the chains effectively. In Ref. [179] the effect of PS film thickness on light transmittance was studied as a function of wavelength. For wavelengths above 280 nm, transmittance is around 80% and only decreases slightly until film thickness increases above $\sim$ 100 µm. For wavelength below 280 nm, UV transmittance reduces much quicker as film thickness increases, but it was shown that for films of 1 µm, there is at least $\sim$ 60% transmittance between 230 nm and 280 nm. Therefore, for all films used in this thesis that are $\sim$ 100 nm, the transmittance would be much higher and the UV radiation would induce reactions in the film effectively.

4.2.2 Experimental details

UV treatment was performed with a Novascan PSD-UV4 Digital UV Ozone System. Its mercury vapour grid lamp with reflector provides high energy ultraviolet light at wave-

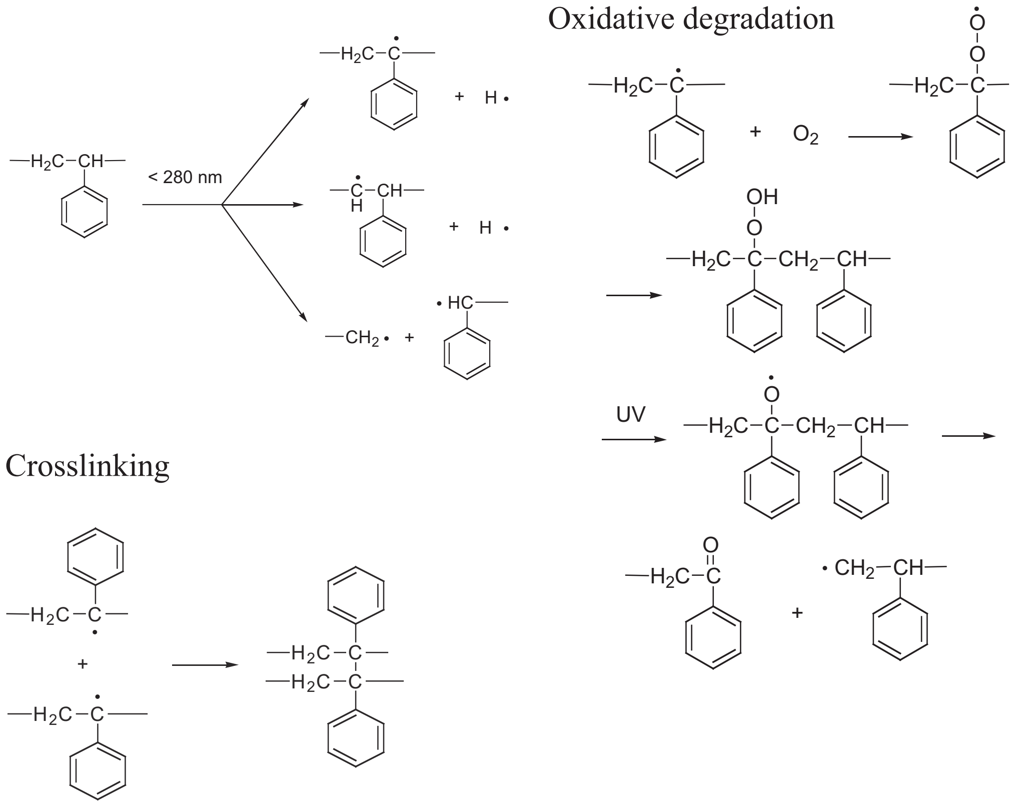

Figure 4.7: Possible reactions in PS under UV radiation. Figure from Ref. [21].

lengths of 185 nm and 254 nm. The lamp is designed to clean substrates such as silicon and glass in air with the UV light and ozone generated. However, in order to achieve an increase in molecular weight with minimal chain scisson or oxidation, all UV treatments in this thesis were conducted in an inert environment. The entire UV system was placed in an airtight plastic bag flushed with nitrogen gas throughout the treatment, which is essential in order to drive away oxygen and potential ozone from the film surfaces. A resealable opening is attached to the bag for convenient transfer of samples and controlled air flow for nitrogen flushing before and during experiments. A home built metal cold stage connected to chiller circulation was used to control the temperature of PS films during the treatment, since the UV lamp heats up under operation. The plastic nitrogen gas tubes leading into the chamber were wrapped with aluminum foil to prevent UV exposure. The lamp gird has a size of 4” by 4”, and the samples were always placed in the center of the stage directly below the lamp, in an area smaller than the lamp grid.

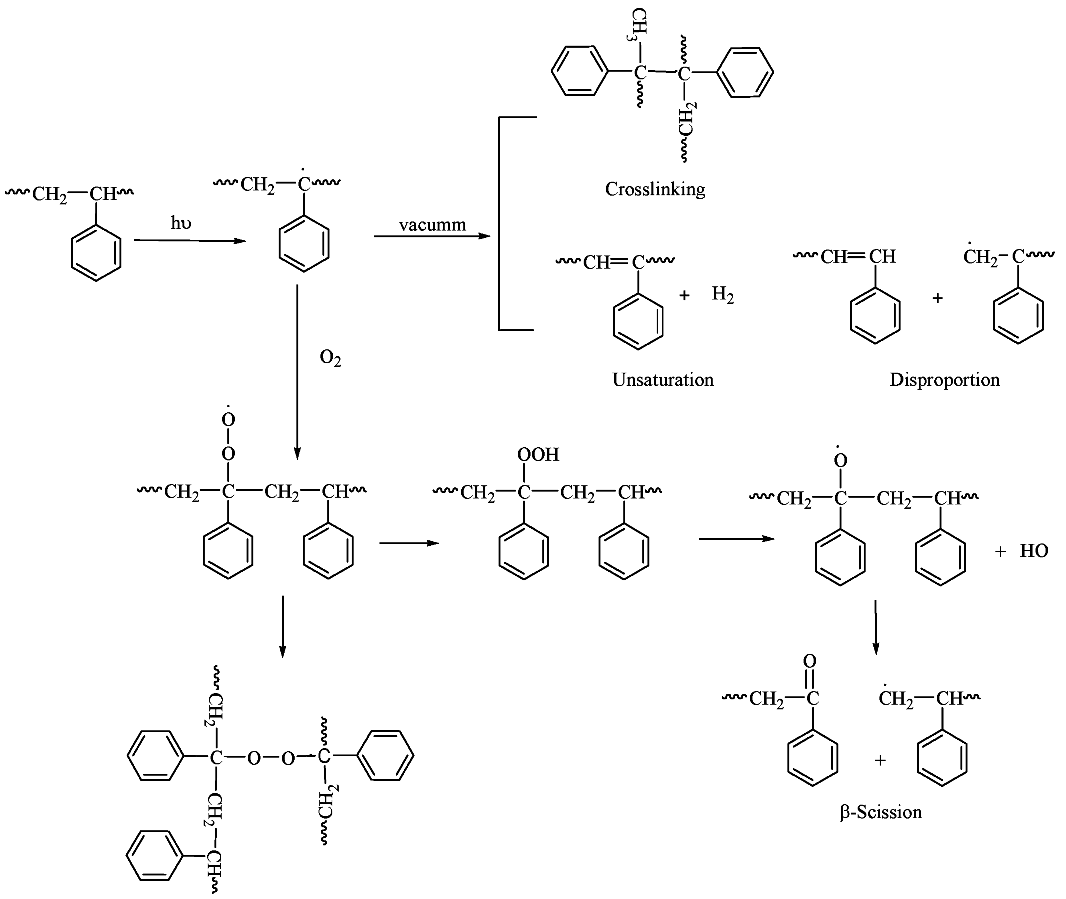

Figure 4.8: Possible reactions in PS under UV radiation. Figure from Ref. [22].

The UV treatment experiments were all performed with the following procedure:

1. Place in PS film samples in the center of the cold stage, and open nitrogen valves.
2. Flush the bag with nitrogen at 10 psi. Once it is fully inflated, open a portion of the resealable opening and deflate the bag before resealing. Repeat 4 to 5 times.
3. Turn on the chiller. Start the UV treatment. Leave a small opening for the bag and keep a nitrogen flow at 4 psi to keep the bag inflated throughout the experiment.
4. When the treatment is done, turn off the UV lamp and the chiller, and close the nitrogen valves.

4.2.3 Molecular weight distribution in crosslinked polymers

A considerable amount of work has been conducted in studying the effect of crosslinking on polymer properties [180, 181, 182, 183, 184, 185, 186, 187, 188, 189, 190, 191, 192]. In this project the purpose of exposing vapour-deposited films to UV radiation is to increase their molecular weight and obtain real "polymeric stable glass". Thus we are mostly interested in its effect on the molecular weight. With crosslinking, the chain size and molecular weight distribution in the system are altered depending on various factors such as the initial distribution and the degree of crosslinking. The molecular size distribution in different crosslinked systems have been studied in detail by Flory [23, 24, 193, 194]. One of those studies investigated the case where chains of uniform length are randomly crosslinked at various points [24]. Our system in this thesis is an approximate representation of this case. The vapour-deposited PS films typically have near uniform chain lengths with 2 or 3 neighbouring components, and the UV induced crosslinking is expected to occur randomly at phenyl-bearing carbon atoms on the backbone. Such crosslinking can in fact be regarded as tetrafunctional branching since the units crosslinked are equivalent to a tetrafunctional unit. The resulting distribution of this type of system has been derived and Fig. 4.9 shows the weight fractions for a few components.

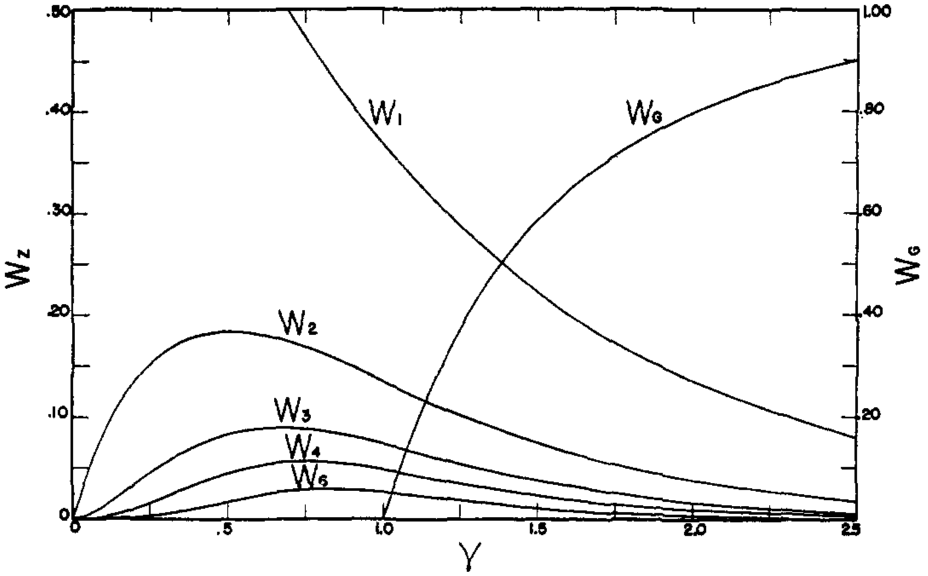

Figure 4.9: Weight fractions W_z of molecules composed of z chains as well as weight fraction W_{G} of gel as a function of the crosslinking index γ. Figure from Ref. [23].

Weight fractions of molecules of 1, 2, 3, 4 and 6 chains are shown as examples in the figure. The crosslinking index γ is defined as the number of crosslinked units in the system divided by the total number of chains. The degree of crosslinking is therefore given by $\gamma/2$ since it is defined as the average number of cross linkages per chain. This figure shows that W_z decreases as z increases. The critical point, or gel point, is at $\gamma = 1$, where gelation occurs and a giant network structure of infinite size appears. Above the gel point, the network grows at the expense of chains of finite sizes. Regardless of the crosslinking index, the original unaltered chains, W_1, are always the component with the highest fraction in all components of finite sizes (the sol, as opposed to gel).

The average molecular sizes have also been derived for such systems. Fig. 4.10 shows the number average $\bar{z}_\mathrm{n}$ and weight average $\bar{z}_\mathrm{w}$ number of chains per molecule as a function of γ. Below the gel point $\bar{z}_\mathrm{n}$ and $\bar{z}_\mathrm{w}$ refer to the entire system, while above the gel point they refer to the sol fraction only.

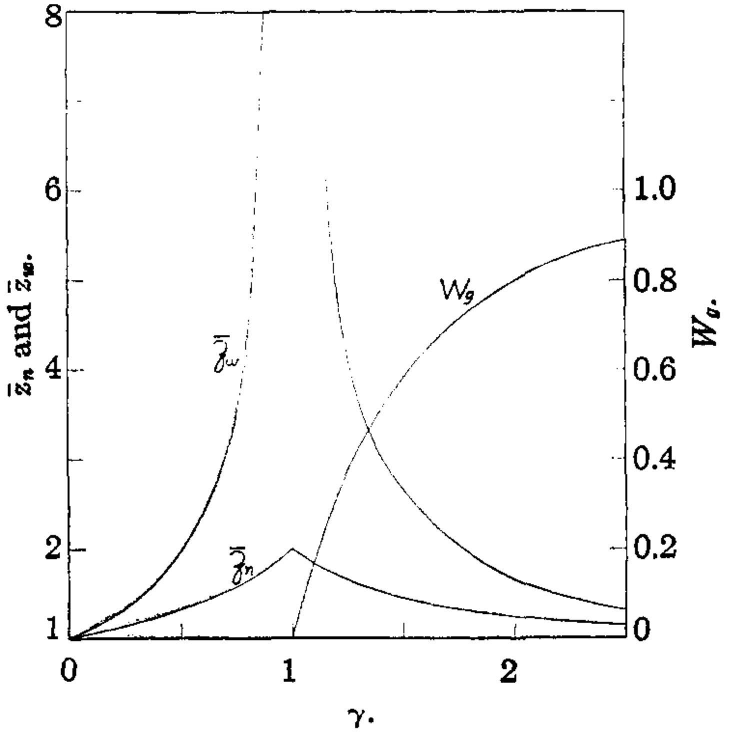

Figure 4.10: Number average $\bar{z}_\mathrm{n}$ and weight average $\bar{z}_\mathrm{w}$ number of chains per molecule as well as weight fraction W_G of gel as a function of the crosslinking index γ. Figure from Ref. [24].

As γ approaches 1, both $\bar{z}_{\mathrm{n}}$ and $\bar{z}_{\mathrm{w}}$ increase to the maximum values. Focusing on $\bar{z}_{\mathrm{n}}$ alone which reaches 2, it may seem that there are barely any large molecules in a system at the gel point. $\bar{z}_{\mathrm{w}}$, on the other hand, grows much faster and reaches infinity when $\gamma = 1$ [24], which seems to suggest that the molecules are massive on average at the gel point. However, the interpretation of these results must be made very carefully. As introduced in Chap. 1, the different definitions of $\bar{z}_{\mathrm{n}}$ and $\bar{z}_{\mathrm{w}}$, or M_{n} and M_{w}, make them sensitive to different components in the polymer mixture. As $\bar{z}_{\mathrm{n}}$ is inversely dependent on the total number of molecules, it is most sensitive to the lowest molecular sizes. $\bar{z}_{\mathrm{w}}$ is instead more sensitive to higher molecular weights and is scarcely affected by the smallest molecules. In describing these systems, it is desirable that both quantities are obtained to determine the polymeric state. Above the gel point, since a part of the system is a network and has infinite molecular weight, the average molecular sizes should be considered for the sol fraction only.

For a system of chains with non-uniform lengths, the gel point is reached at lower γ values. Particularly, for a random distribution of chain lengths, the gel point has been shown to be 0.5 [24]. The resulting molecular size distribution is also dependent on the initial distribution of chain lengths. For example, for an initial Poisson distribution of chain lengths, the final distribution has been studied as a function of crosslinking index γ [25, 195]. The resulting distribution is a compound distribution with multi-modality as shown in Fig. 4.11 through Fig. 4.13. In this example, the initial distribution of chain lengths follows a Poisson distribution with a mean value of 20. x represents the degree of polymerization of a molecule, $w(x)$ represents the weight fraction of molecules with degree of polymerization x.

Same as Fig. 4.9 indicates, Fig. 4.11 through Fig. 4.13 show that the initial chains unaffected by crosslinking are always the most abundant components in the mixture (sol part) at any stage of crosslinking, i.e., before gelation, at the gel point, and post gelation. Comparing the three figures, it can be seen that the weight fraction of initial chains in the sol decreases when γ increases to 1, and then increases when γ increases further. On the other hand, the higher molecular weights, for example, $x = 100$, increase first and then decreases after the gel point.

4.2.4 Characterizing mass distribution in UV treated films

Therefore, it is important to examine and observe the change in the molecular weight distribution before and after our UV treatment. This would allow us to describe the polymeric state of the system and the degree of crosslinking. As with most of the thesis,

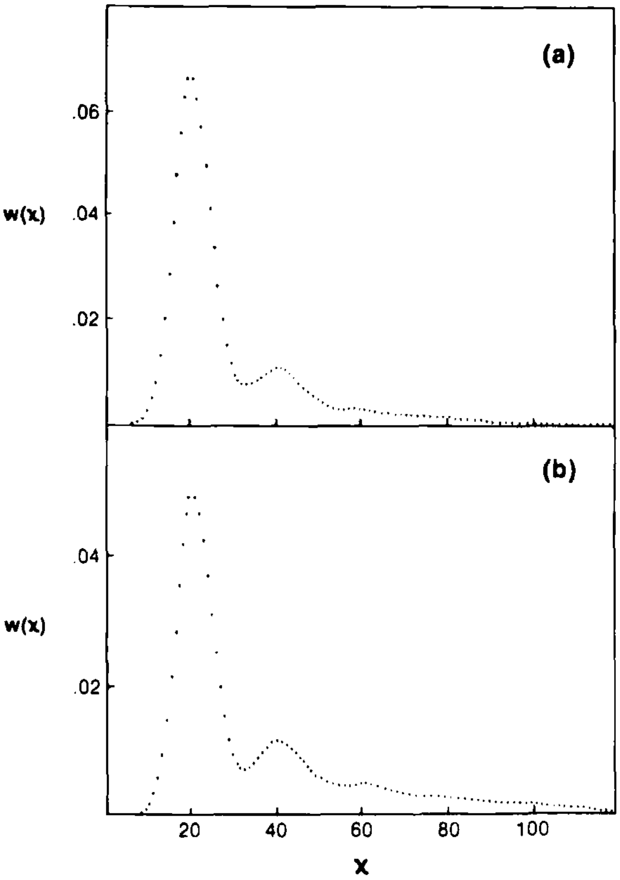

Figure 4.11: Resulting molecular size distribution before gelation with an initial Poisson distribution ($\lambda = 20$) of chain lengths. (a) $\gamma = 0.3$; (b) $\gamma = 0.6$. Figure from Ref. [25].

mass spectrometry was used in this investigation. By measuring the same initial system after different time periods of UV treatment, it was hoped that the UV time could be associated with the degree of crosslinking in the system.

A PS film of 110 nm was deposited at 0.05 nm/s with $T_{\text{sub}} = 261$ K. Fig. 4.14a shows the mass spectrum measured by MALDI and Fig. 4.14b shows the distribution of N's calculated from the MALDI data.

In the mass spectrum, the x-axis, m/z, is the mass-to-charge ratio. In our measurements, Ag^+ is assumed to be the ion attached to molecules and $z = 1$. The peaks represent mixtures of PS, the matrix, and the silver ions. Most peaks on the lower end (below 600)

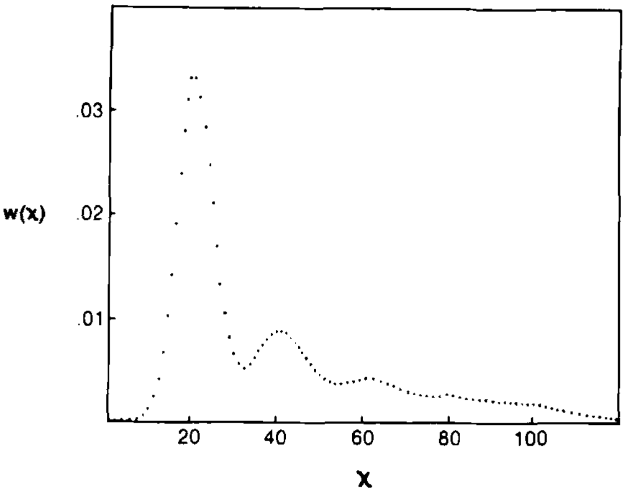

Figure 4.12: Resulting molecular size distribution at the gel point ($\gamma = 1$) with an initial Poisson distribution ($\lambda = 20$) of chain lengths. Figure from Ref. [25].

correspond to the matrix and the silver ions only, as they are present in measurements of the matrix without PS. The peaks from 700 to 1200 with highest intensities contain PS from the deposited film, as the major peaks are 104 Da apart which is the molar mass of styrene. Zooming in on the major peaks, it can be seen that each of them are followed by a few more peaks. Some of them are 16 Da higher than the main peak, which correspond to the extra oxygen on the end group explained in the previous section. Some peaks that are 2 Da apart can be explained by the isotopes of silver. Since laser pulses are introduced on the samples during the measurements, some fragments can also be created and contribute to some of the small peaks.

Fig. 4.14b is the distribution of N's in the PS sample calculated from the MALDI data. Before UV treatment, $N = 7$ and $N = 8$ are the main components. Films from the same deposition were treated in the UV chamber for different time periods from 2 min to 3 h, and then measured with mass spectrometry. Fig. 4.15 shows the results for 2 min, 5 min and 3 h samples.

As expected, the initial components appear to be the most abundant in all three samples. Compared to the peak intensities of the matrix components, there is a relative decrease in PS peaks after longer UV treatment. This can be interpreted as the formation of larger molecules through crosslinking at the cost of the initial chains, so their fraction in the PS-matrix mixture reduces. As the literature suggests [23, 25], the second most

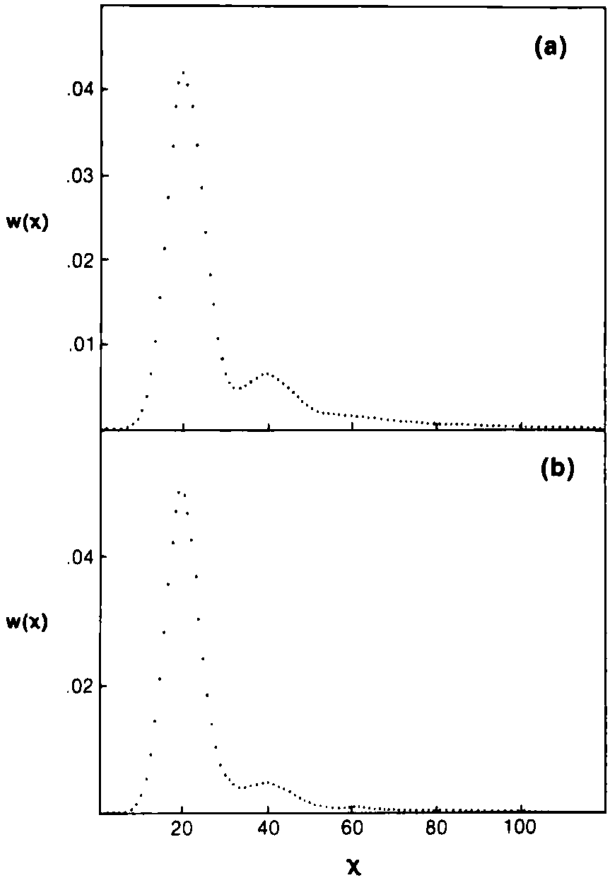

Figure 4.13: Resulting molecular size distribution post gelation with an initial Poisson distribution ($\lambda = 20$) of chain lengths. (a) $\gamma = 1.3$; (b) $\gamma = 1.6$. Figure from Ref. [25].

abundant fraction should be molecules consisting of two initial chains crosslinked together. However, hardly anything can be seen in the mass range of 1300–2300. The fact that initial chains reduce in amount and no significant chain scissions can be seen from the mass spectrum means that higher molecular weight molecules must be formed. This is also supported by ellipsometry measurements on these samples included later in this section, where T_{g} increases by 5 K after 3 h of UV treatment. However, the larger molecules after crosslinking are not detected, even the components with the highest fraction. It is believed that the crosslinking products with various molecular weights are spread out in the mass range. Even though the mass spectrometer is sensitive enough for sample sizes as small as our thin films, when the distribution is too broad, each fraction is still too scarce to be

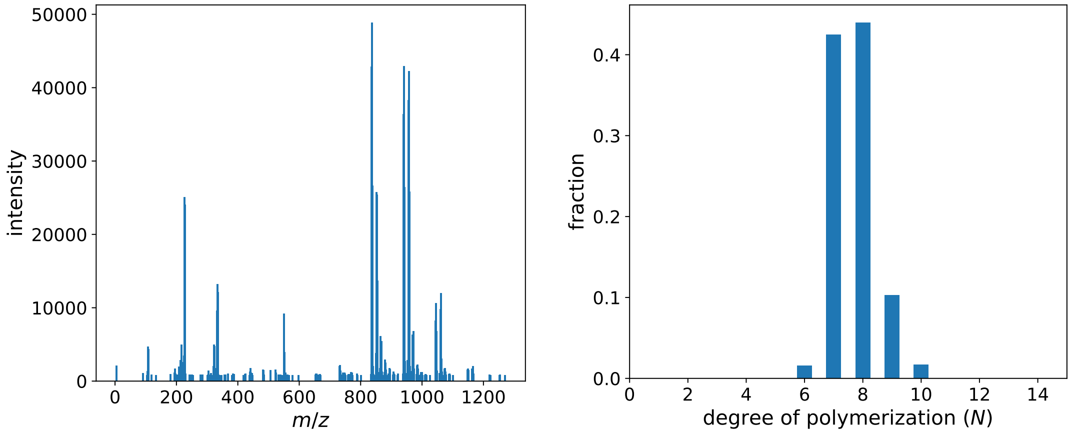

(a) Mass spectrum.

(b) N distribution.

Figure 4.14: Mass spectrometry results on the PS film before UV treatment.

detected against noise.

Various mass ranges up to 140k Da have also been tested in the MALDI measurements, but no higher molecular weight signal from the sample can be identified out of the background. Another PS film from a similar deposition with 7 h of UV treatment was also measured, and the sample spectrum at higher mass range was also indistinguishable from the matrix spectrum.

Gel permeation chromatography (GPC) was also considered for mass analysis, but the small amount of thin film samples are not enough for GPC measurements which typically require milligrams of each sample.

Since mass analysis does not provide information on the degree of crosslinking in the system, solubility tests have been conducted in order to determine the change in films after crosslinking. As shown in Fig. 4.16a, vapour-deposited films ($T_{\mathrm{sub}} = 300$ K deposited at 0.05 nm/s) after different time periods of UV treatment are tested with dichloromethane (DCM). The top row shows films before introducing the solvent, and the bottom row shows films after dropping DCM on top. From left to right are films after 0 h, 3 h, 5 h, and 7 h of UV treatment.

It is evident from Fig. 4.16a that the as-deposited film easily dissolves in DCM. With longer UV time the film dissolves less and less, and after 7 h, the film is largely undissolved by DCM. In comparison, Fig. 4.16b shows a high molecular weight PS film with $M_{\mathrm{n}} = 996$ kg/mol which fully dissolves in DCM. This test demonstrates that with increasing UV

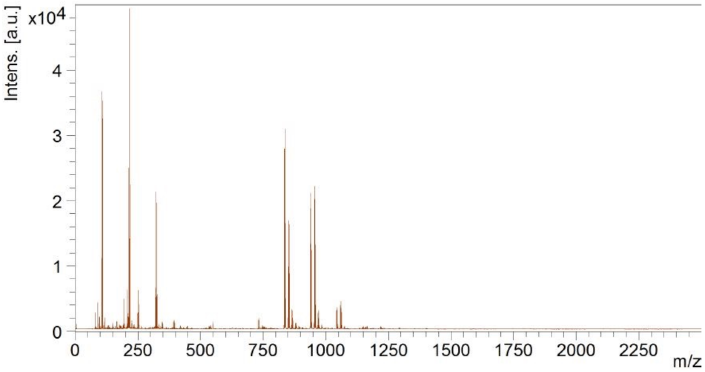

(a) UV treated for 2 min.

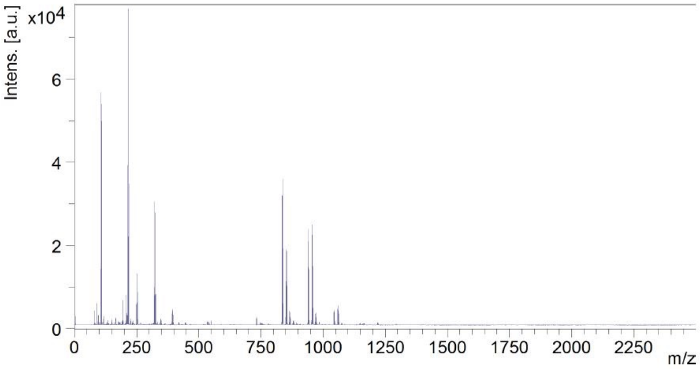

(b) UV treated for 5 min.

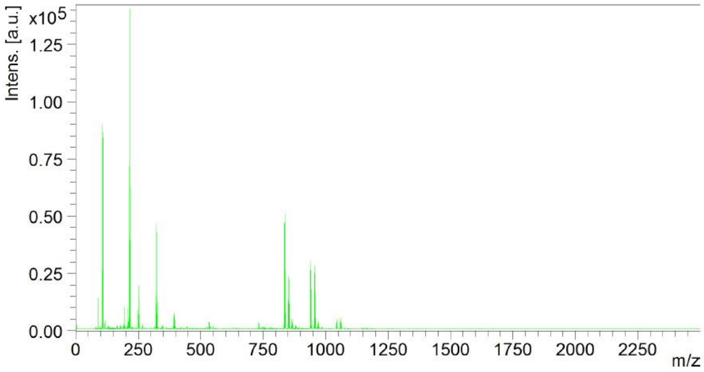

(c) UV treated for 3 h.

Figure 4.15: Mass spectrometry results on the PS film after UV treatment.

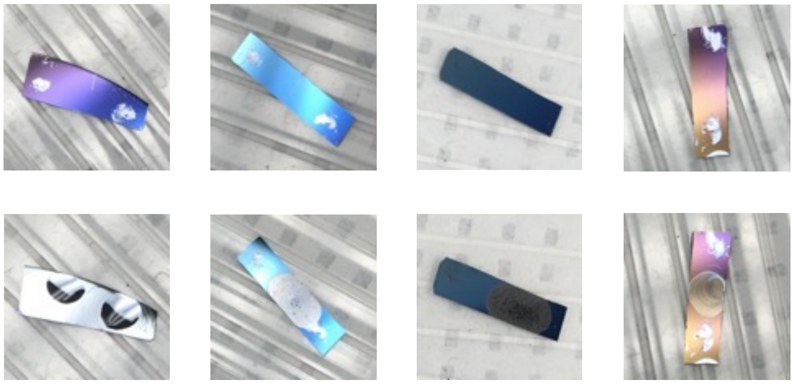

(a) Solubility tests with DCM on films treated with UV for 0 h, 3 h, 5 h, and 7 h from left to right.

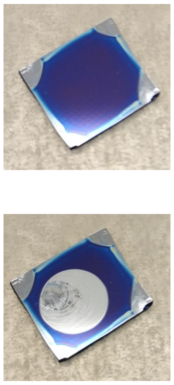

(b) PS film ($M_\mathrm{n} = 996$ kg/mol) before and after DCM treatment.

Figure 4.16: Solubility tests with DCM.

time, higher and higher molecular weight components are formed by crosslinking. After a few hours of UV treatment, a fraction of the as-deposited film is crosslinked into a network and becomes insoluble. Fig. 4.17 shows another set of solubility tests with toluene. As-deposited films were immersed in toluene for 10 min after different time periods of UV treatment. The results from the solubility tests with DCM vs toluene could be different due to toluene being a better solvent for PS as well as the difference in film thicknesses. Nevertheless it is evident from both tests that more fraction of the film became insoluble with longer UV treatment.

As discussed earlier in this section, the resulting molecular weight distribution and the degree of crosslinking also depend on the initial chain distribution. The vapour-deposited films used in this study are PS with relatively low degrees of polymerization. Compared to

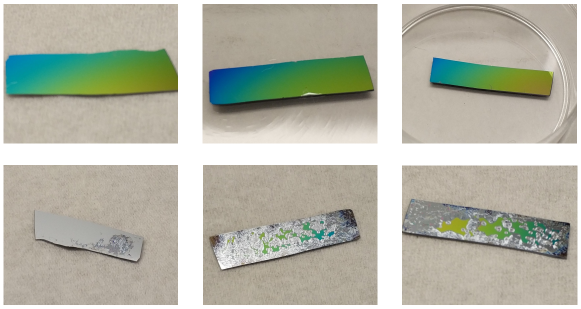

Figure 4.17: Solubility tests with toluene on films treated with UV for 30 min, 7 h and 9 h from left to right.

high molecular weight PS, the number of chains are greater in a film of the same size. Since the degree of crosslinking is defined as the average number of cross linkages per chain, it is expected to be lower in our vapour-deposited films under the same UV treatment. A solubility test was also performed in this regard. Fig. 4.18a shows a vapour-deposited film after 1 h of UV treatment. Note that the UV lamp used here was not the same one as other experiments in this chapter, but the conclusion is unchanged. Fig. 4.18b shows a spincast PS film with $M_{\mathrm{w}} = 545$ kg/mol after the same UV treatment. While the vapour-deposited film was completely dissolved by toluene, the high molecular weight PS was almost unchanged after being immersed in toluene.

4.2.5 Ellipsometry measurements on UV treated films

In the pursuit of real polymer stable glass, UV treatment is shown to successfully increase the molecular weight of vapour-deposited PS. The next step is to determine whether they still have the properties of a stable glass through ellipsometry measurements. Fig. 4.19a shows the thickness change of an as-deposited PS film with $\bar{N} = 8$ during heating and cooling scans. With $T_{\mathrm{g}} - T_{\mathrm{f}} = 24$ K and $T_{\mathrm{onset}} - T_{\mathrm{g}} = 14$ K, it is a stable glass. A film from the same deposition was UV treated for 6 h and Fig. 4.19b shows its ellipsometry measurement.

Compared to the as-deposited film, the crosslinked film has an increase of 6 K in T_{g}, indicating the increased molecular weight [187]. With $T_{\mathrm{g}} - T_{\mathrm{f}} = 5$ K and $T_{\mathrm{onset}} - T_{\mathrm{g}} = 5$ K, it is still a stable glass, although it has lower thermodynamic stability as well as lower kinetic stability compared to the as-deposited glass. The density increase in the as-deposited glass is present after the UV treatment but also reduced. This is the first evidence that real polymer stable glass is made by UV crosslinking vapour-deposited glass. The reduced

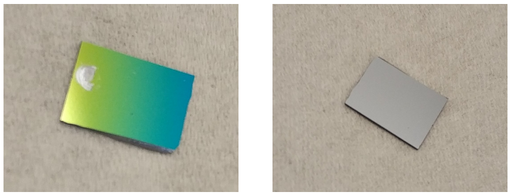

(a) UV treated vapour-deposited PS film before and after toluene treatment.

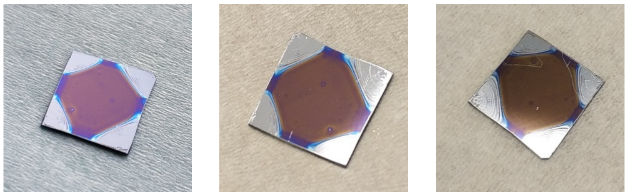

(b) Spincast PS film (M_w = 545 kg/mol) before UV treatment, after UV treatment and then after toluene treatment.

Figure 4.18: Solubility tests with toluene on PS films of different molecular weights under the same UV treatment.

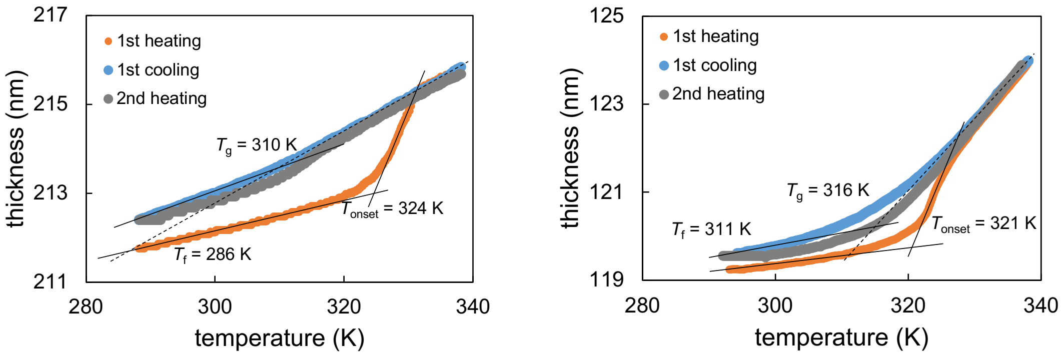

(a) As-deposited film.

(b) UV 6 h.

Figure 4.19: Thickness change with respect to temperature of a PS film deposited at T_sub = 263 K and UV treated for 6 h.

stability, however, indicates that the UV treatment has more complex effect on vapour-deposited glass. In addition to creating larger molecules as expected, it also affects the glass stability, which is worth further investigation.

In order to better understand the effect of UV radiation on vapour-deposited glass, stable glass and rejuvenated glass were compared. With two films from the same deposition, one was rejuvenated into a regular glass by heating and then liquid cooling while the other was unaltered as a stable glass. The ellipsometry measurement on an as-deposited glass from the same deposition is shown in Fig. 4.20. $T_\mathrm{g} - T_\mathrm{f} = 23$ K and $T_\mathrm{onset} - T_\mathrm{g} = 21$ K show that the glass is stable before any treatment.

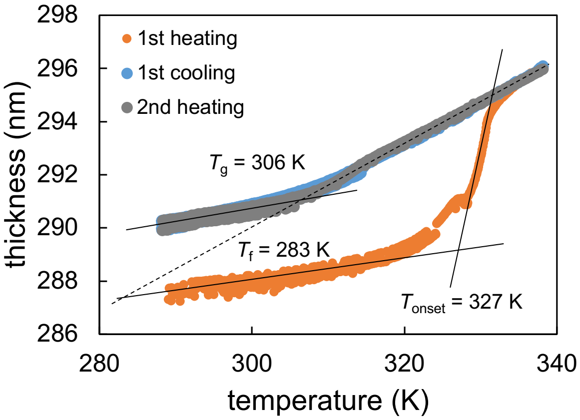

Figure 4.20: Thickness change with respect to temperature of a PS film deposited at T_sub = 261 K.

The rejuvenated film and the as-deposited were then both UV treated for 3 h, before being measured with ellipsometry. Fig. 4.21a shows that rejuvenation has removed the stability from the film, giving a $T_\mathrm{f} \approx T_\mathrm{g}$. UV has also increased the molecular weight of the film as shown from the increased T_g. Fig. 4.21b shows the result of the as-deposited film directly treated with UV radiation. After UV treatment, the stable glass has achieved a similar T_g increase as the previously rejuvenated film, suggesting that the degree of crosslinking is similar in the two types of glasses. Consistent with the previous experiment, the thermodynamic stability, kinetic stability as well as the density increase are all reduced in the stable glass after UV treatment.

The two sets of UV experiments from Fig. 4.19a to Fig. 4.21b both show apparent increase in T_f. To relate this change to the UV treatment, Fig. 4.22 shows the apparent T_f increase as a function of UV time from a series of experiments. A monotonic relation indicates that as UV treatment goes on, the stability in the film is continuously taken away from the glass.

It is known that heating is one way of reducing glass stability, and even full rejuvenation is possible at high enough temperatures. During UV treatment, it is also known that the lamp produces heat in the chamber and could potentially heat up the sample surfaces.

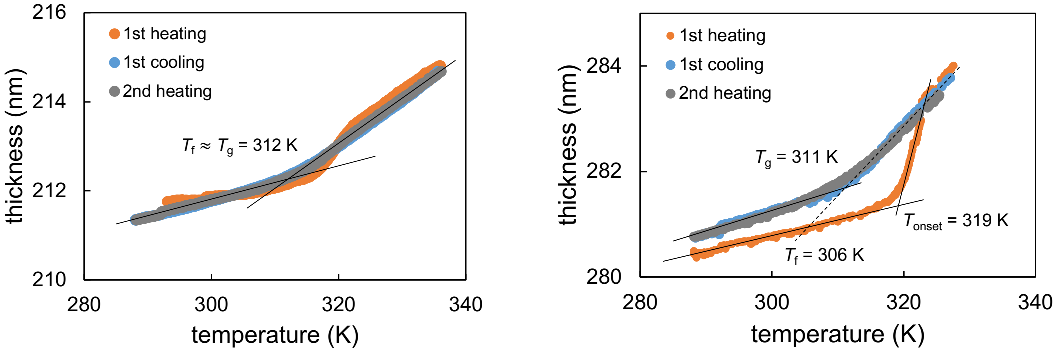

(a) Rejuvenated first.

(b) As-deposited.

Figure 4.21: Ellipsometry results of the rejuvenated and as-deposited films after 3 h of UV treatment.

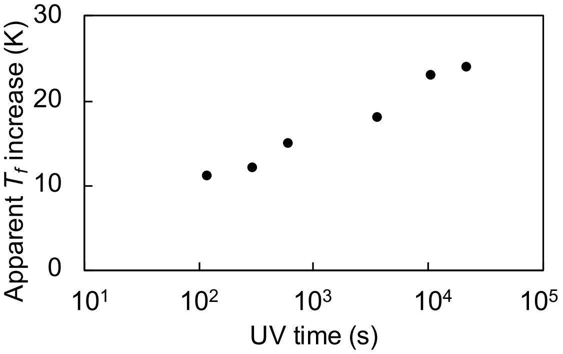

Figure 4.22: Apparent T_f increase in UV treated vapour-deposited PS films.

In order to test whether glass stability is reduced by elevated temperature, measurements on the substrate temperature were performed under several conditions and the results are shown in Fig. 4.23.

A thermocouple wire was attached to a PS film placed on the sample stage in the UV chamber. In the first case, the chamber was left sealed after initial nitrogen flushing. No continuous nitrogen flow was provided and active cooling was turned off. In two hours while the UV lamp was on, the temperature increased by $\sim$ 15 K and appeared to have reached a plateau. In the second case, continuous nitrogen flushing was kept on during the UV treatment without active cooling. The temperature behaviour almost overlapped with the first case and in about one hour of UV treatment, the temperature increased by $\sim$ 10

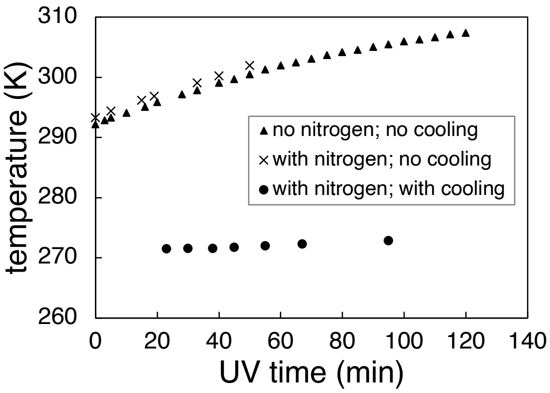

Figure 4.23: Temperature tests in the UV chamber under different conditions.

K. In the last case, nitrogen was continuously flushed while the UV lamp was on and active chiller cooling was provided, with the chiller set at 253 K. In $\sim$ 80 min, the temperature only increased by 1.4 K, which demonstrates the effectiveness of active cooling. 25 min after the UV lamp was turned off, the temperature was measured again and it recovered by 0.6 K since the last data point.

During real experiments, active cooling is always provided as in the third case. Since the UV lamp does not affect the substrate temperature, external heating is ruled out as the reason of reduced glass stability after UV treatment. Therefore, it is reasonable to deduce that UV radiation may cause local structure changes in the glass and the efficient packing may be diminished, resulting in lower stability after longer UV treatment. When cross linkages are formed between chains, the intermolecular forces change to covalent bonds, and the distance as well as local packing in the system are altered.

For regular liquid-cooled glasses, since there is no enhanced stability to start with, the effect of UV and UV-induced crosslinking is only seen from the increase of T_g, without any change in stability. With increased degree of crosslinking, bulk T_g and the apparent breadth of the glass transition increase [184, 187]. The magnitude of T_g-confinement effect in thin films was also shown to increase in crosslinked PS [196]. In the present study, increased T_g is also observed, although the thin film effect has not been investigated as most of our films are above 100 nm.

In this project, crosslinking is assumed to be the main reaction during UV treatment. However, as introduced earlier, other types of reactions including photooxidation and chain scissions could also happen with oxygen present. For sample sizes as small as the thin films we use, they could be highly sensitive to even low concentration of oxygen in the environment and undesired chain modifications could occur. A sign of photodegradation happening is that for some of the films after UV treatment, the film changes colour slightly and appears to be thinner than before UV treatment. This may be related to the oxygen level in the UV chamber, the N value of the glass, and its enhanced density, etc. Once these photodegradation reactions happen, the composition of the system is altered, and undoubtedly the local structures and the efficient packing will be affected. Efforts in preventing these reactions have been made such as improving the nitrogen level, using higher molecular weight glasses and more stable glasses. A more quantitative investigation on this phenomenon has not been covered in this thesis.

Photodegradation and photostability in vapour-deposited glasses has been studied in organic glasses [197, 198]. Experiments and simulations showed that photostability is improved in vapour-deposited glasses and the resistance to photo-induced processes are correlated to the enhanced density. In our system, it is reasonably expected that the degree of stability would also affect photo-induced reactions including both crosslinking and photodegradation processes. In fact we have seen evidence showing difference in the degree of crosslinking in glasses with different stabilities. In a preliminary solubility test using toluene, glasses that were rejuvenated before 4 h of UV treatment did not dissolve in toluene, while as-deposited glasses with 5 h of UV treatment still dissolved. It later dissolved after three more hours of UV treatment. Such differences could be due to the increased density in the vapour-deposited glasses as Ref. [197] and Ref. [198] suggests. A systematic study on such relations has not been conducted in this thesis, and it would be worth studying in future work.

Ref. [197] also investigated the effect of irradiation temperature on the photostability of vapour-deposited glasses. It was found that not only a higher stability led to more resistance to photodegradation, but a lower irradiation temperature also resulted in slower photodegradation. This raises the following question for the present study. In trying to eliminate the loss in glass stability due to the heat from the UV lamp, the substrate temperature has always been kept as low as possible, in most cases around 273 K as shown in Fig. 4.23. However, if the irradiation temperature has a similar effect on the efficiency of photocrosslinking as well as photodegradation, it means low temperatures may not be optimal for crosslinking to occur. A balance between these factors may need to be considered in future work.

Fig. 4.19 through Fig. 4.21 show results from film thickness measurements where the UV crosslinked glasses still retain part of its stability, although the stability is reduced compared to before UV treatment. This stability as shown from the film thickness is not always measured in our experiments. In some measurements on film thickness, the enhanced density appear to be completely removed and the film could even be thicker on the first heating during the ellipsometry run compared to subsequent cooling and heating runs.

Fig. 4.24 shows the ellipsometry measurements on the film thickness and refractive index change with respect to temperature of a film deposited at $T_{\mathrm{sub}} = 293$ K. Some films from this deposition were rejuvenated to regular glass, while the rest was left as stable glass. Both types of films were then UV treated at the same time and ellipsometry was done on films after different time periods of UV as shown in Fig. 4.25 and Fig. 4.26.

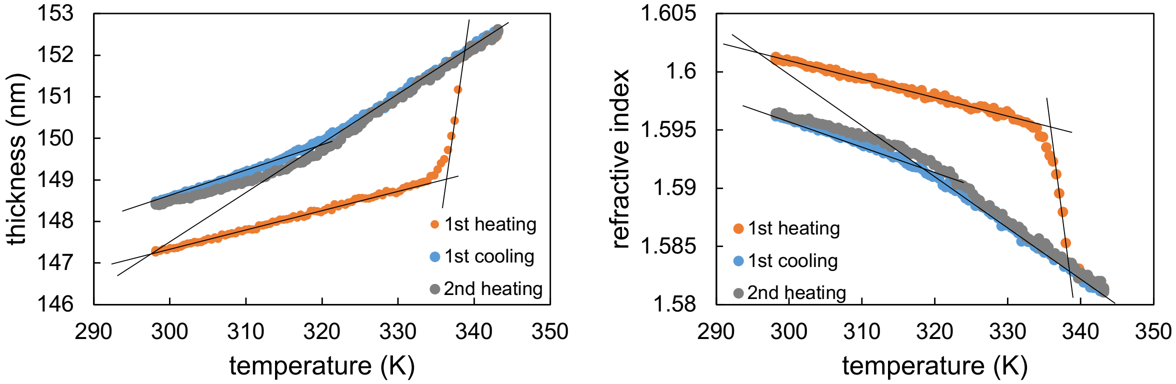

Figure 4.24: Thickness and refractive index change with respect to temperature of a PS film deposited at $T_{\mathrm{sub}} = 293$ K.

Fig. 4.25 shows films that were stable glass before being treated with UV for 2 h, 4 h and 6 h. Fig. 4.26 shows films that were first rejuvenated to regular glass before going through the same UV treatment. First, an increase of ~ 10 K in T_{g} is observed in both films after 2 h. After 4 h and 6 h, the glass transition is broader and less evident as seen from both data, particularly in refractive index.

Based on the film thickness plots of the as-deposited films, all films appear to have lost stability after even 2 h of UV. The first heating curves all lie above the subsequent cooling and heating runs which means they appear to be thicker after the UV treatment and then thinner after being heated and cooled back down. The typical standard of stable glass include an increased density, a higher T_{onset} and a lower T_{f}. In the thickness data, none of the three properties are observed, so these films do not qualify as stable glasses.

The refractive index n, however, tells a slightly different story. They appear to be higher on the first heating run compared to subsequent runs, which indicates a higher density in the as-deposited and then UV treated films.

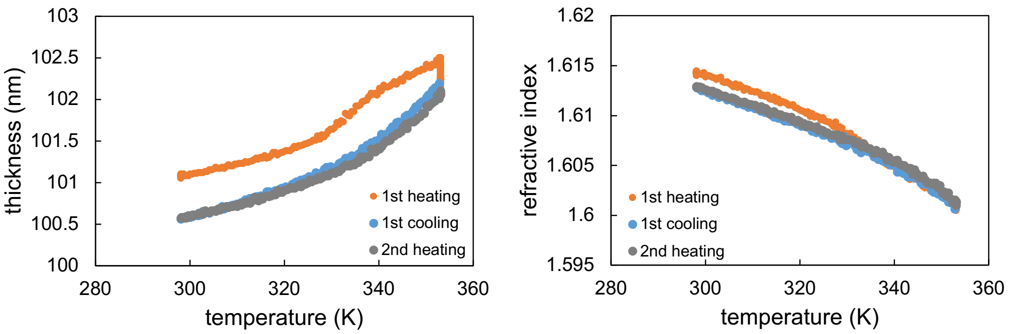

(a) UV 2 h.

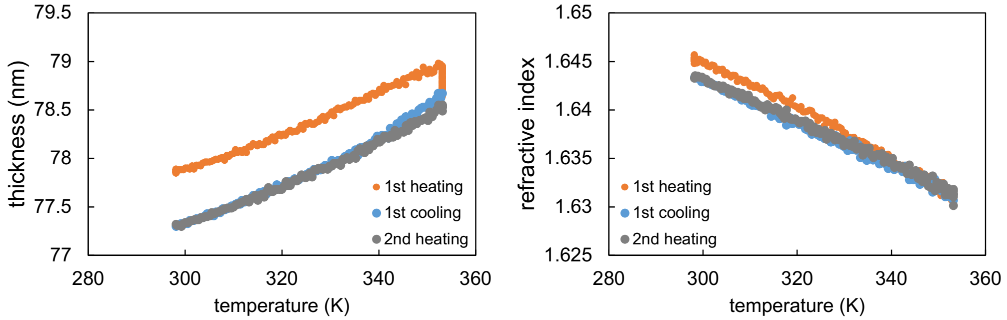

(b) UV 4 h.

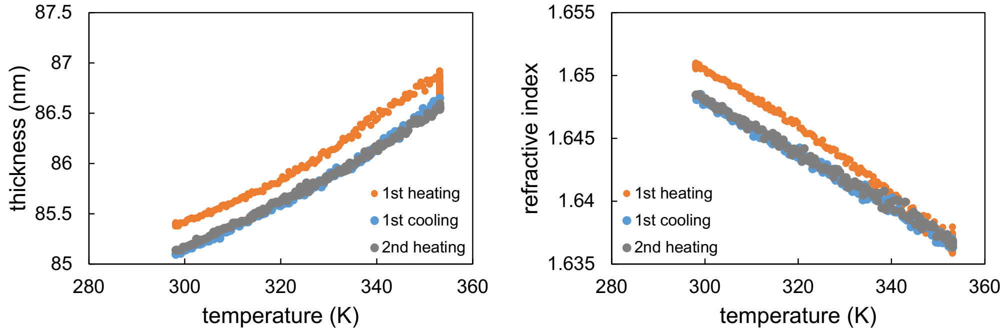

(c) UV 6 h.

Figure 4.25: Thickness and refractive index change with respect to temperature of UV treated as-deposited PS films.

Together, the thickness data reports that the as-deposited films are thicker on the first heating, while the refractive index data reports that they are denser at the same time. This

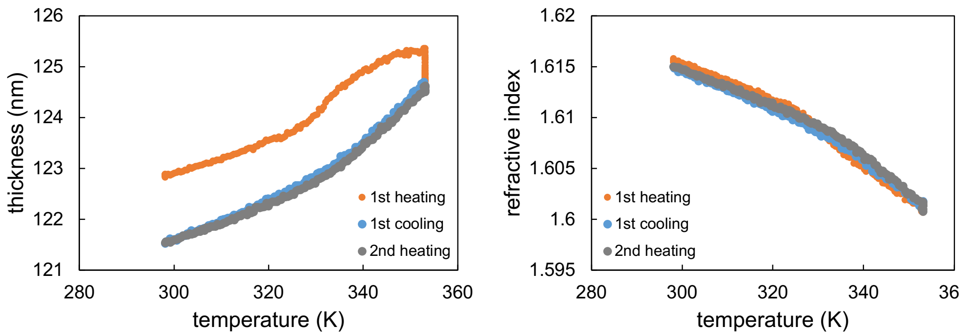

(a) UV 2 h.

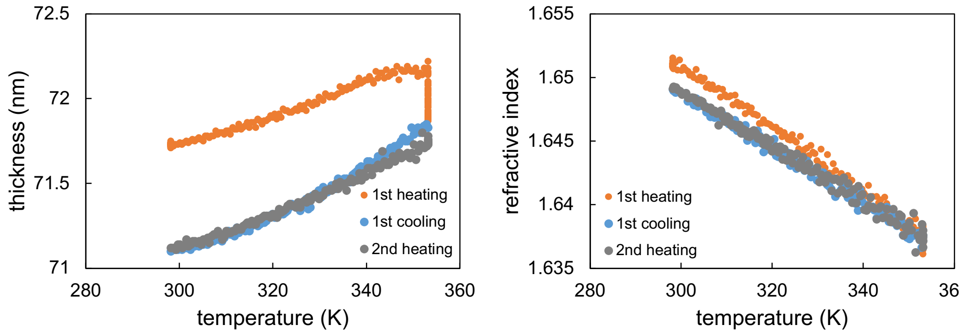

(b) UV 4 h.

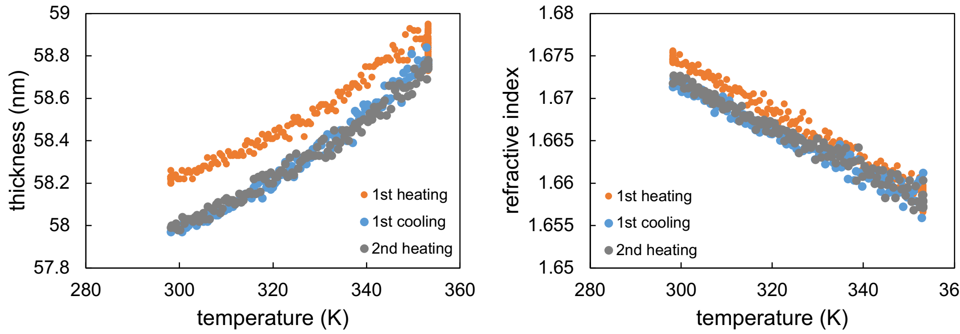

(c) UV 6 h.

Figure 4.26: Thickness and refractive index change with respect to temperature of UV treated rejuvenated PS films.

phenomenon is explained later in this chapter where similar result is shown for another series of experiments.

Comparing the refractive index data of two types of films after 2 h of UV irradiation, the as-deposited film appears to be a marginally stable glass as it has a higher n on the first heating. The rejuvenated film behaves as a regular glass as expected after rejuvenation. After 4 h and 6 h, the refractive index data in both films look very similar, with no distinguishable glass transition after the first heating and the first heating has a higher n than the subsequent runs. Since the stability in the formerly rejuvenated films has been removed before UV treatment, the higher n in the first heating must have originated from the UV process rather than from the vapour deposition. This naturally leads to questions on the cause of the similar higher n in the as-deposited glasses in Fig. 4.25b and Fig. 4.25c. If they have arisen from the same unknown mechanism as in the rejuvenated glasses, the higher refractive index may not indicate residual stability as expected.

When looking at the refractive index plots for both types of films, it is also observed that the values of refractive index increases monotonically with increasing UV time in all films. Compared to the non-UV treated film that has a $n \approx 1.6$, the longest UV treated film has an n increase as high as 4.6%. One possible explanation is that the cross linkages formed during UV treatment may alter the local structure and the packing of the glass by reducing the intramolecular distances through covalent bonds. The specific volume has been shown to decrease with increasing degree of crosslinking [180, 181, 184]. Thus with increased density, the refractive index is also expected to increase according to the Lorentz-Lorenz relation [199], $\frac{n^2-1}{n^2+2} = \frac{4\pi}{3}N\alpha$, where n is the refractive index, N is the number of molecules per unit volume and α is the mean polarizability. The UV induced n increase is more significant in the rejuvenated films than in the as-deposited films under the same conditions, which is also consistent with our previous observation and literature studies [197, 198] that suggest stable glass may be more resistant to UV induced reactions. After the first heating run, the compact structures due to crosslinking may relax to a small extent, leading to a slightly lower n value in the subsequent runs for both types of films.

In literature studies, thermal expansion coefficients of polymers above and below T_{g} have been shown to decrease with increasing degree of crosslinking [184, 185]. From data shown in Fig. 4.24 through Fig. 4.26, thermal expansion coefficients are calculated from different temperature regions and compared in Fig. 4.27.

Thermal expansion coefficients from three linear temperature regions are plotted. The high temperature part on the first cooling curve typically represents the liquid, the low temperature part on the first cooling typically represents the regular liquid-cooled glass, and the low temperature part on the first heating typically represents the as-deposited glass. For the initial film that was not UV treated, the three values are 8.4×10^{-4} K^{-1}, 4.1×10^{-4} K^{-1}, and 3.1×10^{-4} K^{-1}, respectively. Although not monotonic, the decrease in all three numbers is observed in general in both types of glasses. Among them, the

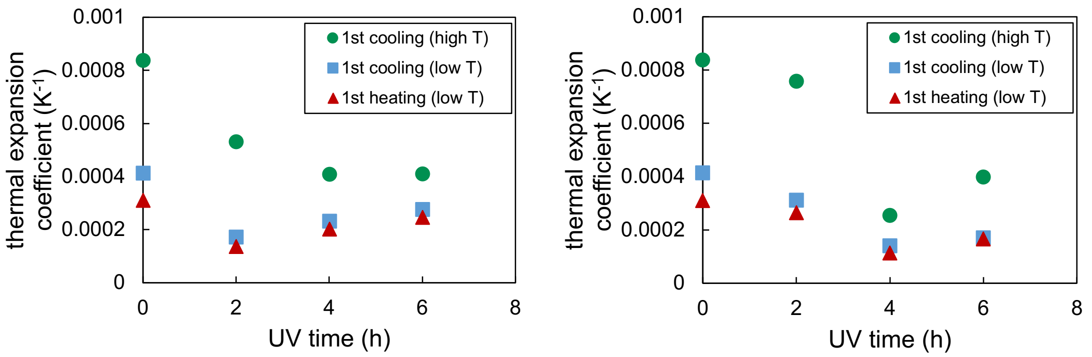

(a) Thermal expansion coefficients of the UV treated as-deposited glasses.

(b) Thermal expansion coefficients of the UV treated rejuvenated glasses.

Figure 4.27: Thermal expansion coefficients with respect to UV time.

"liquid" expansivity drops the most with increasing UV time and becomes closer to the glass expansivity. This indicates that with increasing degree of crosslinking, T_{g} increases and more fraction of the material stay in the glassy state up to the highest temperature measured.

UV treatment also affects the surface dynamics of glassy films. In Sect. 5.1.4 it is shown that the surface morphology evolution at elevated temperatures are inhibited by increased UV time, which is to be expected since the cross linkages formed with UV could decrease the mobility of the system in general.

As discussed in Sect. 4.2.1, although the films in the present study are thin enough, the light traveling through the film is partially absorbed since PS is non-transparent in the UV regime. Near the surface the film is irradiated with the maximum intensity, and as depth increases the intensity decreases due to absorption. Therefore the degree of crosslinking is expected to change over the thickness of the sample and cause a gradient in many properties including molecular weight, thermal expansivity, modulus, etc. This gradient is detected in modeling ellipsometry data of crosslinked films. Although an ideal model of a uniform polymer layer typically results in good fitting, substituting it with a graded layer can sometimes reduce the mean squared error even more. The overall film properties including thermal expansion coefficients and film stability, however, do not show any noticeable change in using either model.

4.2.6 Photodegradation during UV treatment

In addition to crosslinking, photodegradation reactions could also take place in the UV chamber when oxygen is present as discussed earlier. It is worth noting that the PS material that has been used in this project is PS1200 with $-OH$ end groups in a fraction of the material. During the UV radiation, it is unclear whether the hydroxyl groups would accelerate photooxidation reactions or be involved in other undesired reactions. For this concern, we conducted another series of UV experiments with the PS1400 material deposited in Sect. 4.1. PS1400 has sec-butyl end groups as introduced earlier and therefore do not raise such a concern.

The second deposition from PS1400 was used for the UV experiments. Fig. 4.4 and Fig. 4.5 show its N distribution from mass spectrometry and thickness and refractive index measurements from ellipsometry, respectively. After UV treatment of 0.5 h, 1 h, 2 h and 3 h, Fig. 4.28 shows the new ellipsometry results.

Similar to the results from PS1200, no stability is observed from these films. On the first heating run after UV treatment, the films also appear to be "denser and thicker" compared to the subsequent temperature scans. Assuming there is no mass transfer during the temperature ramps, such result is in contradiction to the conservation of mass. In examining this issue, it was realized that the assumption of no mass change in the measurements needed to be carefully examined. From previous experience in Chap. 3, it has been observed that when the N value of the polymer is relatively high and the T_{sub} is set low, the resulting deposited film can have such high kinetic stability that it may not fully rejuvenate on heating, but rather sublimes directly and becomes thinner on the first heating run.

A similar mechanism of sublimation or evaporation can be a possible explanation for the apparent thicker and denser film on the first heating. In fact, one thing to be noticed in all such results is that at the end of the first heating run, the temperature is kept constant but there is a continuous decrease in the film thickness. The high temperature end in the refractive index data, however, does not show such a change. This would be understandable if short chains due to chains scissions or photooxidation are produced during the UV treatment and they evaporate at higher temperatures on the first heating run.

Fig. 4.29 shows that the change in N distribution with UV time increases as measured by mass spectrometry. Compared to the initial film, UV does not change the distribution significantly until 2 h. For 2 h of UV irradiation, the higher N components above 8 reduces and after 3 h no longer chains than $N = 6$ are present, which indicates that they have

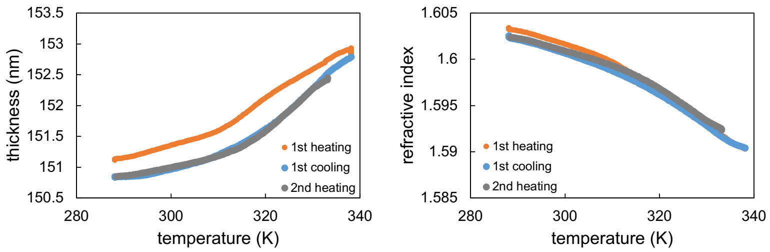

(a) UV 0.5 h.

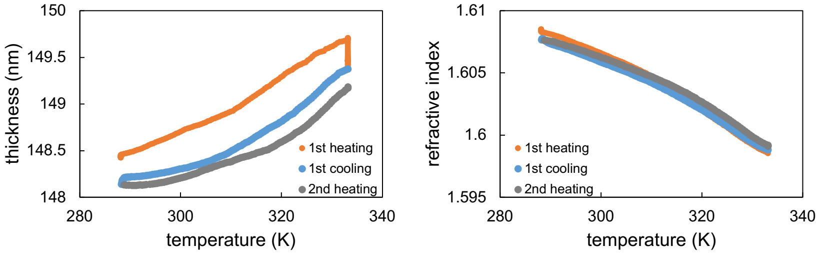

(b) UV 1 h.

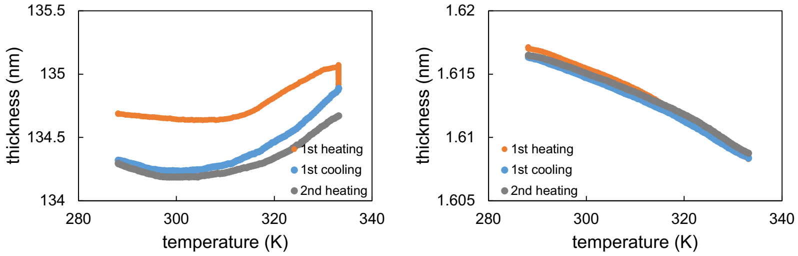

(c) UV 2 h.

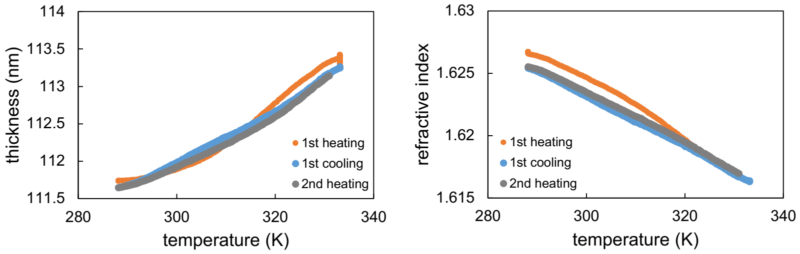

(d) UV 3 h.

Figure 4.28: Thickness and refractive index change with respect to temperature of UV treated PS films deposited from PS1400.

either crosslinked into much higher molecular weight components or have fragmented into smaller pieces. In the initial film as shown in Fig. 4.4 the smallest N present is $N = 4$ with 6%. After 0.5 h of UV, $N = 4$ increases to $\sim 9\%$ and $N = 3$ appears. The fraction of $N = 3$ keeps increasing with longer UV time and becomes the dominant components after 3 h of UV. This is evidence supporting that chain scissions occur during the UV treatment. The "denser and thicker" films could also be explained by such mechanism, where the fragmented chains evaporate at high temperatures on the first heating and result in the apparent decrease in film thickness while the refractive index is unchanged.

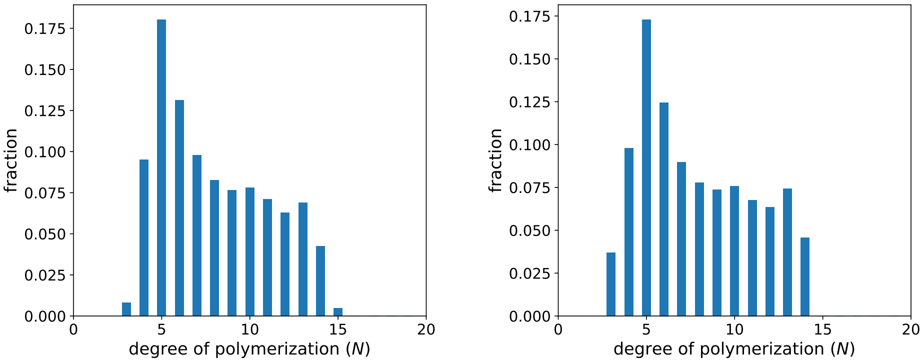

(a) UV 0.5 h. (b) UV 1 h.

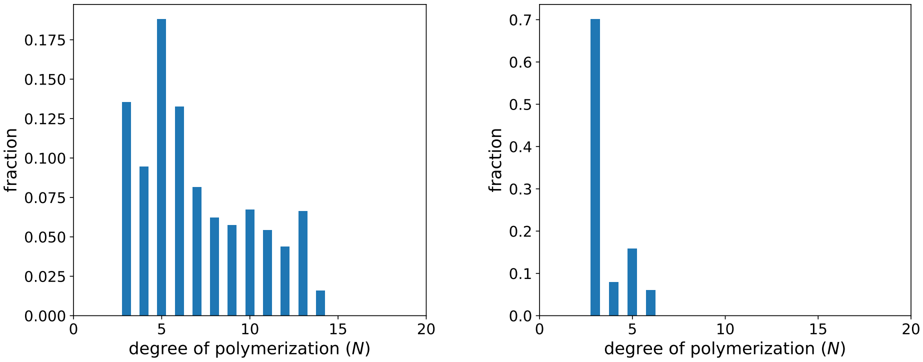

(c) UV 2 h. (d) UV 3 h.

Figure 4.29: N distribution of films deposited from PS1400 after different time periods of UV treatment.

In Chap. 3, it is mentioned that when some vapour-deposited glasses with large N (≥ 10) and high stability are heated, they sublime before they can rejuvenate to liquid because they are too stable. While stability could certainly be one reason of this phenomenon, another possibility could also be proposed based on what we learned in this project. It has been demonstrated with mass spectrometry that when the source temperature is too high during vapour deposition, thermally induced chain scissions occur which could generate a large fraction of oligomers with small N's. When such films are heated, the evaporation of small chains would also result in the deviation in the thickness slope.

If fact when the subliming issue was first observed, we proposed that UV treatment could be applied on such films to potentially prevent them from subliming by crosslinking. Such attempts did not lead to effective results in avoiding the subliming issue and now we realize it is because the UV process would create small chains that have a similar sublimation/evaporation issue.

4.2.7 Conclusion

In this section we explore the possibility of achieving higher molecular weight stable polymer glasses through UV crosslinking. In an inert atmosphere, crosslinking is expected to happen through dehydrogenation and the molecular weight of the material is expected to increase. The mass distribution of UV treated films is characterized using mass spectrometry and there are signs of decreasing fractions of low molecular weight components. Through simple solubility tests we observe lower solubility for films after longer UV treatment, suggesting an increase in the overall molecular weight. The stability of these films are characterized with ellipsometry. For some UV treated films stability is still observed, although the degree of stability appears to decrease with UV treatment. Based on ellipsometry and mass spectrometry measurements it is believed that photodegradation reactions could be the the cause of the stability loss and other abnormal ellipsometry results.

Chapter 5

Surface of vapour-deposited polystyrene glass

During the formation of stable glasses through physical vapour deposition, it is believed that the enhanced surfaced mobility is the mechanism that allows for efficient packing and exceptional properties of stable glasses [134, 135]. The surface mobility of PS glasses has been studied extensively in the past few decades [116, 133], but it is the first time we prepare stable PS glasses through vapour deposition and there is no study on their surfaces yet. It is not clear how the surfaces of vapour deposited low molecular weight PS will compare to the surfaces of high molecular weight PS or spincast PS films. In this chapter we would like to examine the surface of these glasses including their surface morphology and surface dynamics.

5.1 Surface morphology studies on vapour-deposited polystyrene glasses

The work introduced in this section was initiated by unexpected ellipsometry measurement results on vapour-deposited glasses. In understanding the reasons behind the abnormal behaviours, the surface of these glasses were thoroughly examined using techniques including optical microscopy and AFM. During the investigation, a few types of surface features were observed, most of which were not found in the literature to the best of our knowledge. One of the surface structures, surface bumps, appeared to be an ideal candidate for probing the surface dynamics of vapour-deposited glasses, and a study of the bump evolution as a function of time was performed. However, after systematic investigations, it is finally believed that we have a plausible explanation for the abnormal behaviours, and we attribute them to low N polymers accumulated in the deposition chamber. On the one hand, this discovery means the efforts in this project was partly in vain due to some undesirable impurities. On the other hand, we finally solved the problem that was in the way of the overall study on vapour-deposited stable glasses. Moreover, the second section of this chapter was directly built on the experience and skills gained from this work, and revealed the surface relaxation of vapour-deposited PS glasses successfully.

5.1.1 Morphology features

Most of the ellipsometry measurements performed on our vapour-deposited films show expected behaviours of stable glass. However, there were times when the fitting of a regular substrate-polymer-air model had higher MSE or the property changes during a temperature scan simply did not agree with the expected rejuvenation/vitrification/melting process of the material. In the investigation of such issues, one reasonable guess was that the surface may have abnormal roughness which affects the light reflection in the ellipsometry measurements. Some of the films deposited were then examined by optical microscopy and AFM to observe their surface morphology. Many films with normal ellipsometry results had normal surface morphology as well. For example, Fig. 5.1 and Fig. 5.2 show the surface of a film deposited at 296 K, under an optical microscope and an AFM respectively. For comparison, Fig. 5.3 shows the surface of a spincast PS film with $M_\mathrm{n} = 600$ g/mol. Nevertheless, different morphology features were surprisingly found on many of the films that had abnormal ellipsometry results. Some examples are shown in Fig. 5.4 to Fig. 5.10, with features that resemble bumps, flowers, strings, and crystals.

Figure 5.1: Optical microscope image on a PS film deposited at 296 K, with $\bar{N} = 7.4$.

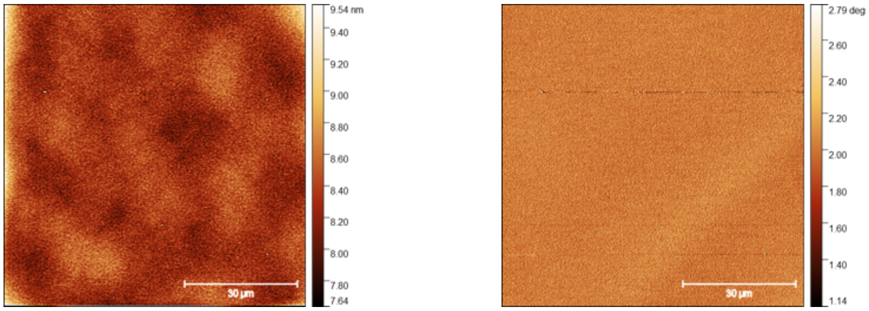

(a) Height image.

(b) Phase image.

Figure 5.2: AFM height and phase images on the same film as shown in Fig. 5.1.

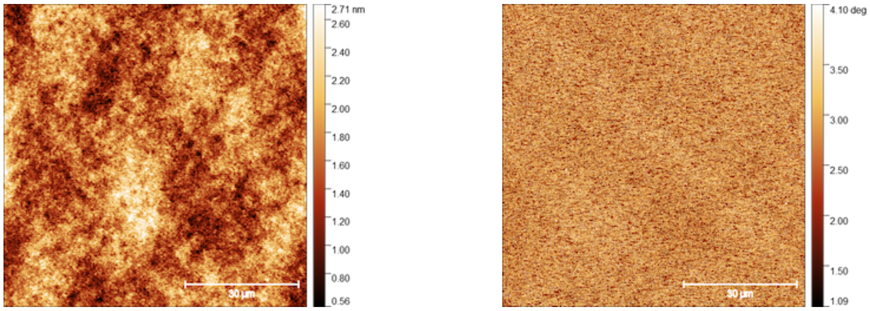

(a) Height image.

(b) Phase image.

Figure 5.3: AFM height and phase images on a spincast PS film with $M_{\mathrm{n}} = 600$ g/mol on silicon.

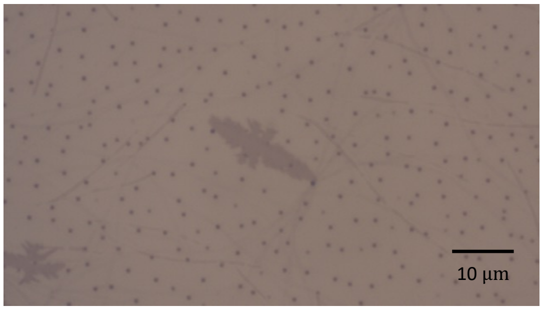

Figure 5.4: Optical microscope image on a PS film deposited at 260 K, with $\bar{N} = 7.5$.

Bumps were found to be the most common feature among most films. Thus most of the investigation later in this section focuses on exploring their distributions, growth,

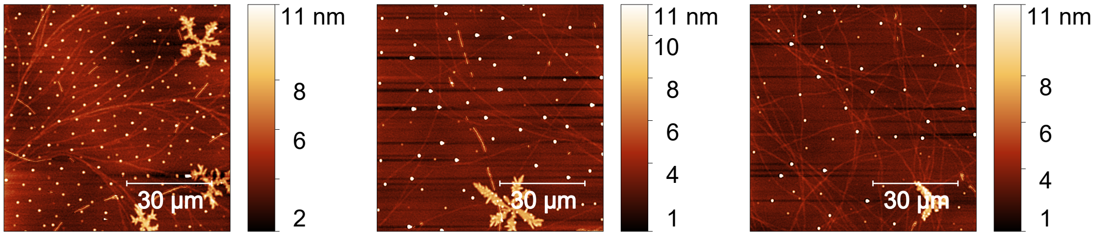

(a) (b) (c)

Figure 5.5: AFM height images on the same film as shown in Fig. 5.4.

(a) Height image. (b) Phase image.

Figure 5.6: AFM images on a PS film deposited at 272 K.

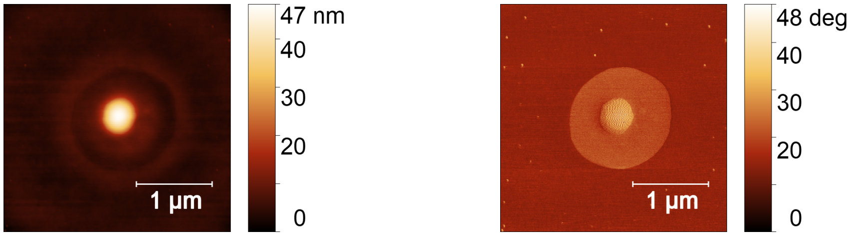

(a) Height image. (b) Phase image.

Figure 5.7: AFM images on a PS film deposited at 259 K.

temperature evolutions, as well as statistical analysis about the bumps.

However, it was not clear yet that the bumps were associated with the polymer, rather than the substrate or contamination. In the study of vapour-deposited α, α, β-trisnaphthylbenzene glasses [139], Dalal *et al* observed two types of surface defects that both resemble cracks on the surface. One type of cracks was attributed to silicon particles as a results of the cleaving of the wafer after deposition, and the other type was attributed to pump oil contamination in the chamber, in which case the cracks only appeared as the

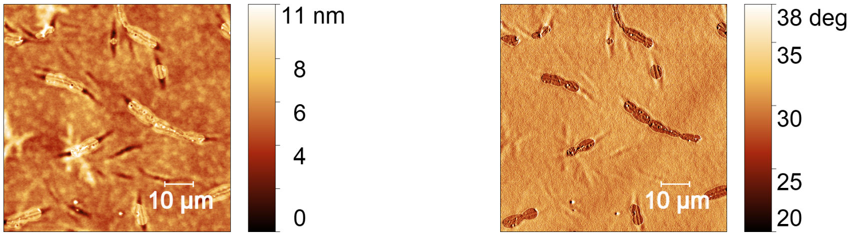

(a) Height image. (b) Phase image.

Figure 5.8: AFM images on the same film as shown in Fig. 5.7.

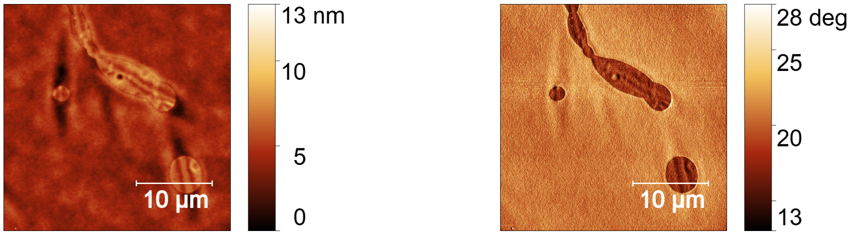

(a) Height image. (b) Phase image.

Figure 5.9: AFM images on the same film as shown in Fig. 5.7.

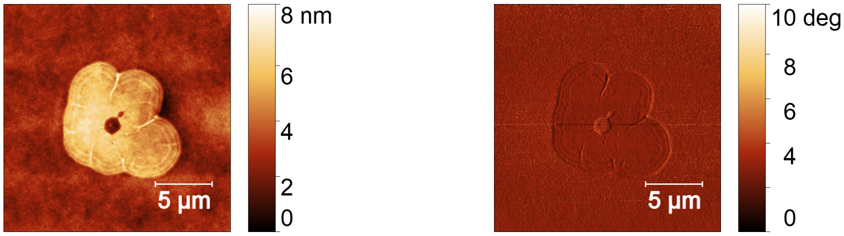

(a) Height image. (b) Phase image.

Figure 5.10: AFM images on a PS film deposited at 259 K.

stable glass was heated to transform to the supercooled liquid. Once the chamber was cleaned, the second type of cracking was eliminated.

In the current study, the optical images were obtained immediately after deposition without cleaving the wafer. Thus it is not related to the presence of bumps, flowers, and strings such as shown in Fig. 5.4. In order to test the effect of pump oil or other contamination source possible in the chamber, a bare silicon wafer was installed on the substrate stage and left under vacuum for a similar period of time as typical depositions, only without heating the deposition source. In this test, bumps were absent from the surface. Therefore, the possibility of pump oil was ruled out and it was believed that the bumps were associated with the polymer itself.

5.1.2 Morphology on different substrates

Most of the samples in this thesis are prepared on silicon substrates. In order to test the effect of substrate material on the surface morphology, silicon and mica were both used for a same deposition. Fig. 5.11 shows that the morphology features introduced earlier such as bumps, flowers and strings are present on film deposited on silicon.

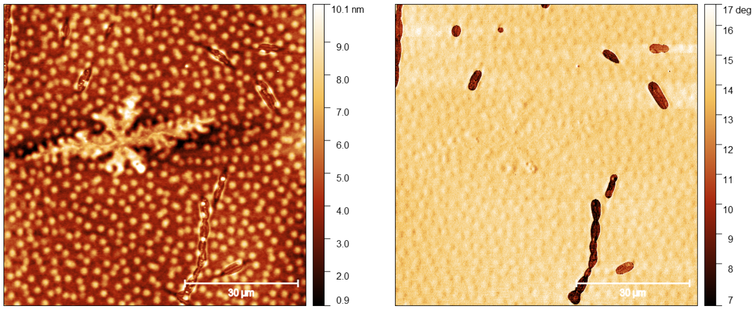

(a) Height image. (b) Phase image.

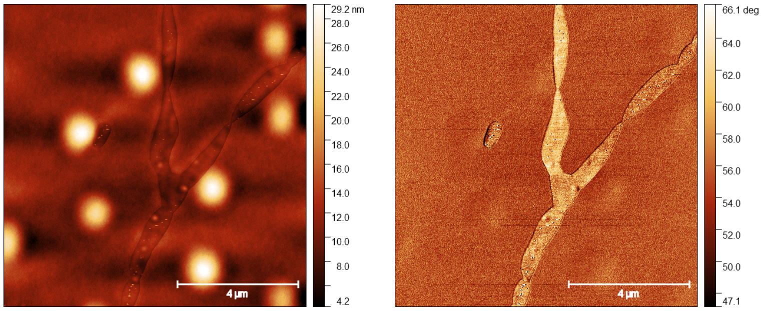

(c) Height image. (d) Phase image.

Figure 5.11: AFM images on a PS film deposited on silicon at 259 K.

The film deposited on mica shows a cleaner surface than that on silicon, without bumps or flowers. The only evident features are the similar strings. For comparison, Fig. 5.13 shows the surface of a spincast PS film with $M_{\mathrm{n}} = 600$ g/mol on mica. It shows a similar surface to the spincast film on silicon as in Fig. 5.3, which indicates that the strings present in Fig. 5.12 are a result of vapour deposition.

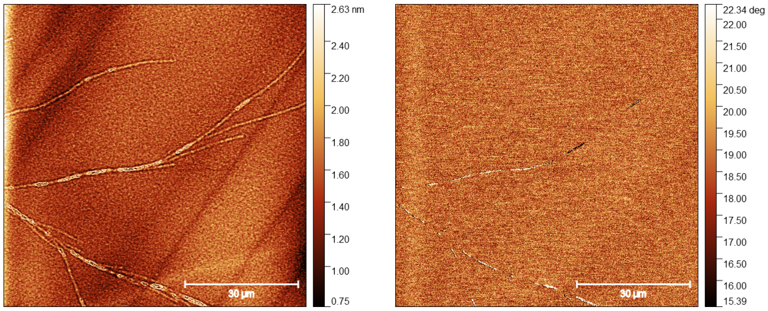

(a) Height image. (b) Phase image.

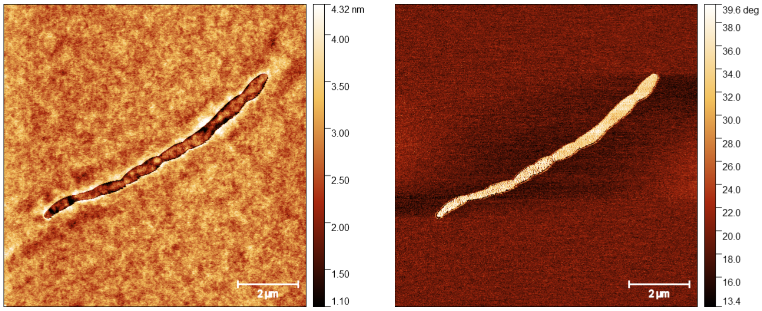

(c) Height image. (d) Phase image.

Figure 5.12: AFM images on a PS film deposited on mica at 259 K.

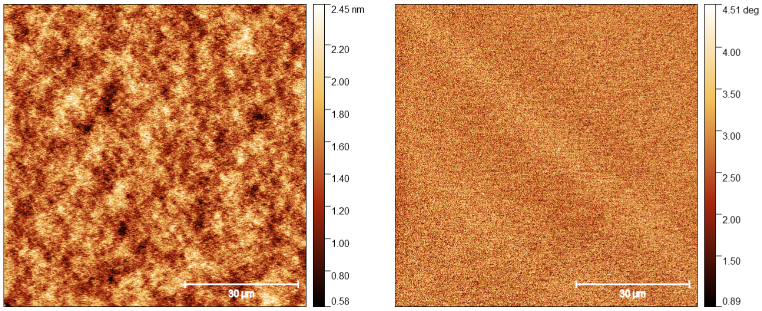

(a) Height image. (b) Phase image.

Figure 5.13: AFM height and phase images on a spincast PS film with $M_\mathrm{n} = 600$ g/mol on mica.

In the rest of this section, these morphology features are investigated, particularly the surface bumps since their circular shape is suitable for analysis such as size, height and density distribution.

5.1.3 Artifacts due to substrate preparation

In examining the morphology features it was accidentally discovered that the cleaning method used on the silicon substrate could lead to artifacts in the film morphology. When preparing for the film shown in Fig. 5.14, Kimwipe tissue was used to gently wipe off silicon dusts from the silicon substrate before deposition. As a result, patterned morphology is observed on the film surface, with flakes/flowers aligned in stripes, conceivably in the direction of the wiping movement. For films deposited on silicon without using Kimwipe, the distribution of the flakes are random as shown in Fig. 5.4. In Ref. [200], Lin *et al* observed similar artifacts on Kimwipe-treated films, where long amyloid fibrils were well oriented on the surface of peptide samples. It is unclear how Kimwipe induces such morphology in our case but it indicates the importance of the cleaning procedure and substrate preparation in vapour deposition. In the rest of this thesis, no such wiping is used for substrate cleaning and only air dusters are used.

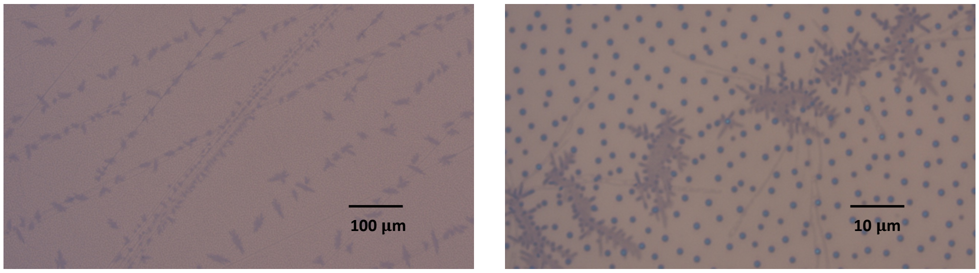

(a) (b)

Figure 5.14: Microscope images on a PS film with the silicon substrate wiped before deposition.

5.1.4 Morphology evolution at elevated temperatures

As seen from Fig. 5.4 and Fig. 5.5, surface bumps and flakes in the shape of stars or daggers are among the most common features on the surface. The flakes vary in size from 2 µm to 30 µm and the bumps are $\sim$ 0.5 µm in size. The heating process of a film deposited at $T_{\text{sub}} = 257$ K with these features was monitored with a microscope and shown in Fig. 5.15.

Throughout heating, the bumps did not change significantly, whereas around the flakes the morphology change was evidently visible. Mountain ridges grew outward originating from the flakes and reach each other. AFM measurements show that such ridges are on the order of $\sim$ 100 nm in height.

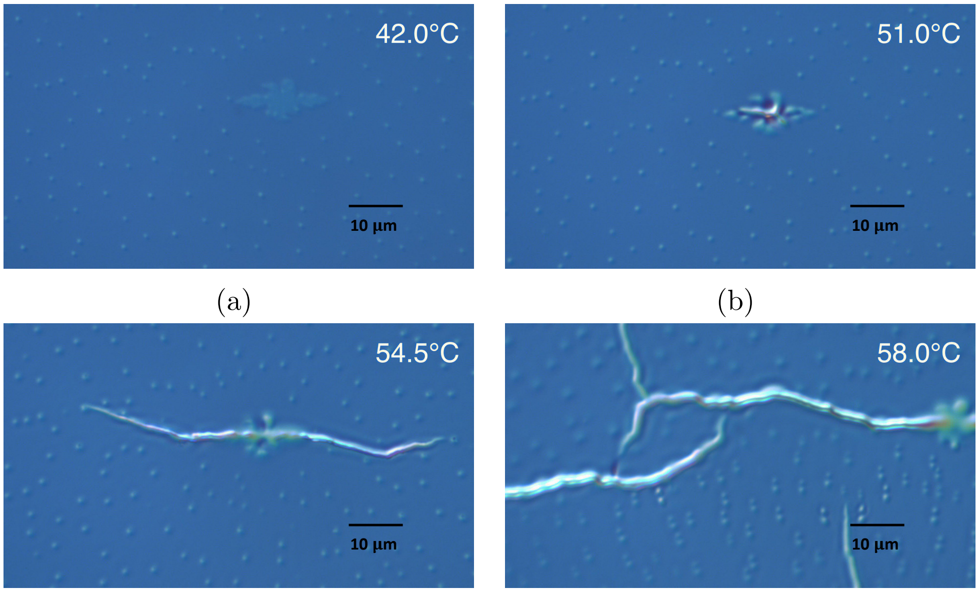

(a) (b) (c) (d)

Figure 5.15: PS film deposited at $T_{\text{sub}} = 257$ K during heating.

This morphology evolution has been reported in our previous studies of vapour-deposited PS glasses [201] and is also similar to that reported for molecular glasses [139]. While Ref. [139] attributes such morphology to contamination by pump oil, Ref. [201] shows that at least for the case of PS samples, pump oil is not a strong contributing factor since the morphology evolution only depends on the thermal treatment. By comparing to other morphologies in the literature [202], it is suggested that they could be stress-induced morphologies. In fact most films with such morphologies have relatively low substrate temperatures during deposition, so it is likely that when they are recovered to room temperature for characterization the change in temperature results in accumulation of stress. It is further mentioned in Ref. [201] that when all other deposition conditions are the same, such morphologies are more common in thicker films but rarely observed in thinner films, supporting the idea of compressive stress in the film.

The wrinkling of thin films has been studied extensively [203, 204, 205, 206, 207]. Typically when there is gradients in mechanical or thermal properties normal to the film surface, in-place compressive stress is created. To relieve the compressive stress beyond a critical value, the surface layer can wrinkle into a random pattern.

Since such ridges increase the surface roughness of the film, it should also be noted that they can affect ellipsometry measurements on films with such features at elevated temperatures.

In Section 4.2 the effect of UV treatment on vapour-deposited films was studied. Some films with these morphology features were also used in the UV studies. It was found that UV treatment did not change the morphology features but could affect how the surface evolves at elevated temperature. Fig. 5.16 shows the film from the same deposition as that in Fig. 5.15 after 9 h of UV treatment. Unlike the non-UV treated film where the mountain ridges started growing at 51°C and fully evolved at 58°C, the UV treated film did not shown such changes at all even at 120°C.

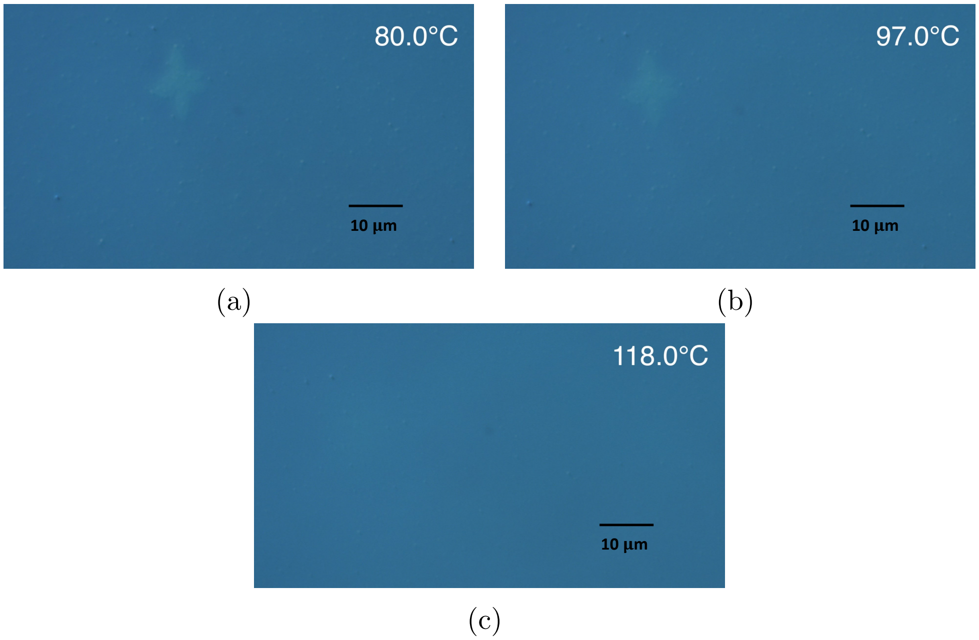

Figure 5.16: PS film deposited at $T_{\mathrm{sub}} = 257$ K, UV treated for 9 h.

In order to study the effect of UV time on the formation of the ridges, a series of UV treatment was conducted on films from the same deposition at $T_{\mathrm{sub}} = 261$ K. Fig. 5.17 shows these UV treated films after being heated to 338 K and cooled to room temperature naturally. The film after 2 min of UV treatment shows similar surface morphology with non-UV treated films after heating. With merely 5 min of UV treatment, the growth of the ridges is greatly inhibited and they evolve to a much smaller extent. Beyond 30 min they become indistinguishable in the microscope images.

These experiments show that UV treatment inhibits the surface evolution, which is

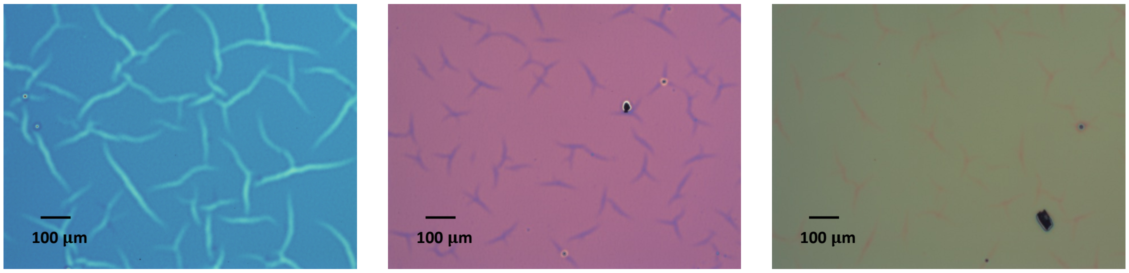

(a) UV 2 min. (b) UV 5 min. (c) UV 10 min.

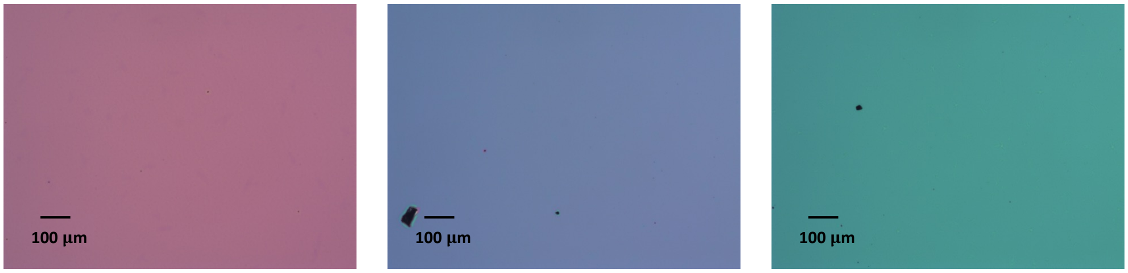

(d) UV 30 min. (e) UV 1 h. (f) UV 3 h.

Figure 5.17: PS films deposited at $T_{\mathrm{sub}} = 261$ K with various UV treatment after heating.

expected from the effect of UV crosslinking. Through the formation of cross linkages the surface mobility as well as the overall mobility of the system are expected to reduce. The modulus is also expected to increase after crosslinking, which can result in higher critical values for wrinkles to form.

Since the formation of ridges may be related to accumulated stress during heating, the difference in mechanical and thermal properties between the film and the substrate could also have an effect, and therefore the role of the substrate was studied. Instead of bare silicon that is used throughout the thesis, spincast PS films on top of silicon were used as new substrates. The $M_{\mathrm{w}} = 1200$ g/mol PS with truncated distribution after distillation (Sect. 2.2) was spincast on silicon and annealed overnight before being used as deposition substrate. T_{g} of this film is 324 K (51°C) as measured by ellipsometry. The substrate temperature for deposition was 260 K. When this bilayer film was heated, the same evolution of ridges was observed as in Fig. 5.15.

Next we tried PS with lower T_{g}'s which would serve as softer substrates. $M_{\mathrm{n}} = 600$ g/mol and $M_{\mathrm{n}} = 950$ g/mol were prepared in the same way and used as deposition substrates, with a substrate temperature of 260 K. $M_{\mathrm{n}} = 600$ g/mol has a T_{g} lower than room temperature, and $M_{\mathrm{n}} = 950$ g/mol has a T_{g} of 306 K (33°C). Fig. 5.18 and Fig. 5.19 show the morphology evolution of the two films during heating at 5 K/min.

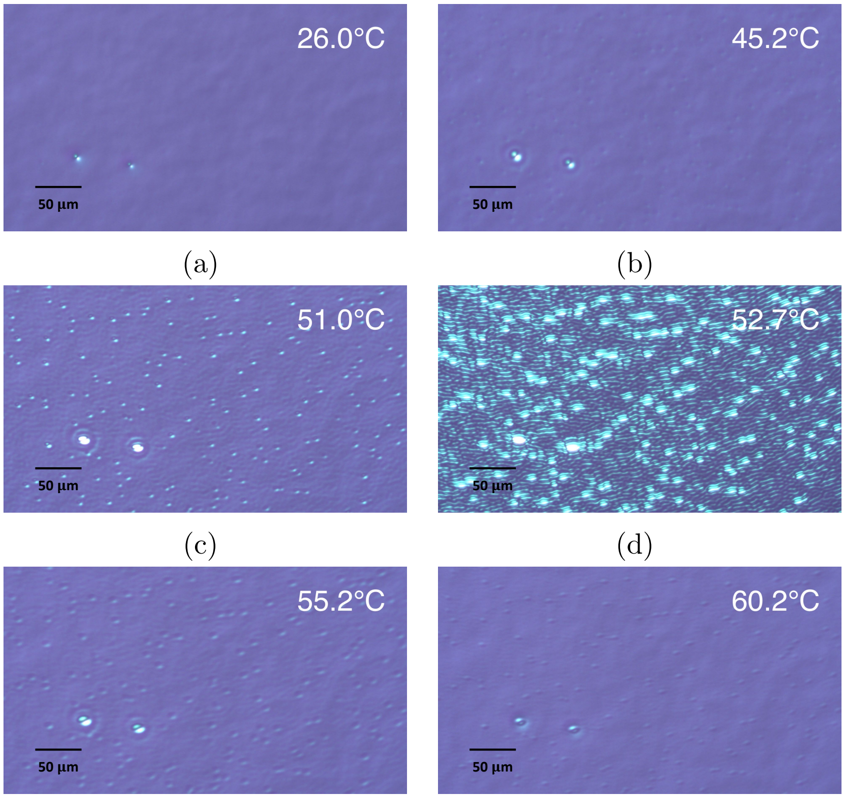

(a) (b)

(c) (d)

(e) (f)

Figure 5.18: PS film vapour-deposited on top of spincast $M_\text{n} = 600$ g/mol PS film.

The bubbles/bumps believed to be dust particles shown in the left of all images were chosen on purpose to help with focus adjustment while the film thickness changes with heating. As shown in both cases, the as-deposited morphology and the morphology evolution are remarkably different from the PS film directly deposited on silicon as shown in Fig. 5.15. In the first image of both films the surface appear smooth without flakes or bumps seen in other films. However, as temperature increases the surface starts to change. For the film deposited on PS $M_\text{n} = 950$ g/mol, ridges start to appear at a similar temperature as the start of ridge growth in Fig. 5.15 on the film deposited on silicon. The difference is that they only grow to a small extent before flattening and the surface becomes smooth again. This can be explained by the role of the soft substrate under the vapour-deposited film. When the modulus and thermal expansivity of the two films are similar, as stress

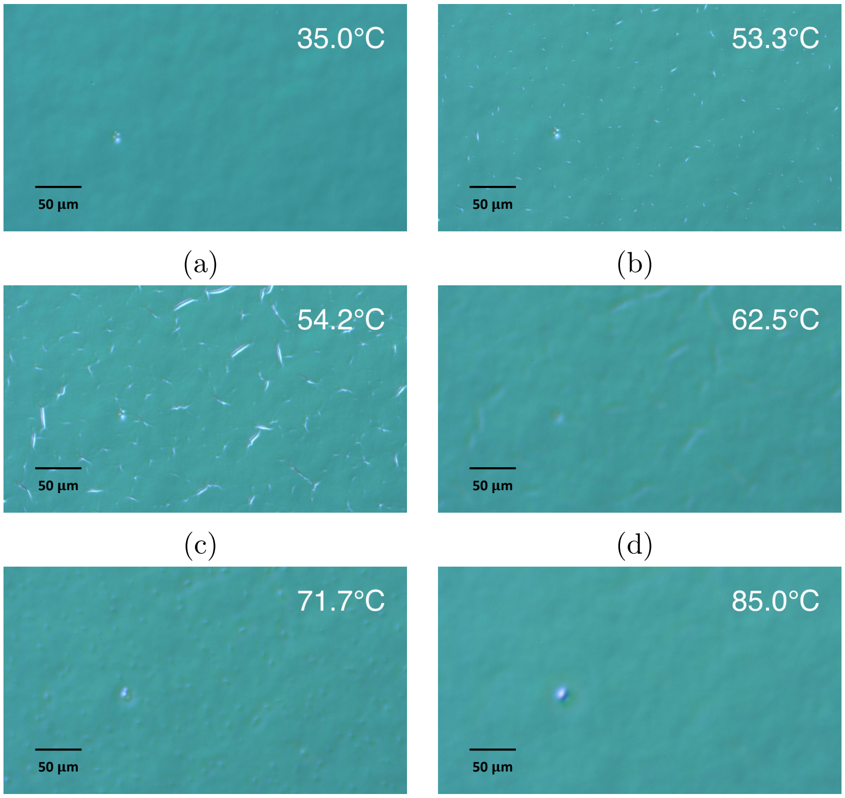

(a) (b) (c) (d) (e) (f)

Figure 5.19: PS film vapour-deposited on top of spincast $M_\mathrm{n} = 950$ g/mol PS film.

accumulate with temperature change, the film underneath helps dissipate the stress and reduce the degree of wrinkle/ridge formation.

When an even lower T_g film serves as the substrate, as shown in Fig. 5.18, the morphology evolution is distinctively different. With the underlying film in the liquid state, the surface morphology goes through a more abrupt and evident transformation. Within only 4 degrees from 51°C to 55°C small bumps and dense wrinkles develop across the film surface in a burst and then quickly flatten out.

5.1.5 Surface bump growth with film thickness

The growth of the surface bumps was examined with the increase of the film thickness from the deposition. Since it is impossible to perform in-situ AFM measurements during the deposition, a series of films with increasing thicknesses was prepared during one deposition. Fig. 5.20 is a schematic illustration of the experimental setup. The shutter was moved away from the surface at the beginning of deposition. After a desired thickness had been deposited according to the QCM, the shutter was turned by a certain degree to cover a part of the substrate such that the film thickness of that part could stay constant. The entire film was thus divided into a few sections with different thicknesses by changing the shutter position. An example of the resulting film is shown in Fig. 5.21.

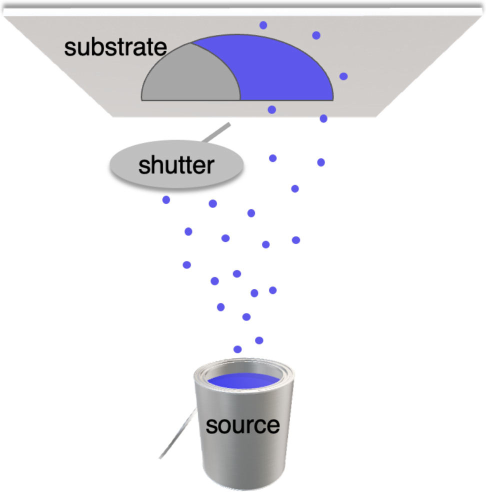

Figure 5.20: Schematic illustration of depositing films with varying thicknesses.

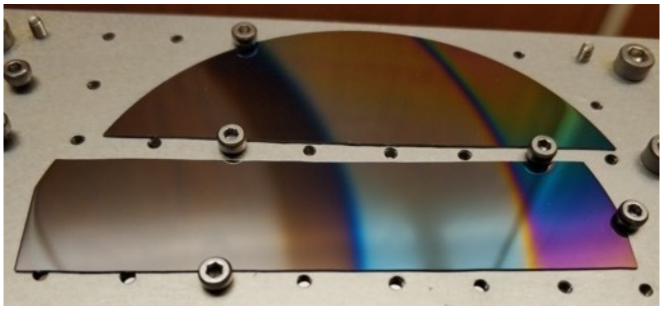

Figure 5.21: Films from one deposition with varying thicknesses.

Next, different sections of the film was examined with AFM. Fig. 5.22 and Fig. 5.23 show two series of depositions with nominal film thicknesses ranging from 1 nm to 10 nm and from 10 nm to 70 nm respectively. It is worth reminding the reader that the series of images appear to be misleading, especially Fig. 5.22, but the bumps/dots in each image are not the same one, but from different positions on the film. From Fig. 5.22(a) to Fig. 5.22(d), the film grows from 1 nm to 10 nm, with the bump evolving evidently. It first appears as a dewetted droplet on the bare silicon substrate, and gradually transitions into a donut-shape structure. As deposition goes on, Fig. 5.23 examines a zoomed-out area on the surface. The donuts grow into bumps and increase in height as the overall film thickness increases.

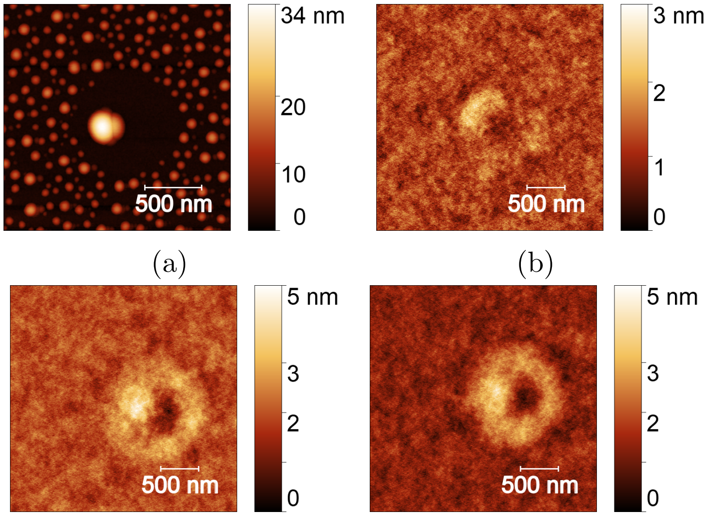

(a) (b)

(c) (d)

Figure 5.22: AFM images on four different sections of vapour-deposited PS sample, with nominal thicknesses of (a) 1 nm, (b) 4 nm, (c) 7 nm, and (d) 10 nm according to QCM measurements. T_{source}= 528 K, T_{sub}= 269 K.

5.1.6 Effect of substrate temperature on surface bumps

Since substrate temperature plays an important role in the preparation of stable glasses using the vapour-deposition technique, it is of interest to investigate its effect on the formation of the surface bumps. As a preliminary experiment, two depositions were performed in succession (such that they had a negligible difference in the $\bar{N}$ values) at different T_{sub}'s. Fig. 5.1 and Fig. 5.2 are images from the film deposited at 296 K, and Fig. 5.4 and Fig. 5.5 are images from the film deposited at 260 K. The $\bar{N}$ values of the two films are 7.4 and 7.5 respectively. The higher T_{sub} film shows a normal surface without abnormal features, while

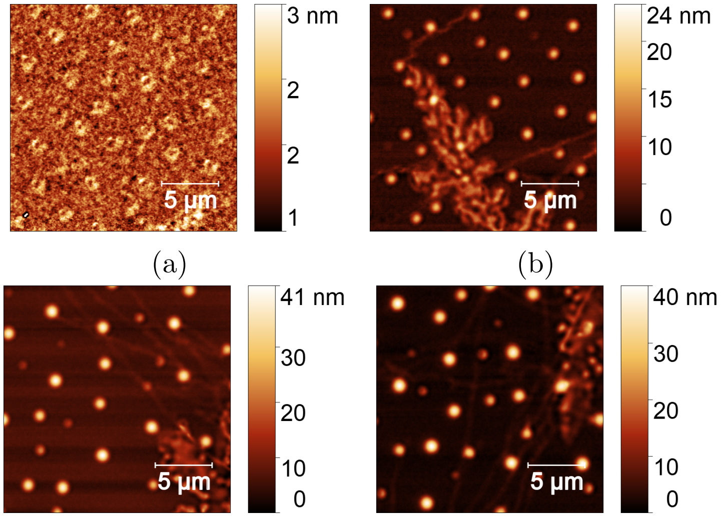

(a) (b)

(c) (d)

Figure 5.23: AFM images on four different sections of vapour-deposited PS sample, with nominal thicknesses of (a) 10 nm, (b) 30 nm, (c) 50 nm, and (d) 70 nm according to QCM measurements. T_{source}= 527 K, T_{sub}= 272 K.

the lower T_{sub} film has features including bumps. This observation indicates that T_{sub} is indeed a strong factor and a more systematic study should be conducted to investigate its effect.

A custom temperature gradient stage was built for the deposition chamber, such that samples at different T_{sub}'s could be created in a single deposition. As seen in Fig. 5.24, the silicon substrate bridges the two ends of the stage, with vacuum grease applied to ensure thermal contact, and then fixed with two clamps. The reason of using this bridge design, adapted from that in Ref. [140], instead of the regular stainless steel stage is to better ensure the temperature gradient. Since the thermal conductivity of silicon and stainless steel are very similar, a regular stage where a stainless steel bridge supports the silicon wafer would introduce ambiguity about the true substrate temperature. When using only silicon to conduct heat between the two ends, a linear temperature gradient across the bridge can be inferred.

Before depositions were performed, the stage was tested to calibrate the temperature against the chiller temperature and the output current on each side. Test results are summarized in Table 5.1, where various chiller temperatures and % current were used. This table acts as a guidance in reaching the desired T_{sub}'s on both sides.

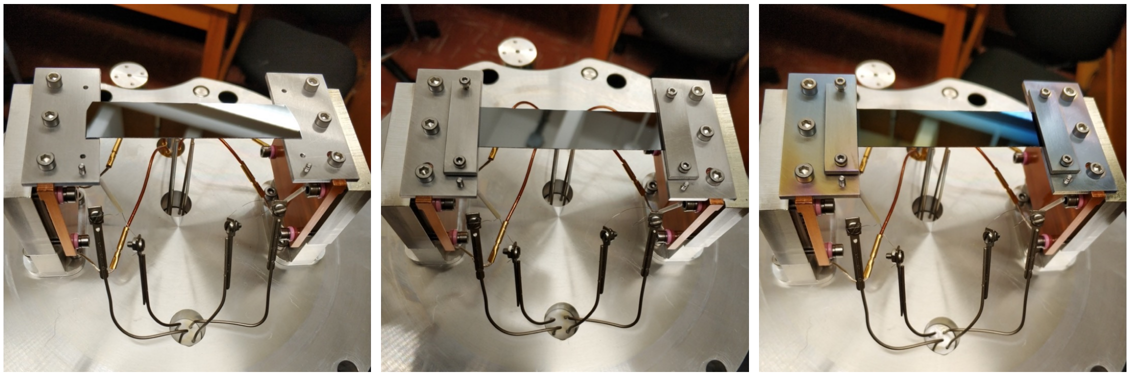

(a) Mounting Si substrate. (b) Fixing substrate on stage. (c) After deposition.

Figure 5.24: Custom built temperature gradient stage.

Both sides on cooling				
T_{chiller} (K)	% current on T_1	T_1 (K)	% current on T_2	T_2 (K)
265	0	279	0	279
265	0	278	25	266
265	40	262	0	276

One side on cooling and one side on heating				
T_{chiller} (K)	% current on T_{cool}	T_{cool} (K)	% current on T_{heat}	T_{heat} (K)
265	40	266	25	321
265	40	263	9	289
266	40	269	10	293
262	40	265	10	293
261	30	265	10	293
261	25	265	10	292
261	20	266	10	292

Table 5.1: Temperature test with custom built stage in deposition chamber.

Fig. 5.25 shows the surface of a film deposited with a temperature gradient from 270 K to 296 K across its length. From Fig. 5.25(a) to Fig. 5.25(k), the corresponding temperature was calculated based on its position coordinate, assuming the temperature gradient is linear from the hot to the cold side. It can be seen that films deposited at above 284 K do not have bumps formed on the surface, while at lower temperatures starting from 282 K, bumps appear and it even seems they grow in both density and height with lower temperatures before reaching a plateau.

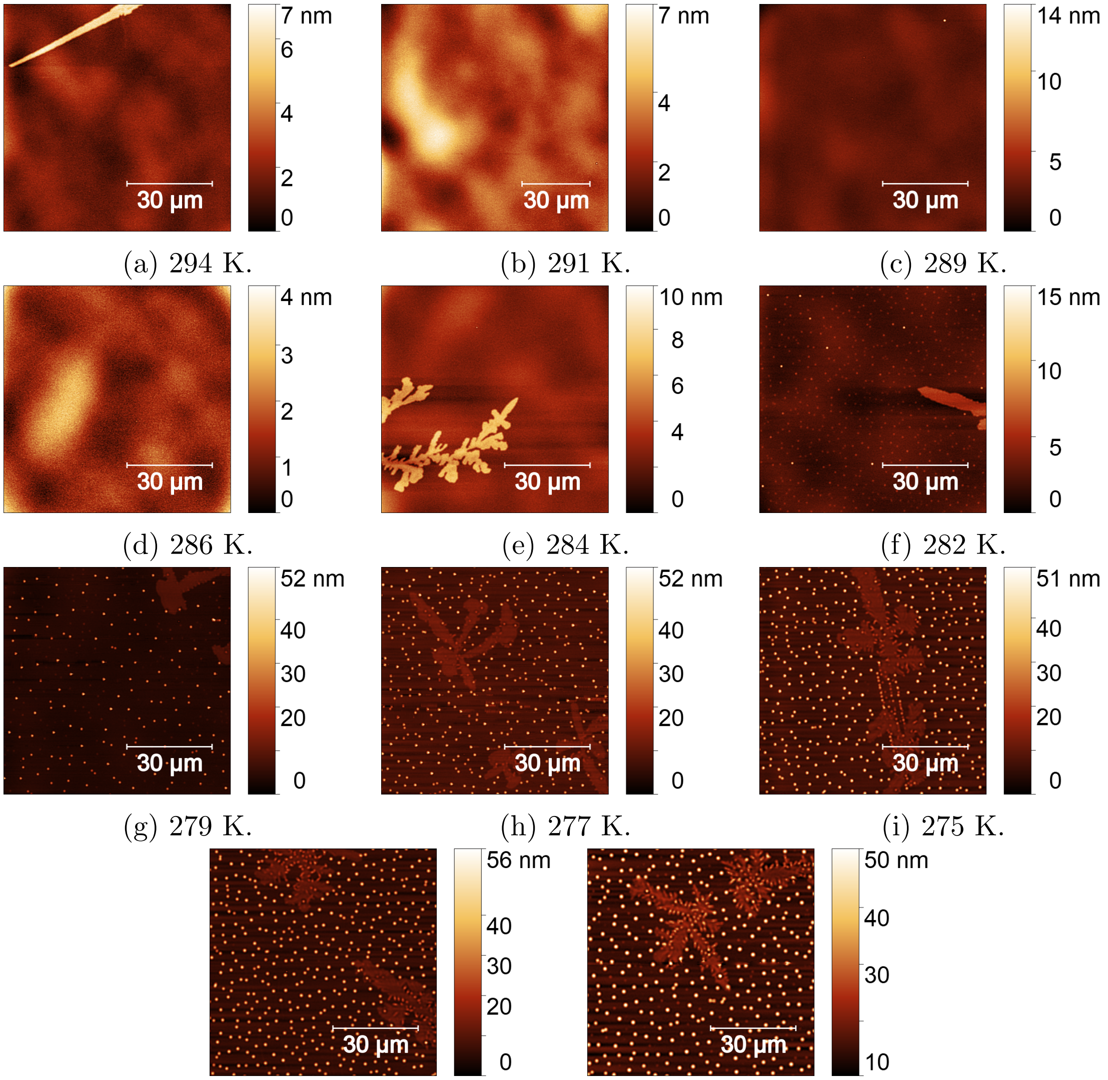

(a) 294 K. (b) 291 K. (c) 289 K.

(d) 286 K. (e) 284 K. (f) 282 K.

(g) 279 K. (h) 277 K. (i) 275 K.

(j) 272 K. (k) 270 K.

Figure 5.25: AFM images on different sections of a PS film deposited at varying T_{sub} from 270 K to 296 K.

In order to perform statistical analysis on the surface bumps, images can be processed with the Gwyddion software with the built-in functionality for analyzing grains. Bumps with heights exceeding a certain threshold can be automatically masked on the image (Fig. 5.26 is an example) and different quantities about the bumps and their statistics can be generated. The same films were also examined at different times after the deposition in order to observe the time evolution of the bumps.

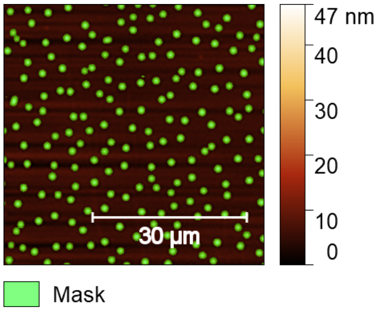

Figure 5.26: Applying masks on an AFM image with surface bumps using Gwyddion.

Fig. 5.27 shows the average bump height and the density of bumps on films shown in Fig. 5.25. As mentioned above, bumps are absent from films deposited at high temperatures. As temperature decreases, both the average height and the density first increase, and reach a plateau or slightly decrease at the lowest temperatures, except the outlier in bump density at 282 K. Looking at the time evolution, the bumps reduce in height with time, while the density stays constant within error bars. A more detailed study on the time evolution of bumps is included in Section 5.1.7.

The shape of the bumps have also been examined using ImageJ. The average circularity is 0.998 from the earliest AFM measurements after deposition. As time goes on, the bumps grow in diameter and finally grow into each other, no longer being individual circles. This is also the reason that the diameter is not selected in the observation of temperature dependence and time evolution.

The films have also been measured with ellipsometry to obtain their thickness and refractive index and their change with temperature. As shown in Fig. 5.28, the film with the highest T_{sub}, 294 K, displays features belonging to stable glasses. The as-deposited film has a higher density and higher kinetic stability than the rejuvenated glass, as seen from both thickness and refractive index.

The ellipsometry results from the film deposited at the lowest T_{sub}, 270 K, is shown in Fig. 5.29. The refractive index shows the normal stable glass behaviours, although the stability is less compared to the previous film. However, looking at both the thickness and the refractive index together, the as-deposited film represented by the first heating curve appear to be thicker and denser at the same time.

From Section 4.2.6 it was learned that such “thicker and denser” glasses could be due to

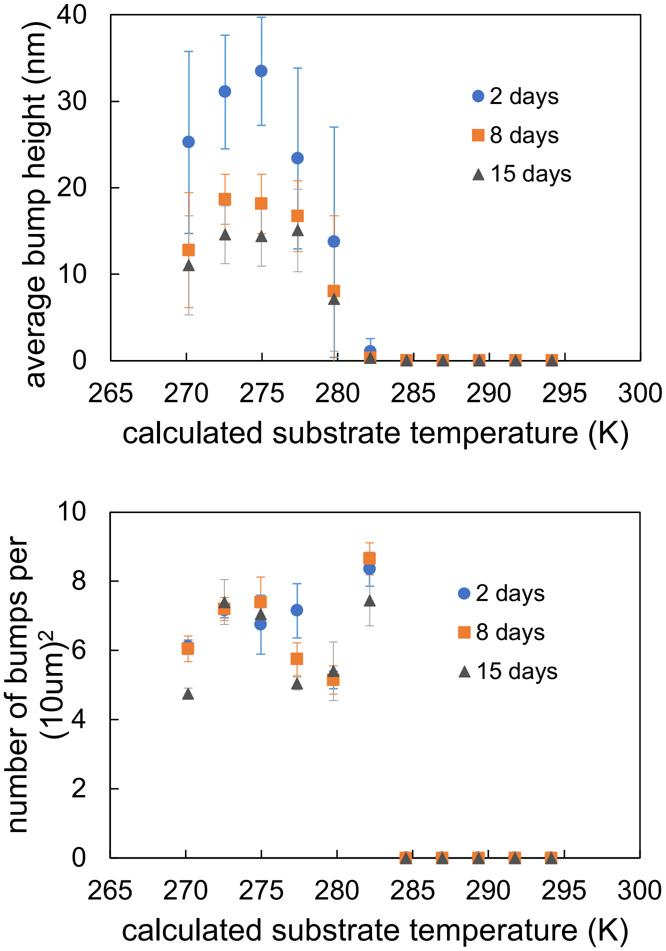

Figure 5.27: Average bump height and bump density on films with different T_{sub}'s, at different times after deposition.

small chains evaporating at high temperatures. Similar phenomenon could be happening in the current measurement. To account for the sublimation/evaporation issue and be able to observe the true temperature dependence of film thickness, the first heating curve can be shifted downward (equivalently, the following cooling and heating curves can be shifted upward) to match the endpoint of the first heating and the starting point of the first cooling curves. Fig. 5.30 shows the thickness plot from the upper panel of Fig. 5.29 after the shift. The result indicates a marginally stable glass, with a lower T_{onset} upon rejuvenation.

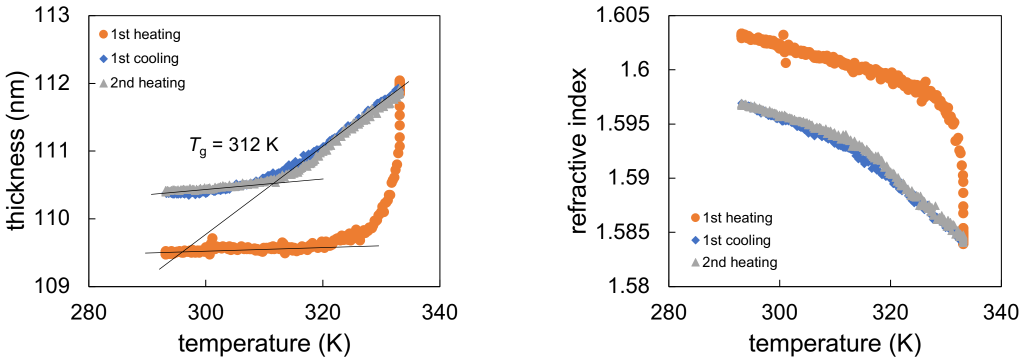

(a) Thickness plot.

(b) Refractive index plot.

Figure 5.28: Thickness and refractive index change with respect to temperature of a PS film deposited at $T_{\text{sub}} = 294$ K.

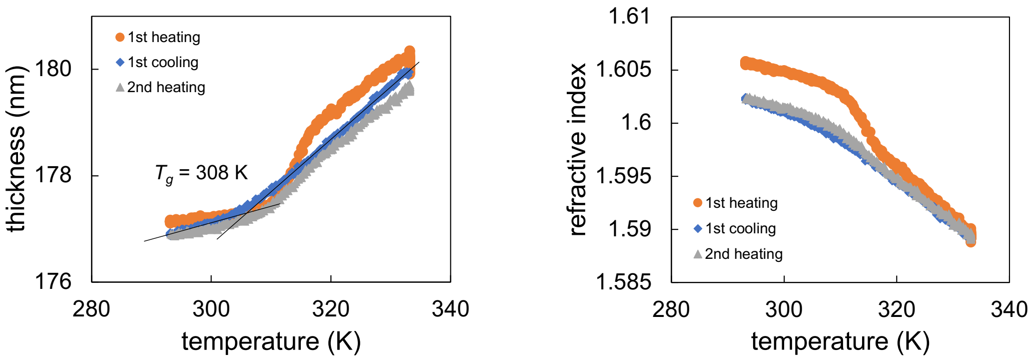

(a) Thickness plot.

(b) Refractive index plot.

Figure 5.29: Thickness and refractive index change with respect to temperature of a PS film deposited at $T_{\text{sub}} = 270$ K.

5.1.7 Using surface bumps to probe surface dynamics

Fig. 5.27 shows that the surface bumps reduce in height as time goes on. This could be a convenient probe to characterize the surface dynamics of vapour-deposited glasses. There have been many studies on surface dynamics of glasses using different methods, among which introducing external probes is a common one. In a study of surface dynamics of PS glasses [16], gold nanoparticles were partially embedded onto the film surface before removal to leave nanoholes on the surface. By monitoring the change in hole depths as a

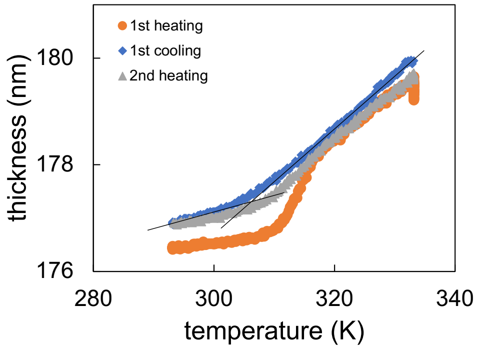

Figure 5.30: Thickness change of the sample in Fig. 5.29, with the first heating curve shifted.

function of time, the surface relaxation time was extracted and investigated as a function of temperature. Ref. [208] studied the surface mobility of PS glass by forming wetting ridges upon the introduction of ionic liquid droplets. In the studies of *N,N'*-bis(3-methylphenyl)-*N,N'*-diphenylbenzidine (TPD) glass surface [124, 125, 126], tobacco mosaic virus was introduced on the surface and the width of material accumulation was measured around the virus, from which the surface diffusion coefficient was extracted. In addition to external probes, sometimes the natural surface structure can be conveniently taken advantage of in quantifying the surface dynamics. For instance, Siretanu *et al* [209] created ion-induced polymer nanostructuration on the surface of PS glasses, and measured quantities about the induced bumps including height and volume in characterizing the surface properties.

In the current study, natural bumps are formed on the surface of vapour-deposited PS glasses. With the precedence of utilizing in-situ bumps in Ref. [209], it was realized that similar experiments could be performed to quantify the surface dynamics. Despite the fact that there have been extensive studies on the surface of glassy PS [116, 133], less is known about the surface of vapour-deposited PS or that of any polymers.

The PS sample used in this experiment was deposited at $T_{\text{sub}} = 275$ K, with a T_{g} of 309 K. After deposition, the film stays at room temperature under the AFM, and the same area is imaged during an extended period of time to observe the evolution of the surface bumps. Fig. 5.31 shows the same area at different times, where it is evident that the bumps grow in diameter and experience a reduction in height.

Since there is a distribution of the height and the diameter of bumps, only one of the bumps was chosen in the measurement of height as a function of time. As shown in Fig. 5.32, its height evolution is recorded with respect to time. Height was measured from

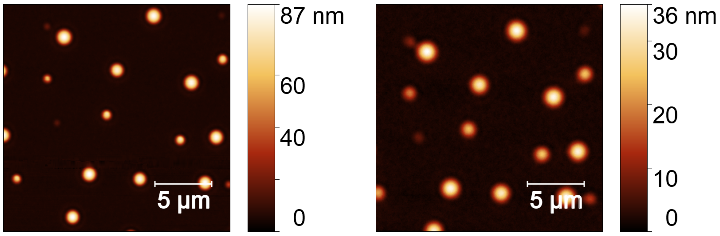

(a) 4 hours. (b) 10.5 hours.

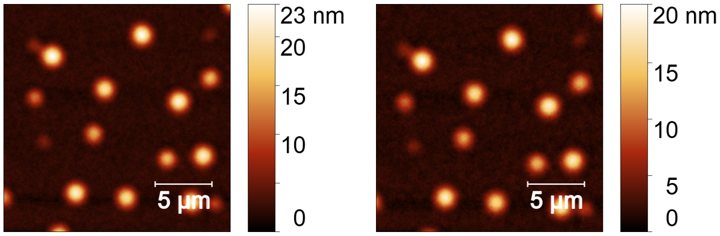

(c) 24.5 hours. (d) 32.5 hours.

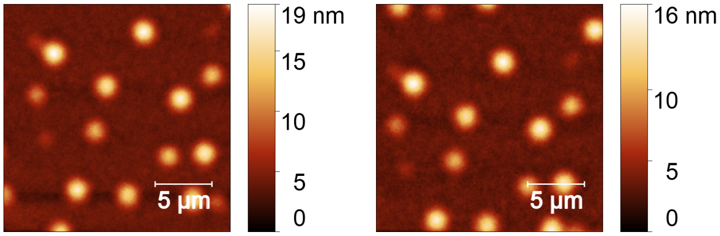

(e) 48.5 hours. (f) 69 hours.

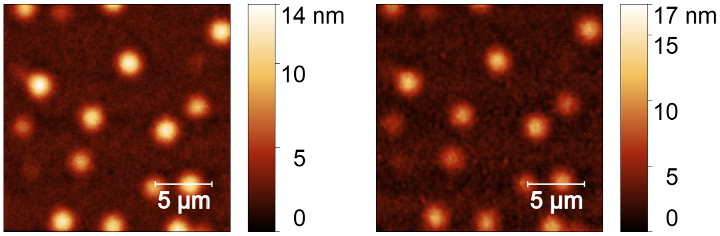

(g) 93.5 hours. (h) 144 hours.

Figure 5.31: AFM images at different times on a PS film deposited at $T_{\mathrm{sub}} = 275$ K, with a T_{g} of 309 K.

two sets of AFM images around the same bump, where one set used a scan area of 20 μm × 20 μm and the other used a scan area of 80 μm × 80 μm. It is to ensure that the scan size does not affect the measured height, and the agreement between the two sets of data show that they are consistent.

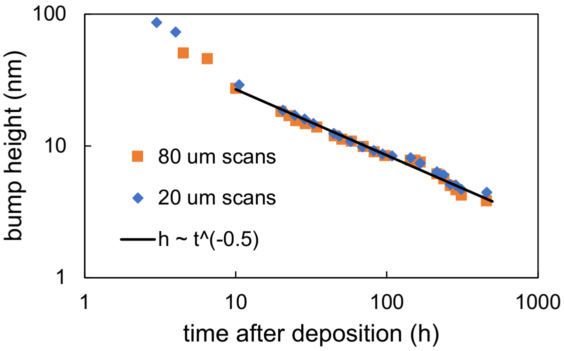

Figure 5.32: Bump height as a function of time on the film surface shown in Fig. 5.31.

From the log-log scale plot, a linear trend is observed, which indicates a power-law relationship between height and time. It is worth noting that in fitting the power law, the first few data points are excluded. This is because immediately after the deposition, the film stayed in the vacuum chamber to slowly recover from the low T_{sub} to room temperature, in order to prevent water condensation on the surface when exposed to air. Therefore in the first few hours after deposition, the treatment temperature was not controlled and thus only data in the later stage is used in the fitting. The scattering in data can also to some extent be explained by the non-steady room temperature, with possible fluctuations of a few degrees throughout the measurement.

One of the most significant findings from this experiment is the enhanced surface dynamics compared to its bulk counterpart. The material has a measured T_{g} of 309 K, which implies that at room temperature, the bulk part of the film is in the glassy state. However, the decrease in the bump height shows that the surface is mobile and flows relatively quickly. Assuming the fictive temperature T_{f} of the film is the same as T_{sub}, the bulk relaxation time can be estimated to be $\sim$ 3 years according to Ref. [1]. Based on Fig. 5.32, the relaxation time of the surface is merely a few days rather than years, which is a direct evidence of the enhanced surface mobility on vapour-deposited PS glass with an in-situ probe.

The same films have also been characterized by ellipsometry to further investigate the effect of bumps on ellipsometry measurement results. Fig. 5.33 and Fig. 5.34 show results obtained 1 day and 19 days after deposition, respectively. Both sets of data show the apparent "thicker and denser" material on the first heating curve, which is consistent with previous observation that surface bumps result in abnormal first heating. From the upper panel of Fig. 5.33 it can be seen that the slope of the first heating curve decreases towards the high temperature end, which can be explained by possible sublimation/evaporation of the film. After 19 days of aging, the first heating curve in Fig. 5.34 appears to be more normal and the liquid parts on all three curves are more parallel. With the change in the ellipsometry results after days of aging, it is natural to ask the question of whether the change is related to the surface relaxation, and more specifically, the evolution of bumps.

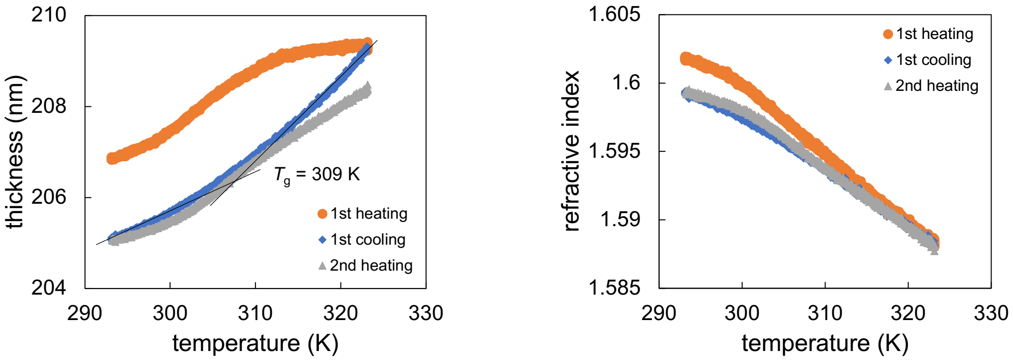

(a) Thickness plot.

(b) Refractive index plot.

Figure 5.33: Thickness and refractive index change with respect to temperature of the sample shown in Fig. 5.31, measured 1 day after deposition.

Assuming a spherical shape for the surface bump, its surface area is $S = \pi(h^2 + r^2)$, where h is the bump height and r is the radius of the base of the cap. The excess surface area compared to a flat surface can also be calculated as $S_{\text{exc}} = \pi(h^2 + r^2) - \pi r^2 = \pi h^2$. Fig. 5.35 shows the change of the excess surface area as a function of time as the bump evolves.

In 19 days, S_{exc} reduces by more than 10 times. If the hypothesis of sublimation or evaporation during first heating is true, a higher surface area will lead to faster sublimation/evaporation, and the slope of the first heating curve will be altered to a larger extent near the high temperature end. When the surface relaxes more and the surface area becomes smaller, it will lead to slower sublimation/evaporation, and the slope of the first heating curve will be less altered near the high temperature end and become more parallel to the normal liquid line.

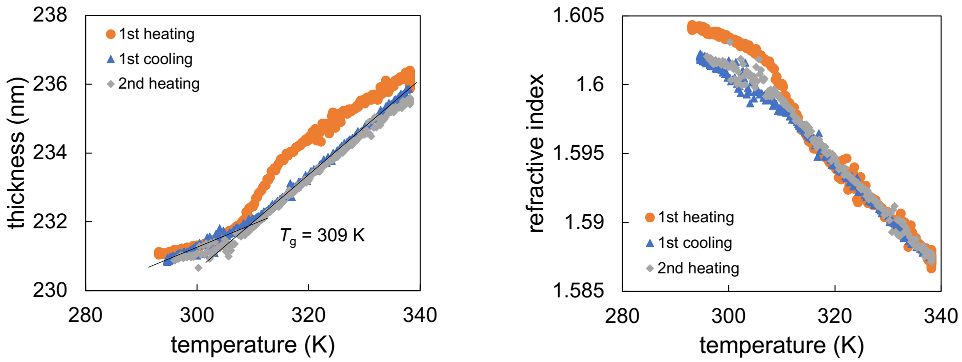

(a) Thickness plot. (b) Refractive index plot.

Figure 5.34: Thickness and refractive index change with respect to temperature of the sample shown in Fig. 5.31, measured 19 day after deposition.

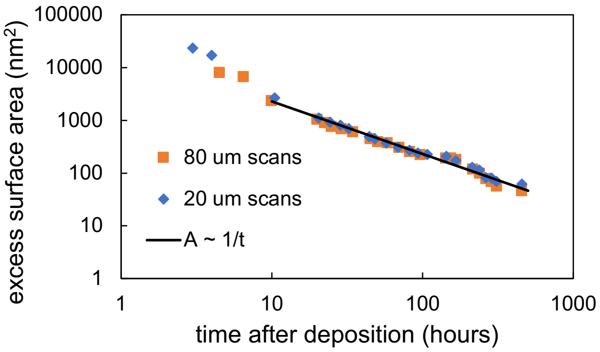

Figure 5.35: Excess surface area as a function of time of a bump on the sample shown in Fig. 5.31.

The same shifting of the first heating curve as in Fig. 5.30 can be done to the thickness plot of the measurement after 19 days (upper panel in Fig. 5.34). The result is shown in Fig. 5.36. After the shifting to account for sublimation/evaporation, it appears to be a marginally stable glass with the normally expected higher density of the as-deposited glass.

The same outcome from Fig. 5.30 and Fig. 5.36 reinforces the hypothesis that sublimation of evaporation of some material happens during the first heating. Some reasonable guesses include pump oil or polymers with small N values. In the beginning of the chapter it was noted that a test experiment was conducted where pump oil was ruled out as the cause. The explanation with small N impurities is a very reasonable one given the observa-

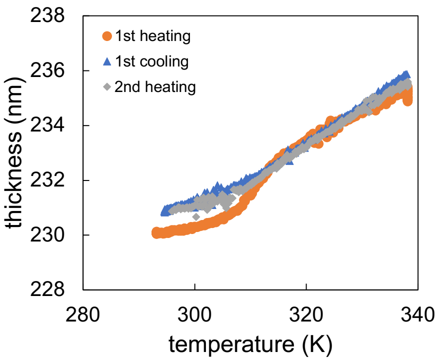

Figure 5.36: Thickness change of the sample in Fig. 5.34, with the first heating curve shifted.

tions from the first heating. During heating, since smaller N's have higher vapour pressure, they can partially evaporate at high temperatures while the main system still stays in the liquid state. Smaller N's also have lower glass transition temperatures, which can also explain the lower onset temperature of the rejuvenation on the first heating (Fig. 5.36). During following cooling and heating runs, the fraction of small N's in the system is less due to evaporation, and the thickness changes behave more as expected, with normal slopes and T_g's.

As depositions go on, the source material in the deposition crucible continues to have higher and higher average N's, since vapour pressure is an increasing function of N and smaller N's are driven off first. In a number of initial depositions, small N's are expected to be present in the deposited film. The fact that films prepared after many depositions of the original source material continue to show the sublimation/evaporation issue suggests that the small N's could come from other parts of the chamber rather than the deposition source.

With this assumption, a thorough cleaning of the chamber including all chamber walls and skeletons was performed. When new depositions were carried out, bumps no longer appear on the surface and the ellipsometry measurements appeared normal. Now we believe that a plausible explanation has been found for the abnormal surface structures related to the evaporation on heating. As depositions continue in the chamber, polymers deposit on the substrate as well as on the walls. As small N's accumulate, there is possibility that they re-deposit on the substrate in future depositions when there is heat, and cause undesirable morphology on the film surface and evaporation when the films are brought to higher temperatures. Referring back to Fig. 5.22 and Fig. 5.23, the growth of films suggests that the small N polymers are deposited first and dewet on the substrate, and then higher N's arrive and form continuous films.

5.1.8 Conclusion

In this section we study the surface morphology of vapour deposited PS glasses. Abnormal morphology features are present on some of the film and they vary with the type of the substrate, sample preparation procedure and temperature. Among the different feature we choose the bumps and study their growth and evolution, and use them to probe the surface dynamics as they evolve with time. In the end the bumps are found to be due to small N impurities accumulated in the deposition chamber and are undesired artifacts on the surface. On the one hand, this study loses value in terms of the goal of probing surface dynamics of vapour-deposited PS glasses. On the other hand, this is an achievement worth celebrating. The mysterious ellipsometry results and the peculiar structures on the surface have been puzzling in understanding the vapour-deposited glasses. With a plausible explanation to the abnormal behaviours and with the ability to produce unstructured and non-evaporating films, the overall exploration of vapour-deposited stable polymer glass can continue. Moreover, the experience and skills gained from this study directly benefited the study in Section 5.2 where the surface relaxation is examined in a similar way using gold nanoparticles as external probes.

5.2 Surface and bulk relaxation of vapour-deposited polystyrene glasses

This section is reproduced from the following paper with the permission of AIP Publishing:

J. Yin, C. Pedersen, M. F. Thees, A. Carlson, T. Salez, & J. A. Forrest. Surface and bulk relaxation of vapor-deposited polystyrene glasses. *The Journal of Chemical Physics*, 158(9), 094901 (2023). DOI: 10.1063/5.0133668 [2].

In this paper we have performed an experimental and theoretical study on the surface and bulk relaxation of vapour deposited PS glasses. As the first author, I was primarily responsible for the experimental part including the sample preparation, all characterizations as well as data analysis. I created all of the figures with the experimental data I collected as well as data from the numerical solutions obtained by my co-author Pedersen. I was also responsible for writing and editing the main paper and the supplementary material, as well as answering reviewer comments.

5.2.1 Abstract

We have studied the liquid-like response of the surface of vapour-deposited glassy films of polystyrene to the introduction of gold nanoparticles on the surface. The build-up of polymer material was measured as a function of time and temperature for both as-deposited films, as well as films that have been rejuvenated to become normal glasses cooled from the equilibrium liquid. The temporal evolution of the surface profile is well described by the characteristic power law of capillary-driven surface flows. In all cases, the surface evolution of the as-deposited films and the rejuvenated films are enhanced compared to bulk and are not easily distinguishable from each other. The temperature dependence of the measured relaxation times determined from the surface evolution is found to be quantitatively comparable to similar studies for high molecular weight spincast polystyrene. Comparisons to numerical solutions of the glassy thin film equation provide quantitative estimates of the surface mobility. For temperatures sufficiently close to the glass-transition temperature, particle embedding is also measured and used as a probe of bulk dynamics, and in particular bulk viscosity.

5.2.2 Introduction

The surface dynamics of glasses is a key area of study in condensed matter and materials physics [133]. In particular, it has become increasingly evident that the first few nanometers of a glassy material can exhibit properties vastly different from the bulk of the glass. In addition to its key role in the ability to form what have been called ultrastable glasses [135], the surface mobility is widely believed to be the key underlying factor in the 25 year long study of reduced glass transition temperatures T_{g} in thin polymer films [12, 17, 116, 210].

Since their discovery 15 years ago [136], kinetically stable glasses produced by vapour deposition have been extensively studied. While most studies have involved molecular glasses, more recent studies have included metallic [153], as well as polymeric glasses [1]. Collectively, these materials have strong similarities to glasses aged to near equilibrium. Many vapour deposited materials have been shown to have lower entropy and be lower in the energy landscape than glasses formed by cooling from the equilibrium supercooled liquid [137, 211, 212]. In fact, recent studies on vapour-deposited polymer glasses have suggested a similarity to materials aged for as much as 10^{13} s [1]. These unique properties are proposed to result from both the enhanced mobility of glassy surfaces, and the layer-by-layer formation associated with the method of vapour deposition [135]. While it might be expected that as-deposited stable films and rejuvenated glassy films both have enhanced surface mobilities, it is not *a priori* obvious if these are identical or not, in terms of either magnitude or temperature dependencies.

Surface mobility in glasses can be measured by the surface response to an external perturbation. In the past few decades, several forms of perturbations have been employed to characterize surface dynamics. A seminal method is provided by gold nanoparticles, in terms of both their embedding into the near-surface region [13, 117, 118], as well as surface flow around the nanoparticles [121, 122]. The response of a polymer surface to the introduction of a gold nanoparticle has been observed directly using transmission electron microscopy [119], and is similar to that observed for molecular glasses in Ref. [121]. Mainly, material was observed to accumulate towards the vicinity of the nanoparticle, before embedding of the latter eventually occurred. External surface perturbations can also be of the form of an initial surface morphology such as a nanohole [16], or a nanostep [18]. More recently, Zhang *et al* [124, 125, 126] have demonstrated that decorating the surface with tobacco mosaic virus (TMV) provides an alternative strategy. Another method to probe the surface mobility of glasses is to use nanobubbles that spontaneously nucleate on the glass surface when submerged into water [213]. An advantage of the nanosteps, the TMV decoration, and the nanobubbles is that these provide perturbations where the response of the surface can be described using a two-dimensional surface-flow equation.

Recently, a quantitative study of surface mobility in stable glasses was performed for *N,N'*-bis(3-methylphenyl)-*N,N'*-diphenylbenzidine (TPD) ($T_\mathrm{g} = 330$ K) [126]. In that work, the evolution of the surface of the glass in response to the presence of a TMV on the surface was measured. The measurements were performed on samples with a wide range (from 296 K to 330 K) of fictive temperatures T_f characterizing the stability of the glass, and at two measurement temperatures of 296 K and 303 K. The surface diffusion constant was found to be independent of the stability of the glass as well as the origin of that stability (*i.e.* aging from liquid cooled glass versus vapour deposition). While there were certainly differences in the surface mobility at the two temperatures considered, a more complete temperature dependence was not measured. In addition, the bulk dynamics were not measured but rather inferred from the Vogel-Fulcher-Tammann (VFT) time-temperature superposition, with parameters determined over a temperature region different from the window of T_f studied.

In a separate study [121], the evolution of the surface of a rejuvenated 1,3-bis-(1-naphthyl)-5-(2-naphthyl)benzene (TNB, T_g = 347 K) glass in response to gold nanoparticles placed on the surface was used to directly compare the temperature dependencies of surface and bulk relaxation processes in a molecular glass former. Surface flow exhibited a weak temperature dependence in that case, compared to bulk flow as characterized through embedding. Perhaps as expected, the temperature dependence of the time scale of nanoparticle embedding was well described there by bulk VFT parameters.

The surface mobility in glassy polystyrene (PS) has been studied extensively [116, 133] compared to most other glassy materials. The much larger molecular size of PS compared to the molecules used in Ref. [126] reopens the question as to whether liquid-cooled versus stable as-deposited glasses have the same surface properties, or not. In addition, there is an extension of the question to whether any form of stable PS glass is the same as the PS liquid-cooled glass, and how either of these compare to glassy PS films made from spin casting – such as the relatively high M_{w} samples of Ref. [16], and the low M_{w} samples of Ref. [18].

5.2.3 Experimental methods

The original material is a broad distribution polystyrene ($M_{\mathrm{w}} = 1200$ g/mol, catalogue no. 1024 from Scientific Polymer Products). The molecular weight distribution of the as-purchased material has been characterized in Ref. [1]. The material was first thermally distilled at increasing temperatures into more monodisperse fractions in a vacuum chamber using a technique reported previously [159]. The distilled product from 538 K was subsequently used as source material for the physical vapour deposition. Deposition was carried out in a Korvus Technologies HEX deposition unit with a base pressure of 10^{-5} mbar and a deposition rate of 0.05 nm/s [1]. The source material was heated in an ORCA temperature-controlled organic materials evaporation source. The source temperature used in generating the sample in this study was 514 K. The silicon substrate was attached to the sample stage which was cooled to a constant temperature of 283 K by a Peltier cooler. Ellipsometry measurements were performed with a J.A. Woollam M-2000 spectroscopic ellipsometer with a Linkam temperature-controlled stage. Heating and cooling rates for ellipsometric measurements were 10 K/min. The deposited film has a T_{g} of 318 K and has a thickness of $\sim$ 100 nm as measured with ellipsometry, with a slight thickness gradient across the substrate. The average degree of polymerization ($\bar{N}$) of the sample is 9.02 and the polydispersity index (PDI) is 1.002, as determined with a Bruker Autoflex Speed MALDI-TOF (Matrix Assisted Laser Desorption/Ionization Time of Flight) mass spectrometer. Note that in using the term “polymer” in this study, it is not the molecular weight that distinguishes the material here from small molecules. Although they have comparable molecular weights, the key difference is that molecular glasses produced in every deposition are the same material, whereas our N-mers even from successive depositions are slightly different materials with slightly different physical properties including T_{g}. While this can introduce difficulties in controlling and comparing the properties of different depositions, it also introduces an extra degree of tunability typical of polymers.

Aqueous solutions of gold nanoparticles with diameter ~ 20 nm were produced by the standard citrate reduction technique [214]. For as-deposited films, the gold nanoparticle solution was directly dropped onto the surface, and after 1-2 min the film was tilted to allow the droplet to flow to the side of the Si wafer and onto a wipe for removal. To study rejuvenated glasses, the as-deposited films were heated to 343 K ($T_{\mathrm{g}} + 25$ K) for 3 min and cooled in ambient air to room temperature before introducing the nanoparticles on the surface. This thermal treatment was found to be sufficient to produce ordinary liquid-cooled glasses. The nanoparticles on the glassy PS surface were imaged using a JPK Nanowizard 3 atomic force microscope (AFM) operating in tapping mode. The surface coverage density was ~ 5 particles/100 $\mu\mathrm{m}^2$ based on AFM measurements. For each film studied at a specific temperature, two nanoparticles were chosen that had at least 500 nm separation from any other nanoparticle (to minimize effects from more than one particle). Once a pair of such particles were located, the AFM hot stage (JPK High Temperature Heating Stage) was set to a certain temperature, and 2 μm × 2 μm regions centered on each nanoparticle were scanned at different times.

5.2.4 Theoretical modelling

We consider a flat glassy polymer film of thickness h_∞ placed on the surface of a horizontal and flat rigid substrate located at vertical coordinate $z = 0$. A nanoparticle of radius R is placed on the surface of the film. We assume a favourable wetting condition and the presence of a liquid-like mobile layer of thickness h^* (with $h^* \ll h_\infty$) at the free surface of the glass. The system then evolves through a three-step process [119]: i) at short time, some surface polymeric material rapidly migrates and fully coats the immobile particle; ii) then, the glass-air interface evolves by surface flow across the still-immobile particle; iii) at long times, the particle eventually embeds in the film, under the action of the capillary pressure. In this last step, the dynamics is limited by the bulk viscous Stokes-like drag acting on the particle. Fig. 5.37 provides a schematic of the processes involved for surface flow and eventual embedding.

We focus only on the second step for now, as it is well separated in time from the two other steps. By considering the very large viscosity of the bulk glass, and that there is only a thin film of flowing material, the interface dynamics can be described by adopting the lubrication theory [215, 216]. The flow is assumed to be incompressible and axisymmetric. Since the flow is localized only near the free surface, the particle can be modelled as an effective substrate, described by its profile $s(r) = \Theta(R - r)[h_\infty + R + \sqrt{R^2 - r^2}]$, with r the radial coordinate and where Θ is the Heaviside function. The glass-air interface profile is defined as $h_{\mathrm{tot}}(r,t) = h(r,t) + s(r)$, where $h(r,t)$ is the glass thickness profile. We define

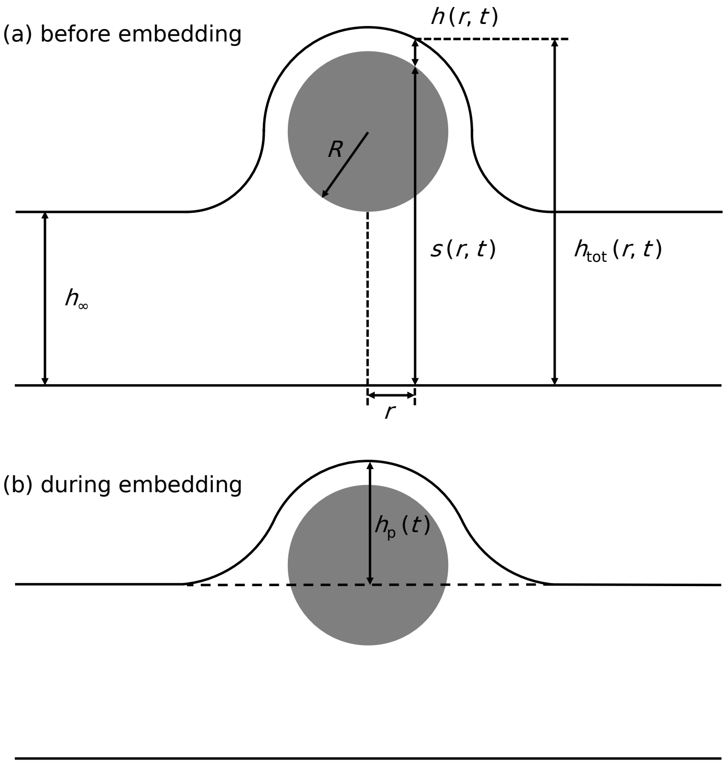

Figure 5.37: Schematic diagram of the relevant processes discussed in the text. Variables used in the calculations and discussed throughout the text are shown in the schematic.

the initial profile $h_{\mathrm{tot}}(r,0)$, from the earliest experimental data available. At time $t=0$, we assume the particle to be already covered by a nanometric layer of polymeric material.

The hydrodynamic flow is described by the pressure field $p(r,z,t)$, in excess to the atmospheric pressure, and the velocity field $\mathbf{v}(r,z,t)$. The material parameters are the polymer-air surface tension γ, and the viscosity of the surface layer η, both assumed to be constant at a given temperature. At the free surface, we impose no shear, *i.e.* $\partial_z(\mathbf{v}\cdot\mathbf{e}_r)|_{z=h_{\mathrm{tot}}}=0$, where $\partial_i\equiv\partial/\partial i$, and $\mathbf{e}_r$ is the unit vector in the radial direction. We also impose no slip at the bottom of the mobile layer, *i.e.* $\mathbf{v}\cdot\mathbf{e}_r|_{z=h_{\mathrm{tot}}-h^*}=0$.

Within the lubrication theory introduced above, the flow is mainly horizontal, *i.e.* $\mathbf{v}=v\,\mathbf{e}_r$. Invoking the Stokes equation, the pressure p is thus invariant in the vertical direction, and by integration the velocity profile in the radial direction is found to be:

$$v(r,z,t)=\frac{1}{2\eta}\left(z^2+h_{\mathrm{tot}}^2-h^{*2}-2zh_{\mathrm{tot}}\right)\partial_r p\ , \tag{5.1}$$

which corresponds to the familiar Poiseuille flow for $h_{\mathrm{tot}}-h^*\leq z\leq h_{\mathrm{tot}}$. For $0\leq z<h_{\mathrm{tot}}-h^*$, we assume zero velocity, since the bulk glass is immobile to lowest order in the description. Furthermore, volume conservation requires that:

$$\partial_t h(r,t)+\frac{1}{r}\partial_r\left(r\int_{h_{\mathrm{tot}}-h^*}^{h_{\mathrm{tot}}}\mathrm{d}z\,v(r,z,t)\right)=0\ . \tag{5.2}$$

The excess pressure $p(r,t)$ can be evaluated at the free interface, and contains two terms: a capillary contribution from the Young-Laplace equation, and an ad-hoc repulsive disjoining contribution [217, 218] ensuring the wettability condition and thus preventing film rupture at the particle tip. All together, and in the limit of small interface slopes, one gets:

$$p(r,t)=-\gamma r^{-1}\partial_r(r\partial_r h_{\mathrm{tot}})+B(h_{\mathrm{eq}}/h(r,t))^9\ , \tag{5.3}$$

where B sets the magnitude of the disjoining pressure, and h_{eq} is the equilibrium film height. As the early time curvature close to the particle can be large, which is not accounted for in this linearized model, we have performed a numerical experiment where we also include the non-linear curvature term in the Laplace pressure. However, the numerical experiment demonstrated that the results reported below were not affected by neglecting this term. For further details regarding the full non-linear curvature model and its numerical routine we refer the reader to [219]. By combining the equations above, we derive the Glassy Thin

Film Equation *atop a Nanoparticle* (GTFEN):

$$\partial_t h(r,t) + \frac{\gamma h^{*3}}{3\eta r}\partial_r \left\{ r\partial_r \left(r^{-1}\partial_r \left[r\partial_r h(r,t) + r\partial_r s(r) \right] - Bh_{\mathrm{eq}}^9/[\gamma h(r,t)^9] \right) \right\} = 0 \ . \qquad (5.4)$$

Written this way, we see that the nanoparticle, through the effective substrate profile $s(r)$ and the disjoining pressure, generates a forcing source within the free Glassy Thin Film Equation (GTFE) [18].

In contrast to simpler and linear versions of GTFE [219, 220], the complex effective substrate and the nonlinear disjoining term in GTFEN require us to perform a numerical integration. We thus introduce dimensionless variables, through: $X = r/R$, $\mathcal{T} = t\gamma h^{*3}/(3\eta R^4)$, $S(X) = s(r)/R$, $H(X,\mathcal{T}) = h(r,t)/R$ and $P(X,\mathcal{T}) = Rp(r,t)/\gamma$. We also fix the two dimensionless parameters of the problem, as follows: i) the aspect ratio h_∞/R is directly estimated from the experimental h_∞ and R values, for each given sample, which in turn fully determines $S(X)$; ii) the dimensionless disjoining magnitude is arbitrarily fixed to $Bh_{\mathrm{eq}}^9/(\gamma R^8) = 10^{-9}$, which for physical parameters relevant to PS on gold in air corresponds to a nanometric h_{eq}. Note however that the late-time interface dynamics is insensitive to small variations around the chosen disjoining magnitude. The dimensionless form of Eq. (5.4) is solved numerically by using a finite-element scheme. The initial condition $H(X,0) = h_{\mathrm{tot}}(R\cdot X,0)/R - S(X)$ is directly constructed from the experimental free surface profile $h_{\mathrm{tot}}(r,0)$ measured at $t=0$. At all times $\mathcal{T} > 0$, we also impose four boundary conditions, namely the vanishing of both $\partial_X H$ and $\partial_X P$, at both $X=0$ and $X \to \infty$ (*i.e.* the far-field bound of the numerical spatial domain).

From fitting the obtained numerical profiles to the experimental ones, and invoking the PS-air surface tension $\gamma \approx 40$ mN/m, we can thus now measure the surface mobility $M = h^{*3}/(3\eta)$ as a single free parameter, for each given sample type and temperature.

5.2.5 Results

Fig. 5.38 shows the ellipsometrically determined film thickness versus temperature T, for an as-deposited supported PS film without nanoparticles. The data in these scans are used to determine the fictive temperature $T_{\mathrm{f}} = 298$ K, as well as the glass transition temperature $T_{\mathrm{g}} = 318$ K. Comparing the thickness of the as-deposited sample versus the one after a full heat/cool cycle is used to determine the increased density of the stable glass. In this case the increase in density of stable glass versus normal glass is $\sim 1\%$. The data also demonstrates enhanced kinetic stability since the material apparently remains in the glassy state even after the temperature has been raised above T_{g}. By comparing

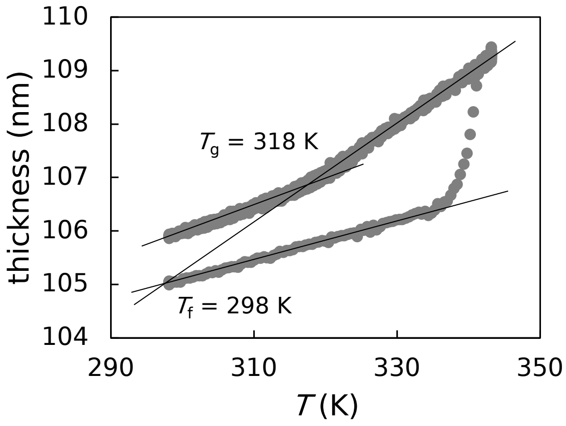

Figure 5.38: Total film thickness versus temperature obtained from ellipsometric scans of the as-deposited samples. The heating (bottom) and subsequent cooling (top) branches are performed with equal rates of 10 K/min. On the first heating the film is held at the highest temperature (343 K) for 2.5 min to ensure full rejuvenation from the stable glass to the normal supercooled liquid, before cooling in the supercooled liquid state and down to the rejuvenated glass. These scans are used to determine the fictive temperature T_f, defined from the intersection between the stable glass and supercooled liquid lines, as well as the glass transition temperature T_g, defined from the intersection between the supercooled liquid and rejuvenated glass lines.

the T_f and T_g with the ones in Ref. [1], we can estimate that the as-deposited material in the present study is analogous to a liquid-cooled glass that would have been aged at T_f for $\sim$ 300 years. It is worth noting that this estimate is based on an Arrhenius law, while using the more conventional VFT law would result in orders of magnitude larger estimates for aging times.

Now, we consider the surface response of the glassy films after nanoparticles have been placed on the surface. Fig. 5.39 shows AFM images of a 16 nm nanoparticle on a rejuvenated PS film at a temperature of 313 K, *i.e.* 5 K below T_g. In the $t = 0$ panel, we see a sharp image of the nanoparticle surrounded by an approximately circular dark region. The latter is a depletion zone where material has moved from in order to cover the nanoparticle. As the evolution progresses from 0 h to 10 h, we can see that there is a brighter area immediately surrounding the nanoparticle, and the depletion zone has moved outwards. By 50 h of evolution, in addition to a continual buildup of material, we can see that the apparent height of the nanoparticle is also decreasing. This indicates an

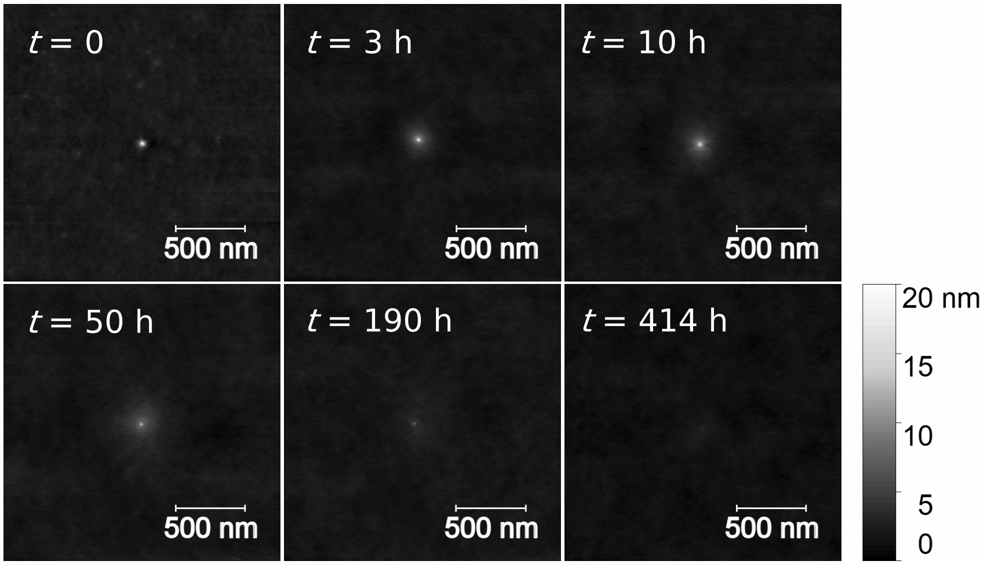

Figure 5.39: AFM images showing the build up and levelling of polymeric material around a gold nanoparticle, as well as the subsequent nanoparticle embedding, for a rejuvenated glassy polystyrene film at $T_\mathrm{g} - 5$ K (313 K).

embedding or engulfment of material which can only occur when there is sufficient bulk mobility (*i.e.* the material is above or very near its T_g). After 414 h of evolution, the nanoparticle has almost completely embedded into the underlying polymer.

Fig. 5.40 shows the radial profiles of the PS-air interface along time, for another nanoparticle but on the same sample and at the same temperature as the AFM images in Fig. 5.39. Each profile $h_\mathrm{tot}(r,t)$ was obtained by angularly averaging the image from the centre of the nanoparticle, and subtracting the base-line height. To determine the latter, a mask was applied to the AFM image, covering the nanoparticle and the depletion zone, and the average height of the 2 μm × 2 μm scan area excluding the mask area was measured. The dark solid line in Fig. 5.40(a) represents the profile at $t = 0$. In this initial profile, we can see a well defined depletion zone with a maximum depletion at about 70 nm from the centre of the nanoparticle. At larger times, there is more and more material accumulation near the nanoparticle, while the depletion zone becomes less pronounced and moves further out from the nanoparticle's vicinity. Note that the depletion zone was clearly evident in the AFM images in Fig. 5.39, and was also observed in the surface evolution of the TNB molecular glass in similar conditions [121]. From the data in Fig. 5.40, we can extract two parameters that characterize separately the near surface and bulk dynamics. For the bulk dynamics, the natural observable is the height $h_\mathrm{p}(t)$ of the nanoparticle. At

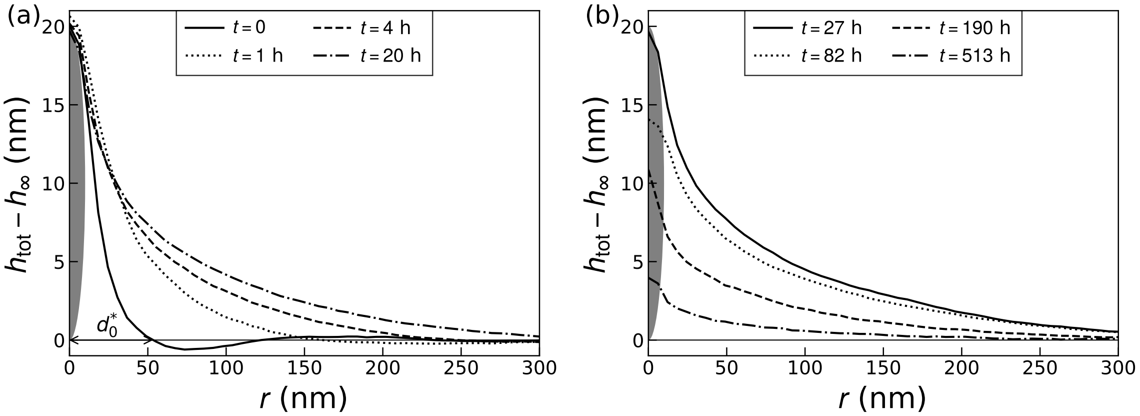

Figure 5.40: Surface profiles at various times as indicated in legend, of a rejuvenated film at $T_\mathrm{g} - 5$ K (313 K). (a) The short-term evolution before embedding occurs. (b) The long-term embedding process. The grey shaded areas indicate the shape of the spherical nanoparticle with a diameter of 20 nm, at $t = 0$. The solid horizontal line indicates the base line reference. d_0^* shown in (a) is the width $d^*(t)$ (defined in text) at $t = 0$.

temperatures near T_g, and for sufficiently long times (such as the ones in Fig. 5.40(b)), the bulk of the material has a large-enough mobility, so that the nanoparticle can embed, and h_p will evolve over time. For the surface dynamics, we define a typical horizontal width $d^*(t)$ of the profile as the minimal value of the radial coordinate r at which the height crosses zero (*i.e.* the base line).

Focusing first on the bulk dynamics, Fig. 5.41 shows the normalized particle height, h_p/h_0 as a function of time for both the as-deposited and rejuvenated films at $T = T_\mathrm{g}$. There are two notable differences between the embedding behaviours in the two systems. The most obvious difference is that, although particle embedding occurs in both the as-deposited and rejuvenated films at this temperature, the embedding occurs earlier in the rejuvenated film. This is true in all cases where embedding can be observed for both types of film. Embedding occurs in the as-deposited films at about an order of magnitude longer time than for the rejuvenated films, in all such cases. Another difference is the shape of the embedding curve. For the rejuvenated (*i.e.* normal glass) film, the exponential fit is an excellent characterization of the data, while for the as-deposited (*i.e.* stable glass) film, there is a significant deviation from an exponential behaviour. In fact, for the as-deposited film, the embedding is better characterized by an affine relation between the apparent height and $\log t$ for times larger than the embedding start time. Unlike the early build-up of material near the nanoparticle, which can occur through surface mobility only,

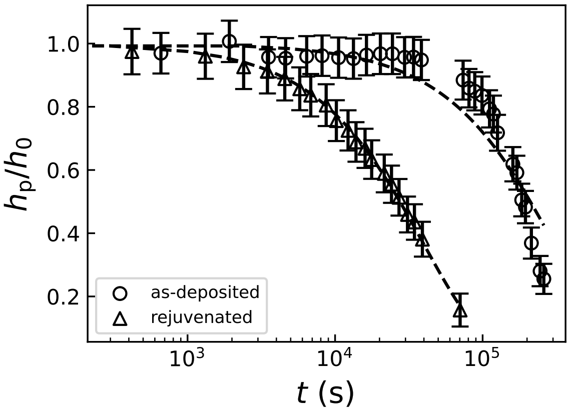

Figure 5.41: h_p/h_0 as a function of time t, in lin-log representation, where $h_0 \equiv h_\mathrm{p}(0)$ is the initial particle height, for both the as-deposited (circles) and rejuvenated (triangles) films, at T_g (318 K). The dashed lines are best exponential fits.

complete embedding requires a bulk response of the polymer. Therefore, the embedding dynamics of the rejuvenated sample would correspond to the bulk response of the material at $T_\mathrm{g} = 318$ K, while the embedding dynamics of the as-deposited sample would correspond to the bulk response of the material at $T_\mathrm{f} = 298$ K, by definition of the fictive temperature (see Fig. 5.38). Interestingly, with these temperatures, we would have expected the ratio between the two embedding times to be much greater (*i.e.* ~7 decades in time). We can rationalize the discrepancy between this expectation and the observation by comparing to the rejuvenation times from Ref. [1]. In that case, we can see that for $T_\mathrm{g}/T = 318$ K/318 K $= 1$, the rejuvenation time (*i.e.* the time for the material to fully convert from a stable glass to a normal supercooled liquid) is about 10^5 s. The latter value compares well with the embedding time of the as-deposited sample in Fig. 5.41. This coincidence suggests that the unexpectedly fast embedding in the as-deposited sample is due to the fact that the sample is actually rejuvenating during the measurements, and the nanoparticle is embedding into the rejuvenated material. This is also consistent with the peculiar shape of the embedding curve for the as-deposited sample, since an affine law is a typical functional form for a rejuvenation front travelling through the film.

Turning now to the the surface dynamics, Fig. 5.42 displays the normalized width d^*/d^*_0 as a function of time, for both the as-deposited and rejuvenated samples at $T_\mathrm{g} - 10$ K. It is clear from this figure that, both qualitatively and quantitatively, there is no discernible difference between the surface flows of as-deposited and rejuvenated glasses. Both types of glass exhibit a mobility enhancement at the surface as compared to the bulk – a feature that has been widely reported for many different glass formers [13, 16, 18, 127, 128, 213, 221]. Moreover, the surface mobilities of the two types of glass studied here are quantitatively the same, within our error bars. Similar plots (not shown) for the entire collection of data at 7 different temperatures indicate that, while there is certainly some scatter in the data, the enhanced surface flows of stable PS glasses and normal PS glasses do not exhibit any discernible difference. Furthermore, Fig. 5.42 indicates the existence of a power law between d^* and t. It has been shown previously [18], that, if the dynamics is governed by capillary-driven surface viscous flow, the associated power-law exponent should be equal to 1/4. The best fits in Fig. 5.42 give exponent values of 0.23 ± 0.02 for the as-deposited sample, and 0.24 ± 0.02 for the rejuvenated sample. Similar best fits (not shown) for the entire collection of data yield exponents in the $0.17 - 0.25$ range. Data at the highest temperatures (where the surface relaxation is more advanced) exhibit exponents closer to 1/4, as compared to data at lower temperatures. This is similar to the results in Ref. [222], where more-evolved profiles were comparatively better described by the expected asymptotic exponent. One might be concerned that the reason the surfaces of as-deposited and rejuvenated films are so similar is that the as-deposited films have at least partially rejuvenated. However, the data of Fig. 5.41 shows that for $T = 318$ K rejuvenation does not begin to occur until $t \sim 5 \times 10^4$ s. For lower temperatures, that onset will be at even greater times [1]. This comparison provides confidence that the surface evolution of as-deposited films is not being influenced by rejuvenation.

Fig. 5.43(a) shows surface profiles for an as-deposited film at $T_\mathrm{g} - 15$ K, for several times where embedding has not yet occurred. Previous works [18, 126] and the fact that we observe $d^* \propto t^{1/4}$ suggest that the data is self-similar, and that replacing r on the x-axis by $\frac{r}{t^{1/4}}$ should result in a collapse of all the curves. The inset of Fig. 5.43(a) shows that this is indeed the case. To go beyond scaling, and quantitatively check the validity of the developed GTFEN model based on capillary-driven surface viscous flow, we fit the experimental profiles by the numerical solutions of Eq. (5.4). The observed agreement between Fig. 5.43(a) and Fig. 5.43(b) confirms the validity of the GTFEN.

We now aim at quantifying the temperature dependencies of the bulk and surface processes. The relaxation time τ of the bulk is obtained from the best exponential fit $\exp(-t/\tau)$ of the $h_\mathrm{p}(t)/h_0$ data in Fig. 5.41. The relaxation time τ of the surface is empirically defined as the time needed for the width d^* to increase from d_0^* to $2d_0^*$ (see Fig. 5.42). We note that the choice of d^* is somewhat arbitrary. For example in [126], the width of the surface profile at a height of 2 nm was monitored. Fig. 5.44(a) displays the temperature dependencies of both these times, for both the as-deposited and rejuvenated samples. For bulk relaxation, despite the difference in magnitudes already discussed above,

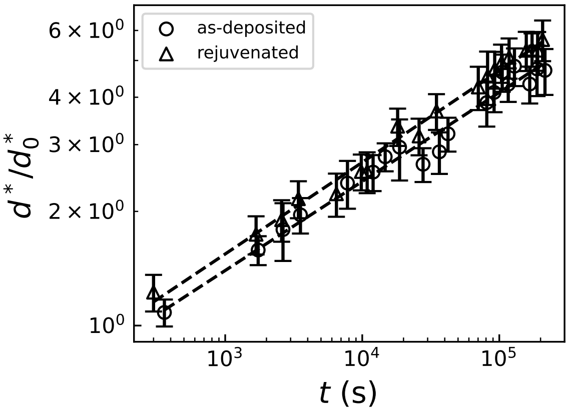

Figure 5.42: Normalized width as a function of time, in log-log representation, where $d_0^* \equiv d^*(0)$ is the initial width, for both the as-deposited (circles) and rejuvenated (triangles) samples, at $T_\mathrm{g} - 10$ K (308 K). The dashed lines are best power-law fits, with exponents 0.23 ± 0.02 (bottom) and 0.24 ± 0.02 (top).

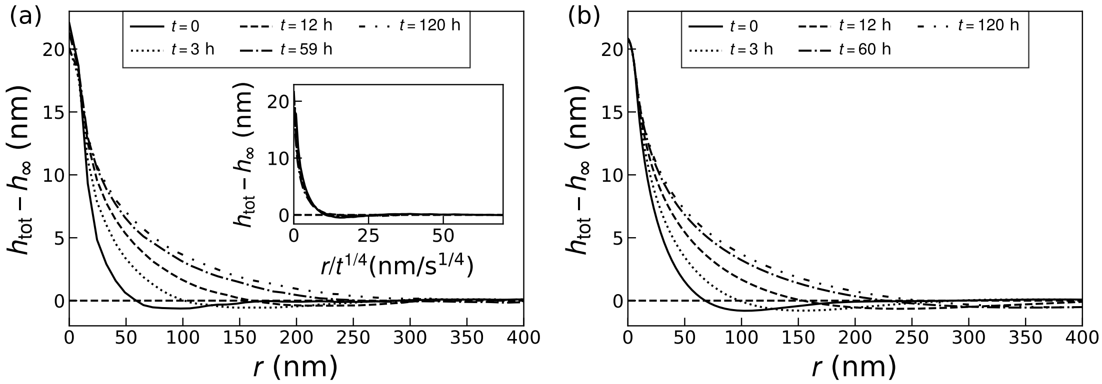

Figure 5.43: (a) Experimental surface profiles at various times as indicated in legend, of an as-deposited film at $T_\mathrm{g} - 15$ K (303 K). The horizontal dashed line indicates the base line reference. (Inset) Same data, but with the indicated rescaling of the x-axis. (b) Numerical solutions of Eq. (5.4) at various times, as indicated, using the experimental initial profile of panel (a) as an input and the surface mobility as a single fit parameter.

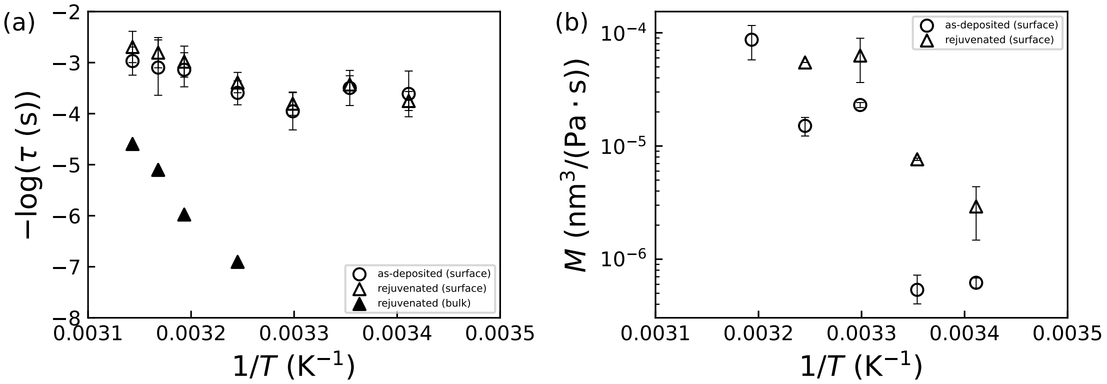

Figure 5.44: (a) Inverse relaxation time $1/\tau$ as a function of the inverse temperature $1/T$, in log-lin representation, as extracted from either the best fit to an exponential embedding law (bulk, see Fig. 5.40) or the width-doubling time (surface, see Fig. 5.42), for two types of samples, as indicated in legend. (b) Surface mobility M as a function of the inverse temperature $1/T$, in log-lin representation, as extracted from the best fit of the experimental surface profile to the numerical solution of Eq. (5.4) (see Fig. 5.43(b)), for the same two types of samples, as indicated in legend.

we observe that characteristic times derived from the as-deposited and rejuvenated data display very similar temperature dependencies. This might be expected, since the as-deposited sample is rejuvenating during the embedding (as discussed above). For surface relaxation times, one observes two qualitative differences with respect to the bulk trend. First, surface relaxation occurs on a much shorter time scale. Secondly, surface relaxation times have a much weaker temperature dependence than the bulk one, which even seems to vanish at low temperature. Nevertheless, the difference between the bulk and surface relaxation times decreases as the temperature is increased. Extrapolations of the bulk and surface trends even suggest that the two processes would have the same relaxation time for $T_{\mathrm{g}}/T = 0.98$. The behaviour exhibited in Fig. 5.44(a) is similar to that reported for spin-coated PS [16], as well as for vapour-deposited TNB [121].

In Fig. 5.44(b), we show the temperature dependence of the surface mobility M, as obtained from the best fits of the experimental surface profiles to the numerical solutions of Eq. (5.4) (see Fig. 5.43(b)). Here, one observes a continuous, Arrhenius-like decay of the mobility as the temperature is lowered, which is qualitatively similar to the behaviour reported for spin-coated PS [18]. However, the surface mobility values in Ref. [18] are comparatively smaller, and in some cases by even a few orders of magnitude. We can understand this observation by taking into account the M_{w} dependence of the mobility. Indeed, in Ref. [222], it was shown that for $T < T_{\mathrm{g}}$ the surface mobility can vary by as much as four orders of magnitude for a one order of magnitude change in M_{w}. It is difficult to be more quantitative, because the samples used in Ref. [222] were much more polydisperse than the samples considered in this work – due to the intrinsic mass-selective nature of vapour deposition – and it is not clear what the effect of polydispersity is on the mobility. We can compare these mobilities to the relaxation times from Fig. 5.44(a). Because the mobility values are given by $(h^*)^3/(3\eta)$ we would might expect that conclusions determined from the temperature dependence of the measured relaxation times would be the same as those arising from the mobility. Differences between Fig. 5.44(a) and Fig. 5.44(b) show that this is surprisingly not the case. They have been found to originate from the choice of d^* used in characterizing the surface relaxation time. A different choice of d^*, as discussed in detail in the Supplementary Information, can result in a different temperature dependence of τ. Since it is influenced by the choice of a local point, τ may not be as good a representation of the global relaxation as the mobility. The temperature dependence of the mobilities is the same within error for the as-deposited and rejuvenated films, but the magnitudes of the mobilities of the as-deposited materials are slightly lower than those of the rejuvenated materials.

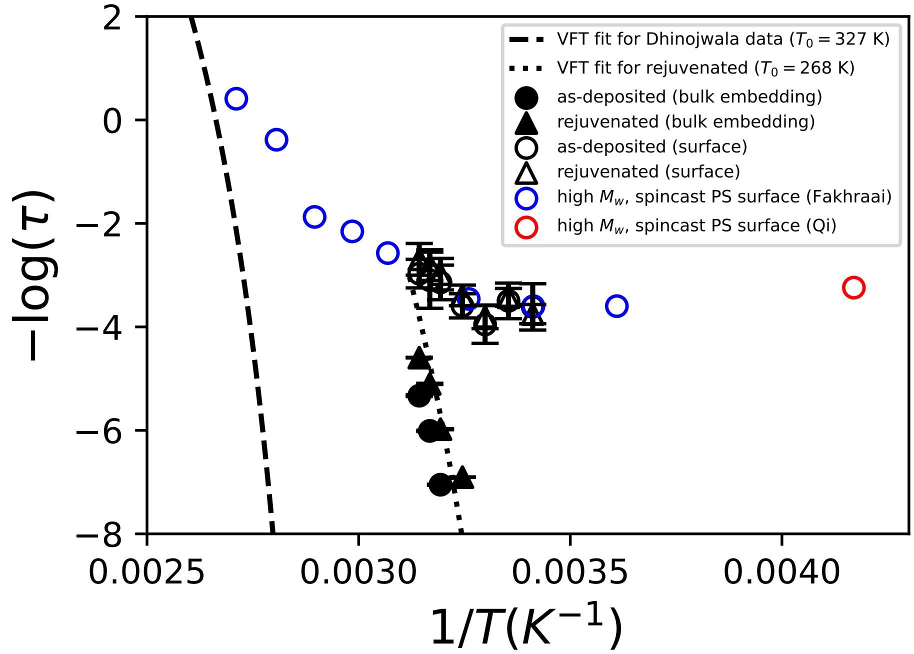

Figure 5.45: Inverse relaxation time $1/\tau$ as a function of the inverse temperature $1/T$, in log-lin representation, as extracted from either the best fit to an exponential embedding law (bulk, see Fig. 5.40) or the width-doubling time (surface, see Fig. 5.41), for two types of samples, as indicated in legend. For comparison, are also shown the high-M_w data of Ref. [16] and Ref. [26]. The dashed line represents the VFT behaviour of high-M_w bulk PS [14], while the dotted line represents the VFT behaviour of low-M_w bulk PS.

5.2.6 Discussion

The fact that the surfaces of the as-deposited and rejuvenated glasses have such similar dynamics is a significant observation. Indeed, it is not necessarily expected that the surface mobility of a material assembled using vapour deposition should be the same as the one of a sample prepared by cooling a liquid. A similar observation was first reported for molecular glasses [126], where the values of the surface diffusion constants for as-deposited, aged, and rejuvenated materials were found to be indistinguishable, for each of the two temperatures considered therein. Our work provides a complementary approach, where we have considered as-deposited and rejuvenated glasses at a number of different temperatures, allowing for the temperature dependencies to be investigated in details. Note that, in

Ref. [126], the T_f values ranged from 296 K to 330 K, while the T_g value was 330 K, which gives a range of $T_\mathrm{g} - T_\mathrm{f}$ of $0 - 34$ K. The T_g of the material in the current work is 318 K, and the T_f of the stable glass is 298 K, which gives $T_\mathrm{g} - T_\mathrm{f} = 20$ K. This is close to the middle of the range of Ref. [126], thus allowing for a reasonable comparison.

Additionally, glassy PS is a system whose surface has been extensively studied in the literature, for M_w values varying by about three orders of magnitude, encompassing oligomeric materials as well as highly entangled systems. We can therefore easily compare our low-M_w results to others. The temperature dependence of surface mobility observed here is similar to that of PS with $M_\mathrm{w} = 1.1$ kg/mol and $M_\mathrm{w} = 1.7$ kg/mol, measured by an entirely different experiment [19]. Two studies for high M_w reported in Refs. [16, 26] are also of particular relevance. In Fig. 5.45, we compare our data on the temperature dependencies of the bulk and surface relaxation times, to the ones from Refs. [16, 26]. Strikingly, for the surface data, there seems to be a universal change from an Arrhenius-like behaviour to an athermal one, as the temperature is decreased. From the Arrhenius-like region, we can estimate a typical activation barrier of $\sim 10^4$ K for both systems. The crossover seems to happen at $1/T \sim 3.25 \times 10^{-3}$ K^{-1}, independently of the T_g values of the materials (which differ by about 60 K). The actual relaxation times from the current study as well as [16, 26] agree with each other quantitatively, but this is likely coincidental as the probed physical phenomena were different in the two cases. Nevertheless, given that the materials studied in the current work are nearly oligomeric, since $M_\mathrm{w} < 1000$ and because it was prepared by vapour deposition, and given that the materials in Ref. [16] have a M_w value of 640,000 g/mol and were prepared by spincoating out of solvent, this apparent coincidence is truly remarkable. It may in fact indicate that the dynamical properties of the mobile surface layers on glassy films are somewhat universal for all PS materials.

The comparison made in the previous paragraph can be qualitatively extended to the measurements of surface mobility in ultrastable metallic glasses [153]. Indeed, the similarity between the temperature dependencies of the surface mobilities of PS, from the oligomeric materials used here and in the literature [18], to the large-M_w materials studied previously [222], and the temperature dependence of surface mobility in metallic glasses is striking too. As discussed above, it is interesting to note the absence of any saturation in the surface mobility at low temperature (see Fig. 5.44(b)), in contrast to the observation made for the surface relaxation time (see Figs. 5.44(a) and 5.45). This subtle apparent discrepancy may simply result from the difference in the considered physical observables, but it may also highlight deeper differences at low temperatures between the quantitative modelling and the simple empirical criterion (see the supplementary material).

Finally, the current work may have some relevance for the continuing discussion around the anomalous glass transition temperatures in thin polymer films. While it has been shown that the free-surface-induced alteration of a dynamical length scale can generate an enhanced surface mobility as compared to the bulk, as well as a T_{g} reduction [210, 223], there is a persistent debate around the possible importance of the non-equilibrium nature of glassy films made from spin-coated polymers [115]. The underlying idea is that such spin-coated PS films exhibit adsorbed layers with strongly out-of-equilibrium extended chain conformations, and that these layers can have a dominant effect on the measured T_{g}. Besides, a previous work [123] has shown that surface dynamics can be affected by the interactions and dynamics near the substrate, which, when combined to the non-equilibrium scenario above, would then imply that the free surfaces of freshly-cooled and near-equilibrium supported glassy films would show significant differences in their dynamics. However, the current work shows that the dynamical surface properties of freshly-cooled glasses are the same as the ones of vapour-deposited stable glasses – equivalent to materials aged for $\sim$ 300 years – and exhibit strong similarities to those of spin-coated high-M_{w} PS films.

In summary, we have made a detailed experimental and theoretical study of the bulk and surface dynamics of glassy polystyrene films produced by vapour deposition. In particular, we have compared the surface relaxation times and mobilities of as-deposited (i.e. stable) glasses to those of rejuvenated (i.e. fresh) glasses. In all cases, shorter surface relaxation times and larger surface mobilities were observed as compared to the bulk values, and the measured surface relaxation times were indistinguishable between the two types of samples. The temperature dependencies of these surface properties were also systematically measured over an extended temperature range, and were found to be mostly indistinguishable between as-deposited and rejuvenated glasses. Finally, strong similarities with the surface behaviours of high-M_{w} PS films prepared by spin-coating, were revealed.

5.2.7 Supplementary material

The supplementary material describes a detailed comparison of dynamics obtained by using an arbitrary (though reasonable) measure of surface evolution and those obtained by fitting the complete set of data to the numerical results of the evolution equation.

From Fig. 5.44 in the main manuscript, it is observed that the temperature dependence of the experimentally defined surface relaxation time τ appears to be different than that of the surface mobility obtained from the best fits to the numerical solutions of the GTFEN model. From high temperatures to above $1/T \sim 3.25 \times 10^{-3}$ K^{-1}, the relaxation time τ transforms from an Arrhenius behaviour to an athermal one, while the same saturation is absent in the surface mobility M. Similarly Fig. 5.44(a) in the main manuscript shows no differences between surface relaxation times of as-deposited and rejuvenated films whereas the mobility shows a small but clear difference.

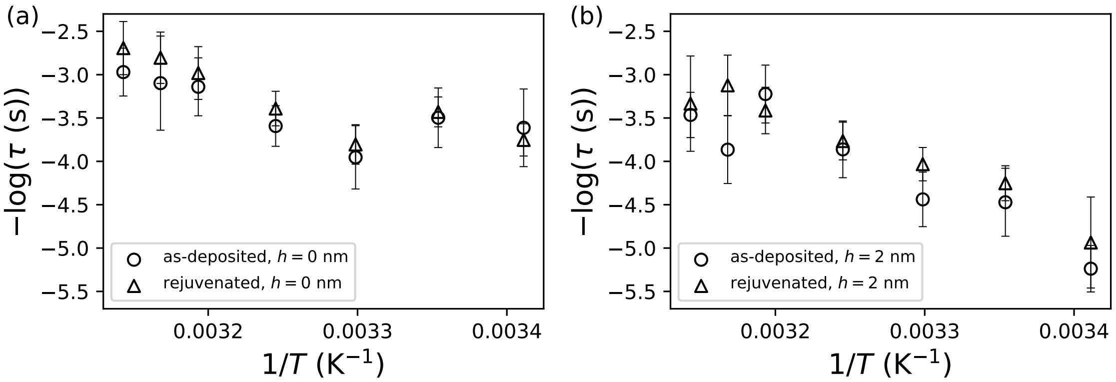

Figure 5.46: The doubling time of a peak width d^* defined in two different ways. In panel (a) d^* is defined as the minimal value of the radial coordinate r at which the height crosses 0 nm, while in panel (b) it is defined as the minimal value of the radial coordinate r at which the height crosses 2 nm.

These differences appear to be due to the choice of the physical quantity used in characterizing the surface relaxation time. While the doubling time of a specific d^* is a very convenient ways to quantify the time scale of the surface relaxation, the choice of d^* itself can lead to quantitatively and sometimes even qualitatively different results. For example, both Fig. 5.46(a) and Fig. 5.46(b) show the doubling time of some width d^* defined from the surface profile. In Fig. 5.46(a) the definition of d^* is exactly the same as presented in Fig. 8(a) in the main manuscript, which is the minimal value of the radial coordinate r at which the height crosses 0 nm, while in Fig. 5.46(b) d^* is chosen as the minimal value of the radial coordinate r at which the height crosses 2 nm (such as that used in ref [126]). It is readily seen that a shift of 2 nm in the observed location changes the temperature dependence of τ significantly. While a d^* at 0 nm leads to an order of magnitude of change in τ within the temperature range investigated, a d^* at 2 nm gives almost two orders of magnitude of change in τ. The transition from an Arrhenius to an athermal behaviour is also only present in one case and not the other. Similarly, while still within quoted uncertainties the as-deposited and rejuvenated samples appear to be less similar when a d^* of 2 nm is chosen.

In obtaining the surface mobility M, the experimental surface profiles, from $r = 0$ to very far from the nanoparticle, are fit to the numerical solutions of the GTFEN model. Unlike the surface mobility M which is a global characteristic of the surface flow, the peak width d^* is a single point, and not every point is equally sensitive to changes in the mobility.

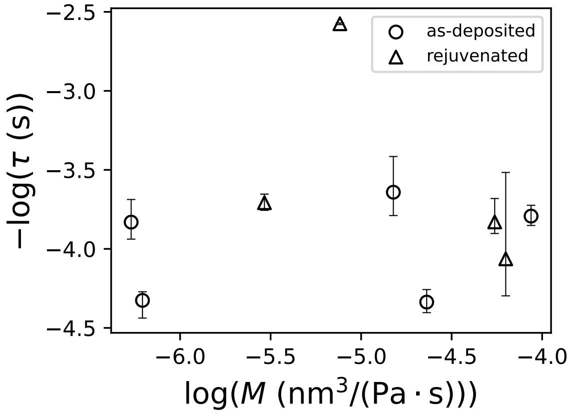

Figure 5.47: The doubling time of a peak width d^* determined from numerically generated profiles for different values of the mobility M.

For example, in ref [18], it is clear that not every point could be used to determine mobility, and the midpoint of the step in that case is in fact a fixed point and completely insensitive to changes in mobility. In general, the globally determined M value is a more reliable and sensitive way to characterize the surface property, while the report from any locally defined doubling time is less sensitive to changes in mobility and also appear to depend strongly on the geometry and the choice of d^*. As a test of this idea we used the profiles generated from the GTFEN model to generate a d^* as a function of time and plotted that doubling time as a function of M. This exercise, the results of which are displayed in Fig. 5.47 revealed that as mobility changes by two orders of magnitude, the times derived from d^* values determined from numerically generated profiles did not similarly change. This demonstrates conclusively that local measurements can result in loss of sensitivity to changes in mobility.

This discrepancy is also reflected in the literature investigating surface properties of glassy films using different methods. In the study of the relaxation of nanoholes on PS thin films [16], the depth of holes are measured and a relaxation time τ is extracted from their time evolution. A levelling-off in the temperature dependence of τ at low temperatures is observed, similar to that of τ in the current study, and even their transition temperatures are strikingly similar. In contrast, in the stepped PS films study by Chai *et al* [18] and in the study of surface evolution of PS films upon annealing by Yang *et al* [17], an Arrhenius behaviour in the surface mobility is observed in both studies, similar to that of M in the current study. It is worth noting that in all of the latter three studies, a mathematical model is built, starting from the Stokes equation, to extract the mobility from experimental surface profiles which cover a wide range of the surface. This apparent disagreement between τ and M can be easily understood with the argument above. When the surface property is described by the time dependence of the profile at a local point, it is influenced by the choice of the point and may not be a good representation of the global relaxation.

Chapter 6

Film thickness dependence in vapour-deposited polymer glass

In liquid cooled polymer thin films, T_{g} changes dramatically with film thickness and it is commonly believed to be due to the existence of a mobile surface layer [116]. For vapour deposited polymer films introduced in this thesis, we would also like to examine the film thickness dependence of their properties including T_{g}. Since they are stable glasses, it is of particular interest to study whether and how the film thickness influences their stability and the rejuvenation process.

6.1 Film thickness dependence of T_{g} and stability

This section is reproduced from the following paper with the permission of American Physical Society:

J. Yin & J. A. Forrest. Film thickness dependent stability and glass transition temperature of polymer films produced by physical vapor deposition. *Physical Review Letters*, 130(16), 168101 (2023). DOI: 10.1103/PhysRevLett.130.168101 [3].

In this paper we have performed an experimental study on the film thickness dependence in vapour deposited PS glassy thin films. As the first author, I was responsible for the experiments including the sample preparation, characterizations as well as data analysis and created all of the figures. I was also responsible for writing and editing the main paper as well as answering reviewer comments.

6.1.1 Abstract

We report measurements of the onset temperature of rejuvenation, T_{onset}, and the fictive temperature, T_{f} for ultrathin stable polystyrene with thicknesses from 10 nm to 50 nm prepared by physical vapor deposition. We also measure the T_{g} of these glasses on the first cooling after rejuvenation as well as the density anomaly of the as-deposited material. Both the T_{g} in rejuvenated films and the T_{onset} in stable films decrease with decreasing film thickness. The T_{f} value increases for decreasing film thickness. The density increase typical of stable glasses also decreases with decreasing film thickness. Collectively, the results are consistent with a decrease in apparent T_{g} due to the existence of a mobile surface layer, as well as a decrease in the film stability as the thickness is decreased. The results provide the first self-consistent set of measurements stability in ultrathin films of stable glass.

6.1.2 Introduction

The glass transition remains one of the most interesting problems in condensed matter physics. Recently, a number of significant advances have been made that promise to increase our understanding of disordered condensed matter. On the theoretical side an exact solution of glasses in infinite dimensions has recently been presented [224]. On the experimental side the recent discovery of ultrastable glasses provides a way to produce near ideal glassy materials [8]. The study of ultrastable glasses produced by physical vapour deposition was originally restricted to molecular liquids, but has since expanded to both metallic glasses [153] and polymers [1]. Experiments on highly confined glass formers has been a key front to learn about dynamical length scales in glass forming materials. This started with the study of materials confined to pores [83], and continued with thin polymer films [116]. It is important to combine these research directions and examine the properties of nanoconfined ultrastable glasses. The first such study was on toluene [225], where it was found that thinner films exhibit higher thermodynamic stability, as indicated by a lower fictive temperature, T_{f}. Thinner films also exhibited a lower kinetic stability, as indicated by a lower value of T_{onset}, a measure of the temperature where the as-deposited stable glass starts rejuvenating into a supercooled liquid. This apparent contradiction between two measures of stability is striking. After first heating, the T_{g} values of the toluene films measured using flash calorimetry showed no dependence on film thickness.

More recently Jin *et al* [27] used ellipsometry measurements to conclude that thin films with thickness less than about 60 nm of stable glass were able to access liquid states that had a higher density than the supercooled liquid extrapolation and in some cases even a higher density than the crystalline phase. This is a significant and surprising conclusion as ordered (crystalline) states are almost exclusively denser than amorphous state. It was suggested that this phenomenon relied on enhanced surface mobility and may be generally observable for thin films of stable glass since the formation of stable glass also relies on the same surface mobility. Since PS has one of the most well-characterized surface mobilities of glass formers (even in the stable glass [2]), studies on thin films of stable PS glass are promising candidates to provide additional support for this idea. While not the focus of Ref. [27], the thickness versus temperature curves in that work show lower T_{onset} values for thin films compared to thick films (there are notable deviations from the glassy slope on first heating near the bulk T_{g}) as well as much lower values of T_{f}. This provides another example where the two measures of stability in thin films give rise to contradictory conclusions about the material stability. Collectively these studies (which are the only cases of ultrathin film stable glasses) are unable to make any conclusions about film thickness dependent changes in the stability. To date there are few studies of ultrathin stable glasses, few studies of polymer stable glass, and no studies on ultrathin studies of polymer stable glass.

The compelling suggestion has been made that surface mobility is the only essential part of thin film T_{g} reductions [210, 223]. In fact this very simple picture has been shown to provide a quantitative description of $T_{\mathrm{g}}(h)$ and at the same time make connections to a length scale for dynamics in the structural glass transition. Conversely, other studies have suggested that T_{g} reduction in thin polymer films may be related to non-equilibrium aspects of the samples [115]. Indeed the fact that spincast films of macromolecular materials are inherently non-equilibrium has been a persistent deterrence in using these fascinating measurements to definitively learn about a length scale of dynamic correlation in glassy materials. A study demonstrating T_{g} reductions in polymer thin film samples that are near equilibrium would significantly change that discussion.

We have recently reported a detailed study [2] of the enhanced mobility of as-deposited kinetically stable films of oligomeric PS. In that work it was shown that the surface properties of kinetically stable PS glass are very similar to those of normal liquid cooled and un-aged glass. That work also showed that the surface of both of these materials display a striking similarity to surface properties of spincast high M_{w} PS glass. This observation suggests that there could be a universal behaviour in the surface among PS glasses with different bulk stabilities, M_{w}, and methods of preparation. If this is correct then it is expected that thin films of stable glass should exhibit similar T_{g} reductions as observed abundantly in spincast PS [10, 11, 93]. Ellison *et al* [226] have shown that the decrease in T_{g} of PS thin films can be suppressed by the addition of small-molecule diluent which decreases the size of cooperatively rearranging regions. For low M_{w} PS, the high volume fraction of chain ends could also act as a diluent and it is not obvious that film thickness dependent T_{g} will be measured in films of very low M_{w} PS. While both Ref. [226] as well as Ref. [227] suggest that changing the $M_{\rm w}$ is unlikely to change the confinement effect, 13.7k is the lowest $M_{\rm w}$ studied so far and it is unclear what will happen at much lower $M_{\rm w}$ values. All of the above highlight the importance of measurements of stability and $T_{\rm g}$ on ultrathin films of stable and rejuvenated low $M_{\rm w}$ PS glass.

6.1.3 Experimental details

The original material is a broad distribution polystyrene ($M_{\rm w}$ = 1200 g/mol) catalogue no. 1024 from Scientific Polymer Products. The molecular weight distribution of the as-purchased material has been characterized in Ref. [1]. The low $M_{\rm w}$ components were evaporated off at 523 K in a separate vacuum chamber [159] before the remaining components were used as source material for the physical vapour deposition. Deposition was carried out in a Korvus technologies HEX deposition unit with a base pressure of 10^{-5} mbar. The source material was heated in an ORCA temperature-controlled organic materials evaporation source. During a single deposition, we can create a series of films spanning a factor of three in film thickness. The range in film thickness required for this study requires multiple depositions. Since we want to have initial films with comparable stability in bulk this can introduce difficulties as different depositions do not give rise to exactly the same material. In order to minimize effects due to this we have considered two depositions that have nearly the same average polymerization index ($\bar{N}$). The source temperatures used in the depositions were 519 K and 521 K, resulting in a constant nominal deposition rate of 0.04 nm/s. The substrate temperature was also constant at 268 K. The deposited films have exceptionally narrow molecular weight distribution, with only 2 or 3 N components in each film. $\bar{N}$ values of the two depositions are 8.3 and 8.6, and the polydispersity index (PDI) is 1.005 for both depositions. These values are determined from the distribution of N in the as-deposited film as determined with a Bruker Autoflex Speed MALDI-TOF (Matrix Assisted Laser Desorption/Ionization-time of flight) mass spectrometer. Because the depositions have similar $\bar{N}$'s, we expect only small differences in the bulk $T_{\rm g}$ between them. Since the stability of deposited materials is determined by the deposition rate and substrate temperature compared to $T_{\rm g}^{\rm bulk}$ we expect samples from these two depositions to have the same stability for thick films. Ellipsometry measurements were performed with a J.A. Woollam M-2000 spectroscopic ellipsometer with a Linkam temperature-controlled stage. Heating and cooling rates for ellipsometric measurements were 2 K/min. The samples were modelled with a three-layer system: PS, silicon oxide, and silicon.

Note that in the current use of the term polymer, it is not the molecular weight that distinguishes this vapour deposited material from other molecules used to make stable glasses. In fact the materials here have a comparable $M_{\rm w}$ to some of those simple liquids.

The key differentiating factor is that in the case of molecular liquids the properties, most notably the T_g value are the same with every deposition. This is not the case for our N-mers and even successive depositions give rise to slightly different materials with slightly different physical properties. While this can introduce difficulties, as mentioned above, it also introduces an extra degree of tunability typical of polymers. For example, we can easily make materials with the same origin but with T_g values that differ by 20 K.

6.1.4 Results

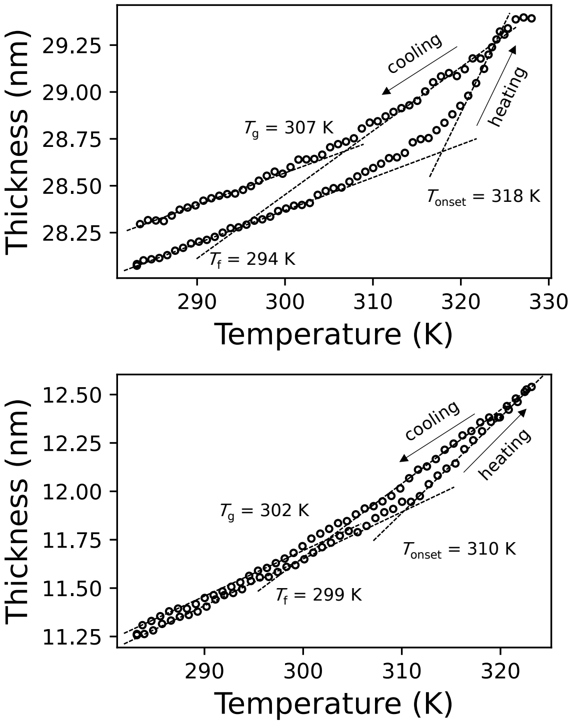

Figure 6.1: Thickness versus temperature of two samples used in this study in order to determine T_g, T_f and T_onset.

Fig. 6.1 shows ellipsometrically determined thickness versus temperature for both a “thick” ($\sim$ 30 nm, top) and “thin” ($\sim$ 11 nm, bottom) film samples during first heating and first cooling. Subsequent heating and cooling scans generally overlap with the first cooling data, with only small deviations depending on the time the sample is aged for before subsequent heating. These data are used to quantify the temperatures T_{g}, T_{f}, and T_{onset}. The T_{g} is obtained as the intersection of the liquid line and the glassy line on cooling and the T_{f} is obtained as the intersection of the extrapolated liquid line from cooling and the as-deposited glassy line on first heating [1]. The T_{onset} is obtained as the intersection of the glassy line on first heating and the line of rejuvenation before changing to the normal liquid line on heating [228]. The density excess $\Delta\rho/\rho$ is determined by $\Delta h/h$ where Δh is the difference between the film thickness at ambient conditions before first heating and after first cooling from the liquid. The thickness data was smoothed by a moving average with a 1.8 K temperature window on both the heating and cooling scans. As has been noted in many other works [93, 117], the contrast between the melt and glass expansivity (important for determining T_{g}) decreases as the film thickness is lowered. The data for the $\sim$ 30 nm film looks essentially the same as that for the much thicker films of vapor deposited PS described in Ref. [1] and exhibits a T_{g} near the bulk value for this particular M_{n}. We can use the ratio $T_{\mathrm{f}}/T_{\mathrm{g}}$ and compare to Ref. [1] to estimate an age of 10^8 s at the T_{f} of 294 K for this thick film sample. In this film, both the lower value of T_{f} and the higher value of T_{onset} compared to $T_{\mathrm{g}}^{\mathrm{bulk}}$ are indications of enhanced stability. The lower graph shows the film thickness for one of the thinnest films used in this study. We notice though that the two measures of film stability do not exhibit the same obvious agreement in this thinner film if we reference to the measured T_{g} rather than bulk value of T_{g}. While the T_{onset} is 8 K greater than the measured T_{g}, the T_{f} value is very near the measured T_{g}. However, it is not clear that the measured T_{g} is the important quantity for such comparisons. Indeed if the apparent T_{g} is simply a result of the contribution of the expansivity of the melt layer, then we should be referencing both T_{f} and T_{onset} to the bulk value of T_{g}. In that case we would say that both T_{onset} and T_{f} indicate a decrease in stability. In order to explore this possibility, we need to examine the measures of stability across a range of thickness encompassing the thickness region where apparent T_{g} reductions are measured.

Fig. 6.2 shows the measured T_{g} on first cooling as a function of the film thickness. The bulk value of T_{g}, $T_{\mathrm{g}}^{\mathrm{bulk}}$ in each deposition, is determined from fitting the data to the functional form from Ref. [210]. The samples from each deposition are then properly normalised by the $T_{\mathrm{g}}^{\mathrm{bulk}}$ value for that deposition. The T_{g} reductions in Fig. 6.2 for the rejuvenated materials agree well with previous measurements of T_{g} in thin supported PS films [12, 93]. These are the first reports of T_{g} reductions in thin films of such low M_{w} polymers. The fact that the $T_{\mathrm{g}}(h)$ for samples produced from near-equilibrium vapour deposited films show such strong resemblance to the $T_{\mathrm{g}}(h)$ measured for spincast polymer films leads to the conclusion that such T_{g} reductions are not due to non-equilibrium effects due to solvent evaporation or chain relaxation (which can not occur in our samples). This means that measured T_{g} reductions are likely an inherent effect simply due to the fact that

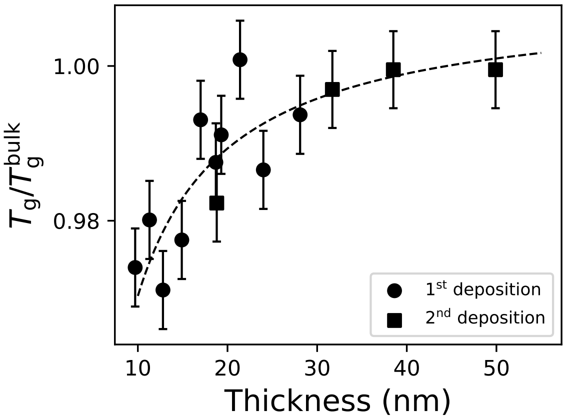

Figure 6.2: T_{g} on first cooling after rejuvenation as a function of film thickness. The two different symbols are from the two different depositions. The $T_{\mathrm{g}}^{\mathrm{bulk}}$ values from those depositions are 309.1 K and 313.3 K. The dashed curve is meant to guide the eye.

PS is a glass forming material with a mobile layer near the free surface. In fact by fitting the T_{g} data to either the model in Ref. [210] or the model by Keddie, Jones and Cory [10] we get a mobile surface layer with a thickness of about 5 nm at room temperature.

Stable glass films have three different measures that show their stability. Upon heating from the as-prepared state, stable glasses will show deviation from glass-like properties as it undergoes rejuvenation to the supercooled liquid state at a temperature T_{onset}. Stable glasses have $T_{\mathrm{onset}} > T_{\mathrm{g}}$ and this is referred to as kinetic stability. Thermodynamic stability is typically characterized by a fictive temperature $T_{\mathrm{f}} < T_{\mathrm{g}}$. Finally stable glasses are denser than glasses freshly cooled from the liquid state. For ellipsometric measurements, the quantity $\Delta h/h \sim \Delta\rho/\rho$ is typically used. Ellipsometric data such as that in Fig. 6.1 is able to provide all three measures of stability within a single heating and cooling scan. Fig. 6.3 exhibits all measures of film stability as a function of film thickness from the two depositions where stability is held as close to constant as possible. It is evident from this figure that all measures of stability demonstrate decreasing film stability with decreasing film thickness, and for films with thickness $\sim$ 10 nm the kinetic stability seems to have vanished. While the scatter in the data does not allow for more quantitative discussion, it is interesting that each stability indicator does not seem to have the exact same dependence on film thickness.

If the T_{g} value were actually changing (rather than the apparent T_{g} defined by the midpoint in expansivity which is affected by a liquid surface layer) then the value of T_{onset}

would simply be offset from T_{g} with no constraints. If instead the film is better described as a bulk-like component and a liquid-like surface component then as the stability decreased T_{onset} will decrease from a values larger than $T_{\mathrm{g}}^{\mathrm{bulk}}$ and reach a limiting value of $T_{\mathrm{g}}^{\mathrm{bulk}}$. Within the scatter of the data, we are not able to unambiguously determine which of the scenarios is occurring, but the observation that T_{onset} for the thinnest films approaches $T_{\mathrm{g}}^{\mathrm{bulk}}$ suggests that the decrease in T_{onset} is due to a decrease in stability with constant T_{g} in the bulk part of the film. Referencing T_{f} to $T_{\mathrm{g}}^{\mathrm{bulk}}$ rather than measured T_{g} also leads to agreement between all measures of stability. The most straightforward explanation of the data is that the proper reference temperature is $T_{\mathrm{g}}^{\mathrm{bulk}}$, the stability of the film decreases with decreasing thickness and the apparent T_{g} being less than $T_{\mathrm{g}}^{\mathrm{bulk}}$ is due to effect of a liquid-like surface layer and its effect on the total expansivity of the film. While we have shown data from two depositions, we have similar data from 2 additional depositions that agrees quantitatively with the data in Figs 6.2 and 6.3. We have chosen not shown that data as the depositions rates, and substrate temperatures were different. Without a concurrent study on the dependence of stability on those parameters in thin films, inclusion of that data would have added an additional variable of film stability which is held constant for the data shown.

In the previous studies on stable glasses of toluene, the film thickness dependent reduction in T_{onset} was taken to mean a loss of kinetic stability. In contrast the film thickness dependent reduction in T_{f} indicated an increase in thermodynamic stability. In addition, neither the fictive nor the onset temperature of the rejuvenated material exhibited a film thickness dependence. This was consistent with A.C. calorimetric results at 20 Hz on thin films of toluene which also exhibited no evidence for reduced T_{g} values in even the thinnest films [229] of a few nm thickness. The lack of reduction in T_{g} could be due to the time scale of the experiment. In Ref. [225], the cooling rate for freshly cooled glasses was 2000 K/s. Time scale is known to impact the ability to measure T_{g} reductions [230, 231]. We can also compare to the recent studies of Ref. [27]. Those studies also seem to indicate that thin films have a lower T_{f}, indicating enhanced thermodynamic stability and a lower T_{onset}, indicating diminishing kinetic stability, compared to thicker films. That study also reported $\Delta\rho/\rho$ values of as large as 8%. The authors suggested that the enhanced surface mobility in thin films allows access to new amorphous states with densities higher than the supercooled liquid and in some cases even greater than the density of the crystal. The remarkable nature of such claims as well as the difficulty in precisely inverting ellipsometric measurements for very thin films means that more experimental evidence of such an effect is critical. Through our measurements, we are unable to provide support for the existence of such density increases for the case of thin films of stable PS glass.

In summary, we have measured the T_{onset}, T_{f}, $\Delta\rho/\rho$, and T_{g} (upon cooling) as a function

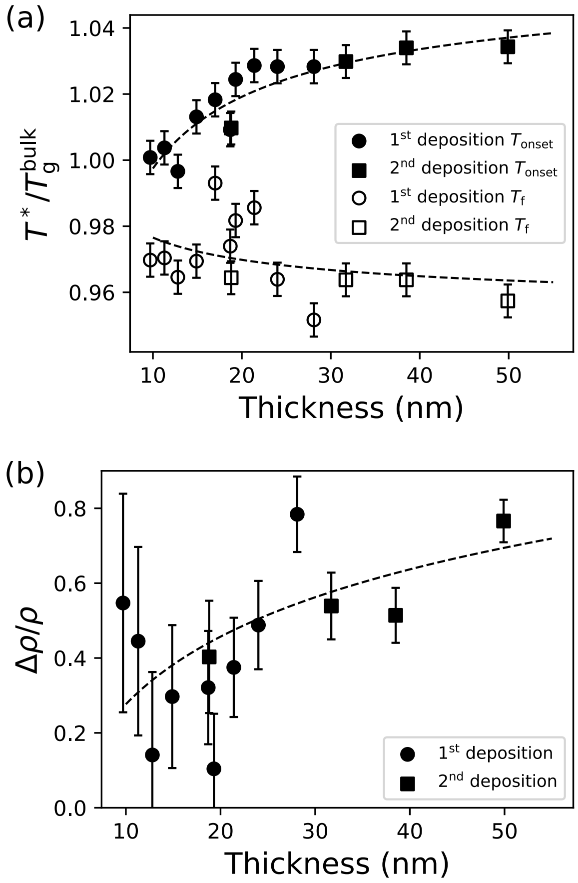

Figure 6.3: Comparing all measures of film stability, including T_f and T_{onset} compared to T_g^{bulk} (a) and the density increase (b) as a function of film thickness. Solid symbols in (a) represent T_{onset} and hollow symbols represent T_f. The two depositions are represented by square and round symbols respectively. All dashed curves are meant to guide the eye.

of film thickness for samples of vapour deposited polystyrene. All measures of the stability indicate a decrease in stability for thin films compared to much thicker bulk-like materials. The T_g values show a decrease with decreasing film thickness in a manner consistent with previous measurements of spincast polystyrene of much higher M_w. The results are consistent with a decrease in apparent T_g caused by the liquid-like region near the free surface and that T_g^{bulk} is still a limiting value of T_{onset} and hence is the only physically relevant temperature for the material.

6.2 Film thickness dependence in the rejuvenation process

This section is based on an ongoing work:

J. Yin, S. Karimi & J. A. Forrest. Rejuvenation in thin films of ultrastable PS prepared by physical vapor deposition. *In preparation* (2023) [4].

In this work we have performed an experimental study on the film thickness dependence in the rejuvenation process in vapour deposited PS glassy thin films. I have been responsible for the experiments including the sample preparation and characterizations and have produced all the preliminary data. I created all the data for the figures included in this section and performed the data analysis.

6.2.1 Introduction

The film thickness effect on glass stability has been demonstrated through different measures including T_{onset}, T_{f}, and $\Delta\rho/\rho$. Apart from these key signatures, the process of rejuvenation itself is also of great interest in the study of vapour deposited stable glasses. The enhanced stability leads to slow kinetics in the glass, which makes the rejuvenation of a stable glass distinct from regular glasses. There has been experimental and theoretical evidence that the transformation from stable glass to supercooled liquid is rather similar to the melting of crystals [232, 233, 234]. In this study we would like to investigate the effect of film thickness on the rejuvenation process with the thin film stable glasses we have been able to prepare.

The rejuvenation process is typically studied in either of the following two ways. In a kinetic scan, the as-deposited glass is heated at a constant rate until the glass fully transforms to a liquid. The stability of the glass is exhibited from the onset temperature which is higher than T_{g}. In an isothermal measurement, the as-deposited glass is quickly heated to a constant temperature, and the response is monitored as a function of time. The relaxation time of the as-deposited glass is then extracted [1, 8] and associated with its stability.

Fig. 6.4 is a typical ellipsometry measurement on a thin film stable glass. Like typical samples seen throughout the thesis, it exhibits stable features including the increased density, higher T_{onset} and lower T_{f}.

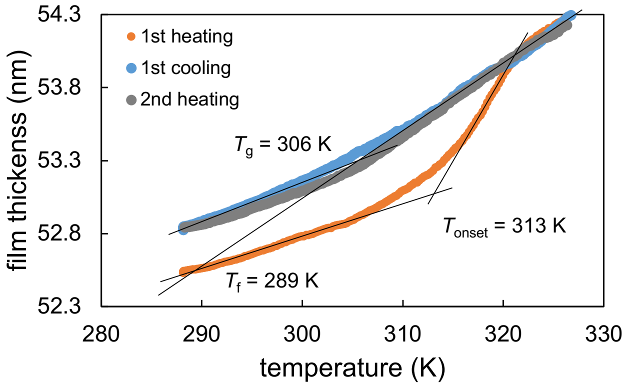

Figure 6.4: Film thickness with respect to temperature of a typical thin film stable glass sample.

6.2.2 Unexpected rejuvenation below T_{onset}

To study the rejuvenation process, we focus on the first heating where the glass starts to transform to a supercooled liquid, as highlighted in Fig. 6.5. It can be noticed that before reaching the traditionally defined T_{onset}, the first heating line already starts to deviate from the glassy slope. We define the temperature where this deviation starts as $T_{\text{onset-}}$.

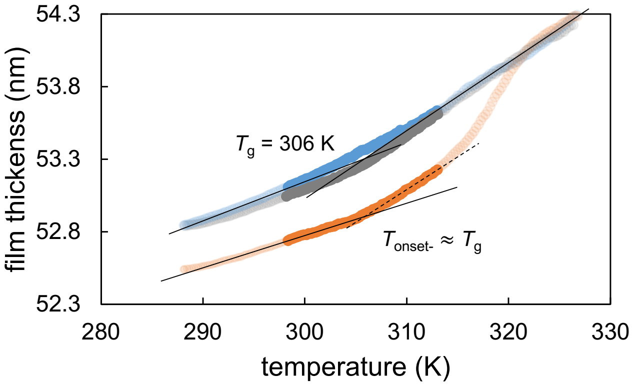

Figure 6.5: Film thickness data in Fig. 6.4, with the initial transformation region highlighted.

This deviation is not a coincidence, but rather a common observation in thin film stable glasses. In Fig. 6.1 in the previous section the first heating lines of the two films (11 nm and

28 nm) both show a deviation before T_{onset}. Similar observations are also found in other studies. For example, Fig. 6.6 shows that in the study by Jin et al. [27], the first heating line also exhibits detectable deviation from the glassy slope at relatively low temperatures for the thinnest films (25 nm and 37 nm).

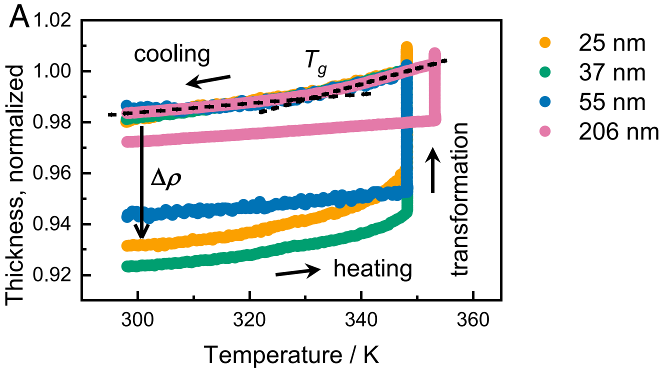

Figure 6.6: Normalized thickness vs. temperature for vapour deposited TPD films with different film thicknesses. Figure from Ref. [27].

In analyzing the film thickness data for a series of vapour deposited thin films, it is observed that $T_{\mathrm{onset-}}$ are surprisingly close to T_{g} for most of the films. Therefore, a comparison between $T_{\mathrm{onset-}}$ and T_{g} is made in Fig. 6.7. The difference between the two is very close to zero within uncertainty for most of the film thicknesses studied, with some data points drifting away from zero for the thinnest films.

The close correspondence between $T_{\mathrm{onset-}}$ and T_{g} suggests that there might be an underlying connection between these two quantities. Normalized against $T_{\mathrm{g}}^{\mathrm{bulk}}$ for each deposition, $T_{\mathrm{onset-}}$ and T_{g} are compared in Fig. 6.8. Both quantities show a constant value close to $T_{\mathrm{g}}^{\mathrm{bulk}}$ at higher thicknesses, and follow a very similar trend as the film thickness decrease.

It is commonly believed that the mobile surface layer is responsible for the T_{g} reductions in polymer thin films, which explains the trend in the T_{g} plot. However, the decreasing trend in $T_{\mathrm{onset-}}$ could not be attributed to the existence of the mobile layer. As shown in Ref. [116], the mobile layer thickness and its dependence on temperature is independent on film thickness. This means that if the change in film expansivity at $T_{\mathrm{onset-}}$ was due to the change in the mobile layer, the temperature where this occurs should be constant across films with different thicknesses. However, Fig. 6.8(a) does not agree with this hypothesis.

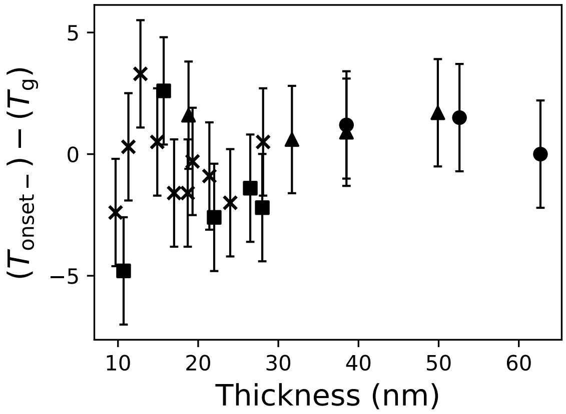

Figure 6.7: $(T_{\text{onset-}}) - (T_{\text{g}})$ versus temperature. Different symbols represent films prepared in different depositions.

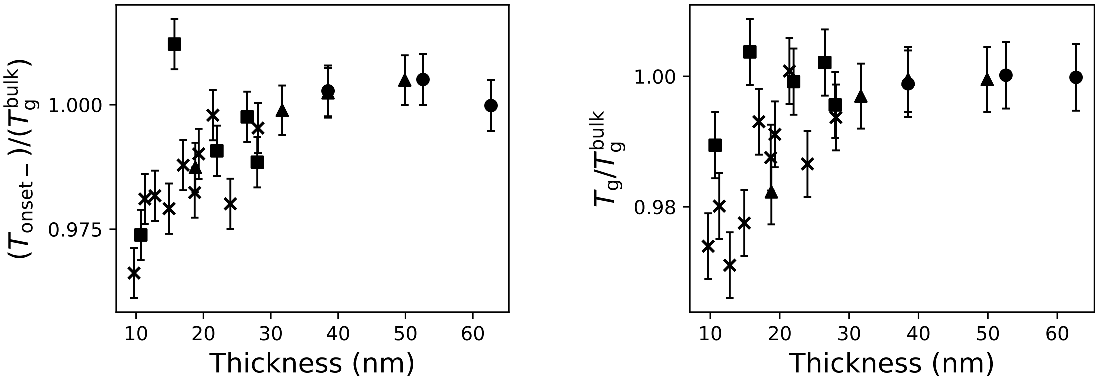

(a)

(b)

Figure 6.8: $T_{\text{onset-}}$ (a) and T_{g} (b) normalized against $T_{\text{g}}^{\text{bulk}}$ for each deposition.

6.2.3 The stable fraction of a stable glass

As shown in Fig. 6.4, compared to the transformation process after T_{onset} where the thickness is linear with temperature, the slope of the line between $T_{\text{onset-}}$ and T_{onset} is still small, which suggests that only a fraction of the film is involved in the initial transformation. Following this observation we would like to conduct quantitative investigations on the transformation process. We hope to be able to answer questions such as whether this initial transformation involves a layer with a constant thickness or whether it is a certain fraction of the entire film thickness.

In Fig. 6.9 we reproduce the data shown in Fig. 6.4, and highlight what happens near T_{onset}. In the analysis we propose a simplified model of the stable glass, where the as-deposited film is divided into a "stable" layer and a "normal" layer. The stable layer is assumed to have the properties as a typical stable glass, including kinetic stability, increased density, and low fictive temperature. The normal layer is assumed to be equivalent to a liquid cooled glass which has no stability and during the first heating could transform to a supercooled liquid below T_{onset} of the stable layer. As shown in the figure, we compare the film thicknesses on the first heating scan and on the first cooling scan both at T_{onset}, and define the fraction of stable layer to be $h_1/(h_1 + h_2)$, and the fraction of the normal layer to be $h_2/(h_1 + h_2)$, with h_1 and h_2 shown in the figure.

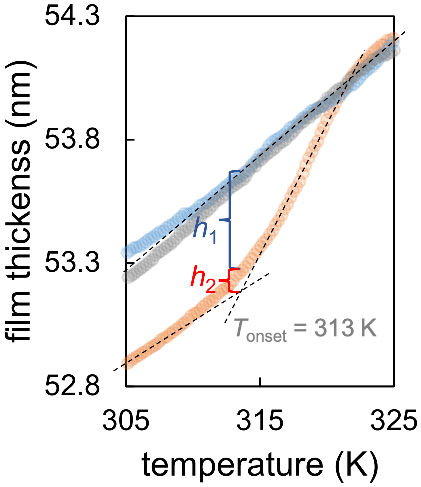

Figure 6.9: Film thickness data reproduced from Fig. 6.4 including only the transformation region near T_{onset}. h_1 is defined as the gap between the first cooling line and the first heating line at T_{onset}. h_2 is defined as the gap between the first heating line and the extrapolated glassy line from the low temperature region on first heating.

Multiplied by the total film thickness, the fraction of the stable layer and the normal layer gives their corresponding layer thickness. As shown in Fig. 6.10, the thicknesses of both layers seem to be proportional to the total film thickness, with the stable layer taking up a larger fraction in the film. Since the thickness of either layer is not a constant value, the fraction of each layer is evaluated next.

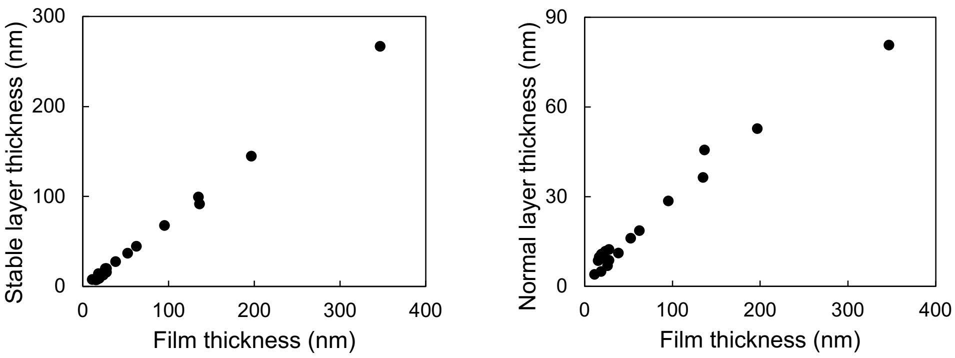

(a) (b)

Figure 6.10: Thickness of the stable layer (a) and the normal layer (b) as a function of total film thickness.

Fig. 6.11 shows that the stable or normal layer is not constant in either thickness or fraction. In fact the fraction depends on the total film thickness. From 10 nm to 100 nm, the fraction of the stable layer is initially as low as 45% but rises rapidly to above 70%. Above 100 nm, it seems to still be an increasing function of film thickness although the dependence is much weaker. Correspondingly, the normal layer has a large fraction in the thinnest films which reduces for thicker films.

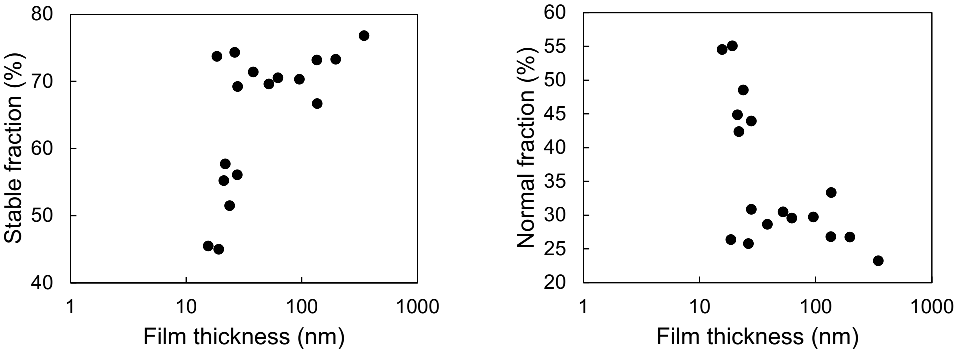

(a) (b)

Figure 6.11: Fraction of the stable layer (a) and the normal layer (b) as a function of total film thickness.

This result is consistent with the observations in the previous section. With a lower fraction of stable glass in the entire film, the reduced stability as measured by $\Delta\rho$, T_{onset} and T_{f} is as expected. It is worth mentioning that this is a simplified model where the as-deposited film is considered to be divided into two different layers. More realistically, one could expect a continuous change in stability throughout the sample from the surface to the substrate as a reasonable physical picture.

6.2.4 Rejuvenation rate

The rejuvenation process of stable glasses have been studied extensively since a transformation mechanism was first suggested by Swallen et al. [235]. Since then, this mechanism has been proved by different studies repeatedly with reports of consistent results [147, 233, 236, 237, 238, 239, 240, 241]. It is commonly believed that the transformation process of a stable glass is analogous to the melting of a crystal. When the film thickness is small, the dominating mechanism of rejuvenation is through a liquid front that travels from the free surface or mobile interfaces into the bulk until the entire film transforms to the liquid state. The mechanism changes when the film thickness is above a certain value which is known as the cross-over length. For thicker films, the system transforms mainly through the growth of liquid patches distributed throughout the bulk. The value of the cross-over length depends on the type of the material, temperature, heating rate, and the glass stability, etc, and different values from a few nanometers to several microns have been reported [233, 242, 243, 244].

As shown in Fig. 6.12, in thin films (a), transformation through both the liquid front that grows parallel to the surface as well as the liquid patches that are distributed in the bulk. Since the front transformation is done in a very short time due to the small thickness of the film, the liquid patches are not the main way of rejuvenation because they are sparse in the system. For thicker films (b) the liquid patches become the dominant way of rejuvenation compared to the parallel liquid front due to the large film thickness. When the film is capped on surfaces (c), the front rejuvenation is prohibited so the liquid patches become the only way of transformation. In any case, the fundamental mechanism is the the difference in mobility between the stable glass and the newly formed liquid phase, whether the transformation front originates from the surface or bulk [232, 245].

With the rejuvenation data for films with various thicknesses, we are interested in the thickness dependence of the process of rejuvenation, specifically, the rejuvenation rate of the film. Assuming the rejuvenation is mostly through the transformation front (to be validated), with isothermal transformation the rejuvenation rate can be defined as the thickness of the film transformed divided by the time needed for complete transformation.

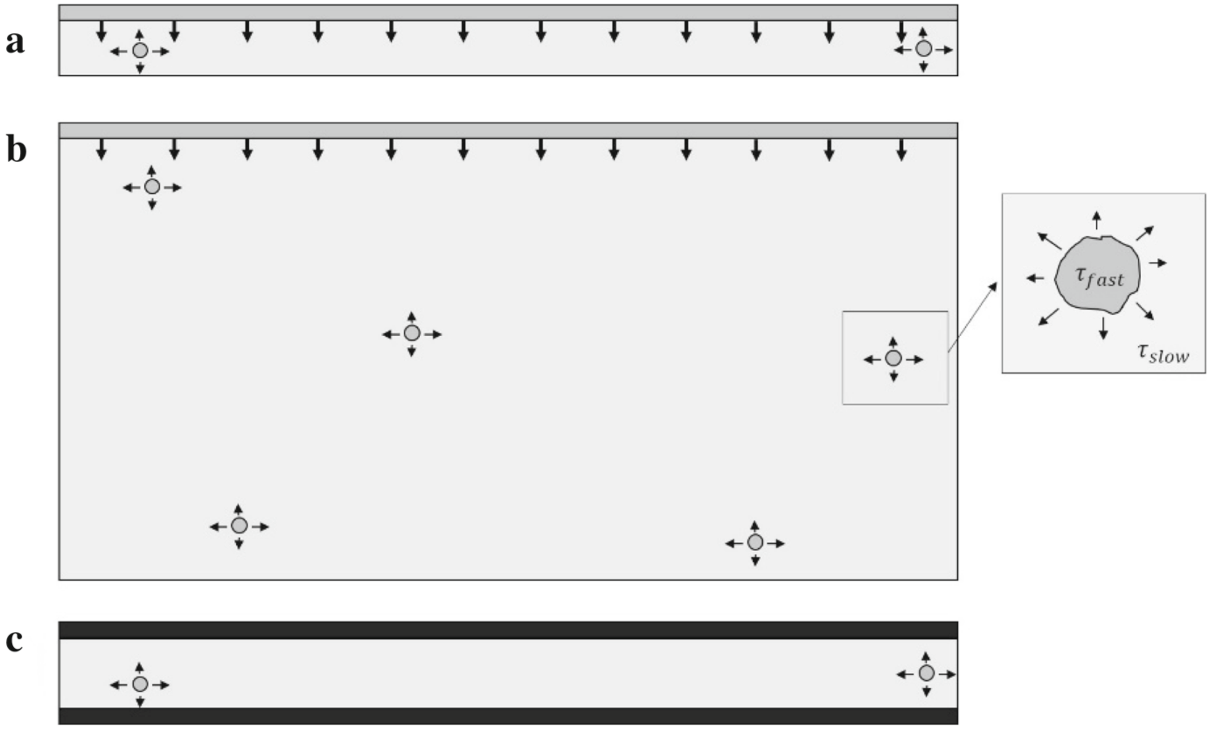

Figure 6.12: Schematic diagram showing the transformation mechanism in thin films (a), thick films (b) and capped films (c). Figure from Ref. [28].

With the kinetic scans as introduced in this section, we use a similar definition as shown in Fig. 6.13.

The total thickness h_{t} is defined as the thickness where the film completes the transformation to liquid. From the first heating curve this is determined from the change of a large slope to the regular supercooled liquid slope. Although the temperature is not constant during the rejuvenation, we can still define a transformation time t as the time spent from heating the system from T_{onset} to the point of full transformation at h_{t}. The rejuvenation rate is thus h_{t}/t. Fig. 6.14 is a collection of results from similar kinetic scans from several series of deposition with various film thicknesses. Also included are two sets of isothermal rejuvenation data where the films were both heated at 10 K/min before sitting at a constant rejuvenation temperature. The rejuvenation rates in such films are simply the total thickness divided by the time for full rejuvenation at the constant temperature.

As indicated in the legend, different heating rates are included in the kinetic scans used

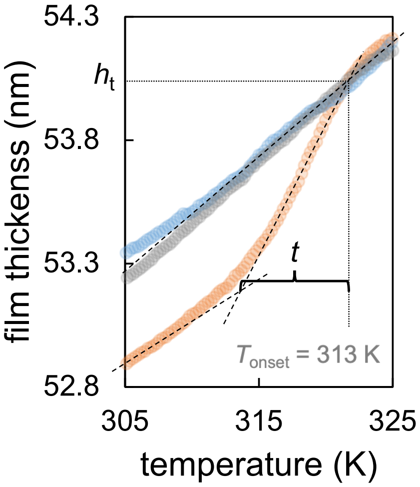

Figure 6.13: Film thickness data reproduced from Fig. 6.4 including only the transformation region near T_{onset}. The total thickness h_{t} is defined as the thickness where the film completes the transformation to liquid as determined from the change of slope on the first heating scan. The transformation time t is defined as the time spent from heating the system from T_{onset} to the point of full transformation at h_{t}.

for creating Fig. 6.14, and it is noticed that the heating rate does have an influence on the rejuvenation rate. From 1 K/min to 10 K/min the rejuvenation rate increases in general. This is considered to be mainly related to the nature of kinetic scans. With a higher heating rate, the time spent for heating the sample up to the temperature where full transformation happens is shorter, thus leading to a higher rejuvenation rate. Once the rejuvenation rates are normalized by the heating rate used in each kinetic measurement, as shown in the inset, the heating rate dependence is eliminated and data for all measurements and all film thicknesses collapse onto one line which is described by a power law relationship.

For the two groups of isothermal transformation data, it is observed that the higher rejuvenation temperature 338 K leads to a much higher rejuvenation rate than that at 333 K. This is consistent with literature studies on the effect of temperature on the rejuvenation rate [164, 233, 244, 246].

The rejuvenation rate is evidently dependent on the film thickness as shown in Fig. 6.14. This observation is in contrast to the measurements in Ref. [164] where the front propagation velocity is found to be the same for two films with thicknesses of 635 nm and 1515 nm during isothermal rejuvenation. There could be a few reasons behind this discrepancy.

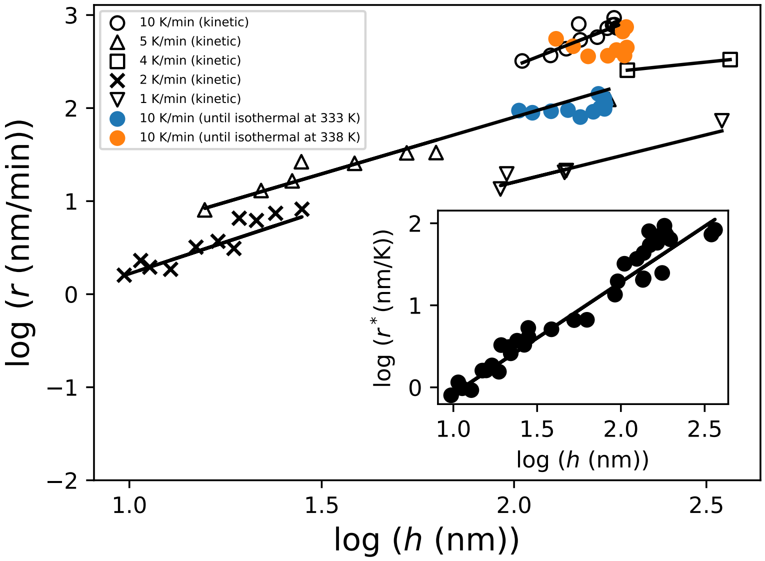

Figure 6.14: Rejuvenation rates in vapour deposited PS glasses with various thicknesses. The inset shows rejuvenation rates normalized by the heating rate used in each kinetic measurement, for all film thicknesses. Solid lines are used to guide the eye.

First, it could be because of the different thickness ranges studied. While the propagation rate is the same for films of 635 nm and 1515 nm, it may have a dependence on film thickness for thinner films as shown in this thesis. Second, the rejuvenation process in our PS samples does not necessarily happen through the mobile front traveling from the surface. If the cross-over length for our samples lies within the film thickness range in the figure, it is not clear that the rejuvenation rates calculated in this way represent the front propagation velocity. Last, most of the rejuvenation rates in the figure are obtained from kinetic scans and it may be unfair to compare them with those obtained from isothermal rejuvenation. As a matter of fact, the two sets of isothermal rejuvenation data in the figure suggest that the rejuvenation rate may not depend on the film thickness, although the range of film thickness in these two sets of data are relatively small for one to draw a conclusion.

As discussed previously in this section, the stable fraction appears to be lower in thinner films. If this correlation is valid, the lower stability could be the reason of the lower rejuvenation rate in thinner films. In fact, the dependence of rejuvenation rate on film thickness can be considered in analogy to the growth rate of polymer crystals [247]. The crystal growth rate is a balance between thermodynamic driving forces and kinetics and depends on the temperature. At high temperatures close to the melting points, the kinetics are fast but there is little driving force to form crystals since the system is too close to equilibrium. At low temperatures close to T_g, the system is far from equilibrium and there is a huge driving force for crystals to be formed but the kinetics are too slow. Only at intermediate temperature can the crystal grow at a high rate with enough driving force and relatively fast kinetics.

Similarly, the rejuvenation rate can be explained in terms of the distance to equilibrium and the thermodynamic driving force. Upon heating, the driving force for rejuvenation depends on how far the system is from equilibrium (the supercooled liquid state). For thinner films with lower stability as has been observed in this study, it is relatively close to equilibrium so the rate of rejuvenation is lower due to the low driving forces. For thicker films which are more stable, the distance from equilibrium supercooled liquid is large and the rate of rejuvenation increases due to large driving forces.

If the glass stability depends on the film thickness as has been discussed, Fig. 6.14 can also be used to analyze the dependence of rejuvenation rate on characteristics such as density. In Ref. [164], the front propagation rate is found to be imperfectly correlated with increased density $\Delta\rho$ for indomethacin. For glasses deposited at the optimal temperature, the increased density is large, while their front propagation rate is found to be low. For glasses deposited below the optimal temperature, they exhibit lower increased density as well as higher propagation rate. Such correlation is also in contrast to the observation in Fig. 6.14 where thicker films which are supposed to have higher density show higher rejuvenation rate, and it is not clear whether this is a difference between PS and indomethacin, a difference caused by kinetic measurements and isothermal measurements, or the association built between film thickness and stability based on our observation. For a more solid understanding, isothermal rejuvenation with a thickness range larger than the two sets of data in Fig. 6.14 is recommended, and the dependence of rejuvenation rate on the fictive temperature, the onset temperature, and the increased density should be studied in further detail.

Since the heating rate used in kinetic scans affects the rejuvenation rate in an inherent way, it is not necessarily fair to directly compare rejuvenation rates obtained from kinetic scans and isothermal rejuvenation. We can instead study the rejuvenation time as a function of film thickness. Fig. 6.15 shows data from the same collection of samples as shown in Fig. 6.14.

The first thing to be noticed from Fig. 6.15 is that except for the thinnest films, the rejuvenation time does not seem to be dependent on the film thickness. It is known that under isothermal rejuvenation, thick films beyond the cross-over length should all take the

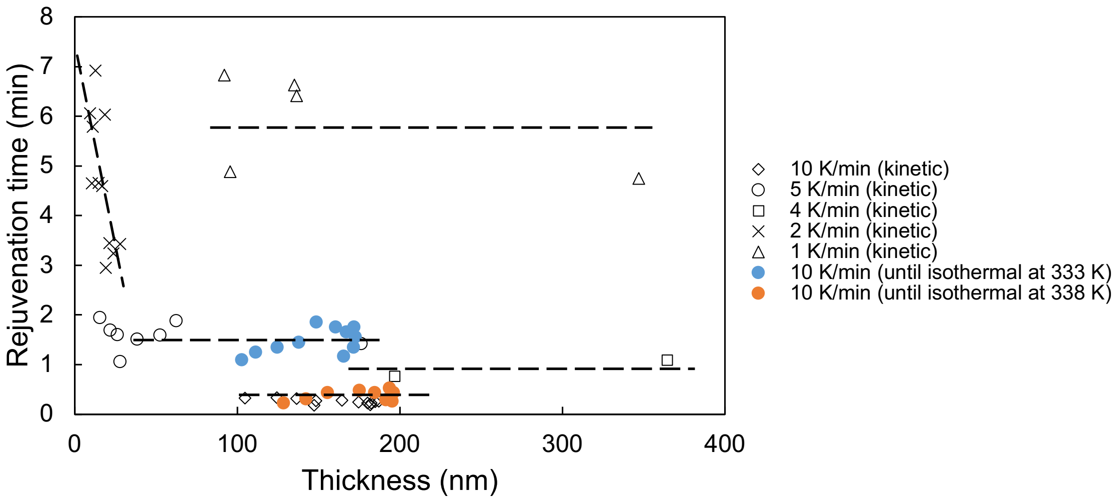

Figure 6.15: Rejuvenation rate in vapour deposited PS glasses with various thicknesses. Dashed lines are used to guide the eye.

same time to fully transform to a supercooled liquid because the transformation through liquid patches happen simultaneously throughout the bulk of the film. Based on where film thickness dependence disappears in Fig. 6.15, we would expect the cross-over length for our systems to be less than 50 nm.

Looking at the effect of heating rate, it is observed that the heating rate in kinetic scans plays a similar role to the isothermal rejuvenation temperature. The isothermal rejuvenation at 333 K and 338 K shows that the rejuvenation time is shorter for higher rejuvenation temperature. Similarly, a higher heating rate in kinetic scans leads to a shorter rejuvenation time in general. This is because when the heating rate is higher, the system spends less time at lower temperatures and quickly reaches high temperatures where rejuvenation happens faster, and thus it has the same effect as a higher rejuvenation temperature.

For the thinnest films in Fig. 6.15, the results are quite interesting. The rejuvenation time is found to decrease with increasing film thickness up to ∼ 30 nm. Typically for thicker films (above a few hundred nanometers), isothermal rejuvenation time is observed to increase with increasing film thickness below the cross-over length [233, 242]. We attribute this discrepancy to the competition between the effect of film thickness and the effect of glass stability.

On the one hand, the thicker the film, the longer time it needs to fully transform through the mobile front at a constant velocity.

On the other hand for films below several tens of nanometers, the thicker the film, the more stability it has as we have learned from Section 6.1. First, if the analogy to polymer crystal growth is correct, the thermodynamic driving force for rejuvenation is stronger in thicker films with higher stability since they are further away from equilibrium (the supercooled liquid state). Therefore their shorter rejuvenation time can be explained by their faster transformation to the equilibrium state. Second, the nature of kinetic scans may affect the rejuvenation time we measure. During kinetic scans we keep increasing the temperature at a constant rate, until the T_{onset} is passed and the film has fully transformed into a supercooled liquid. We have learned that T_{onset} is lower for thinner films. This means that the temperature region we allow the thinner films to rejuvenate is lower that that of the thicker films, and thus the thinner films are expected to have a slower rejuvenation process, which leads to a longer rejuvenation time.

In thick films where the glass stability does not depend on the film thickness, it is not surprising that the isothermal rejuvenation time through the mobile front always increases with increasing film thickness. In thin films as shown in Fig. 6.15, the situation is more complicated due to the competition between the effect of film thickness and the effect of glass stability. From the results we observe, it appears that the effect of glass stability is stronger and wins this competition.

6.2.5 Conclusion

We have studied the film thickness dependence in the rejuvenation process in vapour deposited PS glassy thin films. In contrast to thick films, thin film stable glasses exhibit an unexpected rejuvenation before reaching T_{onset} during the first heating scan. The onset of the deviation from the glassy expansivity is studied and compared to T_{g}. By modeling the film as a two-layer system consisting of a stable layer and a non-stable layer, we extract the stable fraction from the rejuvenation measurements during kinetic scans and show that the stability in thin films decrease with decreasing film thickness, which is consistent with our observations in Section 6.1. We also study the effect of film thickness on the rejuvenation rate and rejuvenation time in thin film and compare to literature studies. Although we are able to extract a cross-over length for our samples and explain some of the film thickness dependence, the nature of the non-isothermal rejuvenation measurements prevents us to draw further definitive conclusions. A more systematic study of isothermal rejuvenation is required for a better understanding of the rejuvenation process in thin film stable glasses.

Chapter 7

Summary and outlook

In this thesis, stable polymer glasses prepared through physical vapour deposition have been investigated from different aspects. This is the first time polymers have been used in simple vapour deposition and made into stable glass.

In Chapter 1 basic concepts about polymers, glasses, and the glass transition are introduced. About the mysterious glass transition, Weitz once joked [248], "There are more theories of the glass transition than there are theorists who propose them." In this thesis we only introduce some of the most basic and useful theories relevant to our studies. Literature studies on glassy thin films and their interfacial dynamics are briefly reviewed. Stable glass, a topic that is perhaps the most relevant in this thesis, is introduced with a light touch on their properties and importance.

In Chapter 2 we demonstrate the experimental techniques used to prepare and characterize stable polymer glasses. Starting from the as-purchased material, we preprocess it with distillation first and then make them stable with physical vapour deposition. Ellipsometry, atomic force microscopy and mass spectrometry are some of the most useful techniques in studying them.

In Chapter 3 we include the first report on the preparation and characterization of ultrastable PS as well as PMMA glasses using simple physical vapour deposition. This demonstrates our ability to create such materials with exceptional stability and extremely long lifetimes. One of the most important factors that differentiates stable polymer glasses from stable molecular glasses is that they have high tunabilities originating from the molecular weight distribution. Although they have relatively low molecular weight, the large range of physical and chemical properties give them endless possibilities in applications. By controlling the substrate temperature and deposition rate, we prepare and characterize a variety of stable polymer glasses and show that these materials exhibit enhanced kinetic stability, low fictive temperatures and high density characteristic of stable glasses

In Chapter 4 we push our limits and pursue stable polymer glass with higher molecular weight, using two different methods including using higher molecular weight sources and crosslinking as-deposited glasses with ultraviolet radiation. This chapter may not seem a very successful attempt but we have learned valuable lessons from it. The outcomes from the first method shows that the highest molecular weight to be achieved from simple vapour deposition is limited by the competition between deposition rate and the rate of chain scission. The UV crosslinking method generates samples with properties more interesting than expected, possibly due to undesired reactions happening in during the treatment.

In Chapter 5 we study the surface of stable polymer glass, since the surface mobility is believed to be key in the formation of stable glasses. We report observations of special morphology features on these glasses and explore the reasons behind them. With the aid of gold nanoparticles, we performed quantitative characterizations of their surface and bulk dynamics. The surface evolution under perturbations of nanoparticles exhibits two steps. The build-up of polymer material around the nanoparticle provides us with a quantitative measure of the surface mobility, and the final bulk embedding of the nanoparticle describes the bulk dynamics of stable polymer glasses. With a slower bulk dynamics in stable glasses as expected, the surface evolution of the as-deposited films and the rejuvenated films are both enhanced compared to bulk and are not easily distinguishable from each other.

In Chapter 6 we investigate stable polymer glasses confined to thin films down to 11 nm. Similar to regular confined films, the film thickness also influences properties of stable glasses. Particularly, we study the thickness dependence of the thermodynamic and kinetic stability, the glass transition temperature, and the transformation process from a stable glass to a supercooled liquid. T_{g} reductions observed in vapour deposited polymer glasses supports the existence of a surface mobile layer, and it is observed that glass stability decreases with decreasing film thickness, as determined by different measures of stability. Investigations on the rejuvenation process from a stable glass to a supercooled liquid show that rejuvenation appears to happen before reaching the traditionally defined onset temperature, suggesting that a fraction of the film is not stable in the as-deposited glasses. The fraction of stable glasses is quantitatively analyzed in thin films, and the rejuvenation rate is also found to be dependent on film thickness.

The study of glass transition in polymer thin films has been a thriving research area since the first report by Keddie, Jones and Cory [10]. The new type of material–stable glass–has also attracted great research interest since it was first discovered by the Ediger group [136]. At the intersection of these two research fields, stable polymer glasses are an excellent candidate for contributing into both fields and hopefully will open up a new area of research on its own. By studying these materials from different aspects, we hope to provide valuable insights into many fundamental questions about the surface dynamics in thin films, the limit of packing in amorphous materials, and the nature of the complex and fascinating phenomenon–the glass transition. On the applied level, stable polymer glass is a novel type of material with exceptional properties and high tunabilities and has many potential applications in materials technology.

The studies in this thesis also suggest some future work in exploring these new materials. During the preparation of stable polymer glass, the as-purchased material is first preprocessed by either distilling into monodisperse fractions or removing the low N fractions by distillation. Either method is not the most efficient yet. Other methods such as solvent extraction of low N fractions as a preprocessing step can be investigated. For vapour deposited polymer glasses after UV treatment, there are signs of increased molecular weight, but there are also subliming issues due to possible chain scissions. It is crucial to prevent thermal oxidation or degradation from occurring by further decreasing oxygen levels in the system. In order to keep subliming from happening, UV treated films could also be capped with another film with a higher T_g in addition to choosing the correct time period for UV treatment. From the studies on the surface relaxation of stable polymer glasses, the value of the surface mobility has been extracted which is expressed in terms of a surface viscosity and a surface mobile layer thickness. In future work, it would be worth determining the mobile layer thickness separately and compare to literature results. In studying the relationship between enhanced surface dynamics and film thickness dependence of stability, the films could also be capped with higher T_g materials. In literature studies it has been shown that once the surface is capped the enhanced surface dynamics could be eliminated and the film thickness dependence would disappear. It would be interesting to see whether this is also true in stable polymer glasses. Lastly, a systematic study on isothermal rejuvenation of films with different thicknesses and stabilities would greatly benefit our understanding of the rejuvenation process in stable polymer glasses.

References

[1] A. N. Raegen, J. Yin, Q. Zhou, and J. A. Forrest, “Ultrastable monodisperse polymer glass formed by physical vapour deposition,” *Nature Materials*, vol. 19, no. 10, pp. 1110–1113, 2020.

[2] J. Yin, C. Pedersen, M. F. Thees, A. Carlson, T. Salez, and J. A. Forrest, “Surface and bulk relaxation of vapor-deposited polystyrene glasses,” *The Journal of Chemical Physics*, vol. 158, no. 9, p. 094901, 2023.

[3] J. Yin and J. A. Forrest, “Film thickness dependent stability and glass transition temperature of polymer films produced by physical vapor deposition,” *Physical Review Letters*, vol. 130, no. 16, p. 168101, 2023.

[4] J. Yin, S. Karimi, and J. A. Forrest, “Rejuventation in thin films of ultrastable ps prepared by physical vapor deposition,” *In preparation*, 2023.

[5] L. Berthier and M. D. Ediger, “Facets of glass physics,” *Physics Today*, vol. 69, pp. 40–46, 2016.

[6] V. Lubchenko and P. G. Wolynes, “Theory of structural glasses and supercooled liquids,” *Annual Review of Physical Chemistry*, vol. 58, pp. 235–266, 2007.

[7] M. D. Ediger, C. A. Angell, and S. R. Nagel, “Supercooled liquids and glasses,” *The Journal of Physical Chemistry*, vol. 100, no. 31, pp. 13200–13212, 1996.

[8] M. D. Ediger, “Perspective: Highly stable vapor-deposited glasses,” *The Journal of Chemical Physics*, vol. 147, no. 21, p. 210901, 2017.

[9] R. P. White and J. E. Lipson, “Polymer free volume and its connection to the glass transition,” *Macromolecules*, vol. 49, no. 11, pp. 3987–4007, 2016.

[10] J. L. Keddie, R. A. Jones, and R. A. Cory, "Size-dependent depression of the glass transition temperature in polymer films," *Europhysics Letters*, vol. 27, no. 1, p. 59, 1994.

[11] J. Forrest, K. Dalnoki-Veress, J. Stevens, and J. Dutcher, "Effect of free surfaces on the glass transition temperature of thin polymer films," *Physical Review Letters*, vol. 77, no. 10, p. 2002, 1996.

[12] J. S. Sharp and J. A. Forrest, "Free surfaces cause reductions in the glass transition temperature of thin polystyrene films," *Physical Review Letters*, vol. 91, no. 23, p. 235701, 2003.

[13] J. H. Teichroeb and J. A. Forrest, "Direct imaging of nanoparticle embedding to probe viscoelasticity of polymer surfaces," *Physical Review Letters*, vol. 91, no. 1, p. 016104, 2003.

[14] A. Dhinojwala, G. K. Wong, and J. M. Torkelson, "Rotational reorientation dynamics of disperse red 1 in polystyrene: α-relaxation dynamics probed by second harmonic generation and dielectric relaxation," *The Journal of Chemical Physics*, vol. 100, no. 8, pp. 6046–6054, 1994.

[15] J. Cavaille, C. Jourdan, J. Perez, L. Monnerie, and G. Johari, "Time-temperature superposition and dynamic mechanical behavior of atactic polystyrene," *Journal of Polymer Science Part B: Polymer Physics*, vol. 25, no. 6, pp. 1235–1251, 1987.

[16] Z. Fakhraai and J. A. Forrest, "Measuring the surface dynamics of glassy polymers," *Science*, vol. 319, no. 5863, pp. 600–604, 2008.

[17] Z. Yang, Y. Fujii, F. K. Lee, C.-H. Lam, and O. K. Tsui, "Glass transition dynamics and surface layer mobility in unentangled polystyrene films," *Science*, vol. 328, no. 5986, pp. 1676–1679, 2010.

[18] Y. Chai, T. Salez, J. D. McGraw, M. Benzaquen, K. Dalnoki-Veress, E. Raphaël, and J. A. Forrest, "A direct quantitative measure of surface mobility in a glassy polymer," *Science*, vol. 343, no. 6174, pp. 994–999, 2014.

[19] W. Zhang and L. Yu, "Surface diffusion of polymer glasses," *Macromolecules*, vol. 49, no. 2, pp. 731–735, 2016.

[20] B. Voigtländer, *Scanning probe microscopy: Atomic force microscopy and scanning tunneling microscopy.* Springer, 2015.

[21] M. Yan and B. Harnish, "A simple method for the attachment of polymer films on solid substrates," *Advanced Materials*, vol. 15, no. 3, pp. 244–248, 2003.

[22] M. Palacios, O. Garcia, and J. Rodriguez-Hernandez, "Constructing robust and functional micropatterns on polystyrene surfaces by using deep uv irradiation," *Langmuir*, vol. 29, no. 8, pp. 2756–2763, 2013.

[23] P. J. Flory, "Constitution of three-dimensional polymers and the theory of gelation.," *The Journal of Physical Chemistry*, vol. 46, no. 1, pp. 132–140, 1942.

[24] P. J. Flory, "Molecular size distribution in three dimensional polymers. iii. tetrafunctional branching units," *Journal of the American Chemical Society*, vol. 63, no. 11, pp. 3096–3100, 1941.

[25] J. F. Yan, "Cross-linking of polymers with a primary size distribution. ii. calculation of size distributions in the sol fraction of nonlinear polymers," *Polymer-Plastics Technology and Engineering*, vol. 14, no. 1, pp. 47–62, 1980.

[26] D. Qi, *On near-free-surface dynamics of thin polymer films.* PhD thesis, Waterloo, Ontario, Canada, 2009.

[27] Y. Jin, A. Zhang, S. E. Wolf, S. Govind, A. R. Moore, M. Zhernenkov, G. Freychet, A. Arabi Shamsabadi, and Z. Fakhraai, "Glasses denser than the supercooled liquid," *Proceedings of the National Academy of Sciences*, vol. 118, no. 31, p. e2100738118, 2021.

[28] C. Rodriguez-Tinoco, M. Gonzalez-Silveira, M. A. Ramos, and J. Rodriguez-Viejo, "Ultrastable glasses: new perspectives for an old problem," *La Rivista del Nuovo Cimento*, vol. 45, no. 5, pp. 325–406, 2022.

[29] "Through the glass lightly," *Science*, vol. 267, no. 5204, pp. 1609–1618, 1995.

[30] J. Ràfols-Ribé, P.-A. Will, C. Hänisch, M. Gonzalez-Silveira, S. Lenk, J. Rodríguez-Viejo, and S. Reineke, "High-performance organic light-emitting diodes comprising ultrastable glass layers," *Science Advances*, vol. 4, no. 5, p. eaar8332, 2018.

[31] N. Wolchover, "To make the perfect mirror, physicists confront the mystery of glass," *Quanta Magazine*, 2020.

[32] J. Yin, A. Raegen, S. H. Idziak, and J. A. Forrest, "Crystallization and melting of highly monodisperse poly (ethylene-oxide)," *Soft Matter*, vol. 16, no. 34, pp. 7958–7969, 2020.

[33] M. Rubinstein and R. H. Colby, *Polymer Physics.* Oxford University Press, 2003.

[34] V. K. Thakur and M. K. Thakur, *Handbook of Sustainable Polymers: Processing and Applications.* CRC Press, 2016, illus. ed., 2016.

[35] C. E. Carraher, *Carraher's Polymer Chemistry.* CRC press, 2017.

[36] R. J. Young, *Introduction to Polymers, third edition.* CRC Press, 2017.

[37] N. A. Dotson, R. Galvan, R. L. Laurence, and M. Tirrell, *Polymerization Process Modeling.* John Wiley & Sons, illus. ed., 1996.

[38] P. Jenniskens and D. F. Blake, "Structural transitions in amorphous water ice and astrophysical implications," *Science*, vol. 265, no. 5173, pp. 753–756, 1994.

[39] G. Jaeger, "The ehrenfest classification of phase transitions: introduction and evolution," *Archive for History of Exact Sciences*, pp. 51–81, 1998.

[40] H. Vogel, "Das temperatur-abhängigkeitsgesetz der viskosität von flüssigkeiten," *Physikalische Zeitschrift*, vol. 22, pp. 645–646, 1921.

[41] G. S. Fulcher, "Analysis of recent measurements of the viscosity of glasses," *Journal of the American Ceramic Society*, vol. 8, no. 6, pp. 339–355, 1925.

[42] G. Tammann and W. Hesse, "Die abhängigkeit der viscosität von der temperatur bie unterkühlten flüssigkeiten," *Zeitschrift für anorganische und allgemeine Chemie*, vol. 156, no. 1, pp. 245–257, 1926.

[43] M. Williams, R. Landel, and J. Ferry, "Mechanical properties of substances of high molecular weight. 19. the temperature dependence of relaxation mechanisms in amorphous polymers and other glass-forming liquids," *Journal of the American Chemical Society*, vol. 77, no. 14, pp. 3701–3707, 1955.

[44] P. G. Debenedetti and F. H. Stillinger, "Supercooled liquids and the glass transition," *Nature*, vol. 410, no. 6825, pp. 259–267, 2001.

[45] R. Kohlrausch, "Theorie des elektrischen rückstandes in der leidener flasche," *Annalen der Physik*, vol. 167, no. 2, pp. 179–214, 1854.

[46] G. Williams and D. C. Watts, "Non-symmetrical dielectric relaxation behaviour arising from a simple empirical decay function," *Transactions of the Faraday society*, vol. 66, pp. 80–85, 1970.

[47] R. Richert, “Homogeneous dispersion of dielectric responses in a simple glass,” *Journal of Non-Crystalline Solids*, vol. 172, pp. 209–213, 1994.

[48] G. P. Johari and M. Goldstein, “Viscous liquids and the glass transition. iii. secondary relaxations in aliphatic alcohols and other nonrigid molecules,” *The Journal of Chemical Physics*, vol. 55, no. 9, pp. 4245–4252, 1971.

[49] H. Stanley, *Introduction to phase transitions and critical phenomena.* International series of monographs on physics, Oxford University Press, 1971.

[50] W. Kauzmann, “The nature of the glassy state and the behavior of liquids at low temperatures.,” *Chemical Reviews*, vol. 43, no. 2, pp. 219–256, 1948.

[51] L. Berthier, P. Charbonneau, D. Coslovich, A. Ninarello, M. Ozawa, and S. Yaida, “Configurational entropy measurements in extremely supercooled liquids that break the glass ceiling,” *Proceedings of the National Academy of Sciences*, vol. 114, no. 43, pp. 11356–11361, 2017.

[52] J. H. Gibbs and E. A. DiMarzio, “Nature of the glass transition and the glassy state,” *The Journal of Chemical Physics*, vol. 28, no. 3, pp. 373–383, 1958.

[53] C. Angell, “Oxide glasses in light of the “ideal glass” concept: I, ideal and nonideal transitions, and departures from ideality,” *Journal of the American Ceramic Society*, vol. 51, no. 3, pp. 117–124, 1968.

[54] L. Boltzmann, “On the relation between the second law of the mechanical theory of heat and the probability calculus with respect to the theorems on thermal equilibrium,” *Kais Akad Wiss Wien Math Natumiss Classe*, vol. 76, pp. 373–435, 1877.

[55] G. Adam and J. H. Gibbs, “On the temperature dependence of cooperative relaxation properties in glass-forming liquids,” *The Journal of Chemical Physics*, vol. 43, no. 1, pp. 139–146, 1965.

[56] C. Angell, “Landscapes with megabasins: polyamorphism in liquids and biopolymers and the role of nucleation in folding and folding diseases,” *Physica D: Nonlinear Phenomena*, vol. 107, no. 2-4, pp. 122–142, 1997.

[57] L. Berthier, M. Ozawa, and C. Scalliet, “Configurational entropy of glass-forming liquids,” *The Journal of Chemical Physics*, vol. 150, no. 16, p. 160902, 2019.

[58] L. Berthier, P. Charbonneau, A. Ninarello, M. Ozawa, and S. Yaida, "Zero-temperature glass transition in two dimensions," *Nature Communications*, vol. 10, no. 1, pp. 1–7, 2019.

[59] T. Kirkpatrick and P. Wolynes, "Stable and metastable states in mean-field potts and structural glasses," *Physical Review B*, vol. 36, no. 16, p. 8552, 1987.

[60] T. R. Kirkpatrick, D. Thirumalai, and P. G. Wolynes, "Scaling concepts for the dynamics of viscous liquids near an ideal glassy state," *Physical Review A*, vol. 40, no. 2, p. 1045, 1989.

[61] S. Franz and G. Parisi, "Recipes for metastable states in spin glasses," *Journal de Physique I*, vol. 5, no. 11, pp. 1401–1415, 1995.

[62] S. Franz and G. Parisi, "Phase diagram of coupled glassy systems: A mean-field study," *Physical Review Letters*, vol. 79, no. 13, p. 2486, 1997.

[63] P. Charbonneau, J. Kurchan, G. Parisi, P. Urbani, and F. Zamponi, "Fractal free energy landscapes in structural glasses," *Nature Communications*, vol. 5, no. 1, pp. 1–6, 2014.

[64] P. Charbonneau, J. Kurchan, G. Parisi, P. Urbani, and F. Zamponi, "Glass and jamming transitions: From exact results to finite-dimensional descriptions," *Annual Review of Condensed Matter Physics*, vol. 8, pp. 265–288, 2017.

[65] G. Biroli, J.-P. Bouchaud, A. Cavagna, T. S. Grigera, and P. Verrocchio, "Thermodynamic signature of growing amorphous order in glass-forming liquids," *Nature Physics*, vol. 4, no. 10, pp. 771–775, 2008.

[66] W. Kob and L. Berthier, "Probing a liquid to glass transition in equilibrium," *Physical Review Letters*, vol. 110, no. 24, p. 245702, 2013.

[67] M. Goldstein, "Viscous liquids and the glass transition: a potential energy barrier picture," *The Journal of Chemical Physics*, vol. 51, no. 9, pp. 3728–3739, 1969.

[68] F. H. Stillinger, "A topographic view of supercooled liquids and glass formation," *Science*, vol. 267, no. 5206, pp. 1935–1939, 1995.

[69] Z. Raza, B. Alling, and I. A. Abrikosov, "Computer simulations of glasses: the potential energy landscape," *Journal of Physics: Condensed Matter*, vol. 27, no. 29, p. 293201, 2015.

[70] T. G. Fox and P. J. Flory, "Second-order transition temperatures and related properties of polystyrene. i. influence of molecular weight," *Journal of Applied Physics*, vol. 21, no. 6, pp. 581–591, 1950.

[71] T. G. Fox and P. J. Flory, "Further studies on the melt viscosity of polyisobutylene.," *The Journal of Physical Chemistry*, vol. 55, no. 2, pp. 221–234, 1951.

[72] T. G. Fox and P. J. Flory, "The glass temperature and related properties of polystyrene. influence of molecular weight," *Journal of Polymer Science*, vol. 14, no. 75, pp. 315–319, 1954.

[73] M. H. Cohen and D. Turnbull, "Molecular transport in liquids and glasses," *The Journal of Chemical Physics*, vol. 31, no. 5, pp. 1164–1169, 1959.

[74] D. Turnbull and M. H. Cohen, "Free-volume model of the amorphous phase: glass transition," *The Journal of Chemical Physics*, vol. 34, no. 1, pp. 120–125, 1961.

[75] R. Simha and R. Boyer, "On a general relation involving the glass temperature and coefficients of expansion of polymers," *The Journal of Chemical Physics*, vol. 37, no. 5, pp. 1003–1007, 1962.

[76] T. G. Fox and P. J. Flory, "Second-order transition temperatures and related properties of polystyrene. i. influence of molecular weight," *Journal of Applied Physics*, vol. 21, no. 6, pp. 581–591, 1950.

[77] A. K. Doolittle, "Studies in newtonian flow. ii. the dependence of the viscosity of liquids on free-space," *Journal of Applied Physics*, vol. 22, no. 12, pp. 1471–1475, 1951.

[78] D. M. Colucci, G. B. McKenna, J. J. Filliben, A. Lee, D. B. Curliss, K. B. Bowman, and J. D. Russell, "Isochoric and isobaric glass formation: Similarities and differences," *Journal of Polymer Science Part B: Polymer Physics*, vol. 35, no. 10, pp. 1561–1573, 1997.

[79] L. Yang, D. J. Srolovitz, and A. F. Yee, "Molecular dynamics study of isobaric and isochoric glass transitions in a model amorphous polymer," *The Journal of Chemical Physics*, vol. 110, no. 14, pp. 7058–7069, 1999.

[80] E. Leutheusser, "Dynamical model of the liquid-glass transition," *Physical Review A*, vol. 29, no. 5, p. 2765, 1984.

[81] U. Bengtzelius, W. Gotze, and A. Sjolander, "Dynamics of supercooled liquids and the glass transition," *Journal of Physics C: Solid State Physics*, vol. 17, no. 33, p. 5915, 1984.

[82] W. Kob and H. C. Andersen, "Testing mode-coupling theory for a supercooled binary lennard-jones mixture i: The van hove correlation function," *Physical Review E*, vol. 51, no. 5, p. 4626, 1995.

[83] C. L. Jackson and G. B. McKenna, "The glass transition of organic liquids confined to small pores," *Journal of Non-Crystalline Solids*, vol. 131, pp. 221–224, 1991.

[84] J. Schüller, Y. B. Mel'Nichenko, R. Richert, and E. W. Fischer, "Dielectric studies of the glass transition in porous media," *Physical Review Letters*, vol. 73, no. 16, p. 2224, 1994.

[85] S. Simon, J.-Y. Park, and G. McKenna, "Enthalpy recovery of a glass-forming liquid constrained in a nanoporous matrix: Negative pressure effects," *The European Physical Journal E*, vol. 8, pp. 209–216, 2002.

[86] T. Kawase, T. Shimoda, C. Newsome, H. Sirringhaus, and R. H. Friend, "Inkjet printing of polymer thin film transistors," *Thin Solid Films*, vol. 438, pp. 279–287, 2003.

[87] W. H. Meyer, "Polymer electrolytes for lithium-ion batteries," *Advanced Materials*, vol. 10, no. 6, pp. 439–448, 1998.

[88] J. L. Keddie, R. A. Jones, and R. A. Cory, "Interface and surface effects on the glass-transition temperature in thin polymer films," *Faraday Discussions*, vol. 98, pp. 219–230, 1994.

[89] J. Keddie and R. Jones, "Glass transition behavior in ultra-thin polystyrene films," *Israel Journal of Chemistry*, vol. 35, no. 1, pp. 21–26, 1995.

[90] J. Forrest, K. Dalnoki-Veress, and J. Dutcher, "Interface and chain confinement effects on the glass transition temperature of thin polymer films," *Physical Review E*, vol. 56, no. 5, p. 5705, 1997.

[91] K. Fukao and Y. Miyamoto, "Glass transitions and dynamics in thin polymer films: dielectric relaxation of thin films of polystyrene," *Physical Review E*, vol. 61, no. 2, p. 1743, 2000.

[92] K. Fukao and Y. Miyamoto, "Slow dynamics near glass transitions in thin polymer films," *Physical Review E*, vol. 64, no. 1, p. 011803, 2001.

[93] J. A. Forrest and K. Dalnoki-Veress, "The glass transition in thin polymer films," *Advances in Colloid and Interface Science*, vol. 94, no. 1-3, pp. 167–195, 2001.

[94] J. Sharp and J. Forrest, "Thickness dependence of the dynamics in thin films of isotactic poly (methylmethacrylate)," *The European Physical Journal E*, vol. 12, pp. 97–101, 2003.

[95] C. Roth and J. Dutcher, "Glass transition temperature of freely-standing films of atactic poly (methyl methacrylate)," *The European Physical Journal E*, vol. 12, pp. 103–107, 2003.

[96] C. J. Ellison, M. K. Mundra, and J. M. Torkelson, "Impacts of polystyrene molecular weight and modification to the repeat unit structure on the glass transition-nanoconfinement effect and the cooperativity length scale," *Macromolecules*, vol. 38, no. 5, pp. 1767–1778, 2005.

[97] C. Roth, A. Pound, S. Kamp, C. Murray, and J. Dutcher, "Molecular-weight dependence of the glass transition temperature of freely-standing poly (methyl methacrylate) films," *The European Physical Journal E*, vol. 20, pp. 441–448, 2006.

[98] R. D. Priestley, M. K. Mundra, N. J. Barnett, L. J. Broadbelt, and J. M. Torkelson, "Effects of nanoscale confinement and interfaces on the glass transition temperatures of a series of poly (n-methacrylate) films," *Australian Journal of Chemistry*, vol. 60, no. 10, pp. 765–771, 2007.

[99] R. D. Priestley, L. J. Broadbelt, J. M. Torkelson, and K. Fukao, "Glass transition and α-relaxation dynamics of thin films of labeled polystyrene," *Physical Review E*, vol. 75, no. 6, p. 061806, 2007.

[100] J.-L. Masson and P. F. Green, "Viscosity of entangled polystyrene thin film melts: Film thickness dependence," *Physical Review E*, vol. 65, no. 3, p. 031806, 2002.

[101] T. Koga, C. Li, M. Endoh, J. Koo, M. Rafailovich, S. Narayanan, D. Lee, L. Lurio, and S. Sinha, "Reduced viscosity of the free surface in entangled polymer melt films," *Physical Review Letters*, vol. 104, no. 6, p. 066101, 2010.

[102] C. M. Stafford, C. Harrison, K. L. Beers, A. Karim, E. J. Amis, M. R. VanLandingham, H.-C. Kim, W. Volksen, R. D. Miller, and E. E. Simonyi, "A buckling-based

metrology for measuring the elastic moduli of polymeric thin films," *Nature Materials*, vol. 3, no. 8, pp. 545–550, 2004.

[103] P. O'Connell and G. McKenna, "Dramatic stiffening of ultrathin polymer films in the rubbery regime," *The European Physical Journal E*, vol. 20, pp. 143–150, 2006.

[104] J. M. Torres, C. M. Stafford, and B. D. Vogt, "Elastic modulus of amorphous polymer thin films: relationship to the glass transition temperature," *ACS Nano*, vol. 3, no. 9, pp. 2677–2685, 2009.

[105] R. A. Riggleman, K. Yoshimoto, J. F. Douglas, and J. J. de Pablo, "Influence of confinement on the fragility of antiplasticized and pure polymer films," *Physical Review Letters*, vol. 97, no. 4, p. 045502, 2006.

[106] P. Z. Hanakata, J. F. Douglas, and F. W. Starr, "Local variation of fragility and glass transition temperature of ultra-thin supported polymer films," *The Journal of Chemical Physics*, vol. 137, no. 24, p. 244901, 2012.

[107] C. Zhang and R. D. Priestley, "Fragility and glass transition temperature of polymer confined under isobaric and isochoric conditions," *Soft Matter*, vol. 9, no. 29, pp. 7076–7085, 2013.

[108] C. M. Evans, H. Deng, W. F. Jager, and J. M. Torkelson, "Fragility is a key parameter in determining the magnitude of t g-confinement effects in polymer films," *Macromolecules*, vol. 46, no. 15, pp. 6091–6103, 2013.

[109] E. C. Glor, R. J. Composto, and Z. Fakhraai, "Glass transition dynamics and fragility of ultrathin miscible polymer blend films," *Macromolecules*, vol. 48, no. 18, pp. 6682–6689, 2015.

[110] C. Ellison, S. Kim, D. Hall, and J. Torkelson, "Confinement and processing effects on glass transition temperature and physical aging in ultrathin polymer films: Novel fluorescence measurements," *The European Physical Journal E*, vol. 8, pp. 155–166, 2002.

[111] R. D. Priestley, L. J. Broadbelt, and J. M. Torkelson, "Physical aging of ultrathin polymer films above and below the bulk glass transition temperature: Effects of attractive vs neutral polymer-substrate interactions measured by fluorescence," *Macromolecules*, vol. 38, no. 3, pp. 654–657, 2005.

[112] J. E. Pye, K. A. Rohald, E. A. Baker, and C. B. Roth, "Physical aging in ultrathin polystyrene films: Evidence of a gradient in dynamics at the free surface and its connection to the glass transition temperature reductions," *Macromolecules*, vol. 43, no. 19, pp. 8296–8303, 2010.

[113] D. Cangialosi, A. Alegria, and J. Colmenero, "Effect of nanostructure on the thermal glass transition and physical aging in polymer materials," *Progress in Polymer Science*, vol. 54, pp. 128–147, 2016.

[114] S. Napolitano and M. Wübbenhorst, "The lifetime of the deviations from bulk behaviour in polymers confined at the nanoscale," *Nature Communications*, vol. 2, no. 1, p. 260, 2011.

[115] A. Panagopoulou and S. Napolitano, "Irreversible adsorption governs the equilibration of thin polymer films," *Physical Review Letters*, vol. 119, no. 9, p. 097801, 2017.

[116] M. D. Ediger and J. A. Forrest, "Dynamics near free surfaces and the glass transition in thin polymer films: a view to the future," *Macromolecules*, vol. 47, no. 2, pp. 471–478, 2014.

[117] J. S. Sharp, J. H. Teichroeb, and J. A. Forrest, "The properties of free polymer surfaces and their influence on the glass transition temperature of thin polystyrene films," *The European Physical Journal E*, vol. 15, no. 4, pp. 473–487, 2004.

[118] S. A. Hutcheson and G. B. McKenna, "Nanosphere embedding into polymer surfaces: A viscoelastic contact mechanics analysis," *Physical Review Letters*, vol. 94, no. 7, p. 076103, 2005.

[119] R. D. Deshmukh and R. J. Composto, "Direct observation of nanoparticle embedding into the surface of a polymer melt," *Langmuir*, vol. 23, no. 26, pp. 13169–13173, 2007.

[120] M. Ilton, D. Qi, and J. Forrest, "Using nanoparticle embedding to probe surface rheology and the length scale of surface mobility in glassy polymers," *Macromolecules*, vol. 42, no. 18, pp. 6851–6854, 2009.

[121] C. R. Daley, Z. Fakhraai, M. D. Ediger, and J. A. Forrest, "Comparing surface and bulk flow of a molecular glass former," *Soft Matter*, vol. 8, no. 7, pp. 2206–2212, 2012.

[122] D. Qi, C. R. Daley, Y. Chai, and J. A. Forrest, "Molecular weight dependence of near surface dynamical mechanical properties of polymers," *Soft Matter*, vol. 9, no. 37, pp. 8958–8964, 2013.

[123] D. Qi, Z. Fakhraai, and J. A. Forrest, "Substrate and chain size dependence of near surface dynamics of glassy polymers," *Physical Review Letters*, vol. 101, no. 9, p. 096101, 2008.

[124] Y. Zhang, R. Potter, W. Zhang, and Z. Fakhraai, "Using tobacco mosaic virus to probe enhanced surface diffusion of molecular glasses," *Soft Matter*, vol. 12, no. 44, pp. 9115–9120, 2016.

[125] Y. Zhang and Z. Fakhraai, "Decoupling of surface diffusion and relaxation dynamics of molecular glasses," *Proceedings of the National Academy of Sciences*, vol. 114, no. 19, pp. 4915–4919, 2017.

[126] Y. Zhang and Z. Fakhraai, "Invariant fast diffusion on the surfaces of ultrastable and aged molecular glasses," *Physical Review Letters*, vol. 118, no. 6, p. 066101, 2017.

[127] L. Zhu, C. Brian, S. Swallen, P. Straus, M. Ediger, and L. Yu, "Surface self-diffusion of an organic glass," *Physical Review Letters*, vol. 106, no. 25, p. 256103, 2011.

[128] R. Malshe, M. Ediger, L. Yu, and J. De Pablo, "Evolution of glassy gratings with variable aspect ratios under surface diffusion," *The Journal of Chemical Physics*, vol. 134, no. 19, p. 194704, 2011.

[129] Z. Yang, C.-H. Lam, E. DiMasi, N. Bouet, J. Jordan-Sweet, and O. K. Tsui, "Method to measure the viscosity of nanometer liquid films from the surface fluctuations," *Applied Physics Letters*, vol. 94, no. 25, p. 251906, 2009.

[130] C. W. Brian, L. Zhu, and L. Yu, "Effect of bulk aging on surface diffusion of glasses," *The Journal of Chemical Physics*, vol. 140, no. 5, p. 054509, 2014.

[131] Y. Chen, W. Zhang, and L. Yu, "Hydrogen bonding slows down surface diffusion of molecular glasses," *The Journal of Physical Chemistry B*, vol. 120, no. 32, pp. 8007–8015, 2016.

[132] S. Ruan, W. Zhang, Y. Sun, M. Ediger, and L. Yu, "Surface diffusion and surface crystal growth of tris-naphthyl benzene glasses," *The Journal of Chemical Physics*, vol. 145, no. 6, p. 064503, 2016.

[133] H. Tian, Q. Xu, H. Zhang, R. D. Priestley, and B. Zuo, "Surface dynamics of glasses," *Applied Physics Reviews*, vol. 9, no. 1, p. 011316, 2022.

[134] K. L. Kearns, S. F. Swallen, M. D. Ediger, T. Wu, Y. Sun, and L. Yu, “Hiking down the energy landscape: Progress toward the kauzmann temperature via vapor deposition,” *The Journal of Physical Chemistry B*, vol. 112, no. 16, pp. 4934–4942, 2008.

[135] L. Berthier, P. Charbonneau, E. Flenner, and F. Zamponi, “Origin of ultrastability in vapor-deposited glasses,” *Physical Review Letters*, vol. 119, no. 18, p. 188002, 2017.

[136] S. F. Swallen, K. L. Kearns, M. K. Mapes, Y. S. Kim, R. J. McMahon, M. D. Ediger, T. Wu, L. Yu, and S. Satija, “Organic glasses with exceptional thermodynamic and kinetic stability,” *Science*, vol. 315, no. 5810, pp. 353–356, 2007.

[137] E. Leon-Gutierrez, A. Sepúlveda, G. Garcia, M. T. Clavaguera-Mora, and J. Rodríguez-Viejo, “Stability of thin film glasses of toluene and ethylbenzene formed by vapor deposition: an in situ nanocalorimetric study,” *Physical Chemistry Chemical Physics*, vol. 12, no. 44, pp. 14693–14698, 2010.

[138] S. Singh and J. J. de Pablo, “A molecular view of vapor deposited glasses,” *The Journal of Chemical Physics*, vol. 134, no. 19, p. 194903, 2011.

[139] S. S. Dalal, A. Sepúlveda, G. K. Pribil, Z. Fakhraai, and M. Ediger, “Density and birefringence of a highly stable α, α, β-trisnaphthylbenzene glass,” *The Journal of Chemical Physics*, vol. 136, no. 20, p. 204501, 2012.

[140] S. S. Dalal, Z. Fakhraai, and M. D. Ediger, “High-throughput ellipsometric characterization of vapor-deposited indomethacin glasses,” *The Journal of Physical Chemistry B*, vol. 117, no. 49, pp. 15415–15425, 2013.

[141] Y. Chua, M. Ahrenberg, M. Tylinski, M. Ediger, and C. Schick, “How much time is needed to form a kinetically stable glass? ac calorimetric study of vapor-deposited glasses of ethylcyclohexane,” *The Journal of Chemical Physics*, vol. 142, no. 5, p. 054506, 2015.

[142] K. Dawson, L. A. Kopff, L. Zhu, R. J. McMahon, L. Yu, R. Richert, and M. Ediger, “Molecular packing in highly stable glasses of vapor-deposited tris-naphthylbenzene isomers,” *The Journal of Chemical Physics*, vol. 136, no. 9, p. 094505, 2012.

[143] S. Singh, M. D. Ediger, and J. J. De Pablo, “Ultrastable glasses from in silico vapour deposition,” *Nature Materials*, vol. 12, no. 2, pp. 139–144, 2013.

[144] K. L. Kearns, S. F. Swallen, M. Ediger, T. Wu, and L. Yu, “Influence of substrate temperature on the stability of glasses prepared by vapor deposition,” *The Journal of Chemical Physics*, vol. 127, no. 15, p. 154702, 2007.

[145] T. Liu, K. Cheng, E. Salami-Ranjbaran, F. Gao, C. Li, X. Tong, Y.-C. Lin, Y. Zhang, W. Zhang, L. Klinge, *et al.*, “The effect of chemical structure on the stability of physical vapor deposited glasses of 1, 3, 5-triarylbenzene,” *The Journal of Chemical Physics*, vol. 143, no. 8, p. 084506, 2015.

[146] Z. Fakhraai, T. Still, G. Fytas, and M. Ediger, “Structural variations of an organic glassformer vapor-deposited onto a temperature gradient stage,” *The Journal of Physical Chemistry Letters*, vol. 2, no. 5, pp. 423–427, 2011.

[147] D. Bhattacharya and V. Sadtchenko, “Enthalpy and high temperature relaxation kinetics of stable vapor-deposited glasses of toluene,” *The Journal of Chemical Physics*, vol. 141, no. 9, p. 094502, 2014.

[148] K. L. Kearns, P. Krzyskowski, and Z. Devereaux, “Using deposition rate to increase the thermal and kinetic stability of vapor-deposited hole transport layer glasses via a simple sublimation apparatus,” *The Journal of Chemical Physics*, vol. 146, no. 20, p. 203328, 2017.

[149] T. Hales, M. Adams, G. Bauer, T. D. Dang, J. Harrison, H. Le Truong, C. Kaliszyk, V. Magron, S. McLaughlin, T. T. Nguyen, *et al.*, “A formal proof of the kepler conjecture,” in *Forum of Mathematics, Pi*, vol. 5, Cambridge University Press, 2017.

[150] J. Kepler, *The Six-Cornered Snowflake.* Paul Dry Books, 2010.

[151] M. Mezard and A. Montanari, *Information, physics, and computation.* Oxford University Press, 2009.

[152] H.-B. Yu, Y. Luo, and K. Samwer, “Ultrastable metallic glass,” *Advanced Materials*, vol. 25, no. 41, pp. 5904–5908, 2013.

[153] P. Luo, C. R. Cao, F. Zhu, Y. M. Lv, Y. H. Liu, P. Wen, H. Y. Bai, G. Vaughan, M. Di Michiel, B. Ruta, *et al.*, “Ultrastable metallic glasses formed on cold substrates,” *Nature Communications*, vol. 9, no. 1, p. 1389, 2018.

[154] V. Svorcik, V. Rybka, K. Efimenko, and V. Hnatowicz, “Deposition of polystyrene films by vacuum evaporation,” *Journal of Materials Science Letters*, vol. 16, no. 19, pp. 1564–1566, 1997.

[155] J. Zhang, C. Con, and B. Cui, "Electron beam lithography on irregular surfaces using an evaporated resist," *ACS Nano*, vol. 8, no. 4, pp. 3483–3489, 2014.

[156] M. Wübbenhorst, A. Kasina, S. Capponi, B. Vanroy, and S. Napolitano, "Ultrathin polymer films by single molecule deposition," *Journal of Non-Crystalline Solids*, vol. 407, pp. 270–276, 2015.

[157] Y. Guo, A. Morozov, D. Schneider, J. W. Chung, C. Zhang, M. Waldmann, N. Yao, G. Fytas, C. B. Arnold, and R. D. Priestley, "Ultrastable nanostructured polymer glasses," *Nature Materials*, vol. 11, no. 4, pp. 337–343, 2012.

[158] H. Yoon, Y. P. Koh, S. L. Simon, and G. B. McKenna, "An ultrastable polymeric glass: Amorphous fluoropolymer with extreme fictive temperature reduction by vacuum pyrolysis," *Macromolecules*, vol. 50, no. 11, pp. 4562–4574, 2017.

[159] S. Zhu, Y. Chai, and J. Forrest, "Evaporative purification to produce highly monodisperse polymers: Application to polystyrene for $n = 3 - 13$ and quantification of t_{g} from oligomer to polymer," *Physical Review Materials*, vol. 1, no. 2, p. 025605, 2017.

[160] M. Guaita, "Thermal degradation of polystyrene," *British Polymer Journal*, vol. 18, no. 4, pp. 226–230, 1986.

[161] D. J. De Smet, *A child's garden of ellipsometry.* not published.

[162] The manual book of EXACTA 2000 ellipsometer. Waterloo digital electronics, 1999.

[163] Z. Fakhraai, *Dynamics of polymer thin films and surfaces.* PhD thesis, Waterloo, Ontario, Canada, 2007.

[164] S. S. Dalal and M. D. Ediger, "Influence of substrate temperature on the transformation front velocities that determine thermal stability of vapor-deposited glasses," *The Journal of Physical Chemistry B*, vol. 119, no. 9, pp. 3875–3882, 2015.

[165] M. D. Ediger, J. de Pablo, and L. Yu, "Anisotropic vapor-deposited glasses: Hybrid organic solids," *Accounts of Chemical Research*, vol. 52, no. 2, pp. 407–414, 2019.

[166] I. Lyubimov, L. Antony, D. M. Walters, D. Rodney, M. Ediger, and J. J. de Pablo, "Orientational anisotropy in simulated vapor-deposited molecular glasses," *The Journal of Chemical Physics*, vol. 143, no. 9, p. 094502, 2015.

[167] K. Bagchi, N. E. Jackson, A. Gujral, C. Huang, M. F. Toney, L. Yu, J. J. De Pablo, and M. Ediger, “Origin of anisotropic molecular packing in vapor-deposited alq3 glasses,” *The Journal of Physical Chemistry Letters*, vol. 10, no. 2, pp. 164–170, 2018.

[168] P.-H. Lin, I. Lyubimov, L. Yu, M. Ediger, and J. J. de Pablo, “Molecular modeling of vapor-deposited polymer glasses,” *The Journal of Chemical Physics*, vol. 140, no. 20, p. 204504, 2014.

[169] Y. Chai, A. N. Raegen, S. Zhu, and J. A. Forrest, “Crystallization of low molecular weight atactic polystyrene,” *Soft Matter*, vol. 14, no. 33, pp. 6883–6891, 2018.

[170] I. Ohlídal, J. Vohánka, V. Buršíková, D. Franta, and M. Čermák, “Spectroscopic ellipsometry of inhomogeneous thin films exhibiting thickness non-uniformity and transition layers,” *Optics Express*, vol. 28, no. 1, pp. 160–174, 2020.

[171] B. G. Ranby and J. F. Rabek, *Photodegradation, photo-oxidation, and photostabilization of polymers*. New York, Wiley, 1975.

[172] A. Shyichuk and J. White, “Analysis of chain-scission and crosslinking rates in the photo-oxidation of polystyrene,” *Journal of Applied Polymer Science*, vol. 77, no. 13, pp. 3015–3023, 2000.

[173] E. Yousif and R. Haddad, “Photodegradation and photostabilization of polymers, especially polystyrene,” *SpringerPlus*, vol. 2, no. 1, pp. 1–32, 2013.

[174] B. G. Ranby, “Photodegradation and photo-oxidation of synthetic polymers,” *Journal of Analytical and Applied Pyrolysis*, vol. 15, pp. 237–247, 1989.

[175] S. I. Kuzina and A. I. Mikhailov, “The photo-oxidation of polymers—3. the main reaction of chain propagation in polystyrene photo-oxidation,” *European Polymer Journal*, vol. 34, no. 8, pp. 1157–1162, 1998.

[176] H. Klevens, “Extreme ultraviolet absorption spectra of various polymers,” *Journal of Polymer Science*, vol. 10, no. 1, pp. 97–107, 1953.

[177] T. Li, C. Zhou, and M. Jiang, “Uv absorption spectra of polystyrene,” *Polymer Bulletin*, vol. 25, no. 2, pp. 211–216, 1991.

[178] R. H. Partridge, “Vacuum-ultraviolet absorption spectrum of polystyrene,” *The Journal of Chemical Physics*, vol. 47, no. 10, pp. 4223–4227, 1967.

[179] M. J. Reiney, M. Tryon, and B. Achhammer, "Study of degradation of polystyrene, using ultraviolet spectrophotometry," *Journal of Research of the National Bureau of Standards*, vol. 51, no. 3, pp. 155–165, 1953.

[180] K. Ueberreiter and G. Kanig, "Second-order transitions and mesh distribution functions of cross-linked polystyrenes," *The Journal of Chemical Physics*, vol. 18, no. 4, pp. 399–406, 1950.

[181] T. Fox and S. Loshaek, "Influence of molecular weight and degree of crosslinking on the specific volume and glass temperature of polymers," *Journal of Polymer Science*, vol. 15, no. 80, pp. 371–390, 1955.

[182] D. Roberts and L. Mandelkern, "The melting temperature of natural rubber networks," *Journal of the American Chemical Society*, vol. 82, no. 5, pp. 1091–1095, 1960.

[183] W. Kuhn and G. Balmer, "Crosslinking of single linear macromolecules," *Journal of Polymer Science*, vol. 57, no. 165, pp. 311–319, 1962.

[184] P. Mason, "Thermal expansion and viscoelasticity of rubber in relation to crosslinking and molecular packing," *Polymer*, vol. 5, pp. 625–635, 1964.

[185] K. Shibayama and M. Kodama, "Effects of concentration of urethane linkage, crosslinking density, and swelling upon the viscoelastic properties of polyurethanes," *Journal of Polymer Science Part A-1: Polymer Chemistry*, vol. 4, no. 1, pp. 83–108, 1966.

[186] D. Anderson, "Thermal conductivity of polymers," *Chemical Reviews*, vol. 66, no. 6, pp. 677–690, 1966.

[187] L. E. Nielsen, "Cross-linking–effect on physical properties of polymers," *Journal of Macromolecular Science, Part C*, vol. 3, no. 1, pp. 69–103, 1969.

[188] J. E. Martin and B. Eichinger, "Dimensions of intramolecularly crosslinked polymers. 1. theory," *Macromolecules*, vol. 16, no. 8, pp. 1345–1350, 1983.

[189] J. E. Martin and B. Eichinger, "Dimensions of intramolecularly crosslinked polymers. 2. dilute solution thermodynamic parameters and photon correlation results on the polystyrene/cyclopentane system," *Macromolecules*, vol. 16, no. 8, pp. 1350–1358, 1983.

[190] M. Antonietti and H. Sillescu, "Diffusion of intramolecular crosslinked and three-arm-star branched polystyrene molecules in different matrixes," *Macromolecules*, vol. 19, no. 3, pp. 798–803, 1986.

[191] M. Antonietti, H. Sillescu, M. Schmidt, and H. Schuch, "Solution properties and dynamic bulk behavior of intramolecular cross-linked polystyrene," *Macromolecules*, vol. 21, no. 3, pp. 736–742, 1988.

[192] H. Stutz, K.-H. Illers, and J. Mertes, "A generalized theory for the glass transition temperature of crosslinked and uncrosslinked polymers," *Journal of Polymer Science Part B: Polymer Physics*, vol. 28, no. 9, pp. 1483–1498, 1990.

[193] P. J. Flory, "Molecular size distribution in three dimensional polymers. i. gelation1," *Journal of the American Chemical Society*, vol. 63, no. 11, pp. 3083–3090, 1941.

[194] P. J. Flory, "Molecular size distribution in three dimensional polymers. ii. trifunctional branching units," *Journal of the American Chemical Society*, vol. 63, no. 11, pp. 3091–3096, 1941.

[195] J. F. Yan, "Cross-linking of polymers with a primary size distribution," *Macromolecules*, vol. 12, no. 2, pp. 260–264, 1979.

[196] K. Jin and J. M. Torkelson, "Enhanced T_g-confinement effect in cross-linked polystyrene compared to its linear precursor: roles of fragility and chain architecture," *Macromolecules*, vol. 49, no. 14, pp. 5092–5103, 2016.

[197] Y. Qiu, S. S. Dalal, and M. Ediger, "Vapor-deposited organic glasses exhibit enhanced stability against photodegradation," *Soft Matter*, vol. 14, no. 15, pp. 2827–2834, 2018.

[198] Y. Qiu, L. W. Antony, J. J. de Pablo, and M. Ediger, "Photostability can be significantly modulated by molecular packing in glasses," *Journal of the American Chemical Society*, vol. 138, no. 35, pp. 11282–11289, 2016.

[199] G. Beaucage, R. Composto, and R. Stein, "Ellipsometric study of the glass transition and thermal expansion coefficients of thin polymer films," *Journal of Polymer Science Part B: Polymer Physics*, vol. 31, no. 3, pp. 319–326, 1993.

[200] Y.-C. Lin, M. H. Repollet-Pedrosa, J. J. Ferrie, E. J. Petersson, and Z. Fakhraai, "Potential artifacts in sample preparation methods used for imaging amyloid oligomers and protofibrils due to surface-mediated fibril formation," *The Journal of Physical Chemistry B*, vol. 121, no. 12, pp. 2534–2542, 2017.

[201] A. N. Raegen, Q. Zhou, and J. A. Forrest, "Anisotropy and anharmonicity in polystyrene stable glass," *The Journal of Chemical Physics*, vol. 153, no. 21, p. 214508, 2020.

[202] V. Trujillo, J. Kim, and R. C. Hayward, "Creasing instability of surface-attached hydrogels," *Soft Matter*, vol. 4, no. 3, pp. 564–569, 2008.

[203] N. Bowden, S. Brittain, A. G. Evans, J. W. Hutchinson, and G. M. Whitesides, "Spontaneous formation of ordered structures in thin films of metals supported on an elastomeric polymer," *Nature*, vol. 393, no. 6681, pp. 146–149, 1998.

[204] D.-Y. Khang, H. Jiang, Y. Huang, and J. A. Rogers, "A stretchable form of single-crystal silicon for high-performance electronics on rubber substrates," *Science*, vol. 311, no. 5758, pp. 208–212, 2006.

[205] J. Huang, M. Juszkiewicz, W. H. De Jeu, E. Cerda, T. Emrick, N. Menon, and T. P. Russell, "Capillary wrinkling of floating thin polymer films," *Science*, vol. 317, no. 5838, pp. 650–653, 2007.

[206] D. Chandra and A. J. Crosby, "Self-wrinkling of uv-cured polymer films," *Advanced Materials*, vol. 23, no. 30, pp. 3441–3445, 2011.

[207] H. Hou, K. Hu, H. Lin, J. Forth, W. Zhang, T. P. Russell, J. Yin, and X. Jiang, "Reversible surface patterning by dynamic crosslink gradients: controlling buckling in 2d," *Advanced Materials*, vol. 30, no. 36, p. 1803463, 2018.

[208] Z. Hao, A. Ghanekarade, N. Zhu, K. Randazzo, D. Kawaguchi, K. Tanaka, X. Wang, D. S. Simmons, R. D. Priestley, and B. Zuo, "Mobility gradients yield rubbery surfaces on top of polymer glasses," *Nature*, vol. 596, no. 7872, pp. 372–376, 2021.

[209] I. Siretanu, H. Saadaoui, J.-P. Chapel, and C. Drummond, "Spatial heterogeneity of glassy polymer films," *Macromolecules*, vol. 48, no. 8, pp. 2787–2792, 2015.

[210] J. A. Forrest and K. Dalnoki-Veress, "When does a glass transition temperature not signify a glass transition?," *ACS Macro Letters*, vol. 3, no. 4, pp. 310–314, 2014.

[211] S. L. L. M. Ramos, M. Oguni, K. Ishii, and H. Nakayama, "Character of devitrification, viewed from enthalpic paths, of the vapor-deposited ethylbenzene glasses," *The Journal of Physical Chemistry B*, vol. 115, no. 49, pp. 14327–14332, 2011.

[212] E. Leon-Gutierrez, A. Sepúlveda, G. Garcia, M. T. Clavaguera-Mora, and J. Rodríguez-Viejo, "Correction: Stability of thin film glasses of toluene and ethylbenzene formed by vapor deposition: an in situ nanocalorimetric study," *Physical Chemistry Chemical Physics*, vol. 18, no. 11, pp. 8244–8245, 2016.

[213] S. Ren, C. Pedersen, A. Carlson, T. Salez, and Y. Wang, "Capillary deformation of ultrathin glassy polymer films by air nanobubbles," *Physical Review Research*, vol. 2, no. 4, p. 043166, 2020.

[214] J. Turkevich, P. C. Stevenson, and J. Hillier, "A study of the nucleation and growth processes in the synthesis of colloidal gold," *Discussions of the Faraday Society*, vol. 11, pp. 55–75, 1951.

[215] G. K. Batchelor, *An introduction to fluid dynamics.* Cambridge University Press, 1967.

[216] A. Oron, S. H. Davis, and S. G. Bankoff, "Long-scale evolution of thin liquid films," *Reviews of Modern Physics*, vol. 69, no. 3, p. 931, 1997.

[217] J. Eggers, "Contact line motion for partially wetting fluids," *Physical Review E*, vol. 72, no. 6, p. 061605, 2005.

[218] S. Poulain, A. Carlson, S. Mandre, and L. Mahadevan, "Elastohydrodynamics of contact in adherent sheets," *Journal of Fluid Mechanics*, vol. 947, p. A16, 2022.

[219] C. Pedersen, S. Ren, Y. Wang, A. Carlson, and T. Salez, "Nanobubble-induced flow of immersed glassy polymer films," *Physical Review Fluids*, vol. 6, no. 11, p. 114006, 2021.

[220] T. Salez, J. D. McGraw, O. Bäumchen, K. Dalnoki-Veress, and E. Raphaël, "Capillary-driven flow induced by a stepped perturbation atop a viscous film," *Physics of Fluids*, vol. 24, no. 10, p. 102111, 2012.

[221] C. R. Cao, Y. M. Lu, H. Y. Bai, and W. H. Wang, "High surface mobility and fast surface enhanced crystallization of metallic glass," *Applied Physics Letters*, vol. 107, no. 14, p. 141606, 2015.

[222] Y. Chai, T. Salez, and J. A. Forrest, "Using M_{w} dependence of surface dynamics of glassy polymers to probe the length scale of free-surface mobility," *Macromolecules*, vol. 53, no. 3, pp. 1084–1089, 2020.

[223] T. Salez, J. Salez, K. Dalnoki-Veress, E. Raphaël, and J. A. Forrest, “Cooperative strings and glassy interfaces,” *Proceedings of the National Academy of Sciences*, vol. 112, no. 27, pp. 8227–8231, 2015.

[224] G. Parisi, P. Urbani, and F. Zamponi, *Theory of simple glasses: exact solutions in infinite dimensions*. Cambridge University Press, 2020.

[225] E. Leon-Gutierrez, G. Garcia, A. F. Lopeandia, M. T. Clavaguera-Mora, and J. Rodriguez-Viejo, “Size effects and extraordinary stability of ultrathin vapor deposited glassy films of toluene,” *The Journal of Physical Chemistry Letters*, vol. 1, no. 1, pp. 341–345, 2010.

[226] C. J. Ellison, R. L. Ruszkowski, N. J. Fredin, and J. M. Torkelson, “Dramatic reduction of the effect of nanoconfinement on the glass transition of polymer films via addition of small-molecule diluent,” *Physical Review Letters*, vol. 92, no. 9, p. 095702, 2004.

[227] O. K. Tsui and H. Zhang, “Effects of chain ends and chain entanglement on the glass transition temperature of polymer thin films,” *Macromolecules*, vol. 34, no. 26, pp. 9139–9142, 2001.

[228] S. S. Dalal and M. D. Ediger, “Molecular orientation in stable glasses of indomethacin,” *The Journal of Physical Chemistry Letters*, vol. 3, no. 10, pp. 1229–1233, 2012.

[229] M. Ahrenberg, Y. Z. Chua, K. R. Whitaker, H. Huth, M. D. Ediger, and C. Schick, “In situ investigation of vapor-deposited glasses of toluene and ethylbenzene via alternating current chip-nanocalorimetry,” *The Journal of Chemical Physics*, vol. 138, no. 2, p. 024501, 2013.

[230] Z. Fakhraai and J. A. Forrest, “Probing slow dynamics in supported thin polymer films,” *Physical Review Letters*, vol. 95, no. 2, p. 025701, 2005.

[231] Y. P. Koh and S. L. Simon, “The glass transition and enthalpy recovery of a single polystyrene ultrathin film using flash dsc,” *The Journal of Chemical Physics*, vol. 146, no. 20, p. 203329, 2017.

[232] P. G. Wolynes, “Spatiotemporal structures in aging and rejuvenating glasses,” *Proceedings of the National Academy of Sciences*, vol. 106, no. 5, pp. 1353–1358, 2009.

[233] K. L. Kearns, M. Ediger, H. Huth, and C. Schick, "One micrometer length scale controls kinetic stability of low-energy glasses," *The Journal of Physical Chemistry Letters*, vol. 1, no. 1, pp. 388–392, 2010.

[234] R. L. Jack and L. Berthier, "The melting of stable glasses is governed by nucleation-and-growth dynamics," *The Journal of Chemical Physics*, vol. 144, no. 24, p. 244506, 2016.

[235] S. F. Swallen, K. L. Kearns, S. Satija, K. Traynor, R. J. McMahon, and M. Ediger, "Molecular view of the isothermal transformation of a stable glass to a liquid," *The Journal of Chemical Physics*, vol. 128, no. 21, p. 214514, 2008.

[236] S. F. Swallen, K. Traynor, R. J. McMahon, M. Ediger, and T. E. Mates, "Stable glass transformation to supercooled liquid via surface-initiated growth front," *Physical Review Letters*, vol. 102, no. 6, p. 065503, 2009.

[237] Z. Chen, A. Sepúlveda, M. Ediger, and R. Richert, "Dynamics of glass-forming liquids. xvi. observation of ultrastable glass transformation via dielectric spectroscopy," *The Journal of Chemical Physics*, vol. 138, no. 12, p. 12A519, 2013.

[238] D. M. Walters, R. Richert, and M. D. Ediger, "Thermal stability of vapor-deposited stable glasses of an organic semiconductor," *The Journal of Chemical Physics*, vol. 142, no. 13, p. 134504, 2015.

[239] M. Tylinski, A. Sepúlveda, D. M. Walters, Y. Chua, C. Schick, and M. Ediger, "Vapor-deposited glasses of methyl-m-toluate: How uniform is stable glass transformation?," *The Journal of Chemical Physics*, vol. 143, no. 24, p. 244509, 2015.

[240] C. Rodríguez-Tinoco, M. Gonzalez-Silveira, J. Rafols-Ribé, A. F. Lopeandía, and J. Rodríguez-Viejo, "Transformation kinetics of vapor-deposited thin film organic glasses: the role of stability and molecular packing anisotropy," *Physical Chemistry Chemical Physics*, vol. 17, no. 46, pp. 31195–31201, 2015.

[241] J. Ràfols-Ribé, A. Vila-Costa, C. Rodríguez-Tinoco, A. F. Lopeandía, J. Rodríguez-Viejo, and M. Gonzalez-Silveira, "Kinetic arrest of front transformation to gain access to the bulk glass transition in ultrathin films of vapour-deposited glasses," *Physical Chemistry Chemical Physics*, vol. 20, no. 47, pp. 29989–29995, 2018.

[242] A. Sepúlveda, M. Tylinski, A. Guiseppi-Elie, R. Richert, and M. Ediger, "Role of fragility in the formation of highly stable organic glasses," *Physical Review Letters*, vol. 113, no. 4, p. 045901, 2014.

[243] J. Ràfols-Ribé, M. Gonzalez-Silveira, C. Rodríguez-Tinoco, and J. Rodríguez-Viejo, "The role of thermodynamic stability in the characteristics of the devitrification front of vapour-deposited glasses of toluene," *Physical Chemistry Chemical Physics*, vol. 19, no. 18, pp. 11089–11097, 2017.

[244] C. Rodriguez-Tinoco, M. Gonzalez-Silveira, J. Rafols-Ribe, A. Vila-Costa, J. C. Martinez-Garcia, and J. Rodriguez-Viejo, "Surface-bulk interplay in vapor-deposited glasses: Crossover length and the origin of front transformation," *Physical Review Letters*, vol. 123, no. 15, p. 155501, 2019.

[245] A. Wisitsorasak and P. G. Wolynes, "Fluctuating mobility generation and transport in glasses," *Physical Review E*, vol. 88, no. 2, p. 022308, 2013.

[246] C. Rodríguez-Tinoco, M. Gonzalez-Silveira, J. Ràfols-Ribé, A. F. Lopeandía, M. T. Clavaguera-Mora, and J. Rodríguez-Viejo, "Evaluation of growth front velocity in ultrastable glasses of indomethacin over a wide temperature interval," *The Journal of Physical Chemistry B*, vol. 118, no. 36, pp. 10795–10801, 2014.

[247] G. R. Strobl and G. R. Strobl, *The physics of polymers*, vol. 2. Springer, 1997.

[248] K. Chang, "The nature of glass remains anything but clear," *The New York Times*, 2008.

APPENDICES

Appendix A

List of publications

1. A. N. Raegen, **J. Yin**, Q. Zhou, & J. A. Forrest. Ultrastable monodisperse polymer glass formed by physical vapour deposition. *Nature Materials*, 19(10), 1110-1113 (2020). DOI: 10.1038/s41563-020-0723-7 [1].
2. **J. Yin**, A. N. Raegen, S. H. J. Idziak, & J A. Forrest. Crystallization and melting of highly monodisperse poly(ethylene-oxide). *Soft Matter*, 16(34), 7958-7969 (2020). DOI: 10.1039/D0SM00559B [32].
3. **J. Yin**, C. Pedersen, M. F. Thees, A. Carlson, T. Salez, & J. A. Forrest. Surface and bulk relaxation of vapor-deposited polystyrene glasses. *The Journal of Chemical Physics*, 158(9), 094901 (2023). DOI: 10.1063/5.0133668 [2].
4. **J. Yin** & J. A. Forrest. Film thickness dependent stability and glass transition temperature of polymer films produced by physical vapor deposition. *Physical Review Letters*, 130(16), 168101 (2023). DOI: 10.1103/PhysRevLett.130.168101 [3].
5. **J. Yin**, S. Karimi & J. A. Forrest. Rejuvenation in thin films of ultrastable PS prepared by physical vapor deposition. *In preparation* (2023) [4].